Experimental Investigation of Granular Flow and Mixing

Diploma Thesis

by Daniel Brandl

Graz, July 2010

Institute for Process and Particle Engineering

Graz University of Technology

Graz, Austria

Declaration

The work presented in this diploma thesis is to the best of my knowledge and belief, original, except as acknowledged in the text. This material has not been submitted, either in the whole or in part, for a degree at this or any other university.

_____ _____

Place, Date Signature

Eidesstattliche Erklärung

Ich erkläre an Eides Statt, dass ich die vorliegende Arbeit selbstständig und ohne fremde Hilfe verfasst, andere als die angegebenen Quellen nicht benutzt und die den benutzten Quellen wörtlich und inhaltlich entnommenen Stellen als solche kenntlich gemacht habe. Ich versichere, dass ich dieses Diplomarbeitsthema bisher weder im In- noch im Ausland in irgendeiner Form als Prüfungsarbeit vorgelegt habe.

_____ _____

Ort, Datum Unterschrift

Danksagung

Ich möchte mich an dieser Stelle bei den Personen herzlich bedanken, die mir bei der Erstellung dieser Diplomarbeit geholfen haben.

Ich bedanke mich herzlich für die moralische, organisatorische und fachliche Unterstützung, die ich vom Institut für Prozess- und Partikeltechnik erhalten habe. Zunächst möchte ich gerne Herrn Prof. Dipl.-Ing. Dr. Khinast Johannes für die interessante Aufgabestellungen und Themen im Zuge der Diplomarbeit danken, und für das Vertrauen, diese mit bestem Gewissen zu meistern. Ganz besonders bedanken möchte ich mich bei Dipl.-Ing. Radl Stefan für die tatkräftige Unterstützung bei der Erstellung sowie der Korrektur der Diplomarbeit. Vielen Dank für die hilfreichen Ratschläge und die Engelsgeduld. Ich möchte mich auch bei Grubbauer Johann aus der Werkstatt des Instituts für die Mithilfe zur Entwicklung und Fertigung der experimentellen Versuchsaufbauten bedanken. Weiters bedanke ich mich herzlich für die Mitwirkung von Heimburg Hanna, die bei der Abwicklung von Experimenten und deren Auswertungen geholfen hat. Vielen Dank auch allen anderen Mitarbeitern des Instituts für hilfreiche Tipps und Unterstützung.

Ich möchte mich noch bei meiner Familie für die seelische und moralische Unterstützung bedanken. Vor allem meinen Eltern und Großeltern gebührt mein größter Dank für ihr Interesse und die finanzielle Unterstützung.

Nicht zuletzt möchte ich mich noch bei meinen Studienkollegen herzlich bedanken. Die Gesellschaft während des gesamten Studiums, die Unterstützung beim Lernen für Prüfungen sowie die Zusammenarbeit bei diversen Übungen war äußerst lehrreich und hat den Studien Alltag etwas aufgelockert.

Abstract

The understanding of wet granular flows is essential, e.g., to improve the quality of drying or mixing processes. While particle flow simulations have become an important tool, experimental data on granular flows are still important for the validation of these simulations.

This work focuses on the experimental investigation of dry and wet granular flow. A novel two-dimensional setup was constructed and built-up in order to move a bed of particles over an obstacle. Furthermore, the flow of wet and dry granular matter in a four-bladed mixer was investigated. For the observation of granular flow we used a high speed camera and granular particle image velocimetry (gPIV) to calculate the velocity field from an image sequence. The main goal was the analysis and comparison of the calculated velocity fields for different process parameters. The velocity field calculations were done with MatLab and the open-source PIV software “MatPIV”.

In the two-dimensional experimental setup the influence of the particle size, the bed height, blade speed, blade position and the blade geometry was analyzed. The influence of the particle size, moisture content, filling height, stirrer speed and the stirrer position was investigated in the four-bladed mixer. The experiments involving the two-dimensional setup provided details on the flow over a single blade from a perspective parallel to the blade edge. This situation mimics the flow in a cylindrical cross section of the four-bladed mixer, highlighting velocity fields important for granular mixing. The results show various flow features, e.g., heap formation, recirculation in front of the blades that are in qualitative agreement with literature data, as well as with previous simulation results. Also, agglomerate formation, in case of wet granular matter, caused a significant change in the flow pattern on top of the particle bed.

Kurzfassung

Das Verständnis von feuchten granularen Strömungen ist von essentieller Bedeutung, um bestimmte Prozesse wie z.B. Trocknungs- oder Mischvorgänge verbessern zu können. Während die Simulation der Partikelströmungen dafür ein wichtiges Instrument geworden ist, sind experimentell ermittelte Daten immer noch sehr wichtig, um die Ergebnisse aus den Simulationen überprüfen zu können.

Diese Arbeit beschäftigt sich mit der experimentellen Untersuchung von trockenen und feuchten granularen Strömungen. Zu diesem Zweck wurde ein neuartiger Versuchsaufbau entwickelt, und in Betrieb genommen, um ein Partikelbett über ein Hindernis zu bewegen. Weiters wurde die Strömung von trockenen und nassen Partikelschüttungen in einem Rührwerksmischer untersucht. Für die Untersuchungen wurde eine spezielle Hochgeschwindigkeitskamera und die granulare Particle Image Velocimetry (gPIV) eingesetzt, um aus den Bildsequenzen Geschwindigkeitsfelder zu ermitteln. Hauptziel war die Analyse und der Vergleich der ermittelten Geschwindigkeitsfelder für verschiedene Prozessparameter. Die Geschwindigkeitsfelder wurden mit MatLab, sowie der PIV-Software „MatPIV“ ermittelt.

Im zweidimensionalen Versuchsaufbau wurde der Einfluss der Partikelgröße, der Partikelbetthöhe, sowie der Geschwindigkeit, Position und Geometrie des Rührerblattes analysiert. Im Rührwerksmischer wurde der Einfluss von Partikelgröße, Feuchtegehalt, Füllhöhe, Geschwindigkeit und Position des Rührers untersucht. Mit Hilfe des zweidimensionalen Versuchaufbaus konnte ein Einblick in die Strömung innnerhalb des Rührwerksmischers erreicht werden. Die zweidimensionalen Strömungsfelder zeigen das Verhalten der Strömung in einem gedachten (zylindrischen) Schnitt durch den Rührwerkmischer. In den Resultaten wurden verschiedene Strömungserscheinungen wie z.B. Hügelbildung oder Rezirkulation vor dem Rührerblatt beobachtet, die mit vorliegenden Simulationsergebnissen und der Literatur gut übereinstimmen. Außerdem führte die Bildung von Agglomeraten im Falle von feuchten Schüttungen, zu einer signifikanten Veränderung des Geschwindigkeitsfeldes an der Oberfläche des Partikelbetts.

Table of Contents

1. Introduction

1.1. Motivation

Mixing and drying is an important operation in the pharmaceutical industry, food technology, biotechnology and much more. Due to the frequent application of mixers, the behavior of flow and aggregation of powders is of major importance for these industries. Especially the flow of wet granular matter is essential for the proper engineering of these processes, because wet granulation is frequently employed in, e.g., the pharmaceutical industry. However, the description of wet powder flow is still demanding and far from being understood. Recent analysis ([31], [28], [29]) relied on the observation of dry powder flow at the free surface or near the wall in an agitated device ([7], [10], [11], [12], [14]). Still it is very difficult to observe the flow of granular matter inside the drying device. Consequently, this has been done up to no only by a few researches using PEPT [32]. By using specialized simulation techniques it is possible to get a deep inside into granular flow at relatively low cost and within a fraction of time an experimental setup would require. For example, Zhou et al [20] investigated the flow and segregation of particles over flat blades in a vertical cylindrical mixer by using the discrete element method ([25], [26]). However, the validation of these simulations is still necessary with experimental data for selected flow configurations that resemble real world situations.

In this diploma thesis a two-dimensional experimental setup to move a bed of dry and wet granular matter over an obstacle is constructed and built-up. This setup will show the flow of granular matter in a cross section of the particle bed parallel to the flow direction. Such a setup has been build up only once by other researchers in the past [28]. However, in their work they did no include a detailed analysis of flow and mixing using digital particle image velocimetry. Experimental data on the flow behavior could help in designing of improved apparatuses for mixing, coating, granulation, etc. on an industrial scale. By the use of modern digital cameras it is possible to record images with better resolution and shorter time delay.

1.2. Goals

The individual goals of this diploma thesis are:

- an experimental setup for investigating 2D granular flows has been constructed, built-up, tested and started up,
- a particle image velocimetry (PIV) system has been installed on the 2D experimental apparatus,
- PIV techniques using patterned light for cohesive powders have been investigated,
- the granular flow has been analyzed in the two-dimensional experimental setup, and the following influences on the flow field have been investigated:
  - particle size,
  - filling height,
  - blade speed (Froude number),
  - blade position, and
  - blade geometry.
- the granular flow in a (three-dimensional) vertical mixer has been analyzed and the following influences on the flow field have been investigated:
  - particle size,
  - moisture content,
  - filling height,
  - stirrer (blade) speed (i.e., the Froude number), and
  - stirrer position.

In Chapter 2 of this thesis, the theoretical basis of granular flows is discussed with the focus on dense and wet granular matter. In Chapter 3, the design of the 2D experimental setup is described. The Investigations of granular flow are documented in Chapter 4.1. Comparisons of the experiments in the two-dimensional flow setup are documented in chapter 4.2.

2. Basics of Granular Flows

Granular flows can be understood as movement of particle assemblies. Granular flows occur in nature in the form of avalanches, landslides, volcanic activities, etc.. These flows often include a broad range of sizes and shapes of particle and different materials. For that reason it is difficult to describe the flow of each particle in a particle bed.

The industrial processing of bulk solids consumes roughly 10 % of all the energy produced on this planet. On the one hand these are industries that deal with a large quantity of bulk materials (e.g., mining). Typical problems associated with these industries are the transport of particles through pipes, storage or segregation (i.e., de-mixing). On the other hand, there are the chemical or pharmaceutical industries where materials are prepared in relative small quantities, but with a high value added. In this case, the purity, process reproducibility and mixing quality are the major quality attributes associated with bulk solids.

2.1. Mechanics of Particle Flow

In granular flows a lot of physical phenomena have an effect on individual particle motion. For example, there is an interaction with the outside boundaries (e.g., vessel walls, moving or static obstacles) that may result in stick or slip of particles near these walls. This situation is different, e.g., to the flow of Newtonian liquids, where a no-slip assumption near solid walls (i.e., sticking of the fluid to the wall) is appropriate. Furthermore, in case of wet granular matter, the interaction between particles and liquid bridges has to be also considered.

In the following, some laws for particle interaction and models are detailed. In the basic law for particle motion, i.e., Newton's law of motion (see Eqn. 1), these forces are summed-up and used to determine the velocity and position of individual particles.

$$\rho_p \cdot V_p \cdot \frac{\partial \vec{v}}{\partial t} = \sum F_i \qquad \textbf{(1)}$$

F_i ..... Individual force action on the particle [N]

$\vec{v}$ ..... Velocity of the particle [m/s]

V_p ..... Volume of the particle [m³]

t ..... Time[s]

ρ_p ..... Density of the particle [kg/m³]

2.1.1. Body Force

The gravity force is described as:

$$\vec{F}_g = \rho_p \cdot V_p \cdot \vec{g} \qquad (2)$$

$\vec{F}_g$ ..... Gravity force on a particle [N]

$\vec{g}$ ..... Acceleration of gravity [m/s²]

2.1.2. Collision Forces

In a granular bed in motion, collisions between particles and particle and a wall have an influence on the flow. When a single particle hits another, its kinetic energy will be transformed into elastic and inelastic deformation energy. The elastic energy causes the particle to rebound, while the inelastic deformation energy is dissipated during the contact.

A detailed calculation of the collision forces is extremely difficult, since the deformation of the colliding particles (or the particle and the wall) would have to be calculated. Hence, often collision forces are modeled with simplified models, e.g., consisting of a spring and a dashpot (see paper of Cundall and Strack [41]).

2.1.3. Friction Force

The friction force F_r is proportional to the normal force F_N (Figure 1) and acts tangential on the interaction plane of the bodies in contact. The friction coefficient μ depends on the material of the interacting bodies. It is necessary to overcome the static friction to get a body sliding. The static friction coefficient μ_0 is greater than the dynamic friction coefficient μ_d where the body is sliding ($\mu_0 < \mu_d$).

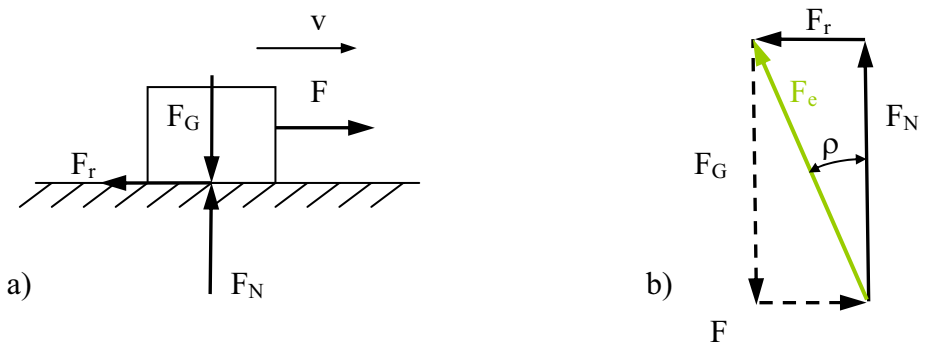

Figure 1: a) Forces on a sliding body: F_G…weight, F_N…normal force, F…applied force to move body, F_r…friction force, v…velocity b) force diagram including the effective force F_e. The friction angle ρ between F_e and F_N describes the magnitude of the friction force [16].

$$F_r = F_N \cdot \mu \qquad (3)$$

F_r..... Friction force [N]

F_N..... Normal force [N]

μ..... Friction coefficient [-] (μ = tan ρ, μ = μ_0 and ρ = ρ_0 for static friction)

2.1.4. Rolling Friction

Due to deformation of the interacting bodies, rolling friction occurs. Thus, the particle has to be lifted over the contact point D (see Figure 2). The rotational moment balance over this contact point D is:

$$\sum M_{(D)} = 0 = F_G \cdot f - F \cdot l \qquad (4)$$

F_G..... Weight of the body [N]

F..... Applied force to roll body [N]

f..... Distance between the contact point D and centre of body in the vertical direction [m]

l..... Distance between the contact point D and the contact point of the applied force in the horizontal direction [m]

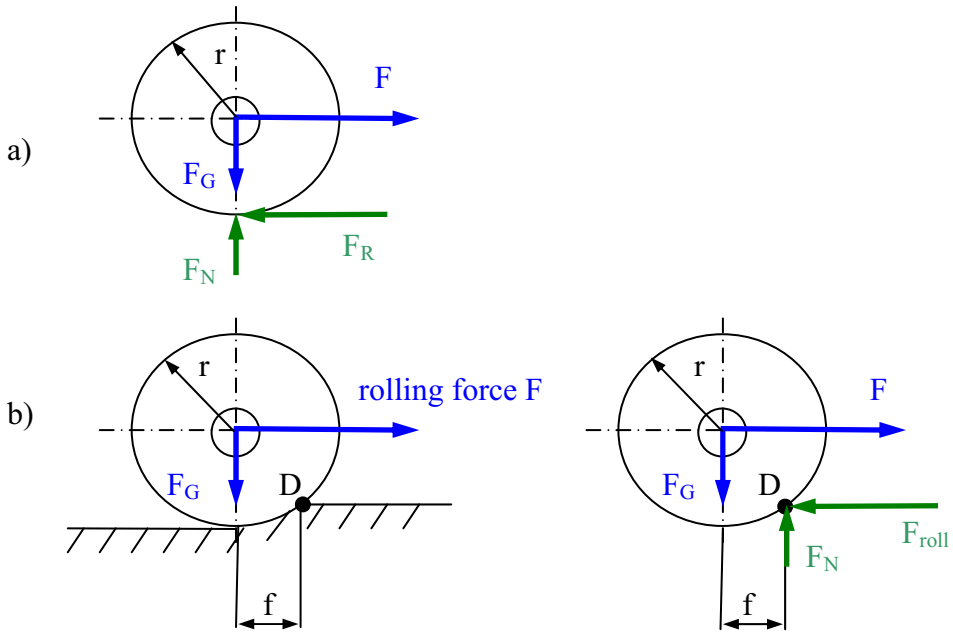

Figure 2: a) Forces on a rolling rigid body, b) forces on a rolling real body [16].

2.2. Forces in Wet Granular Matter

Additional to body, collisional and friction forces, a number of surface forces exist in wet granular matter. Cohesive forces are:

- **Van-der-Waals Forces:** Van-der-Waals forces can be split up into three types of forces: the so-called London forces are caused by transient dipole interactions of non-polar molecules, the Debye forces arise when a polar molecule induces a dipole in a non-polar one, and Keesom forces have their origin in the interaction of molecules with permanent dipoles.

  Van-der-Walls forces are typically relevant only for particles smaller than 100 µm and for small distances between particles or the particle and a wall.

- **Electrostatic Forces:** Electrostatic forces occur between electrical charged particles and can be described by Coulomb's law. They are relevant for charged particles smaller than approx. 1 mm and act on a relatively large distance.

- **Liquid Bridge Forces:** Liquid bridge forces are caused by surface tension effects in wet particle assemblies. They are typically the dominant long-range forces in wet granular matter (because typically the liquid is electrically conducting) and become dominant at a particle diameter of 1 mm. Chapter 2.2.1 provides more details about liquid bridge forces.

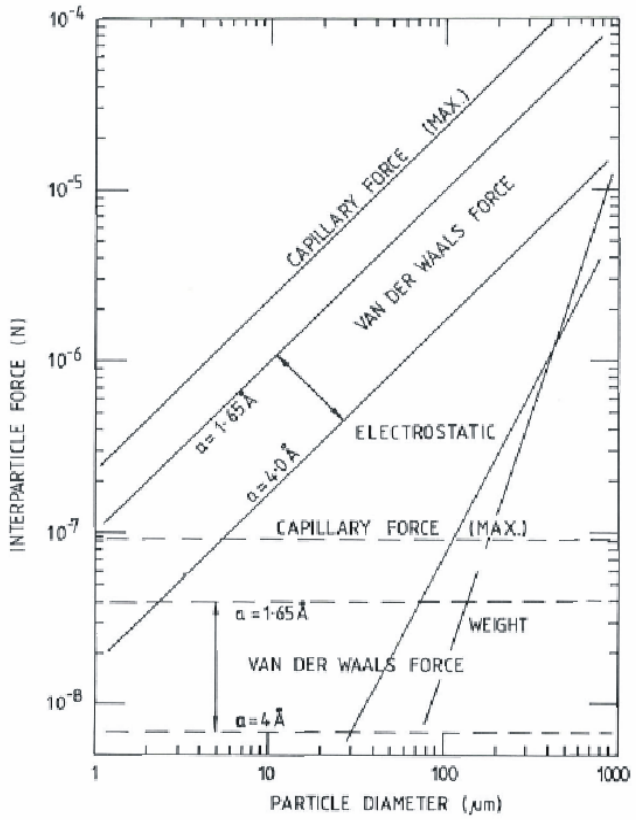

Figure 3: Comparison of the magnitude of cohesive forces over particle diameter (dashed lines indicate asperity-to-plane contact). Theoretical interparticle forces for single-point contact between equal spheres (in air), with particle weight plotted for comparison [42].

2.2.1. Liquid Bridge Forces

A packed bed of wet particles (i.e., a three-phase system of solid particles, a gas phase and a liquid) establishes a certain configuration of liquid bridges between individual particles [22]. The relation between fluid and gas leads to three different regions of fluid distribution, the "capillary state", the "funicular state" and the "pendular state" (Figure 4).

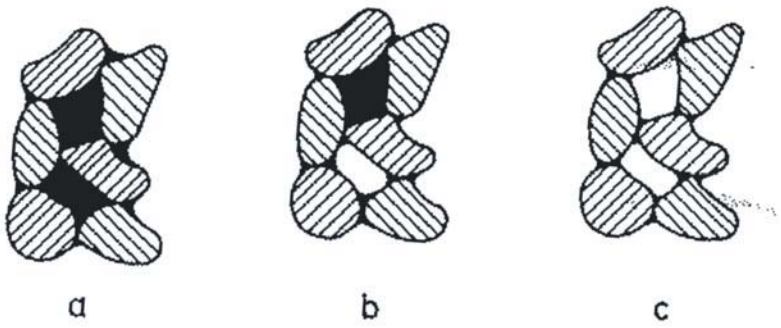

Figure 4: Schematic representation of fluid distribution in particle beds: a) capillary state, b) funicular state, and c) pendular state [21].

In the capillary state, all pore spaces are filled with liquid, and there exist no liquid bridges between the particles (Figure 4a). An intermediate state exists if the fluid fraction in the pore spaces will be particularly reduced, and completely filled pore spaces coexist with liquid bridges (Figure 4b). This state is called funicular state. At an even lower content of fluid in the system, the pendular state is reached. Here a fluid phase exists in the form of liquid bridges (Figure 4c) only between two particles. Only for this state, the shape of the liquid bridges and the associated forces can be calculated relatively easily. This is detailed in the following paragraphs.

Shape and Forces in Liquid Bridges

The calculation of shapes and forces of liquid bridges are shown in Schubert [21], as well as in Sartor [23] and Schaber [24]. The boundary conditions are force equilibrium and a uniform contact angle δ between two solid bodies (Figure 5).

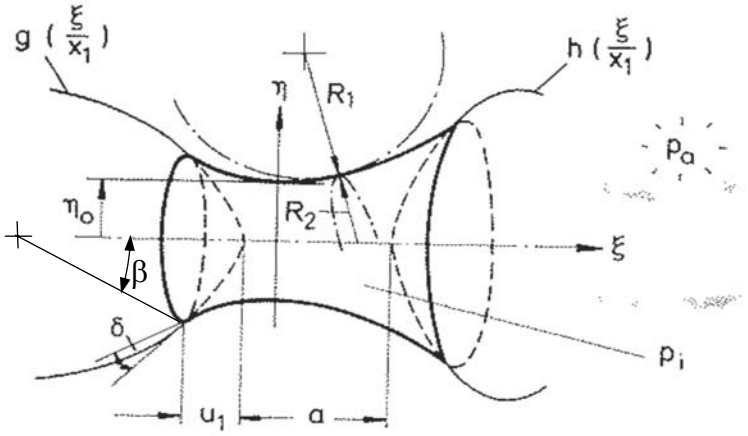

Figure 5: Example of a liquid bridge between two rotation symmetric solid bodies [21].

Two characteristic values were established to describe the liquid bridges between two spheres or between a sphere and a vertical plane:

γ ..... Interfacial or surface tension [N/m²]

x ..... Characteristic length (i.e., the diameter) of spheres [m]

The following values depend on the characteristic length and the surface tension:

$$\frac{p_K \cdot x}{\gamma} = \frac{F}{\gamma \cdot x} = \frac{V_L}{2 \cdot \pi \cdot x^2/6}, \left(\frac{V_L}{\pi \cdot x^3/6}\right)^* = f_i(\beta, \frac{a}{x}, \delta) \quad \textbf{(5)}$$

$\frac{p_K \cdot x}{\gamma}$ ..... Specific capillary pressure [Pa]

$\frac{F}{\gamma \cdot x}$ ..... Specific adhesive force [N]

$\frac{V_L}{2 \cdot \pi \cdot x^2/6}$ ..... Specific fluid volume [m³] for a liquid bridge between two spheres

$\frac{V_L}{\pi \cdot x^3/6}$ ..... Specific fluid volume [m³] for a liquid bridge between a sphere and a flat wall.

β..... Bridge angle [°] (i.e., the angle between the connection line from the center point of the sphere and contact point of the liquid bridge, as well as and the centers of the spheres)

a..... Length of the liquid bridge [m] (= distance between the two bodies in contact at the location of the center line of the sphere)

δ..... Contact angle [°] (= angle between the tangent to the sphere at the contact point of the liquid bridge and the liquid bridge)

The following diagrams show some examples of liquid bridge between two solid bodies:

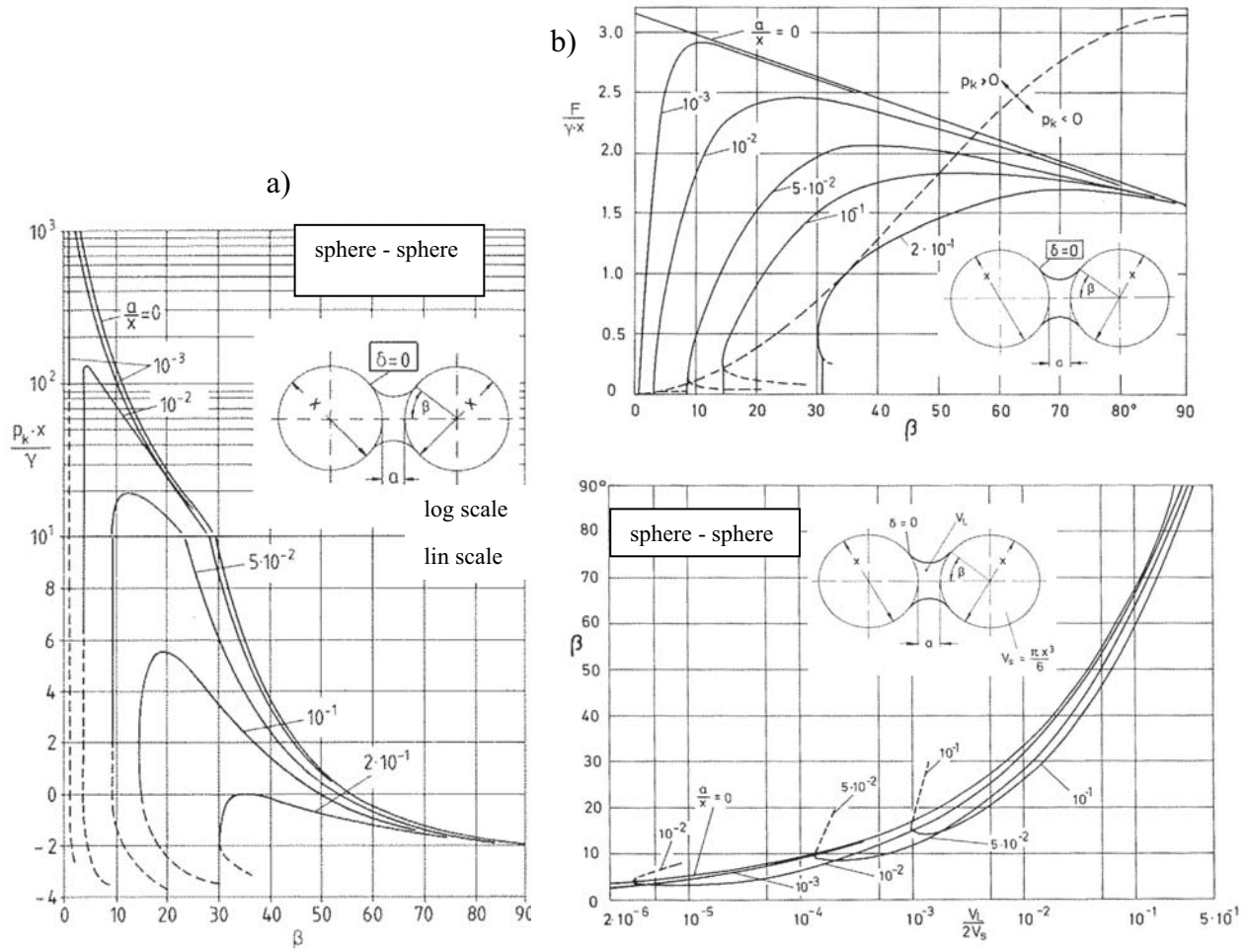

Figure 6: a) specific capillary pressure, b) specific adhesive force and c) specific fluid volume of a liquid bridge between two equal spheres in relation to the bridge angle β for a contact angle δ = 0 [21].

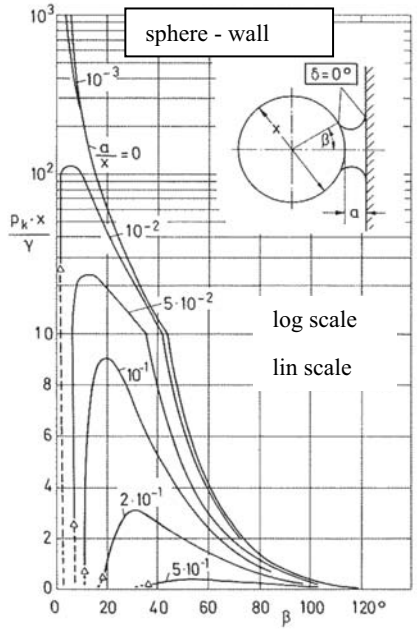

Figure 7: Specific capillary pressure of a liquid bridge between two equal spheres in relation to the bridge angle β for a contact angle δ = 0 [21].

Granular Bond Number

The granular Bond number Bo_g is defined as the ratio of the maximum cohesive force F_C to the particle weight F_w [25].

$$Bo_g = \frac{F_C}{F_w} = \frac{2 \cdot \pi \cdot \gamma \cdot R}{\frac{4}{3} \cdot \pi \cdot g \cdot R^3 \cdot \rho} \tag{6}$$

γ ..... Interface- or surface tension [N/m²]

R ..... Radius of the particle [m]

ρ ..... Density of the particle [kg/m³]

Collision Number

In a sheared system of particles, collision forces play a significant role [26]. Typically, the collision number Co is used to quantify the relative importance of these forces relative to cohesive forces. Co is defined by the ratio of the maximum capillary force to the collision force F_{Bg} due to Bagnold [27].

$$Co = \frac{F_C}{F_{Bg}} = \frac{2 \cdot \pi \cdot \gamma \cdot R}{\pi \cdot \rho \cdot R^4 \cdot \kappa^2 \cdot \left(\frac{d_u}{d_y}\right)^2} = \frac{2 \cdot \pi \cdot \gamma}{\pi \cdot \rho \cdot R^3 \cdot \kappa^2 \cdot \left(\frac{d_u}{d_y}\right)^2} \tag{7}$$

κ^2 ..... Parameter related to the Particle Packing Density [-]

$\left(\frac{d_u}{d_y}\right)^2$ ..... (Squared) shear Rate of the Flowing Region [-]

Three limits for this number can be defined [26]:

- In a slow flow (i.e., the so-called pseudo-static flow) the collision force is small relative to the particle's weight. Thus, $F_{Bg} << F_w < F_C$. In this case $Co >> Bo_g > 1$. The collision force can be neglected in this regime, and hence Bo_g can be used alone to characterized the granular flow.
- In a granular flow, where the collision forces are larger than the particle's weight (i.e., $F_{Bg} >> F_C > F_w$), the relation

  $Bo_g > 1 >> Co$

  holds. This is a fast flow regime, where the particle interaction is primarily dictated by the collision number.

- In an intermediate flow, where the collision force is in the order of the particle weight (i.e. $F_w \approx F_{Bg} < F_C$), the relation

  $Bo_g \approx Co > 1$

  may hold. In such a flow, it is important to consider both the Bo_g number as well as the Co number.

2.3. Description of Granular Flows

2.3.1. Regimes of Granular Flow

Granular flows can be classified into three different regimes. The first regime of granular flow is a dense quasi static regime in which the deformations are very slow and the particles interact by frictional contacts [8]. This behavior appears, e.g., in a mixer filled with sand at low rotational speeds (see region "a" in Figure 8).

The second regime is a dilute, rapid granular flow regime. In this regime the particles interact by collision [9]. For example, in a mixer the effect of the gaseous flow regime occurs at higher rotation speed at the top of the particle bed (see region c in Figure 8).

The third regime is a liquid regime that lies between the regimes of dense and gaseous flow (see region b in Figure 8). In this regime, the material is dense but still flows like a liquid and the particles interact both by collision and friction [10].

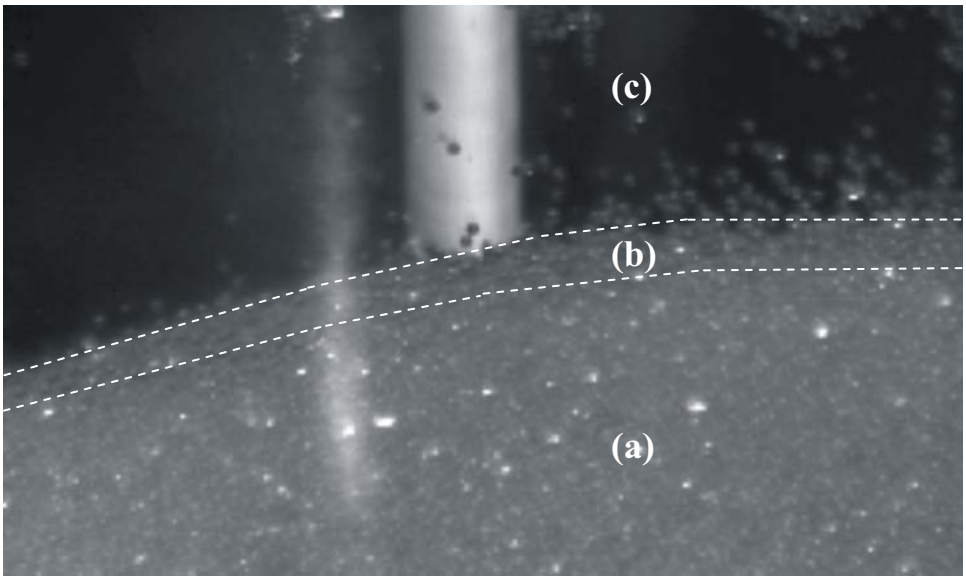

Figure 8: An illustration of the (a) solid, (b) liquid and (c) gas flow regimes obtained in the experiment with stirred glass beads in a bladed mixer.

2.3.2. Angle of Repose, Angle of Movement [1]

If grains (dry sand) are dropped they will build up a pile with a shape that is similar to a cone. After the dropping process is done, all particles will stop moving down the pile and the pile will have a defined slope. The angle θ_r of the slope is then called "angle of repose". If the angle of the slope exceeds a certain value, i.e., the angle of movement $\theta_m > \theta_r$, the pile collapses and individual particles will start to flow down the slope. The difference between θ_m and θ_r is referred to as the relaxation angle δ. δ is about 2° for dry granular matter.

2.3.3. The Dimensionless Shear Rate

Forterre et al. analyzed the behavior of granular matter (i.e., steel beads) flowing a pile [7]. For such a simple (plane) shear flow of rigid particles (i.e., the flow in the top layer of the particles in the pile) a dimensionless shear rate can be defined as:

$$I = \frac{\dot{\gamma} \cdot d}{\sqrt{P/\rho_p}} \qquad \textbf{(8)}$$

I..... Dimensionless shear rate [-]

$\dot{\gamma}$ ..... Shear rate [s^{-1}] ($\dot{\gamma} = \frac{v}{h}$, h…difference between two surfaces in [m], ν… difference of velocity between both surfaces [m/s])

d..... Particle diameter [m]

p..... Pressure [Pa]

ρ_p ..... Density of the particle [kg/m^3]

Small values of I correspond to the quasi static regime, whereas large values of I correspond to rapid granular flow. In the case of the particle flow down an inclined plane, the results are as following:

- the volume fraction is constant across the flowing layer,
- for thick layers, the velocity profile follows the so-called Bagnold profile and varies with the depth to the power of 3/2 [11],
- for thin layers, when h is close to the minimum thickness for the flow, the velocity is closer to linear [12], and

- there is evidence of an empirical flow rule, where the depth-average velocity $\langle u \rangle$ is related to the inclination by an empirical relation of the form $\langle u \rangle / \sqrt{g \cdot h} \cdot \alpha \cdot h / h_{stop}(\theta)$ where $h_{stop}(\theta)$ is the minimum thickness of the flow [13].

In the flow down a pile, a free surface flow develops with a velocity profile approximately linear in the upper region, followed by an exponential creeping tail below [14].

2.3.4. Simple Flow Models [1]

Avalanches are perhaps the most extensively studied phenomenon in the physics of sand piles. Duran [1] presents three different approaches how to describe a flow of granular matter. These avalanche models are fundamentally different to each other, but treating the same phenomenon.

Cellular Automaton Model (CAM)

The CAM was originally proposed by Bak et al. [3], for the purpose of studying systems in a self-organized, so-called "critical" system. It is a model to predict the property of an avalanche with statistical methods. In the CAM, hexagonal boxes (so-called "cells") are stacked up on the top of each other to build columns according to a few simply rules:

- the height difference between two adjacent columns cannot be greater than two units. (i.e., to simulate the angle of repose), and
- when the boxes in a column start to move, e.g., because of an excessive height relative to its neighbor columns, the movement of a set of two other unit cells is induced.

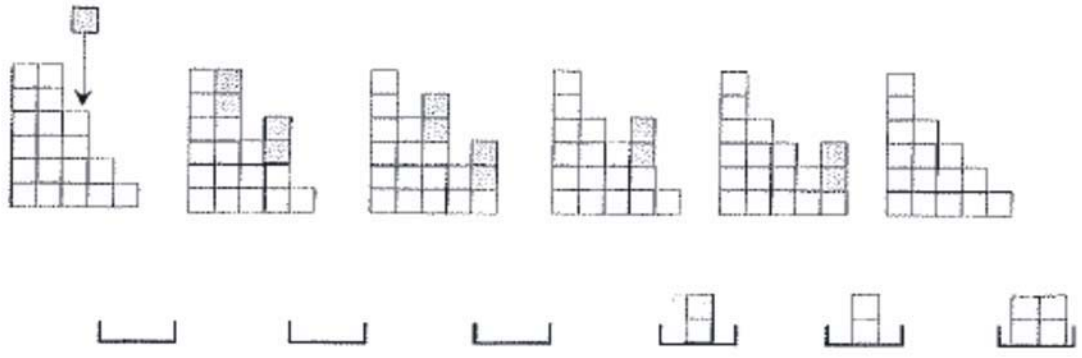

Figure 9: Principle of the one dimensional cellular automation model (CAM) (according to [3]).

Such a CAM is useful for predicting the free surface of granular flows only. The flow, and consequently mixing, of the particles within the bed cannot be calculated. This model is hence not usefully for this study and has been included for completeness.

Stick - Slip Model of Avalanches

This is a simple macroscopic model that establishes a relation between the slope of a pile and the flux of particles. A system of coupled equations is used to describe the behavior of particles sliding down a slope. This is done by considering a set of particles as a box with a spring that is pulled on a frictional surface, i.e., a stick-slip mechanism (see Figure 10).

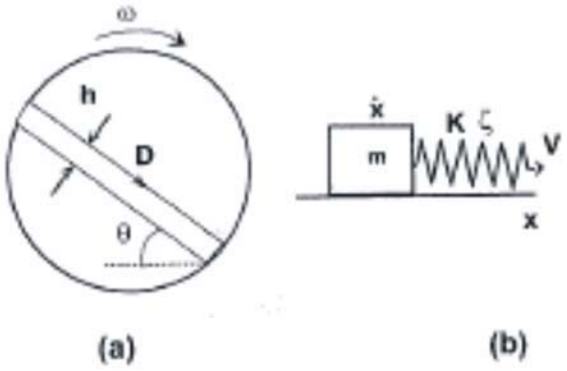

Figure 10: Illustration of (a) the real avalanching processes and (b) the simplified stick-slip mechanism in a rotating cylinder. [1]

h..... Thickness of the set of particles [m]

D..... Flux of particles [m^3/s]

θ..... Inclination angle [°]

ω..... Rotation speed of the cylinder [s^{-1}]

m..... Particle mass [kg]

v..... Velocity of the spring-system [m/s]

K..... Stiffness of the spring [N/m]

ζ..... Deformation of the spring [m]

The two systems (i.e., the real avalanching process and the simplified box model) are governed by the same set of equations.

$$\theta \leftrightarrow \zeta$$

$$D \leftrightarrow \dot{x} \qquad (9)$$

$$\omega \leftrightarrow V$$

When the set of particles is in motion (i.e., slipping occurs), the deformation of the spring is given by the following equation which describes the motion of a harmonic oscillator at an angular frequency of $\omega = \sqrt{K/m}$:

$$m \cdot \frac{d^2\zeta}{dt^2} + K \cdot \zeta = m \cdot g \cdot \mu_d \cdot \left(V - \frac{d\zeta}{dt} \right) \qquad \textbf{(10)}$$

μ_d ..... dynamic friction coefficient [-]

The condition for sticking can be described as following:

$$\frac{d^2\zeta}{dt^2} = 0 \qquad \text{if} \quad \frac{dx}{dt} = 0 \qquad \text{and} \quad K \cdot \zeta < m \cdot g \cdot \mu_s \qquad \textbf{(11)}$$

μ_s..... static friction coefficient [-]

In the results shown in Chapter 4.2.4, particles are moving down the heap formed in front of a moving blade. Such flow characteristics could be described by using this (relatively simple) avalanche model.

The Shallow-Water Description

In the modeling of natural hazards such as landslides or debris flows, Savage et al. [15] derived depth-averaged equations for an two dimensional flow down a slope (Figure 11). He assumed that the granular flow is incompressible in this case.

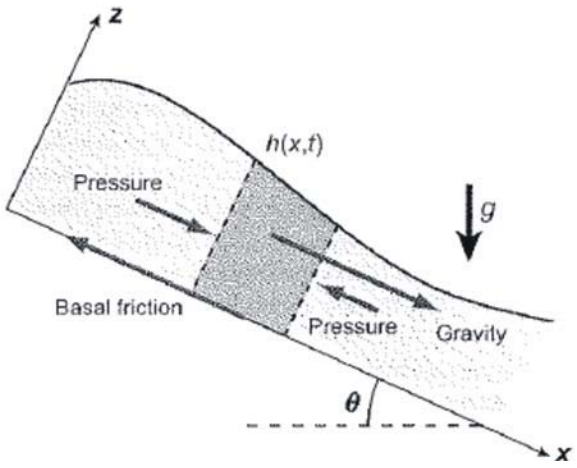

Figure 11: Forces balance in the shallow-water description [15]

The mass and the momentum conservation equation describing the shallow water configuration of granular flow are as follows:

$$\frac{\partial h}{\partial t} + \frac{\partial h\langle u\rangle}{\partial x} = 0 \tag{12}$$

$$\rho_p \cdot \phi \cdot \left(\frac{\partial h\langle u\rangle}{\partial t} + \alpha \cdot \frac{\partial h\langle u\rangle^2}{\partial x} \right) = \left(\tan\theta - \mu_b - K \cdot \frac{\partial h}{\partial x} \right) \cdot \rho_p \cdot \phi \cdot g \cdot h \cdot \cos\theta \tag{13}$$

h ..... Local Thickness of the granular flow [m]

t ..... Time [s]

$\langle u \rangle$ ..... Depth-averaged velocity [m/s]

ϕ ..... Volume fraction [-]

ρ_p ..... Density of the particles [kg/m³]

α ..... Coefficient related to the assumed velocity profile across the layer [-]

μ_b ..... Basal friction coefficient [-]

K ..... Coefficient that represents the ratio of the normal horizontal stress and the normal vertical stress [-]

θ ..... Inclination angle of the slope [°]

Using the shallow water description is another possibility to describe granular shear flows, e.g., particles moving down the heap formed by the blade (see, e.g., the results displayed in Chapter 4.2.4). However, the shallow water equation is only appropriate for the description of thin sheets of flowing particle assemblies.

2.4. Particle Image Velocimetry

Particle image velocimetry (PIV) is an optical measurement technique in the field of fluid flow and solid mechanics. PIV basically consists of image acquisition and a post-processing step to evaluate the flow field in a two-dimensional cross section. Optical flow-analysis is based on the interaction of light with particles, i.e., reflection, absorption or scattering of (visible) light. Unlike the motion of fluid, granular flows need no addition of tracer particles to visualize the flow. Typically, the color or reflection properties of particles are used to calculate the flow field. A measurement system to analyze granular flows consists of the following components:

(Digital) High speed Camera

The high speed camera, which is the core of the PIV-system, is used to record image sequences of granular matter in motion at constant time intervals. Depending on the flow velocity, the acquisition rate is between a few Hertz (for slow flows) and a few kilo-Hertz (for fast flows).

Computer and Image Acquisition Software

Some camera systems don't have an internal memory and the data must be stored on a connected computer. Typically, the camera can be synchronized, e.g., with the motion of a blade, in time.

Software for Calculating Vectors and Vector Fields

To extract the flow field from the image sequence, sophisticated software packages based on numerical algorithms for cross- or autocorrelation of an image pair are used.

2.4.1. The Principle behind PIV

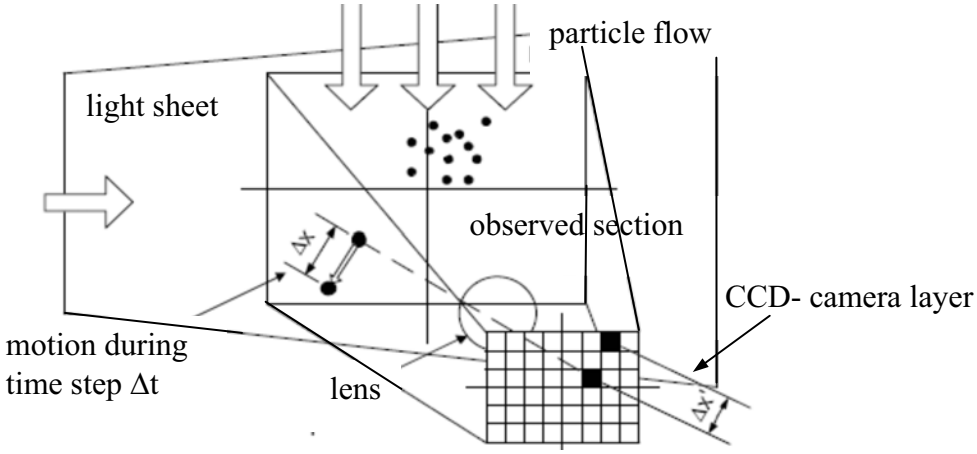

Figure 12: Principle of the PIV-technique (Gleirscher [18]), (CCD….charge coupled device).

A two-dimensional cross-section used for PIV is illuminated with a thin light sheet, and the particles in the light sheet are recorded with the recording medium (i.e., the camera). By comparing an image with a time step later, it is possible to draw conclusions on the movement of the particles. Thus, PIV calculates the displacement of particles between two consecutive images. This calculation is based on auto or cross correlation of two matrices made up the two images.

Auto Correlation

A grid cell ($\hat{I}_{X,Y} \subset I$) (a so-called "interrogation window") is correlated with itself. X and Y describe the grid position. The auto correlation applies for double- or multi exposed single images where the picture of the same particle exists more than one times (Figure 13). This method has been often used for conventionally recorded image sequences, but is not used for state-of-the-art digital recording systems.

Cross Correlation

The grid cell $\hat{I}_{X,Y}$ of the first image is correlated with the same grid cell $\hat{I}_{X,Y}$ of the second image. The cross correlation typically applies for single exposed images (Figure 13).

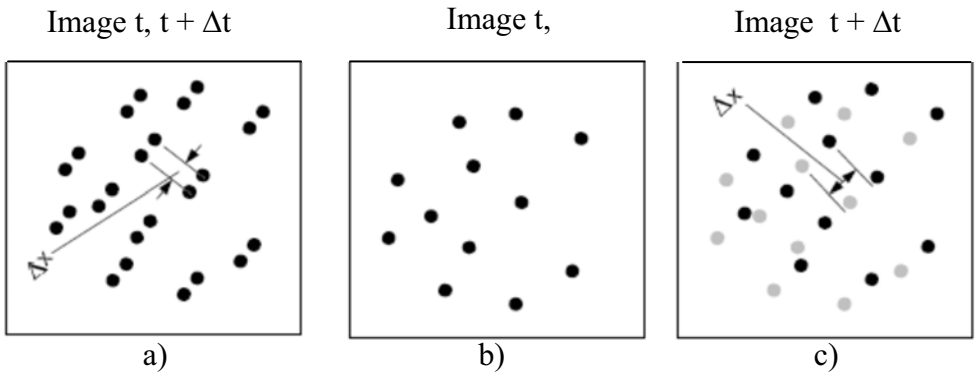

Figure 13: a) double exposed single image for autocorrelation, b) + c) single exposed double image for cross correlation [18]

2.4.2. The Software "MatPIV"

For the calculation of the vector fields the open-source package "MatPIV" is used as an add-on to the software package "MatLab" [33]. An introduction on how to use MatPIV is available in Sveen J.K. [17]. In MatPIV, the cross correlation is used to calculate the particle displacements between two images.

Calculation Procedure

In the first step of the calculation procedure the imported (grayscale) images is divided into a number of grid cells in x- and y- direction of a Cartesian coordinate system. Then, the grid cells are arranged in a matrix. In each individual cell $\hat{I}_{X,Y}$ of this matrix, the program is calculating the differences between two consecutive images and the so-called correlation matrix is calculated. The local maximum in this correlation matrix determinates the direction and the magnitude of the displacement for this cell. Subsequently, the velocity can be

calculated from this displacement and the time difference between the image pair. Following this principle, MatLab calculates the velocities for all grid cells and creates a vector field (see Figure 14, Figure 15 and Figure 16).

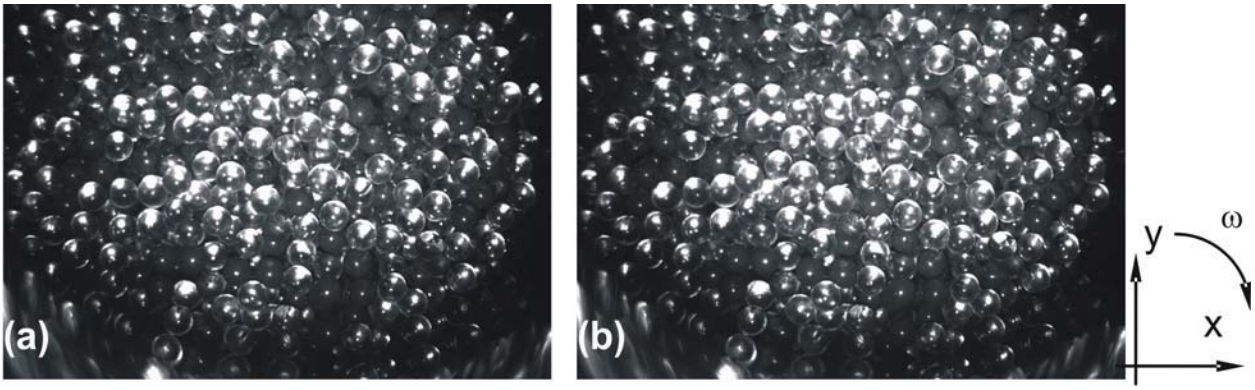

Figure 14: (a) and (b) are two grayscale images from the flow of glass beads at the top of a vessel stirred by a four-bladed mixer with a time delay of 0.002 [s] [19].

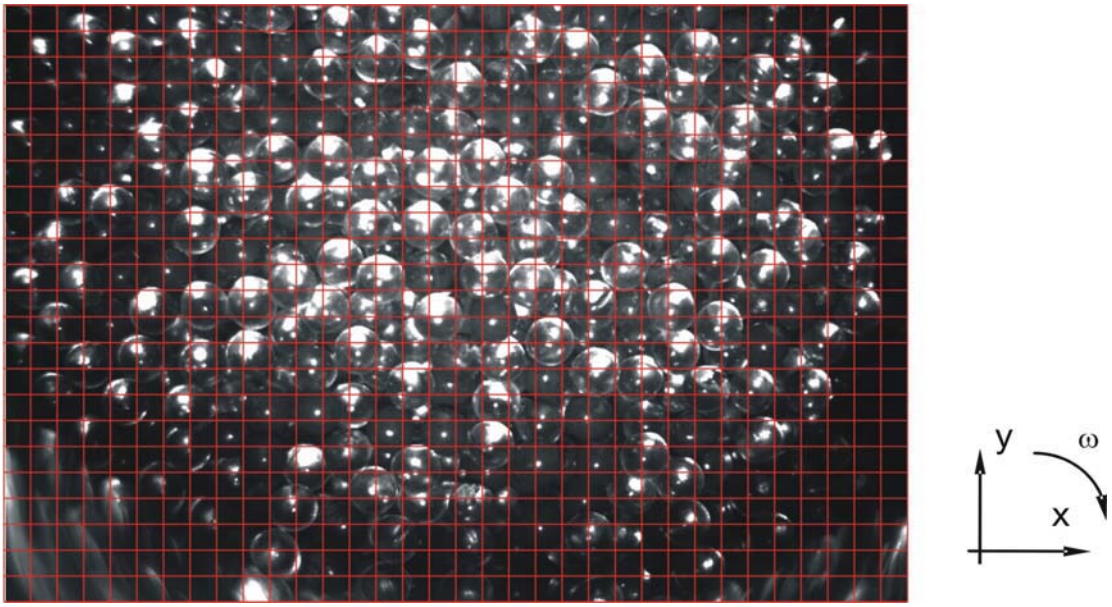

Figure 15: 64x64 pixel grid cells superimposed to the image (b) in Figure 14 [19].

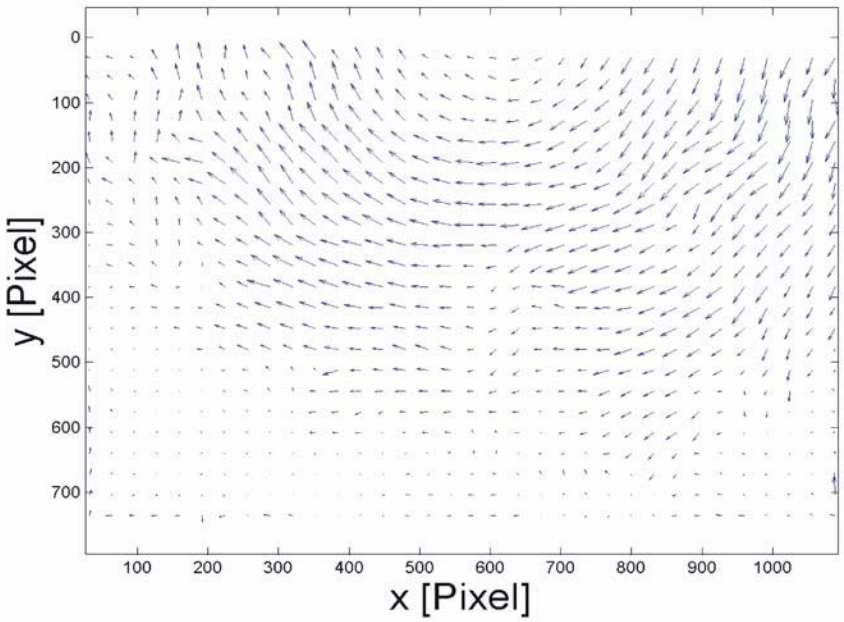

Figure 16: Image shows the resulting vector field from the image data in Figure 14 [19].

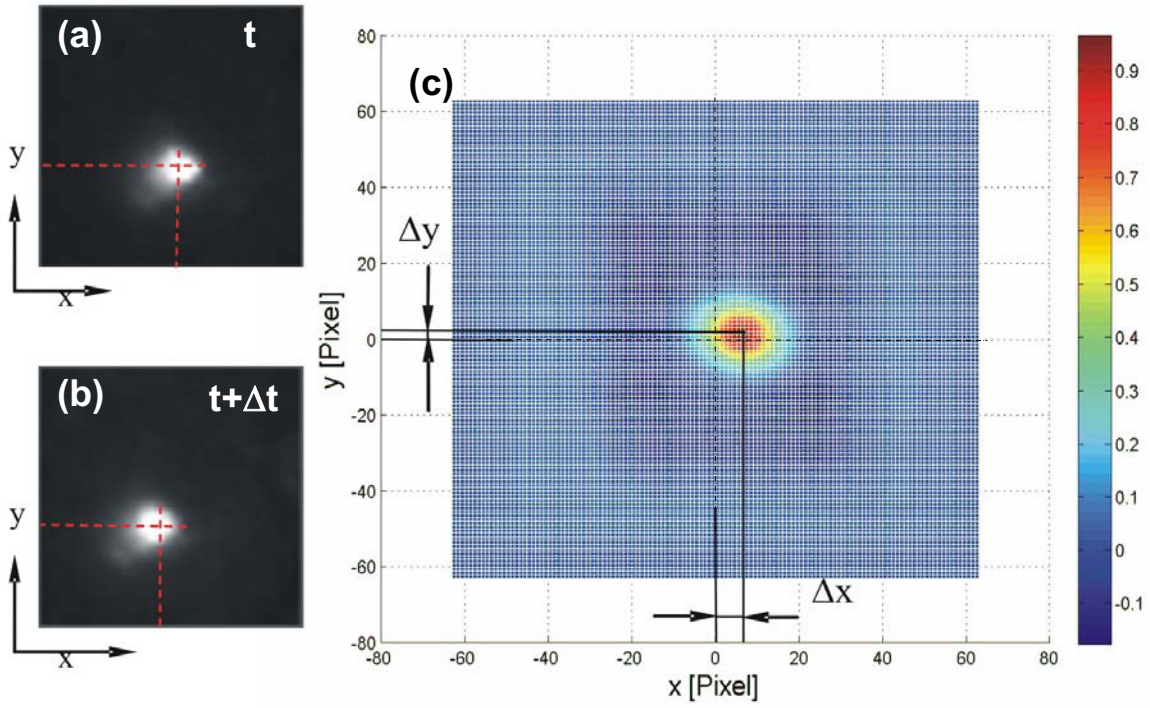

Figure 17: (a) and (b): cell no. 9/17 of the image in Figure 15 for two different time instances; (c): the cross correlation function for the image pair in (a) and (b) [19].

2.5. Background on Experimental Setups for the Flow over a Blade

Bagster and Bridgewater developed an experimental setup to investigate the flow of granular material over a moving blade [28]. They used an open moving box apparatus, while the obstacle (i.e., the blade) was standing still. The dimensions of the box were 600 x 300 x 100 [mm]. The blade (with an inside width of 100 [mm]) was mounted on a long rod and placed inside the box. The front and the rear face were made of glass. For the image acquisition of the granular flow a conventional photographic camera was positioned near the blade (Figure 18). To move the box a variable speed electric motor was used. Glass beads with a mean diameter of 2.13 [mm] and a standard deviation of 0.09 [mm] were taken as sample material for their experiments.

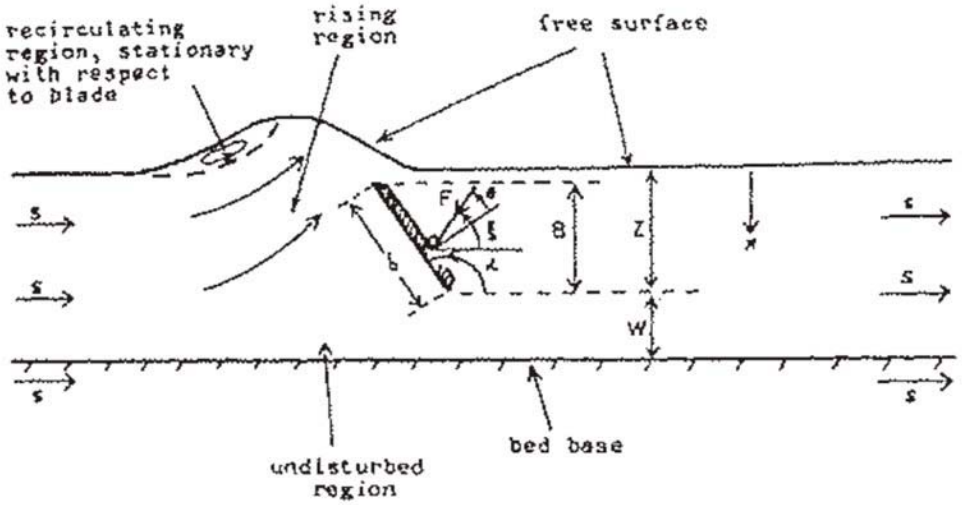

Figure 18: Schematic representation of the flow of granular material over a blade [28].

The main goal of this paper was to investigate effect of different immersion, blade angles, velocities and blade materials. Bagster and Bridgewater measured the force that acts on the blade (see their previous investigations, [29] and [30]).

The study of Lekhal et al. [31] used a particle bed in a cylindrical vessel that was stirred by a bladed mixer. They used a PIV system to observe the granular flow at the free surface and at the side wall of the vessel (Figure 19).

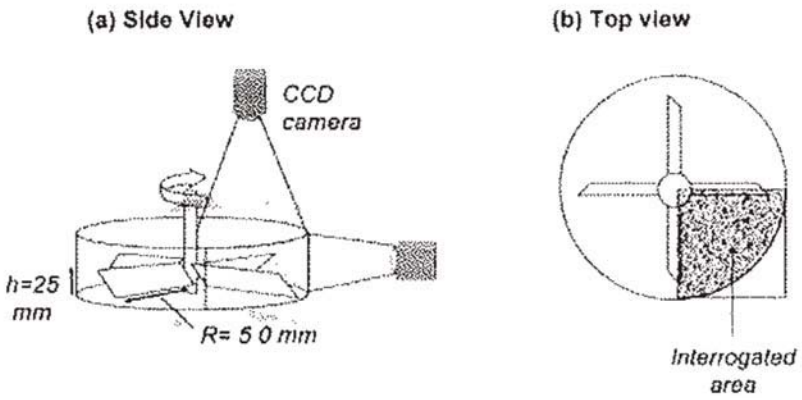

Figure 19: Typical experimental setup to investigate granular flow in a four-bladed mixer [31].

In our previous work [19], an experimental mixer setup including a PIV system was constructed and built-up (Figure 20). In this work we measured the flow cohesionless dry glass beads. The investigation setup was similar to Lekhal et al [31], however, we used a temperature and pressure controlled vessel as well as used glass beads for our experiments. Image acquisition at the free surface of the flow as well as at the bottom and the side wall of the glass vessel were realized using the PIV camera. We also used this setup for perform some measurements for this diploma thesis (see Chapter 4.1). For the investigations of two-dimensional granular flows (Chapter 4.2) we also used the same PIV camera system.

Figure 20: Photography of the vacuum dryer and the PIV camera

Remy et al. [34] performed numerical simulations of granular flow in a cylindrical vessel agitated by a four-bladed impeller with help of the discrete element method (DEM). Newton's

equations of motion were used to describe the flow behavior for each particle within the bed. They investigated the dependence between the magnitude of the shear stresses and the friction coefficient for obtuse and acute blade pitch orientation (Figure 21).

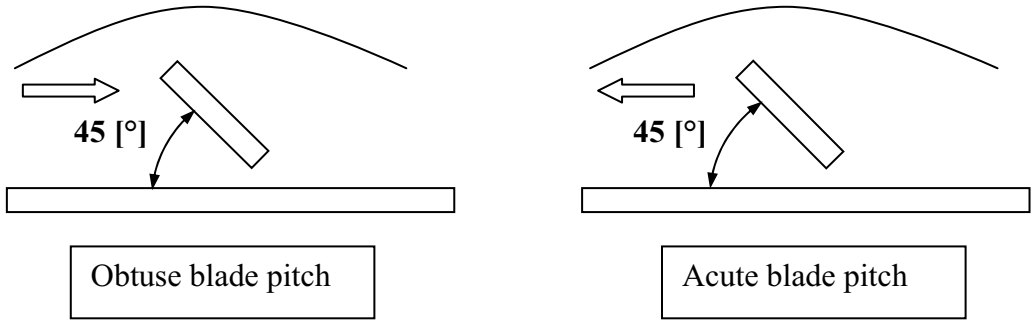

Figure 21: Schematic representation of blade orientation [34].

The study of Conway et al. [37] examined flow and segregation of granular material in a cylindrical mixer geometry agitated by four 45 [°] pitched blades. (Near) monodisperse and polydisperse materials were observed at high and slow shear rate processes (see in Figure 22). They also used a PIV analysis system for their investigations.

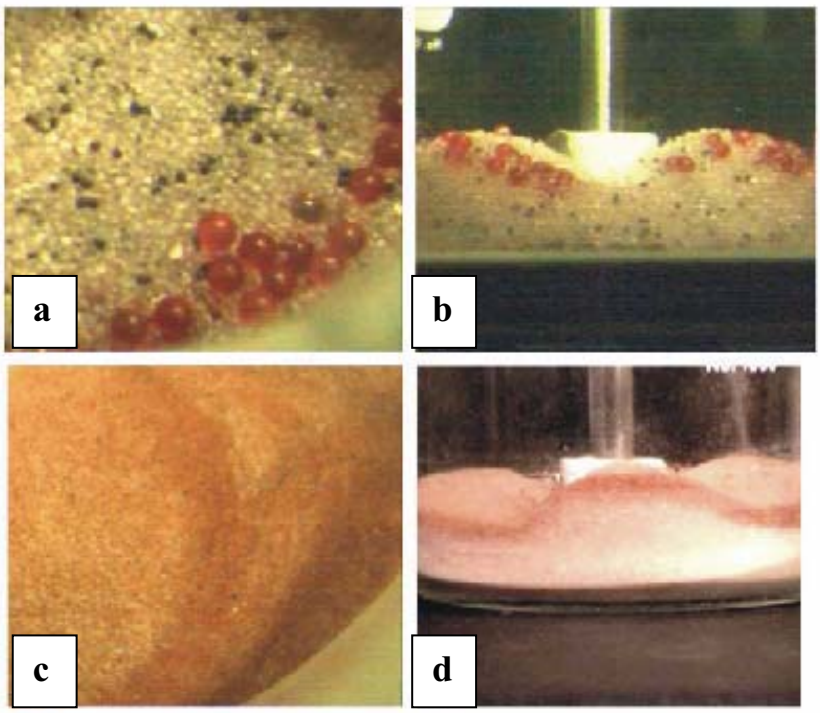

Figure 22: Segregation patterns in a four-bladed mixture. Mixture of 0.9, 1.6 and 4mm glass spheres agitated at 50 rpm (counterclockwise) with obtuse blade pitch shown in (a) overhead view (b) side view. Mixture of 125 and 450 [μm] glass spheres agitated at 50 [rev/min] with obtuse blade pitch shown in (c) overhead view (d) side view [37].

Radl et al. [38] performed numerical simulations of dry and wet granular flow inside a four-bladed (Figure 23) mixer using the discrete element method (DEM). A capillary force model was implemented to mimic the effects of pendular liquid bridges on particle flow.

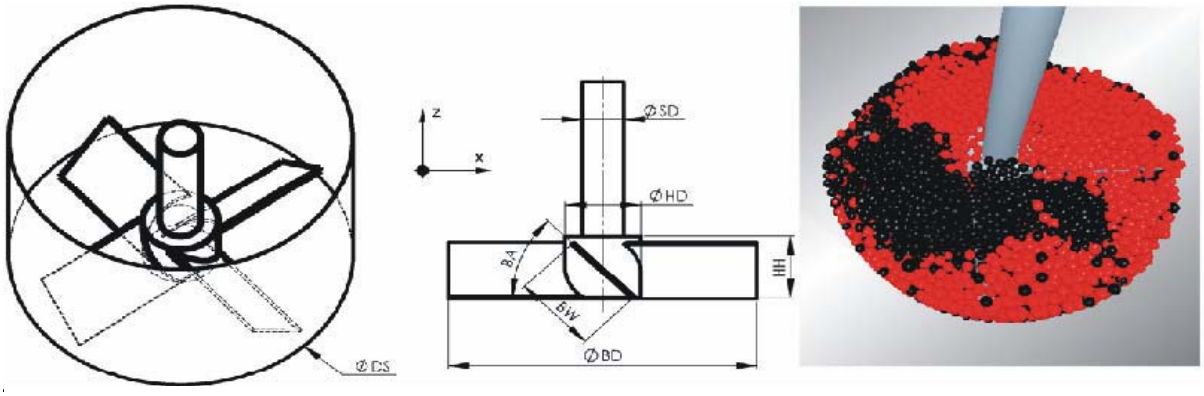

Figure 23: Schematic representation of the bladed mixer (left and middle) and mixer with particles (right, shown is the particle distribution after 1.25 impeller revolutions) [38].

3. Design for an Experimental Setup

In the experiments with the PIV system for the vacuum dryer [19] it was impossible to investigate granular flow in a cross section through the bed. Thus, it is impossible to measure the velocity distribution over the bed height within the particle bed. However, this velocity distribution is important for the mixing of particles. Especially the velocity fluctuations of individual particles behind the blade are expected to be strong. These fluctuations are the main driver for diffusive mixing in the particle bed (see Radl et al. [38]) and hence significantly impact the mixing in the system.

3.1. The Two-dimensional Experimental Setup

For reproducible, experiments of granular flows the following components are necessary:

- a moving box system, that runs smoothly and with a low friction resistance on a translational bearing system. There must be a way to fill and to empty the box with the granular material needed for experiments,
- an electrical drive system, including a speed control of the box,
- a blade, as well as an appropriate support device to create the obstacle for particle flow,
- a PIV system for image acquisition and data analysis,
- illumination equipment that allows short exposure times,
- a position measurement system to record the actual position and velocity of the moving box during the experiment. This system should be synchronized with the PIV system, and
- a damping device to stop the box after at the end of the translational bearing.

The two-dimensional experimental system was designed on a 3D-CAD system, as well as subsequently manufactured and assembled in the workshop of the Institute for Process and Particle Engineering (Figure 24).

Figure 24: Photography of 2D Experimental Device during assembly.

The experimental system consists of the following main components (the drawings can be found in the Appendix, see Chapter 9.2):

- Box (see drawing no. DA01)
- Frame (see drawing no. DA02)
- Obstacle holder (see drawing no. DA03)
- Obstacle (i.e., the blade, see drawing no. DA04_45°)
- Stopper (see drawing no. DA05)
- Gear box assembly (see drawing no. DA06)
- Motor assembly, including the power supply unit (see drawing no. DA07)
- Measurement ruler (see drawing no. DA08)
- Bearing assembly (see drawing no. DA09), including
    - precision shafts (type W30),
    - bearing units (type IALGS 30 SBEUU), and
    - shaft fittings (type IGWA 30).

3.1.1. Construction Details

Box (DA01)

The construction of the two-dimensional system started with the construction of the box. A bended aluminum sheet (3 [mm] thickness) forms the basis of the box. Aluminium was used in order to reduce the mass of the box. The front and the bottom plate are made of polystyrene to observe the granular flow within the box. The box internal space dimensions are 1200 x 52 x 390 [mm] (length x width x height). This space was filled during the experiments with particles to a certain height. At the backside a guide bar is mounted. On this guide bar a gear rack in contact with the gear pinion is mounted. The guide bar is also essential to prevent the deformation of the aluminium box.

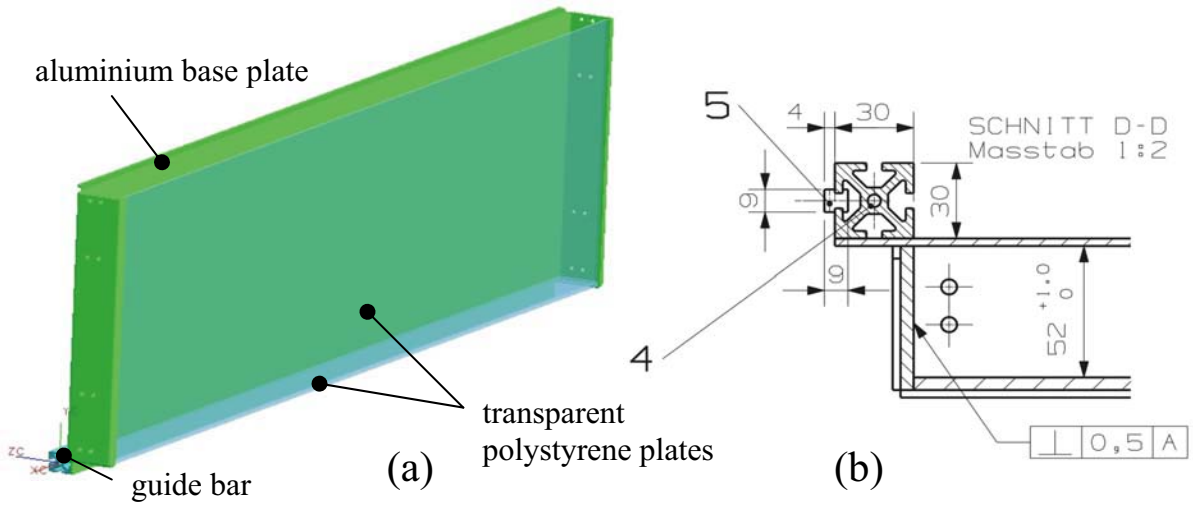

Figure 25: (a) 3D model of the box, and (b) cross-sectional view of the box from drawing DA01 (the view is rotated 90° clockwise). Position 4 is the guide bar; position 5 shows the gear rack.

Frame (DA02)

Four square tubes made of steel (with a cross section of 50x30 [mm]) constitute the basis for the frame of the bearing system. A translational bearing system, including high precision shafts, is fitted to the frame to guide the box.

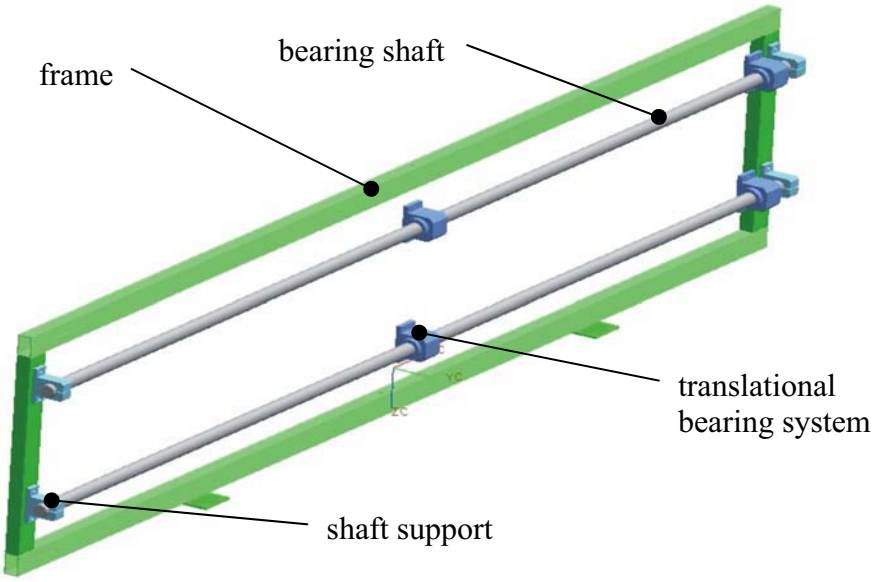

Figure 26: 3D model of the frame including the bearing system.

Obstacle Holder (DA03) and Obstacle (DA04)

The obstacle holder is mounted at the top of the frame. The obstacle (i.e., a blade) is connected with the holder by screws to allow easy assembly and disassembly of the blade, as well as to allow the height adjustment of the blade (see Figure 27).

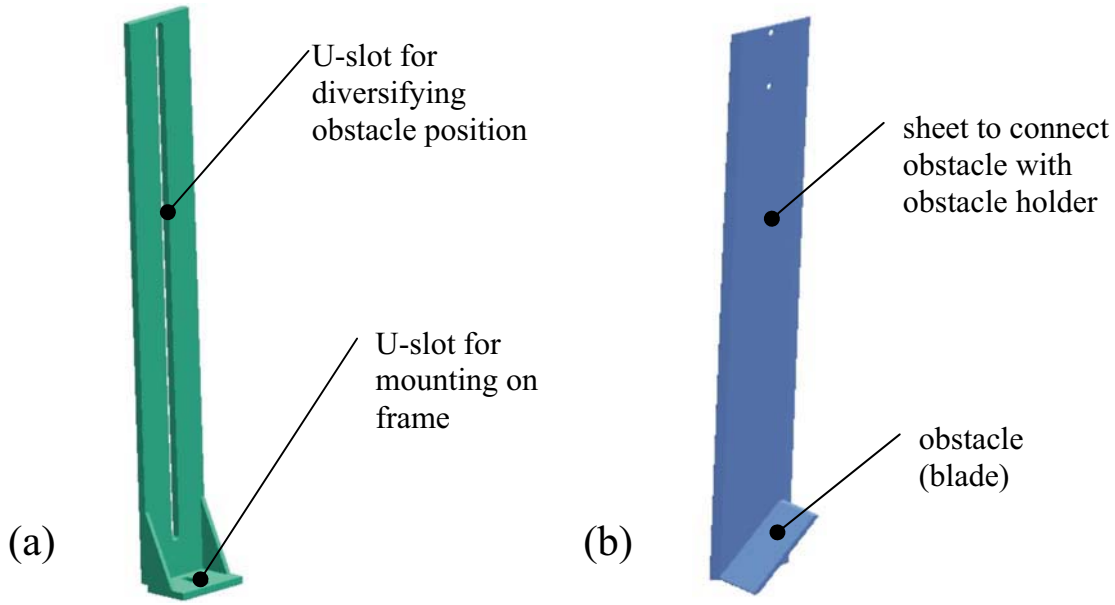

Figure 27: 3D model of (a) the obstacle holder and (b) the obstacle (DA04_45°)

The obstacle (Figure 27b) is an interchangeable part. For investigation of different obstacle shapes it was necessary to fabricate additional obstacles. The primary obstacle is simulating a cut through a stirrer blade, with a blade angle of 45 [°].

Stopper (DA05)

The stopper (Figure 28) has the function to stop the motion of the box at the end of the bearing system. A damping material is used to reduce the noise and the maximum collision force when the box impacts the stopper.

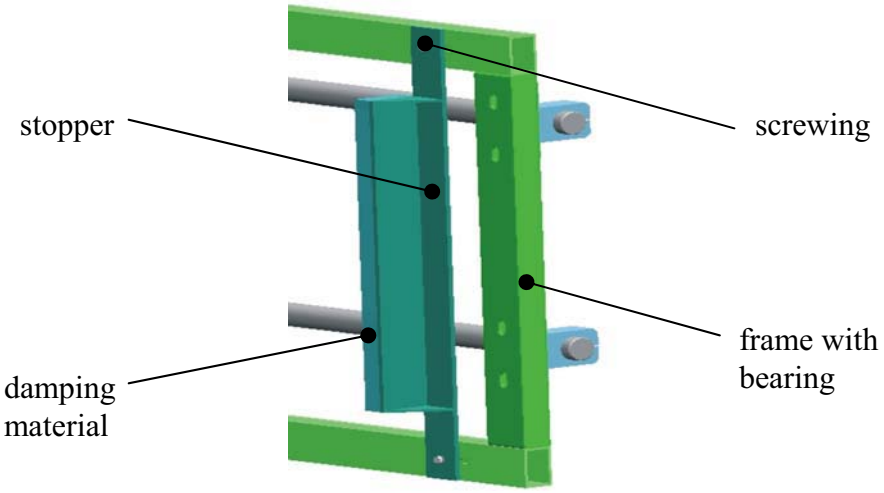

Figure 28: 3D model of the stopper including damping material

Drive Unit

The drive unit consists of four main components: the drive, the spur wheel, the gear rack and the power supply. Calculations (see Chapter 9.1) on the weight of the box and the maximum filling weight of glass beads lead to the selection of a direct current (DC) motor. The nominal speed of the drive was selected as 500 [rev/min] at nominal torque of approximately 1.4 [Nm]. A support is attached to the motor to mount it on a rigid metal bench. The spur wheel has a nominal diameter of 25 [mm] and a gear module of 1. The width of the spur wheel is 11 [mm]. A gear rack is mounted to the guide bar (see Figure 25b). The gear rack is 1100 [mm] long, and has a width of 9 [mm]. An adjustable power supply is used to set the voltage of the DC Motor and hence set its speed.

The calculations of the DC-Motor, the spur wheel and the gear rack are added in the Appendix (see Chapter 9.1). The specifications of the DC motor are shown in Chapter 9.2.

Box Velocity Measurement System

To compare the velocity of the particles with the velocity of the box (Box DA01), a box velocity measurement system has been installed. For this purpose, the measurement system consists of two parts: (i) a measurement ruler, and (ii) a photo sensor. The measurement ruler consists of a thin transparent sheet that is mounted at the guide bar of the box. The scale (1

[mm] spacing) has been printed with a laser printer onto the transparent sheet. The photo sensor is mounted on the metal bench, such that the measurement ruler lies between the two forks of the sensor (Figure 29). The photo sensor is connected to an A-D converter (i.e., a National Instruments cDAQ-9172 data acquisition chassis with a NI 9229 four-channel analog input module), that that transforms the analog signal into a discrete set of pulses. This digital information is recorded by a computer via an USB connection and corresponding software [40]. The box position and velocity is calculated from this signal with a Matlab program. Details of the box velocity measurement and calculation can be found in Chapter 4.2.3.

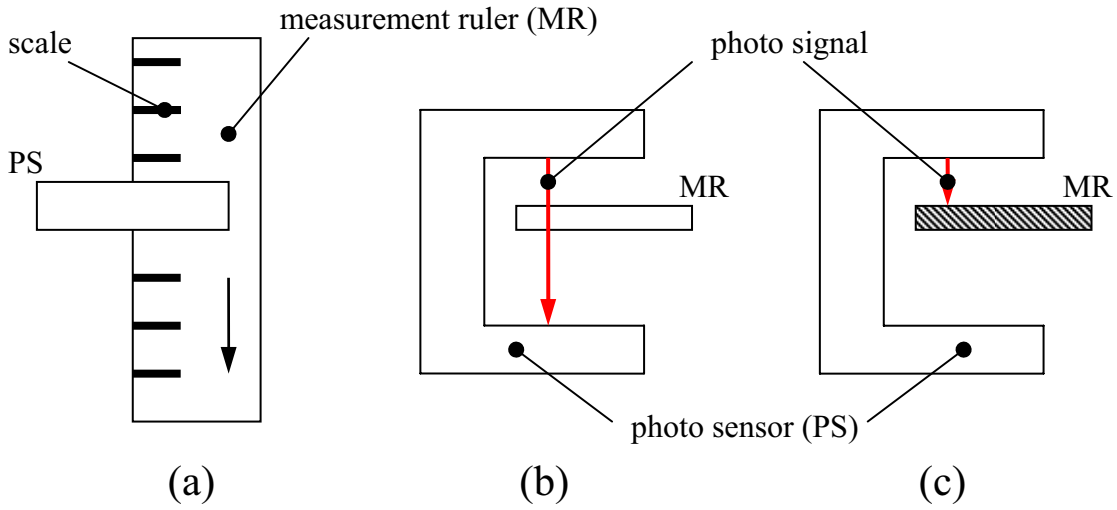

Figure 29: Schematic of the measurement ruler and the photo sensor: a) top view, b) sectional view at a moment of let the signal passing through the transparent material, c) sectional view at the time instant when the signal is interrupted by a scale mark.

3.1.2. PIV Measurement System

A high speed camera with the corresponding lens and support, as well as a high-speed PC interface was used. The camera can be triggered by the signal of the photo sensor to synchronize it with the box velocity measurement system. The high-speed camera system (see Chapter 9.4) supplied by Imaging Solutions GmbH (Germany) consisting of:

- an IDT Motion Scope M3 camera,
- a Motion Scope Camera Link cable set,
- two lenses (i.e., 1 x 50 [mm] focus, and 1 x 35 [mm] focus),
- an advanced tripod,
- a “Magic Friction” support, and

- a mini ball coupling.

3.1.3. Illumination Equipment

For excellent illumination during the experiments we used a cold light source. The cold light source (a “Techno light 270”, supplied by Karl Storz Endoskopie, Germany) is placed behind the PIV camera system. The lamp of the cold light source is connected to the laboratory stand via the “Magic Friction” support and the ball coupling of the PIV system.

4. Investigation of Granular Flow

In the first series of experiments, particle flow at the free surface in a four-bladed mixer has been investigated. Different parameters like particle size, filling height, etc. have been changed and the flow field has been measured with the PIV system. In the second series of experiments, the granular flow over a single blade has been investigated. The second set of experiments was designed to match the parameters of the first experiment in the four-bladed mixer.

4.1. 3D Granular Flow in a Mixer

In the first set of experiments, the interests lie on the observation of granular flows in a four-bladed mixer (see our previous work [19]). For these experiments the sample material are glass beads with a nearly uniform size and shape. Several sizes of the glass beads, different particle bed heights and different moisture conditions have been investigated.

4.1.1. Experimental Setup and Configuration

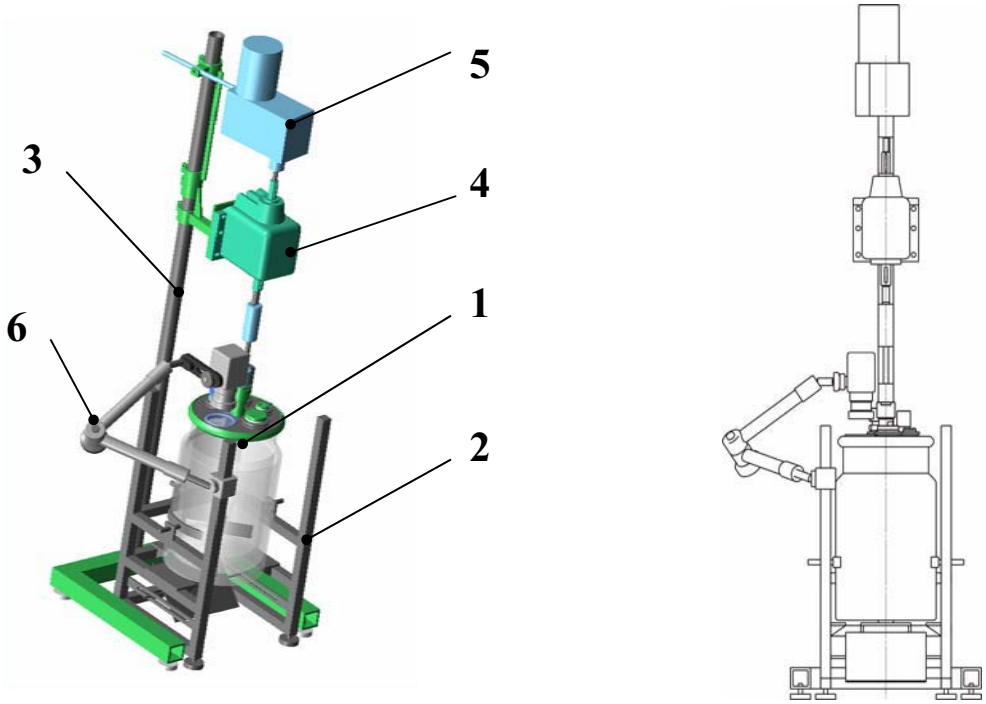

Figure 30: 3-D model of the four-bladed mixer setup (left: isometrical view, right: front view).

The four-bladed mixer consists of six main parts:

Position 1 in Figure 30 is the mixer. The mixer includes a glass vessel, a cover and a stirrer. The vessel has a double wall and the space between is filled with deionized water

to heat the wall of the vessel during drying the experiment. The cover, which is made of stainless steel, holds the bearing for the stirrer, a circular glass window and several nozzles, e.g., for the connection of the vacuum pump or a temperature measurement system. The four-bladed stirrer is made of stainless steel. The blade angle is 45 [°]. The Stirrer geometry is shown in the Appendix (see Chapter 9.3).

Position 2 is the base frame to adjust and fix the mixer. A mirror is mounted to observe the bottom of the glass vessel.

Position 3 is the support for the drive unit. The drive unit consists of a drive unit (Position 5) and a gearbox (Position 4). The drive unit includes an AC motor and allows an adjustment of the number of revolutions. The gearbox is added in this construction for the experiments involving low rotational speeds. The couplings for the power transmission between drive unit, gearbox and stirrer are made of a suitable polymer.

Position 6 is the PIV measurement system which is detailed in Chapter 3.1.2. The camera is positioned directly above the glass window. A cold light source (see Chapter 3.1.3) is fixed in front of the vessel to provide illumination.

4.1.2. Experimental Procedure

The experimental procedure is detailed based on Experiment number 005 (all other experiments can be found in the Excel, see 9.5). Glass beads with a mean particle size of 0.5 [mm] were used for this experiment, the filling height was 40 [mm] and the stirrer was adjusted 10 [mm] above the bottom of the glass vessel. The stirrer speed was set to 60 [rev/min]. The diameter of the glass vessel (stator) is 145 [mm], the stirrer diameter (rotor) is 135 [mm]. All other geometrical details can be found in the Appendix (see Chapter 9.5).

Filling Process

The first step is to fill the vessel with the glass beads. Filling must be done with the cover fixed to the vessel via one of the nozzles. The bed height is checked with a ruler at the side wall of the cylindrical glass container.

Adjustment of the PIV system

The magic friction arm is fixed at the base frame (see Figure 31c). It is possible to adjust the camera's distance, position and the angle to the surface of the particle bed. The PIV camera is connected to the PC via the camera link cable. Finally, the camera position and the focal plane can be adjusted.

Recording of the Image Sequence

During the stirrer is running at uniform speed, the image sequence can be recorded. Therefore, the software "MotionStudio" is used. The camera is controlled by this software, i.e., the software modulates the image size, acquisition frequency, the exposure time, etc. To realize short exposure times, the cold light source from Karl Storz Endoskopie (see Chapter 3.1.3) is used for the illumination of the particle bed. The standard settings used for the image acquisition were:

- the time step between the images was 0.002 [s],
- the number of taken images was 600 (i.e., a recording time of 1.2 [s] was used),

To synchronize the camera with the blade motion, a cylindrical sheet with a slit is placed at the stirrer rod. The photo sensor is positioned so that the cylinder is running over the gap of the photo sensor. The slit in the sheet is then used to trigger the photo sensor and subsequently the camera. The cylinder is configured such, that in the first recorded image the stirrer blade and the x-axis are perpendicular to each other (see Figure 31d).

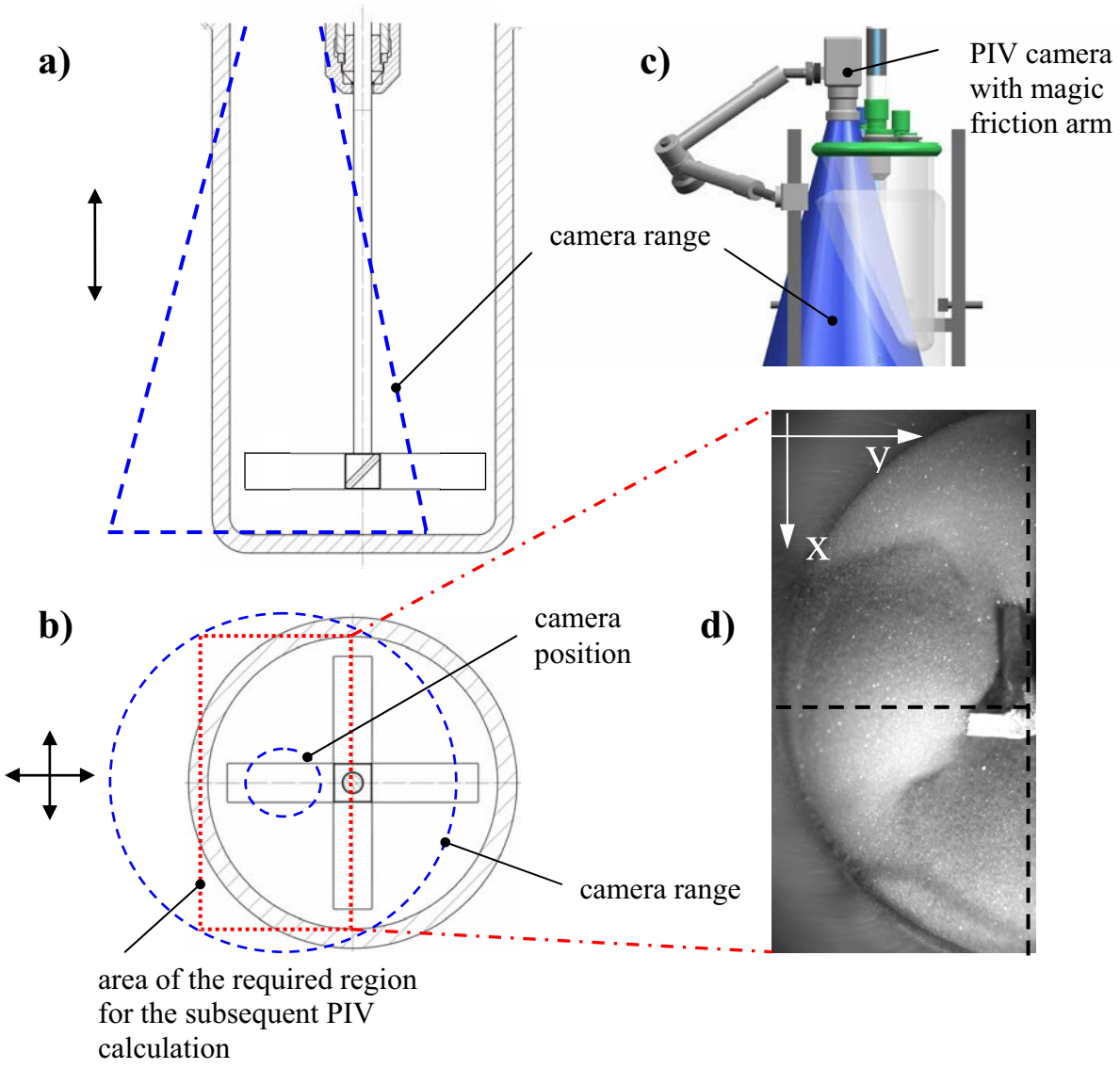

Figure 31: Sectional view of the mixer. a) from the front, b) from the top, c) 3D model of the mixer with camera range, d) image of a bed of glass beads with 0.5 [mm] diameter under motion inside the mixer.

4.1.3. Post-Processing of the Image Data

Using "MatPIV", the whole flow field in the recorded field of view, i.e., the half cylinder as shown in Figure 31, is calculated. From this raw data, we have extracted the velocity profile at a single point. This point has been defined in a cylindrical coordinate system by the radius r and the angle ϕ.

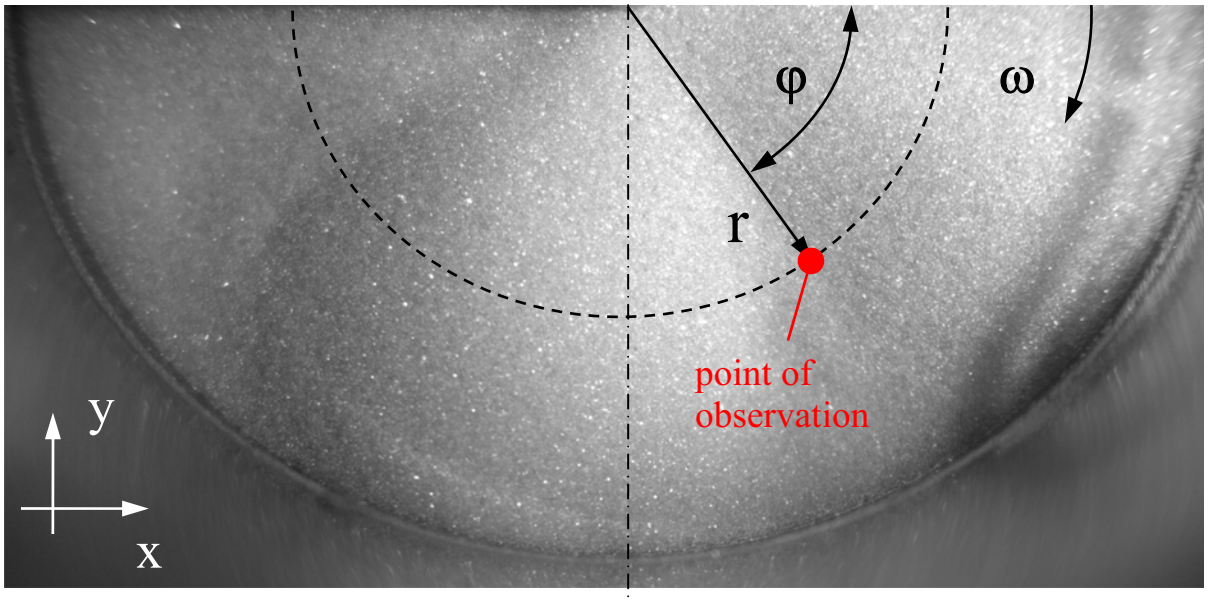

Figure 32: First image (1280x680 Pixel) of experiments no. 005 (Chapter 9.5).

To automatically calculate the velocity field we have used batch files (i.e., "m"-files) in Matlab (refer to the Appendix in Chapter 9.6). The calculation consists of the following steps:

Specifying the Coordinate System

Before the PIV calculation can be started, the image data in pixels has to be scaled to a physical dimension. For this reason we need the image of a grid, which was placed in plane with the particle bed (see Figure 33). The camera position for the grid's image and the image sequence recorded during the experiment must be the same. The grid consists of a series of 5x5 [mm] squares. The MatPIV function "definewoco.m" is used in the batch file called "A_PIV_raster_3D.m" (Chapter 9.6). This file also contains the name of the grid's image and the grid type:

```
definewoco(<RasterPictureName>,<RasterType>);
```

RasterPictureName..... name of the needed grid image (e.g., RA03.tif)

RasterType ..... the grid type (e.g., x)

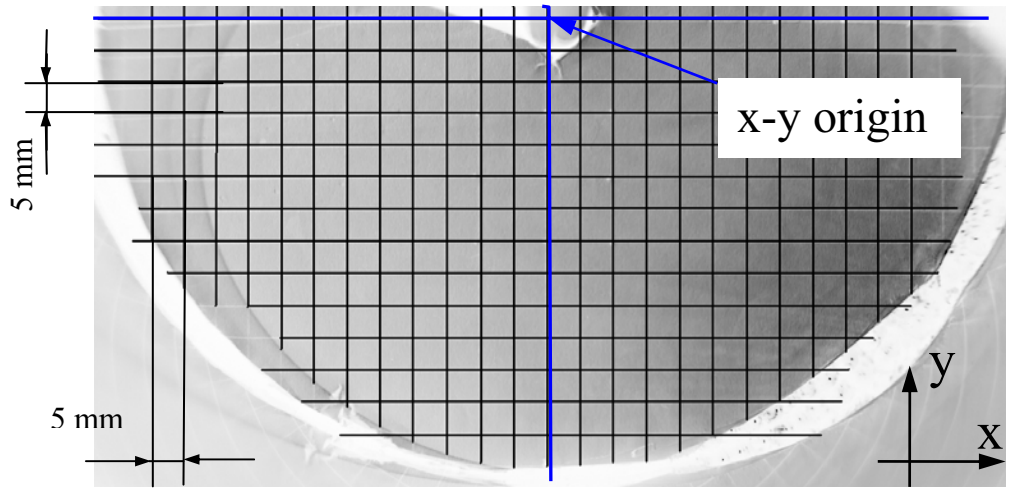

Figure 33: Image "RO03.tif" of the 3D PIV grid (1280x704 Pixel) with a grid of 5x5 [mm] squares, placed inside the glass vessel directly above the particle bed.

The grid type "x" specifies that the grid consist of crossing lines. After loading the image data into Matlab, the figure will be displayed for choosing the coordinate points (see Figure 34). Three or more points have to be selected on the grid in order to define an x-y coordinate system.

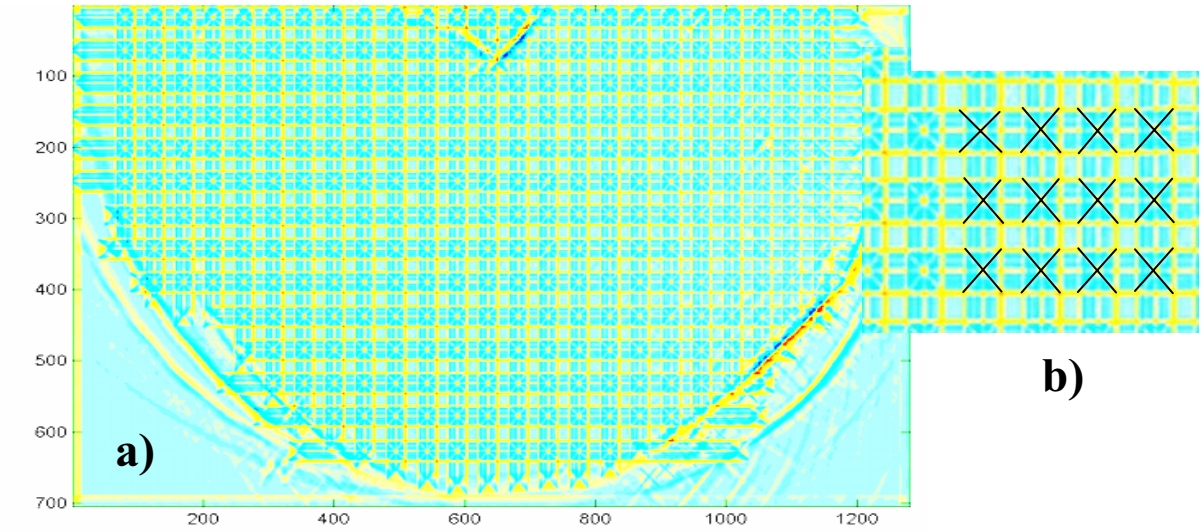

Figure 34: The grid for choosing the points to define the coordinate system. In a) the whole image is shown, b) shows as close up.

Typically, nine points were selected to specify the coordinate system. The points were selected from bottom left to top right. Afterwards, the coordinates in [m] of every point had to be specified. The file including the coordinate system was saved as "worldco1.m".

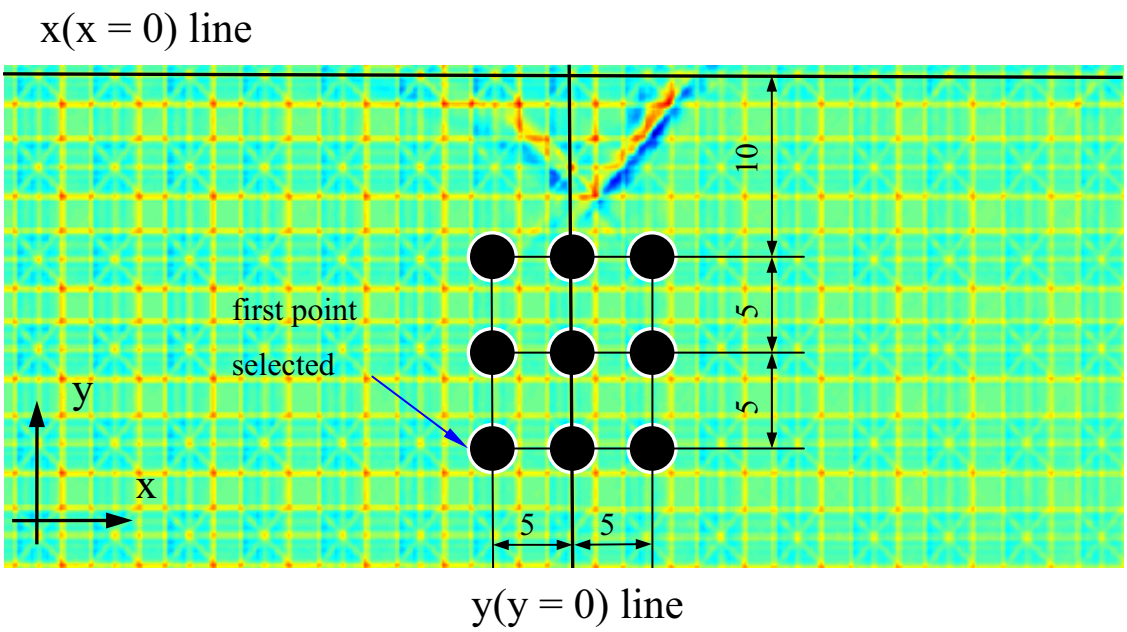

Figure 35: Selected points for specifying the coordinate system. The dimensions are in [mm].

More details on the exact procedure to define the coordinate system are provided in Sveen [17] and Brandl [19].

Mask Function

In the image data there are regions where we do not want to perform the PIV calculation (see, e.g., the red regions in Figure 36). Excluding these regions reduced the time for the PIV calculations, as image data is not processed there.

In MatPIV it is possible to define a mask which prevents the PIV calculation in the selected region. The mask has to be defined by selecting points on the image with the left mouse button. The file including the mask-function was named “C_PIV_mask_3D.m” (Chapter 9.6).

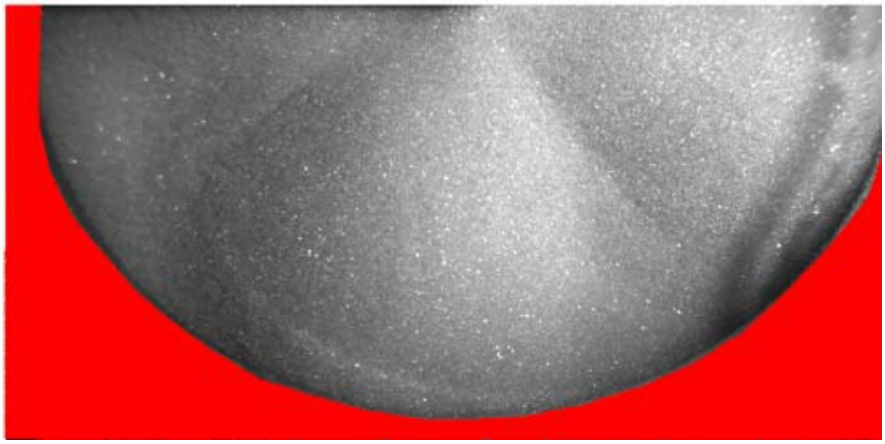

Figure 36: Image PIV000000.tif during the masking procedure. The red colored region highlights the chosen mask. This region is excluded during the post-processing.

PIV Calculation

We are using the batch file "D_PIV_Processor_3D.m" (see Chapter 9.6) for the PIV calculations. The main function is the "matpiv.m" function ([17], [19]) detailed in Chapter 2.4.2. The PIV calculation has been done in multi-processing mode (i.e., the same calculation has been done in triplicate for each interrogation area starting with the result of the previous calculation) to increase the reliability of the calculation.

All PIV calculations used an interrogation window size of 64x64 pixels for the first and the second PIV calculation, as well as an interrogation window with a size of 32x32 pixels for the third and last calculation. The overlapping of the interrogation windows was 50 percent. The time delay of the images was 0.002 [s]. Filtering the obtained velocity fields has been done afterwards. These filters eliminate outliers in the calculated velocity field.

The calculation specifications are:

- time delay = 0.002 [s]..... time delay between an image pair
- interrsize = 64 [Pixel]..... size of an interrogation windows
- overlap = 0.5..... overlap of interrogation windows
- processing mode = 'multi'..... processing mode
- coordinates = worldco1.mat ..... name of the file with the coordinate system [m]
- mask = polymask.mat..... name of the mask file
- noPixStart = 0..... first image to be used for the correlation
- noPixEnd = 1..... second image to be used for the correlation
- deltaPixSequ = 1..... increment of the image pairs to be processed
- totalPix = 600 ..... total number of image pairs to be processed
- snrrange = 1.6 ..... setting for the signal-to-noise–ratio (SNR) filter
- globrange = 3.5..... setting for the global filter
- locrange = 2.5 ..... setting for the local filter
- pkhrange = 0.4..... setting for the peak-high (PKH) Filter

Figure 37 shows the results of such a calculation for experiment no. 5. Each grid cell of this velocity field includes a velocity vector and the corresponding absolute velocity value.

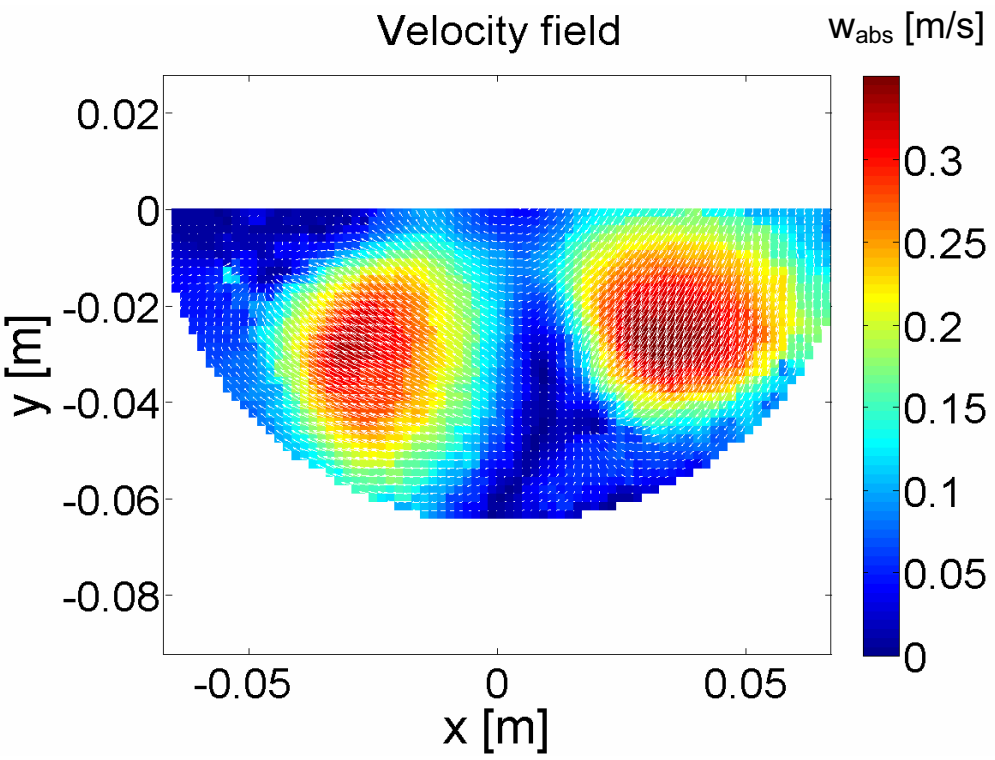

Figure 37: Resulting velocity field of the PIV calculation of experiment no. 005, image number 130. The velocity vectors are indicated as white arrows. The cell color shows the velocity magnitude.

Extracting Point Data

The evolution of the velocity over time at a certain point in the vector field has been investigated. Therefore, a point in a Cylindrical coordinate system has been specified (i.e., a point with a radial distance r and an angle of φ to the x-axis). The batch file "E_PIV_processor_abs_vs_u_3D.m" performs this sampling of the velocity field. Therefore, the cell which is closest to the specified point is detected and the velocities are extracted. The x- and y-velocity in this cell is then transformed into a tangential and a radial velocity component (Figure 38). Both vector components can then be plotted over time in order to quantify the radial and tangential motion in the mixer (see Figure 39).

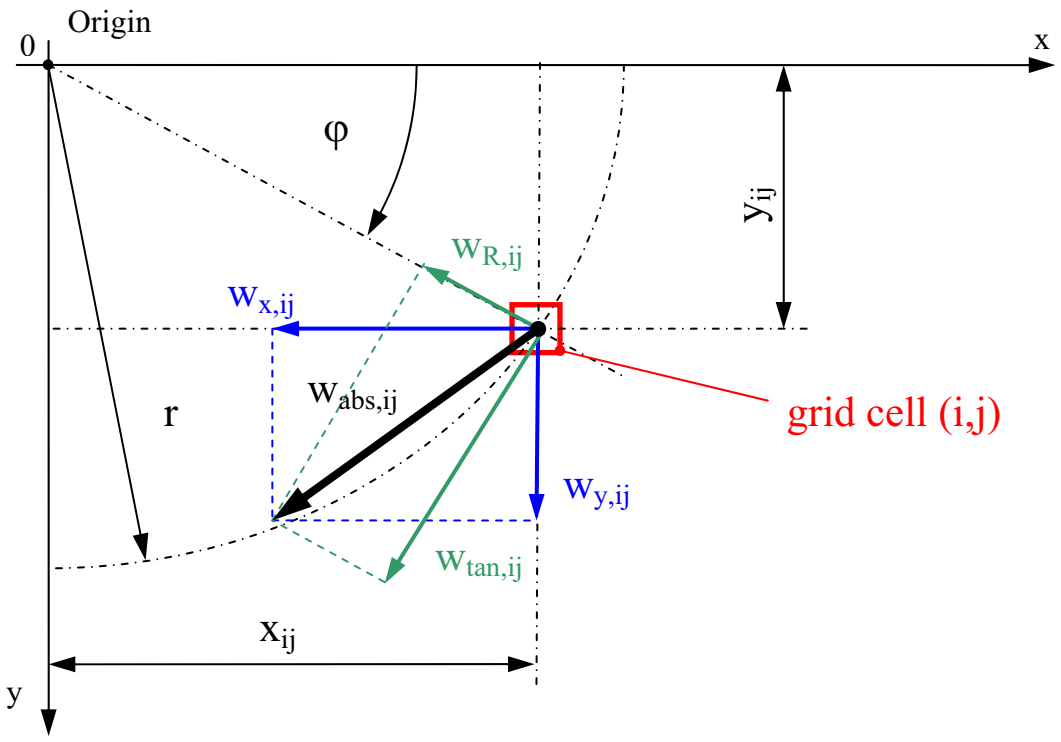

Figure 38: The principle of velocity sampling. The velocity in the Cartesian coordinate system ($w_{x,ij}$, $w_{y,ij}$) is transformed into a tangential and a radial velocity component, i.e., $w_{R,ij}$ and $w_{tan,ij}$. Input for this transformation is the radius r and the angle φ. $w_{abs,ij}$ stands for the absolute velocity in the grid cell (i,j).

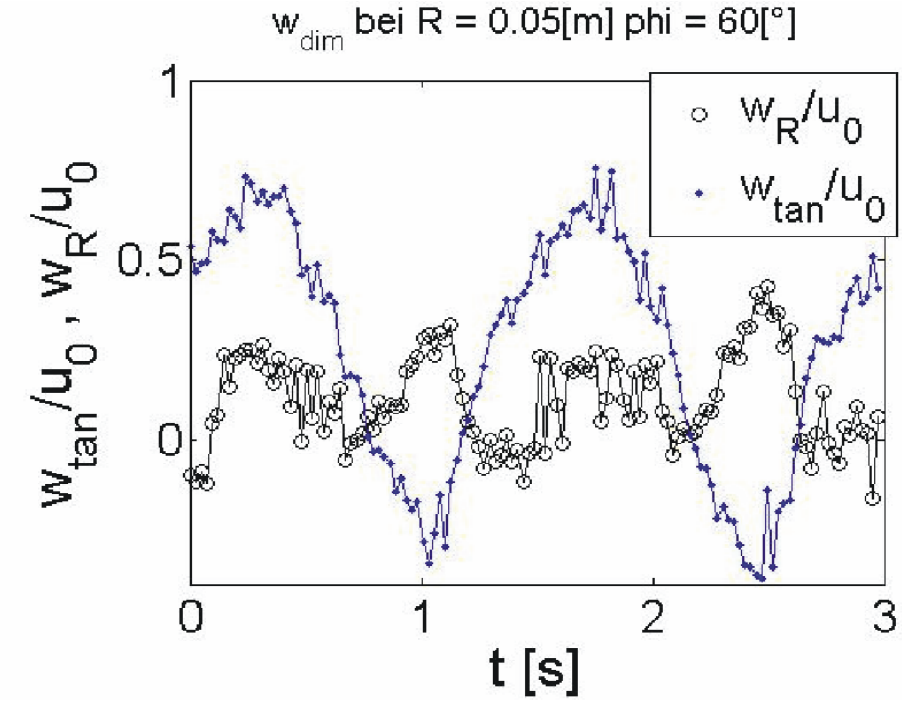

Figure 39: Tangential (w_{tan}) and radial (w_r) velocity component over time. The velocities have been normalized with the tip speed u_0 (experiment no 203).

4.1.4. Results

The experiments have classified in into three sections and are shown in the Appendix (see Chapter 9.5). The drawing "3D_mixer_parameter" (see Chapter 9.5) provides a sketch on all relevant parameters that have been investigated.

Section 1

In the experiments in March 09 2009, glass beads with a particle size d_p of 6 [mm], 4 [mm] and 0.5 [mm] have been used. The influence of liquid bridges for 0.5 [mm] and 4 [mm] glass beads was investigated. The filling height (h_{bed}) was fixed at 40 [mm]. The stirrer was set on two different distances between the bottom edge of the stirrer and the glass vessel bottom ($h_{stirrer}$ = 20 and 10 [mm]). The stirrer speed ($n_{stirrer}$) was 60 [rev/min] and 120 [rev/min].

Section 2

In experiments in July 2009, we investigated the influence of the moisture content of the particle bed. Glass beads with a mean diameter of 0.5 [mm] were used. The stirrer speed was set to 10, 5 and 1 [rev/min] for each configuration. A filling height of 40 [mm] was used. The stirrer was placed 10 [mm] above vessel bottom. As fluid we used deionized water.

Section 3

In the last experiment dated August 2009 the influence of the filling height on the flow field on top of the particle bed was studied. The 0.5 [mm] sized particles were used for that purpose. The stirrer was placed at a position of 10 [mm] above the vessel's bottom. A stirrer speed of 10 and 5 [rev/min] was used for the experiments.

The Effect of the Particle Size

In Figure 40 we compare velocity fields for identical experiment conditions, except for differences in the particle size.

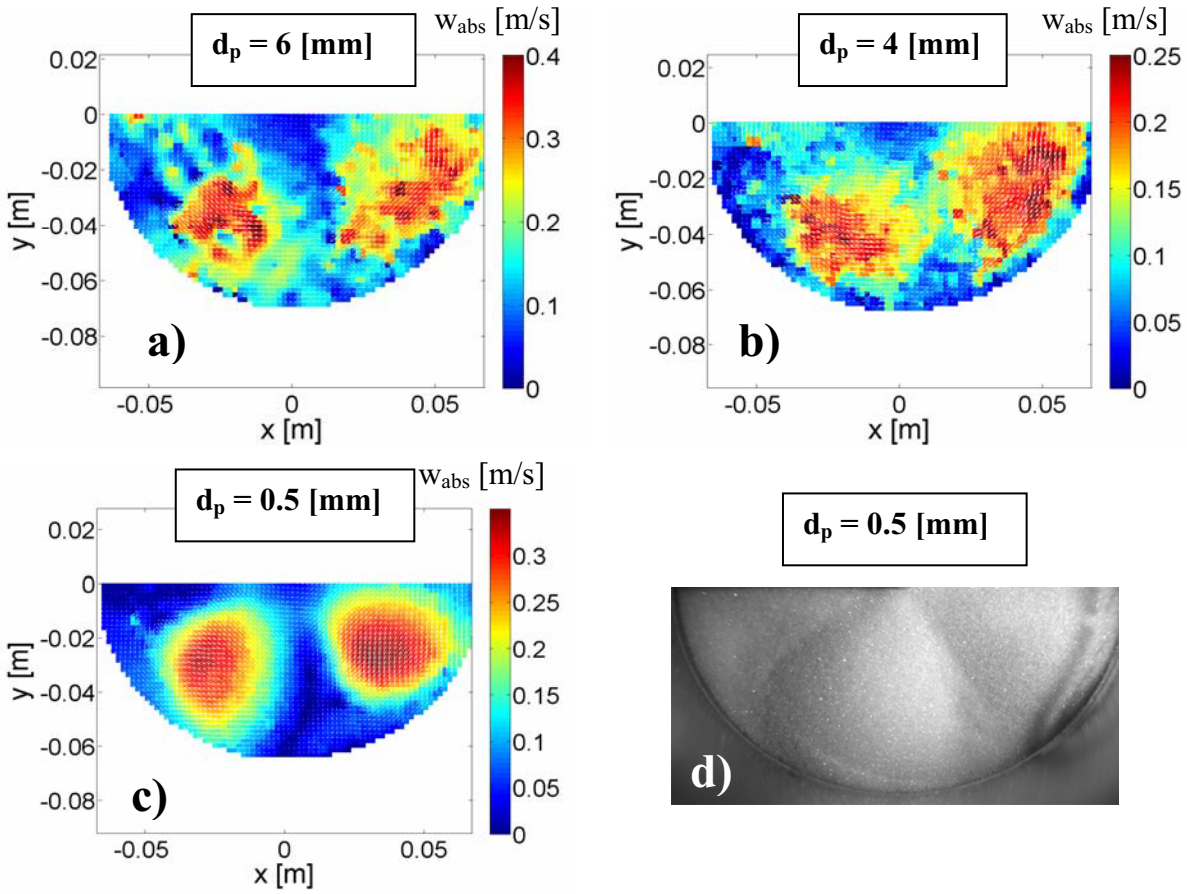

Figure 40: Velocity fields of a stirred particle bed for particles (i.e., spheres) with a different diameter. a) 6 [mm], b) 4 [mm] and c) 0.5 [mm] (stirrer speed is 60 [rev/min], the filling height is 40 [mm]). d) shows the raw image corresponding to velocity field shown in c).

The stirrer blade is located perpendicular to the x-axis in all three images. As can be seen, the blades are pushing forward a heap of particles. This is indicated by the region of higher velocity (i.e., the green-red colored region). The velocity field in Figure 40a (i.e., for a particle size of 6 [mm]) displays an irregular distribution of the velocity field. The wide gaps between the particles result in a roll-and-lock effect causing this velocity distribution. The velocity fields involving the particles with a size of 4 [mm] show a similar trend. Figure 40c shows the velocity field with the 0.5 [mm] particle size. Clearly, for the fine particles the velocity is high in the region where heaps occur. There is a smooth transition between this high velocity region and the region in between the blades where the velocity is low.

The Effect of the Stirrer Speed

In Figure 41 we compare the effect of different stirrer speeds in the bladed mixer.

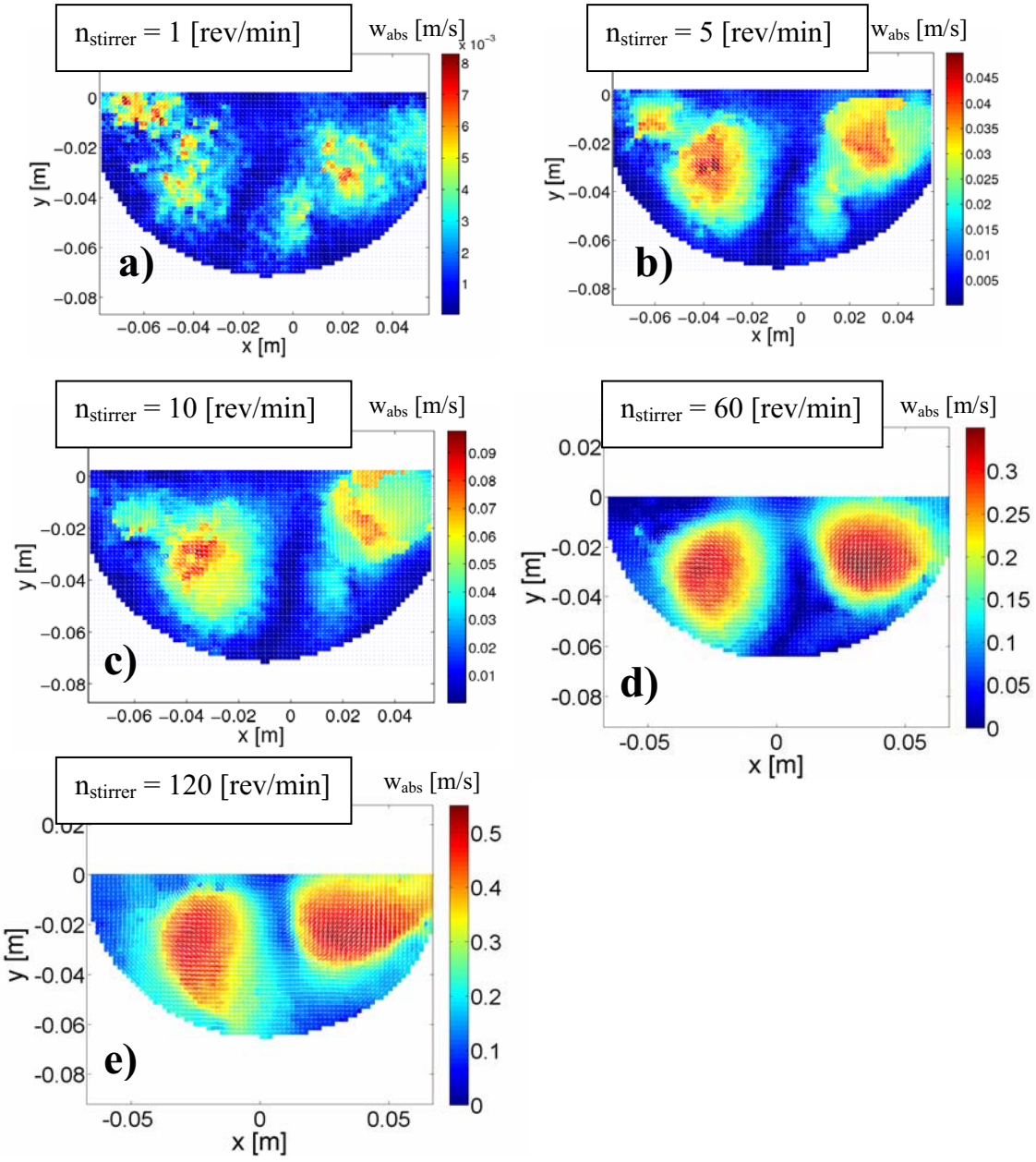

Figure 41: Velocity fields for different stirrer speeds $n_{stirrer}$ (particle size is 0.5 [mm], filling height is 40 [mm]).

Similarly to the particle size, the size of the region with the highest velocity changes with increasing stirrer speed. While at low stirrer speeds there seems to be some erratic particle motion on top of the particle bed, the velocity field becomes smoother with increasing stirrer speed. Also, the shape of the heaps changes significantly between 60 and 120 rpm, i.e., from a nearly circular-shaped region to a wing-shaped region. This is due to the increasing amount of centrifugal forces acting on the particles, such that they are pushed towards the wall of the mixer.

The Effect of the Stirrer Position

Two stirrer positions have been investigated (Figure 42) at a constant filling height. The default stirrer position corresponds to a 10 [mm] gap between the bottom edge of the stirrer and the vessel bottom. At a stirrer position of 20 [mm] above the bottom, the heap's front boundaries are converting into a straight line. Furthermore, the heaps contain less material so that there is less resistance for the stirrer. Therefore, the mean heap velocity in the velocity field shown in Figure 42b is higher than in Figure 42a.

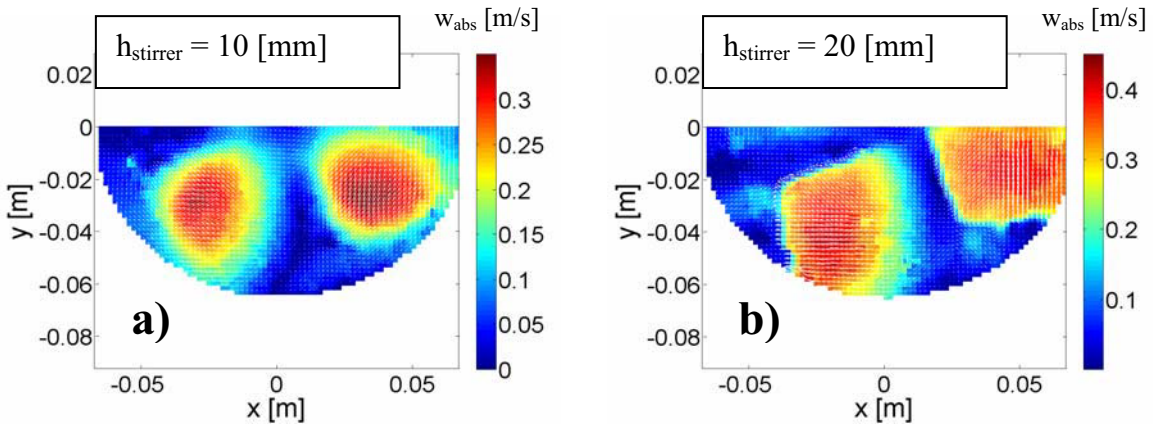

Figure 42: Velocity field of 40 [mm] high particle bed, using a stirrer height $h_{stirrer}$ from a) 10 and b) 20 [mm]. Stirrer Speed is 60 [rev/min].

The Effect of the Moisture Content

Deionized water has been used as fluid for the experiments involving a wet granular bed. When the particle size is small enough, the liquid bridge forces have an effect on the particle flow (see Figure 43 a to f). Adding water to particles with a size of 4 and 6 [mm] had no clear effect on the flow behavior. However, adding water to 0.5 [mm] particles shows a clear effect on the measured velocity field. The moisture content has been specified as the ratio of the liquid volume and the particle bed's volume. The stirrer speed has been set to 1, 5 and 10 [rev/min] and the filling height was 40 [mm].

$$\Phi_l = \frac{V_l}{V_{bed}} \cdot 100\% \qquad \textbf{(14)}$$

Φ_l ..... [vol%]

V_l ..... [m³]

V_{bed} ..... [m³]

Clearly, while there is a gap between regions with a low velocity for the dry particles, this gap is getting smaller when moisture is added to the particle bed. Above a moisture content of approximately 0.2 [vol%] the high velocity regions start to coalesce.

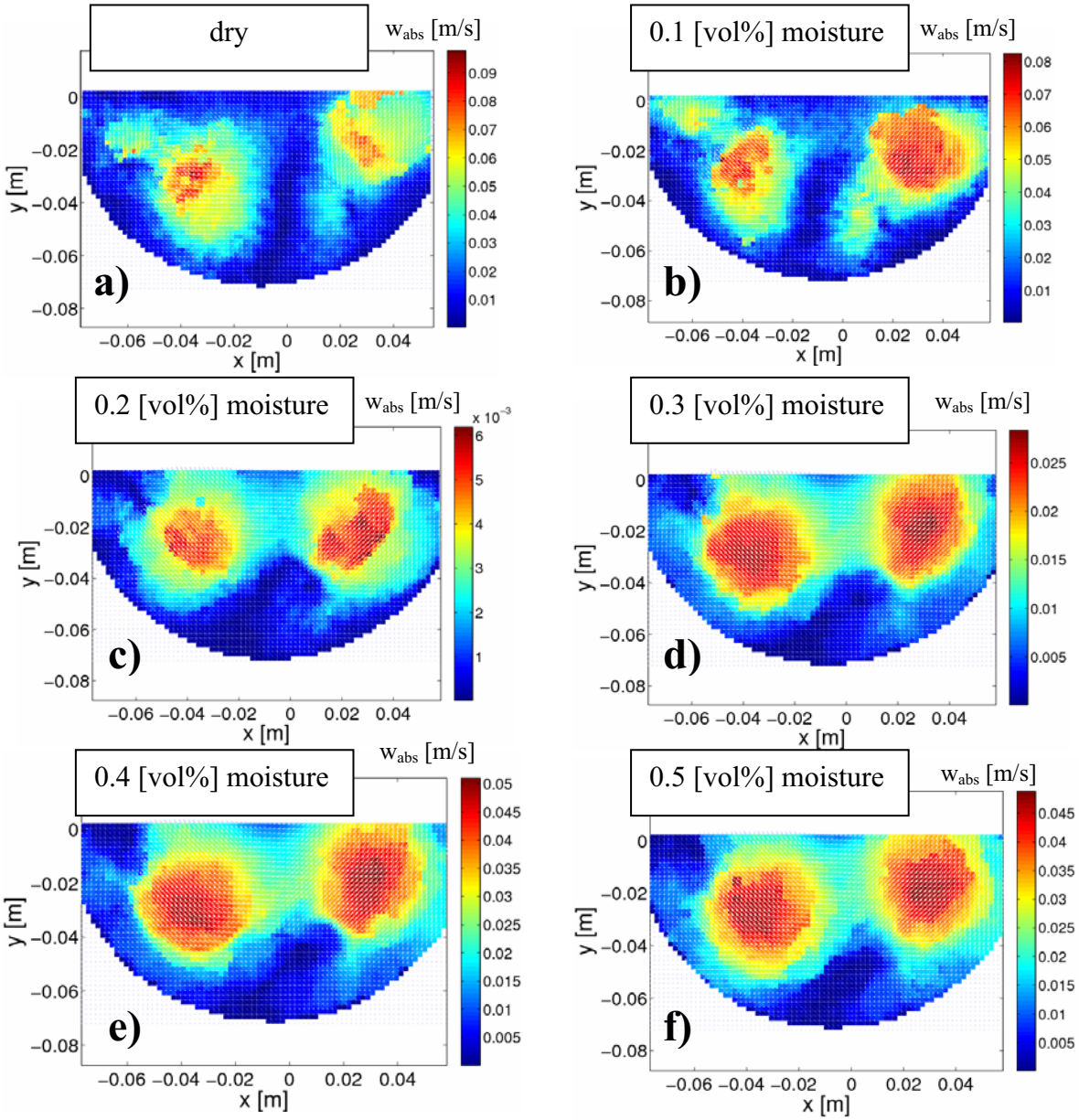

Figure 43: Velocity fields of particle beds having different moisture content. a) dry conditions, b) 0.1, c) 0.2, d) 0.3, e) 0.4 and f) 0.5 [vol%] moisture content.

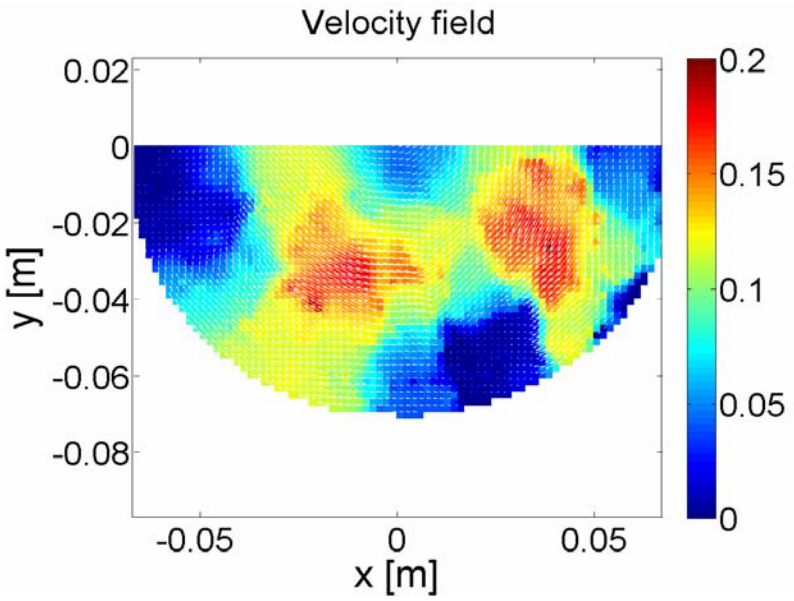

Figure 44: Velocity field of particles containing a moisture content of 2 [vol%].

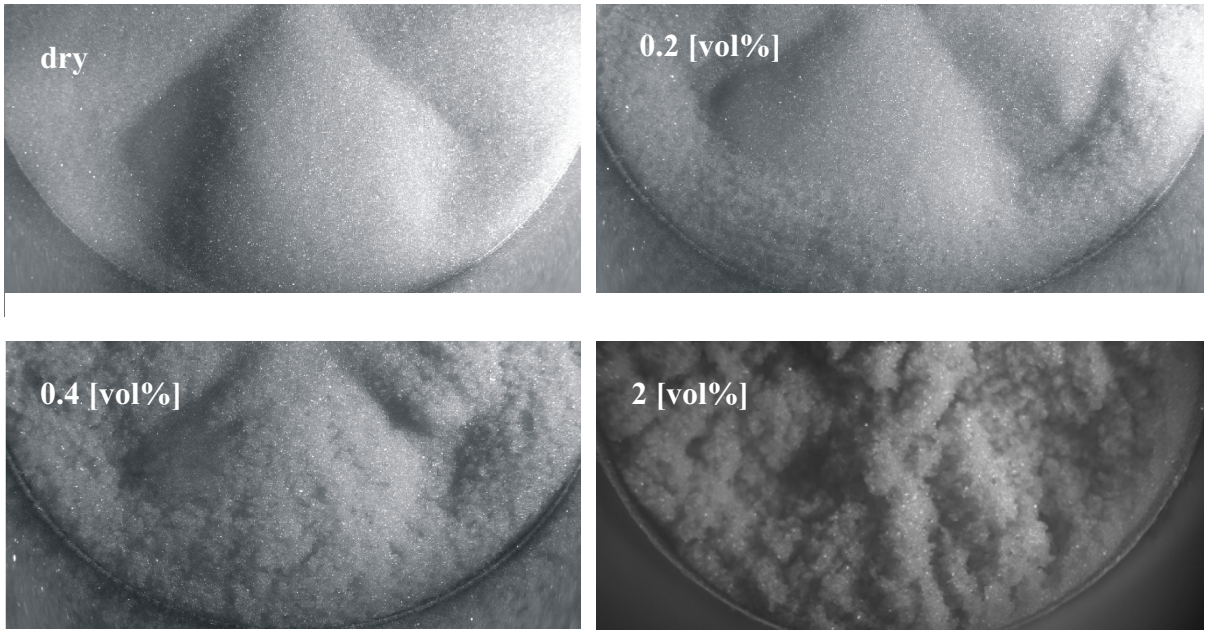

Figure 45: Raw images with different moisture specification.

The Effect of the Filling Height

The effect of the filling height in the mixer was analyzed with particles having a nominal diameter of 0.5[mm], as well as at a stirrer speeds of 5 and 10 [rev/min] (see Figure 46).

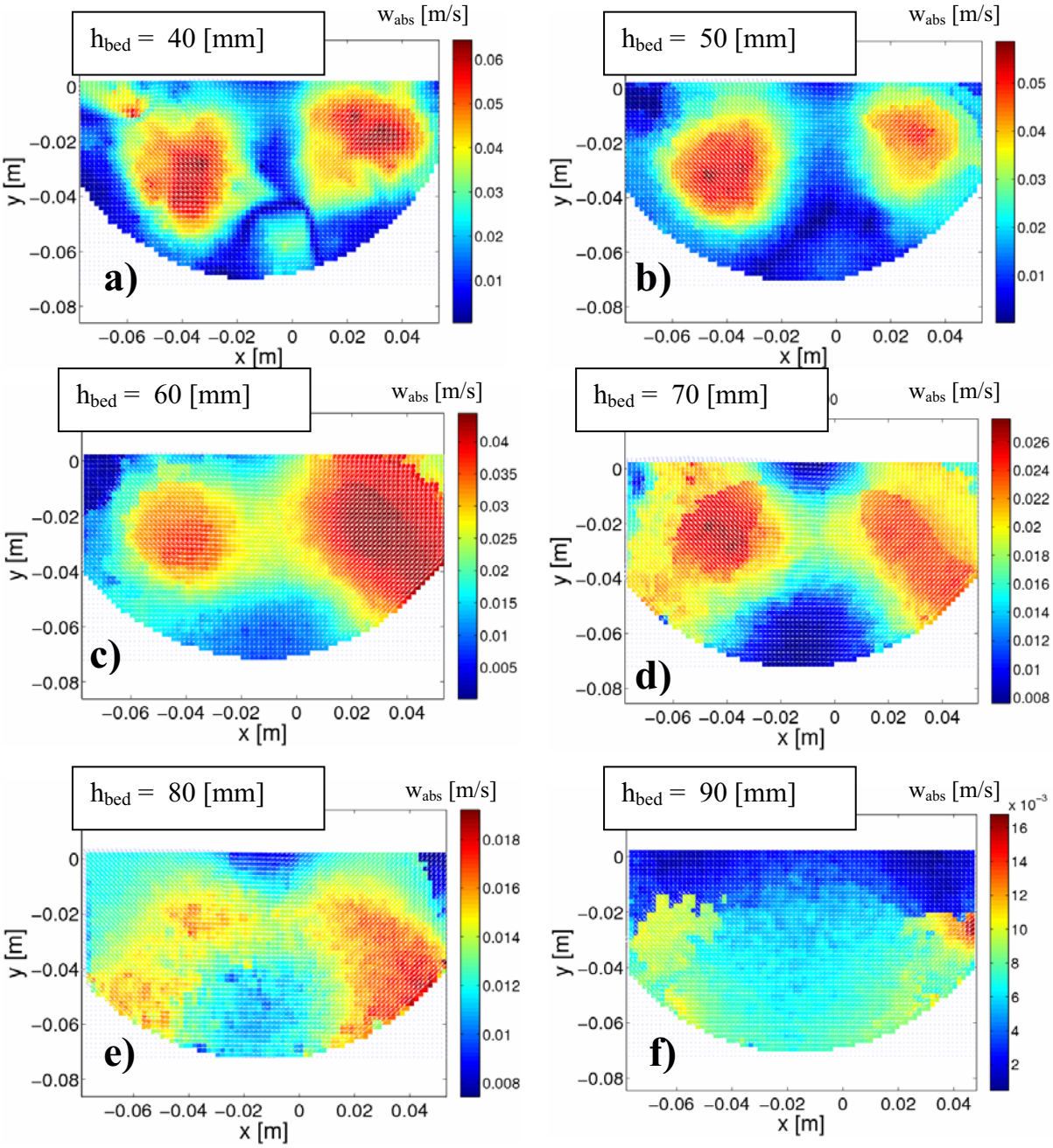

Figure 46: Velocity fields of particle beds at different filling heights.

When the filling height increases, the effect of the rotating stirrer speed on the bed's surface velocity is becoming smaller. Also, heaps are getting smaller until they disappear. At a filling height of about 90 [mm] the PIV calculations become more and more challenging due to the low surface velocity (i.e,. the displacement between subsequent images becomes smaller).

Single Point Observations

For the above reported experiments, velocity data at a single point has been extracted and plotted over time. Similar conclusions as those reported in the previous paragraphs can be drawn out of these plots, which are shown in Figure 47 to Figure 50.

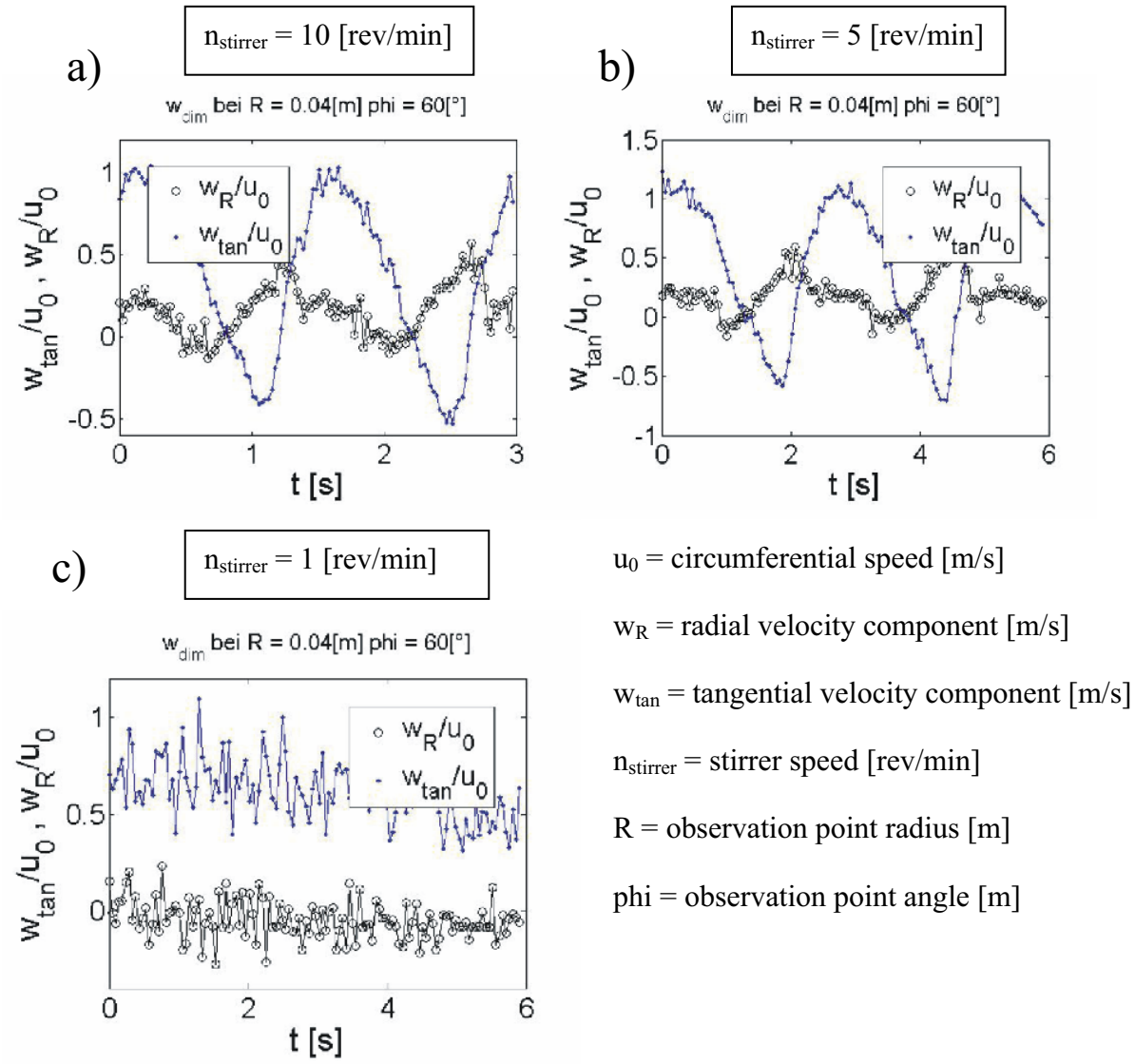

u_0 = circumferential speed [m/s]

w_R = radial velocity component [m/s]

w_{tan} = tangential velocity component [m/s]

$n_{stirrer}$ = stirrer speed [rev/min]

R = observation point radius [m]

phi = observation point angle [m]

Figure 47: Point-Velocity profiles for different stirrer speeds.

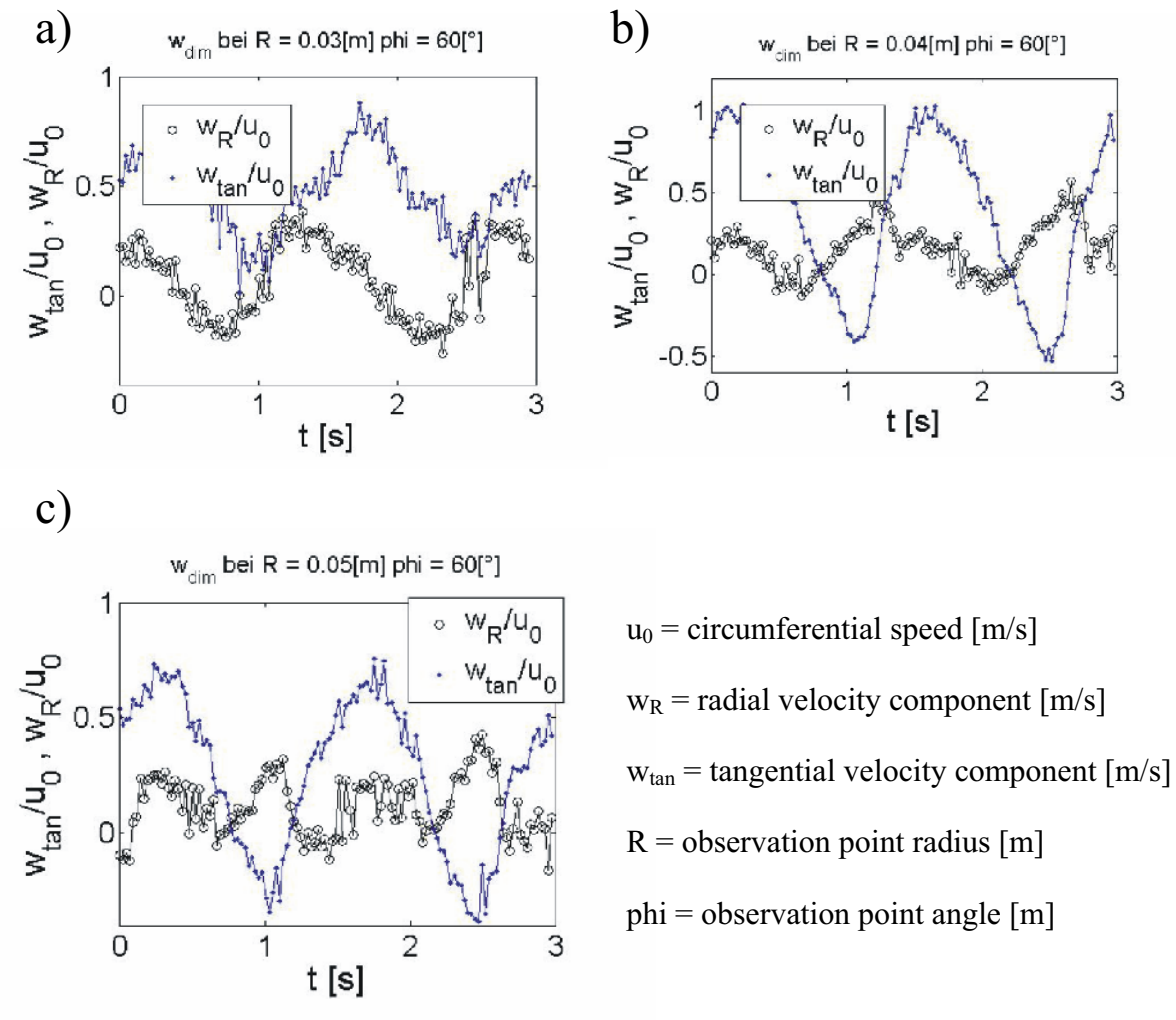

Figure 48: Comparison of the results for three different radial distances for an identical experiment. (a) R = 0,03 [mm], (b) R = 0,04 [mm], (c) R = 0,05 [mm].

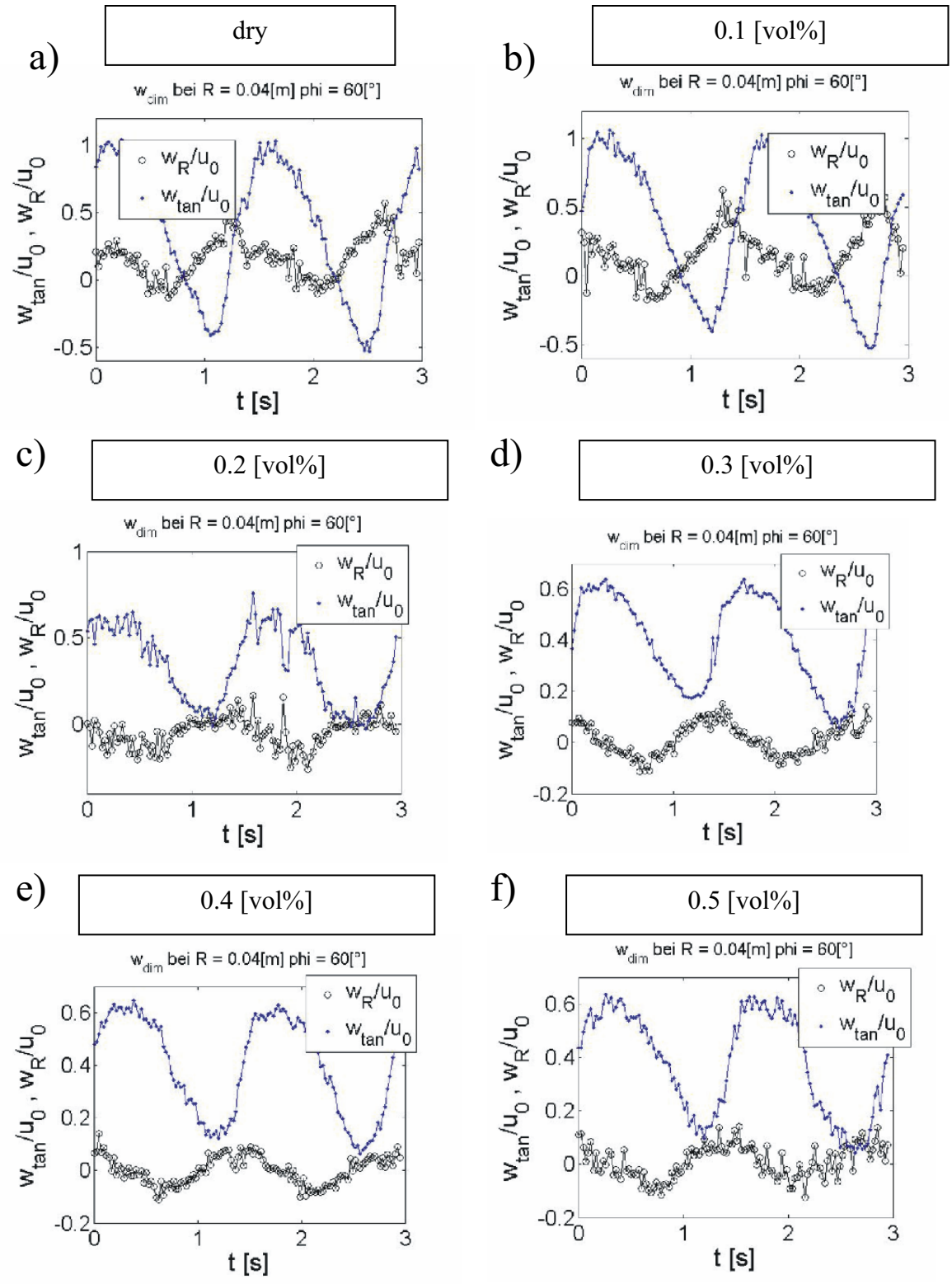

Figure 49: Velocity profiles at a point in the mixer for different moisture contents.

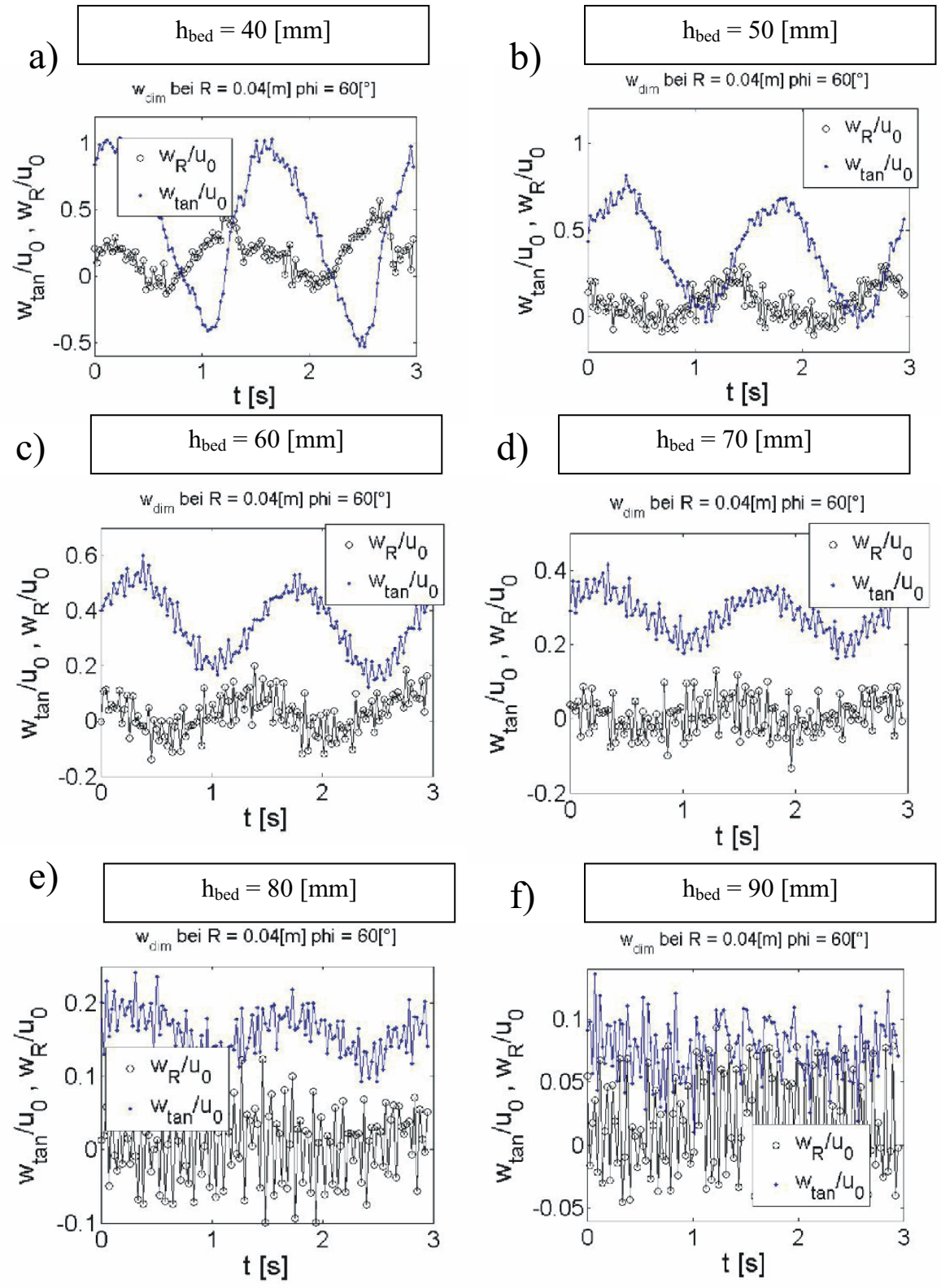

Figure 50: Effect of filling height on the velocity on top of the particle bed.

4.2. Granular Flow in a Two-Dimensional Setup

The flow over a single blade has been investigated and the effect of various parameters (i.e., particle size, filling height, blade speed, geometry and position) has been analyzed.

4.2.1. Experimental Setup and Configuration

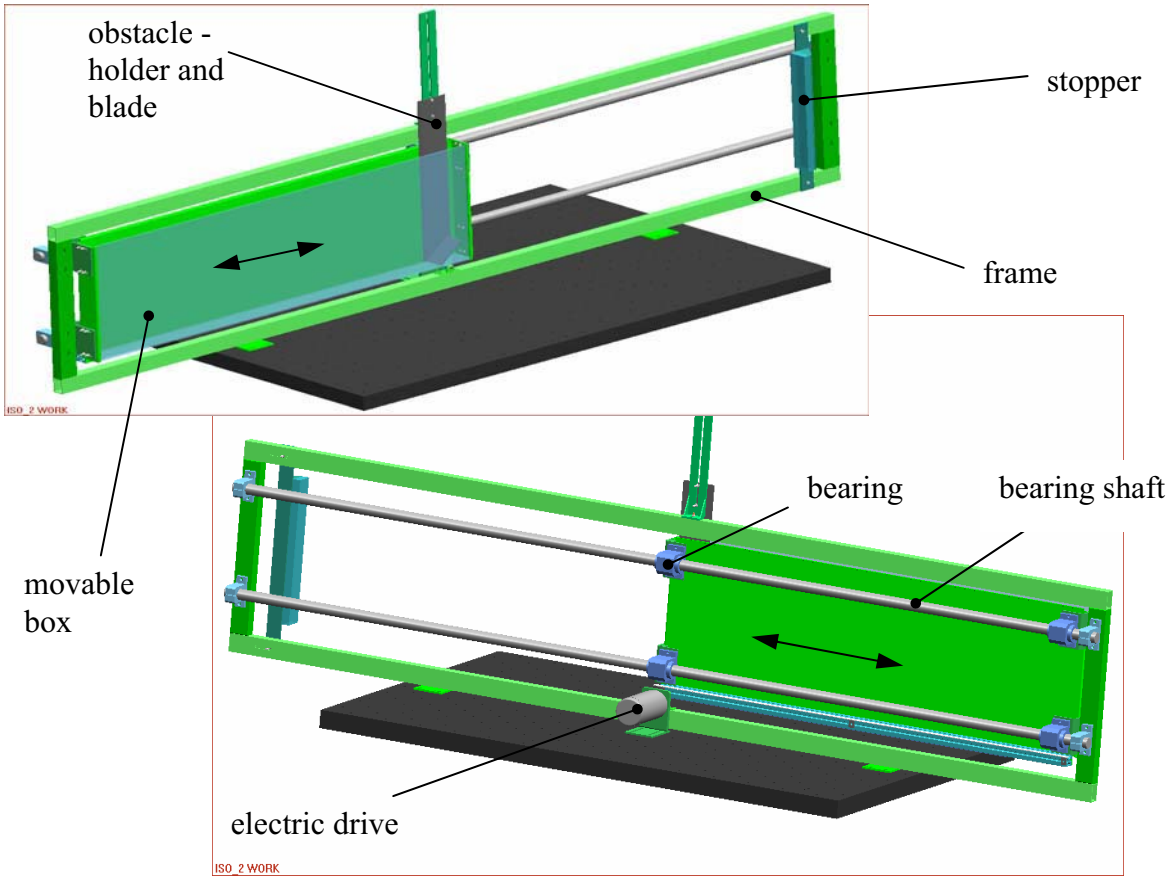

Figure 51: Isometric views of the 2D experimental setup.

For the box it is possible to move in left or right direction inside the frame. During the box movement the blade stands still. If the box is filled with particles, they have to pass the blade. This is similar to a stirring process in the cylindrical mixer, because this linear transition simulates rotation of the blade, i.e, the flow of particles in a (cylindrical) cross section at a certain radial distance of the bladed mixer.

4.2.2. Experimental Procedure

The experimental procedure to obtain the flow field in the two-dimensional blade system is detailed based on experiment no. 044 (see Chapter 9.10). In this experiment, particles with a mean particle size of 1.675 [mm] and a bed height of 50 [mm] were used. The power supply's voltage was 9 [V]. The blade named "DA04S_45°" (see Chapter 9.2 for the drawing) was used for this experiment, the blade position was 0 [mm].

Filling Process

The box was filled from the top with glass beads until the desired bed height has been obtained.

Fixing and Adjusting the PIV system

The PIV camera was positioned in front of the box aligned with the blade's vertical position. The magic friction arm is used to hold the lamp of the illumination equipment, which is placed behind the camera.

Motor Adjustment

With a power supply the motor's supply voltage can be set. The change of voltage of the power supply regulates the power and the box velocity at the end.

Recording of the Image Sequence

With the selected motor voltage and after synchronizing the PIV camera with the box velocity measurement system, the experiment can be started. The camera is triggered (and the recording starts) when the first mark of the measurement ruler passes the photo sensor. The default parameters for the image sequence of experiment no. 044 are:

- the time step between the images is 0.002 [s]
- the total number of recorded images is 1500 (i.e., a total of 3.0[s] has been recorded).

For the calculation of a mean velocity field, an image series of 200 consecutive images (PIV000850.tif - PIV001049) has been selected. Time range of this image sequence corresponds to 1.7- 2.1 [s] after passing the photo sensor. Figure 52 show a raw image of this image sequence and the corresponding box velocity profile. The mean box velocity during the image sequence was approximately 0.145 [m/s].

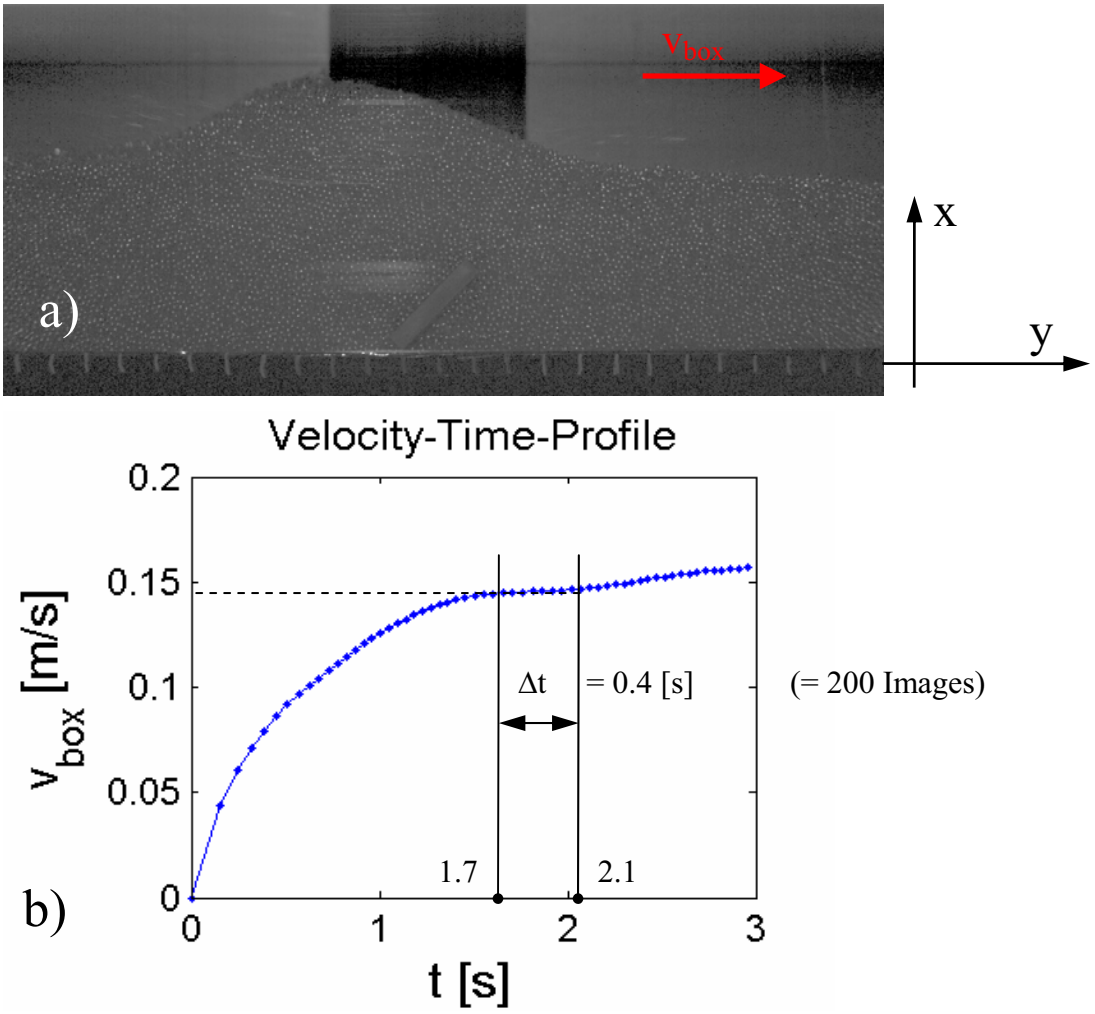

Figure 52: a) image PIV000850.tif of experiment 044, b) shows the corresponding box velocity profile (9.10).

4.2.3. Post-Processing of the Image Data

Calculation of velocity fields and box velocity profiles has been done in Matlab. The calculations are performed via batch files as shown in the Appendix (see file "E_Box_vel_Meassure_2D.m" in Chapter 9.7). The calculation procedure is as follows:

Box velocity Calculation

The principle of this calculation is the counting the black colored marks of a 1 [mm] scale on measurement ruler. Such a black colored mark interrupts the photo sensor's signal, which is then recorded as a voltage pulse. There are a maximum and a minimum value of voltage. The Voltage reaches a minimum during the interruption and a maximum otherwise. It is then possible to count the black colored marks and to convert them into position and velocity data. Typical results are indicated in Figure 52.

Specifying the Coordinate System and the Mask Function

The batch file for specifying the coordinate system is saved as “A_PIV_raster_2D.m” (9.7). The grid consists of 10x10 [mm] squares. Similar to the 3D coordinate specification detailed in Chapter 4.1.3, a grid of type “x” is used for the two-dimensional coordinate system (see Figure 53).

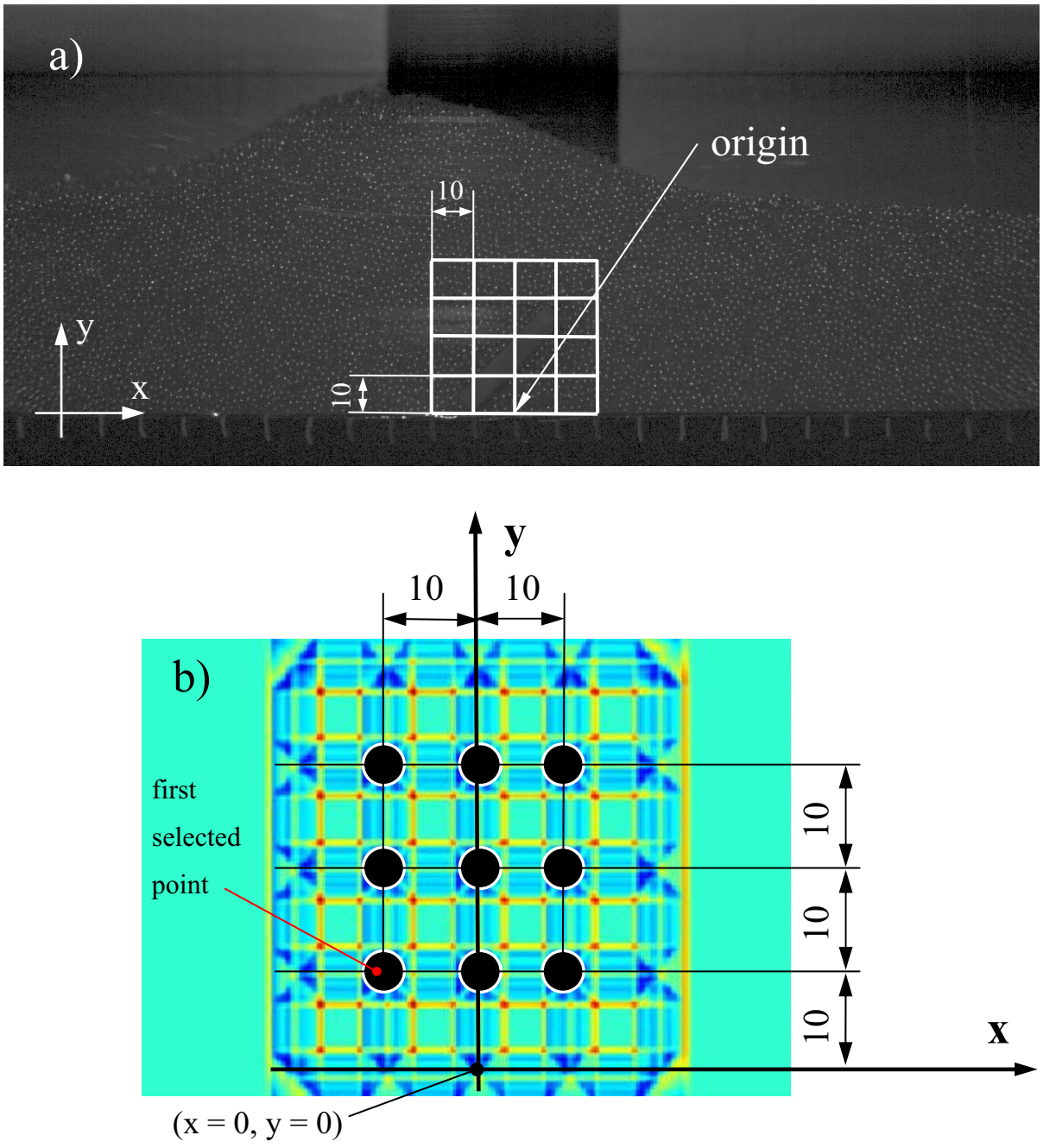

Figure 53: a) The image “Raster02.tif”, used for specifying the coordinate system; b) the grid for selecting the reference points. Points have been selected from bottom left to top right. Dimensions are in [mm].

Also, the mask function has been used for the two-dimensional experiments to exclude regions where a velocity calculation is not necessary (see Figure 54).

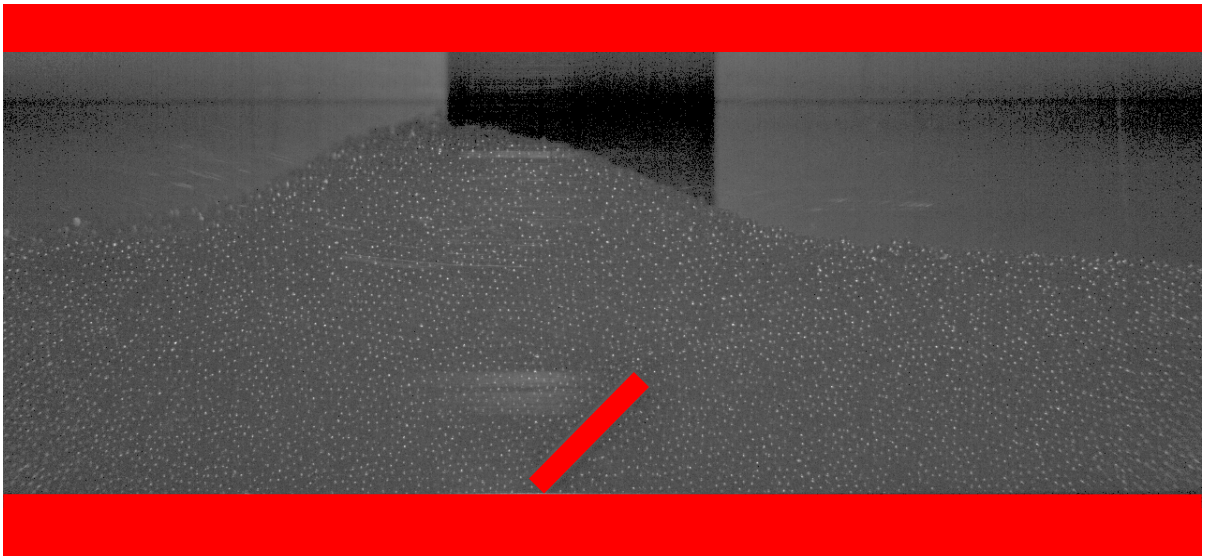

Figure 54: Image PIV999999.tif during the masking procedure. The red colored region highlights the chosen masks.

PIV Calculation

The velocity fields were calculated using the batch file ”D_PIV_calculations_2D.m” (9.7). All 2D PIV calculations used an interrogation window size of 32x32 pixels for both the first and the second calculation. 16x16 pixels were used for the third and last calculation cycle. The overlapping of the interrogation windows was 50 percent. The time delay of the images was 0.002 [s]. Filtering the obtained velocity fields has been done afterwards. These filters eliminate outliers in the calculated velocity field.

The calculation specifications for experiment 044 were:

- time delay = 0.002 [s]..... time delay between an image pair
- interrsize = 32 [Pixel]..... size of the interrogation windows
- overlap = 0.5..... overlap of the interrogation windows
- processing mode = ’multi’..... processing mode
- coordinates = worldco1.mat ..... name of the file including the coordinates in [m]
- mask = polymask.mat..... name of the mask file
- noPixStart = 850..... first image to be used for the correlation
- noPixEnd = 851..... second image to be used for the correlation

- deltaPixSequ = 1..... increment of the image pair to be processed
- totalPix = 200 ..... total number of image pairs to be processed
- snrrange = 2.3 ..... rate for the signal-to-noise–ratio (SNR) filter
- globrange = 10.0..... rate for the global filter
- locrange = 8.0 ..... rate for the local filter
- pkhrange = 0.23..... rate for the peak-high (PKH) Filter

Figure 55 shows the results of the PIV calculation for experiment no. 044. Figure 55a shows the instantaneous velocity field after a time of 1.7 [s], and Figure 55b shows time-averaged velocity data.

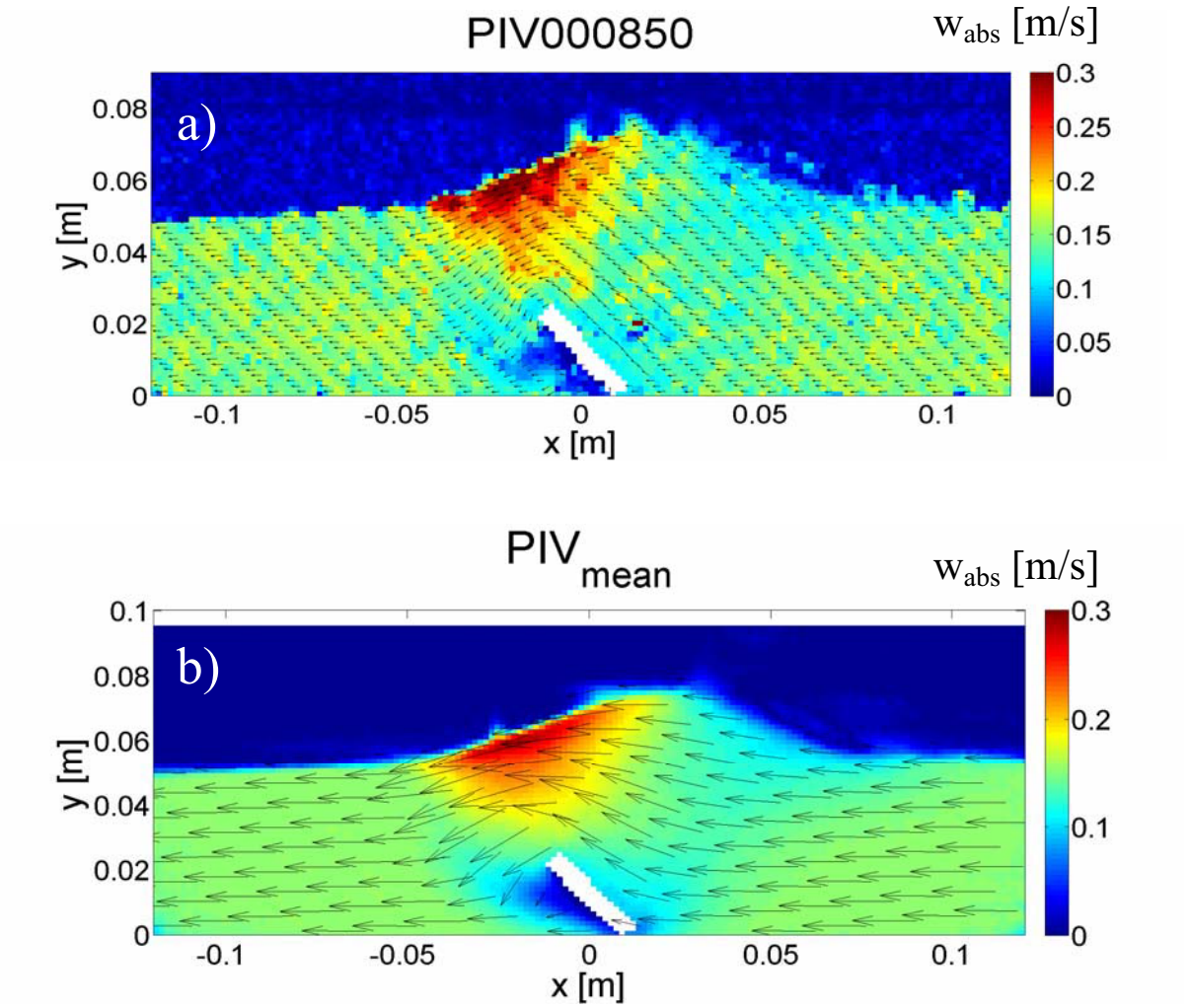

Figure 55: a) Instantaneous velocity field for experiment no. 044, and b) resulting mean velocity field.

4.2.4. Results

The experiments have been classified into three sections and are shown in the Appendix (see Chapter 9.5). The drawing ""D_mixer_parameter" (see Chapter 9.5) provides a sketch on all relevant parameters that have been investigated.

Section 1

In the experiments in October 2009, different bed heights, blade positions and several blade speeds have been investigated. The particle size d_p for these experiments was 4 [mm]. The blade "DA04_45°" (9.2) was installed in the experimental system.

Section 2

In the experiments in November 2009, the influence of the particle size and blade angle was investigated. Three different particle sizes (i.e., d_p of 4, 1.675 and 0.5 [mm]) were used. The drawings of the three blades used are shown in the Appendix (see Chapter 9.2). Each configuration was investigated under three different box velocities.

Experiment's evaluations will be discussed by going through each parameter. We will take mean velocity fields for discussion, which are collected in the Appendix (see Chapter 9.11).

The Effect of the Box velocity

Both experiments results contain velocity fields at different blade (box) velocities. Figure 56 shows velocity fields for various box velocities and blade sizes. The faster moving blade leads to a higher pile and a greater slope angle. Also, a recirculation region is clearly visible in front of the blade, which becomes weaker in experiment 44 and 45.

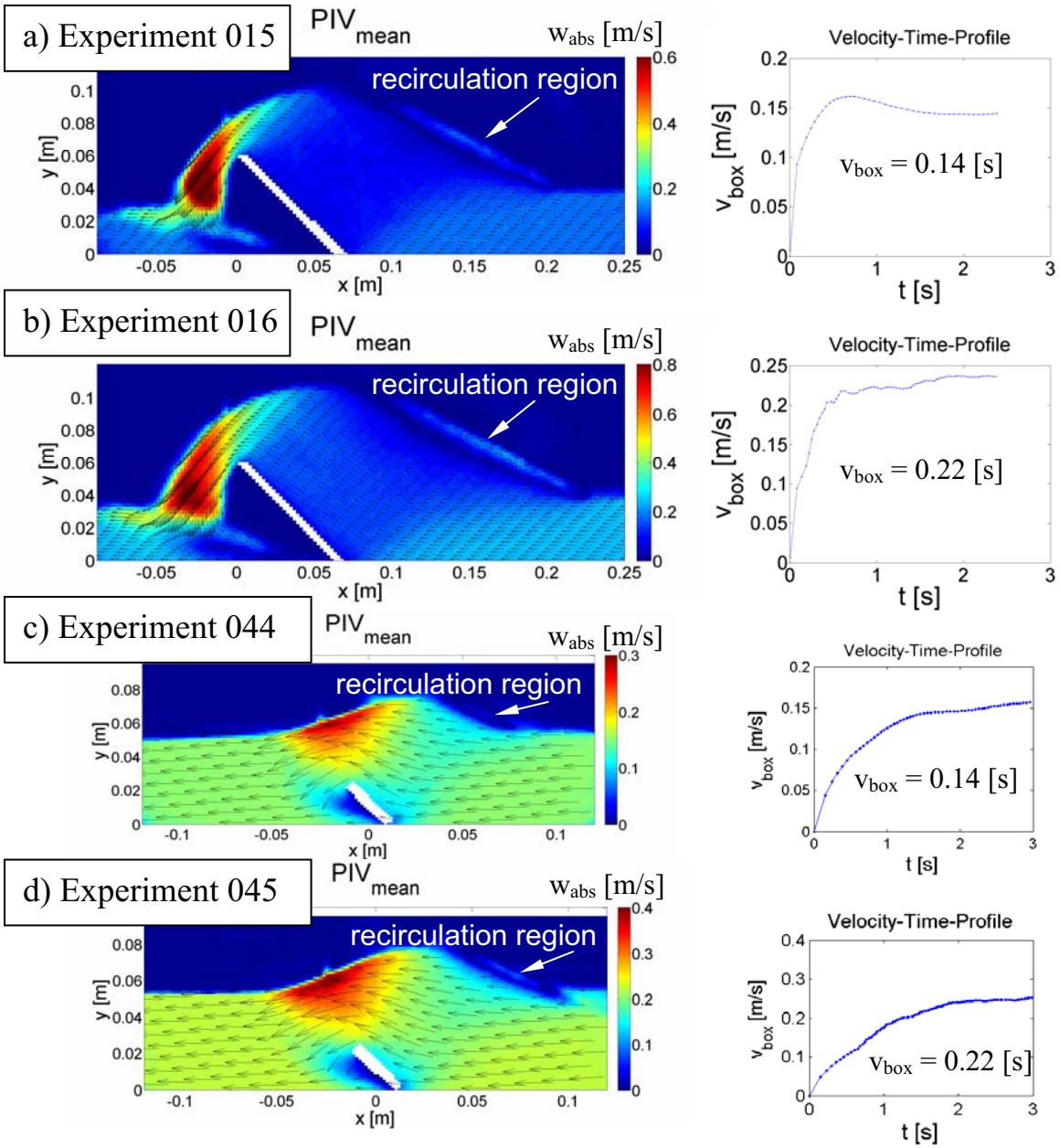

Figure 56: a) and b) indicate results for the velocity fields for 4 [mm] glass beads, the blade with the number DA04_45° and a bed height of 40 [mm]. c) and d) show velocity fields for 1.675 [mm] glass beads, the blade with the number DA04S_45° and a bed height of 50 [mm] (see Chapter 9.11 for details).

The Effect of the Bed Height

Also, the bed height has an effect on the flow behind the blade. Starting with a bed height of 40 [mm] (Figure 57a) the maximum velocity is decreasing when the bed height increases.

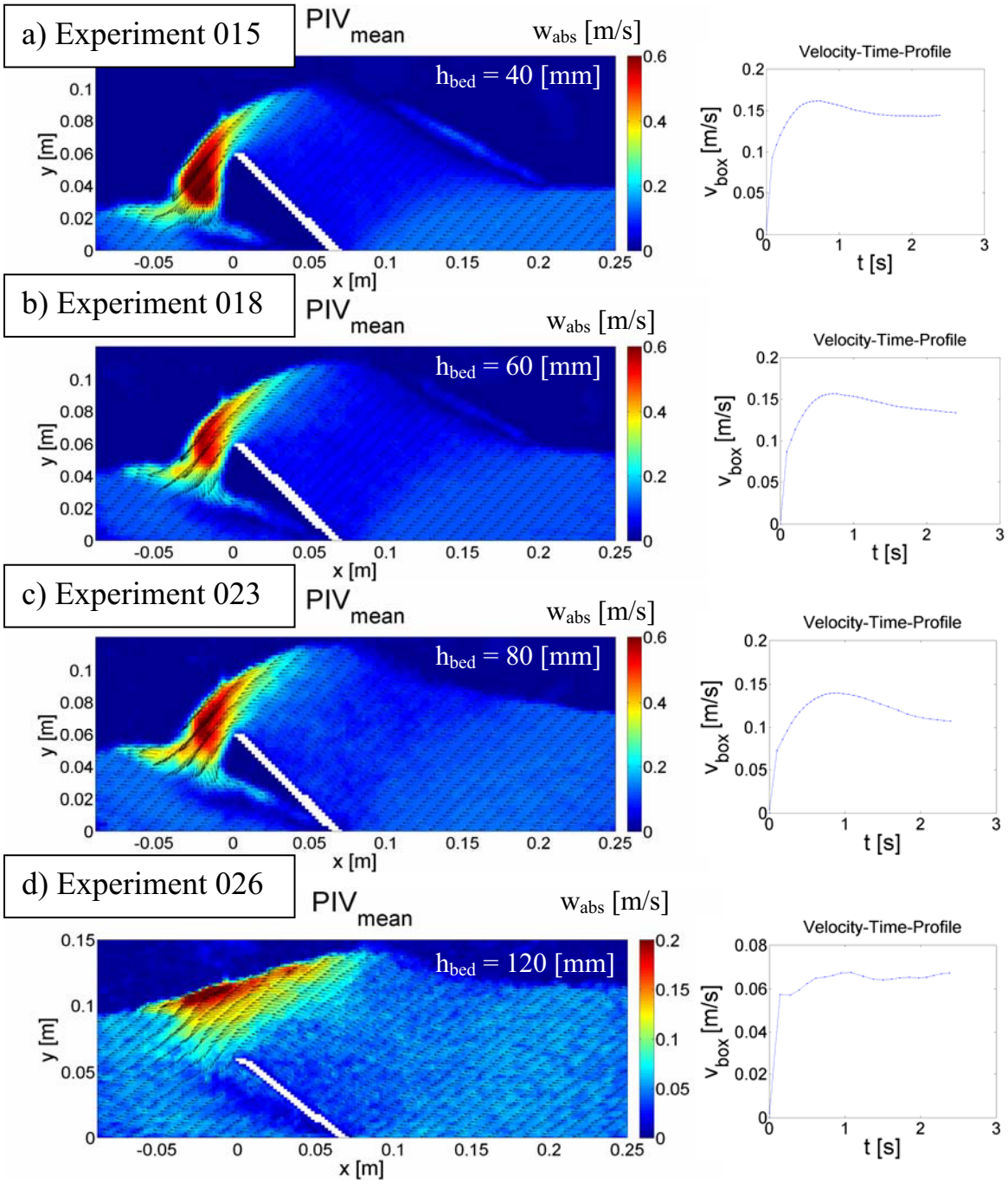

Figure 57: Comparison of velocity fields at four different bed heights (h_{bed}): (a) 40, (b) 60, (c) 80, (d) 100 [mm] (see Chapter 9.11 for details).

The Effect of the Blade Position

Rising the blade, i.e., increasing the blade's vertical position in the particle bed, leads to different flow pattern over the blade. Fixing the blade at a higher position has the inverse effect than increasing the bed height at constant blade position.

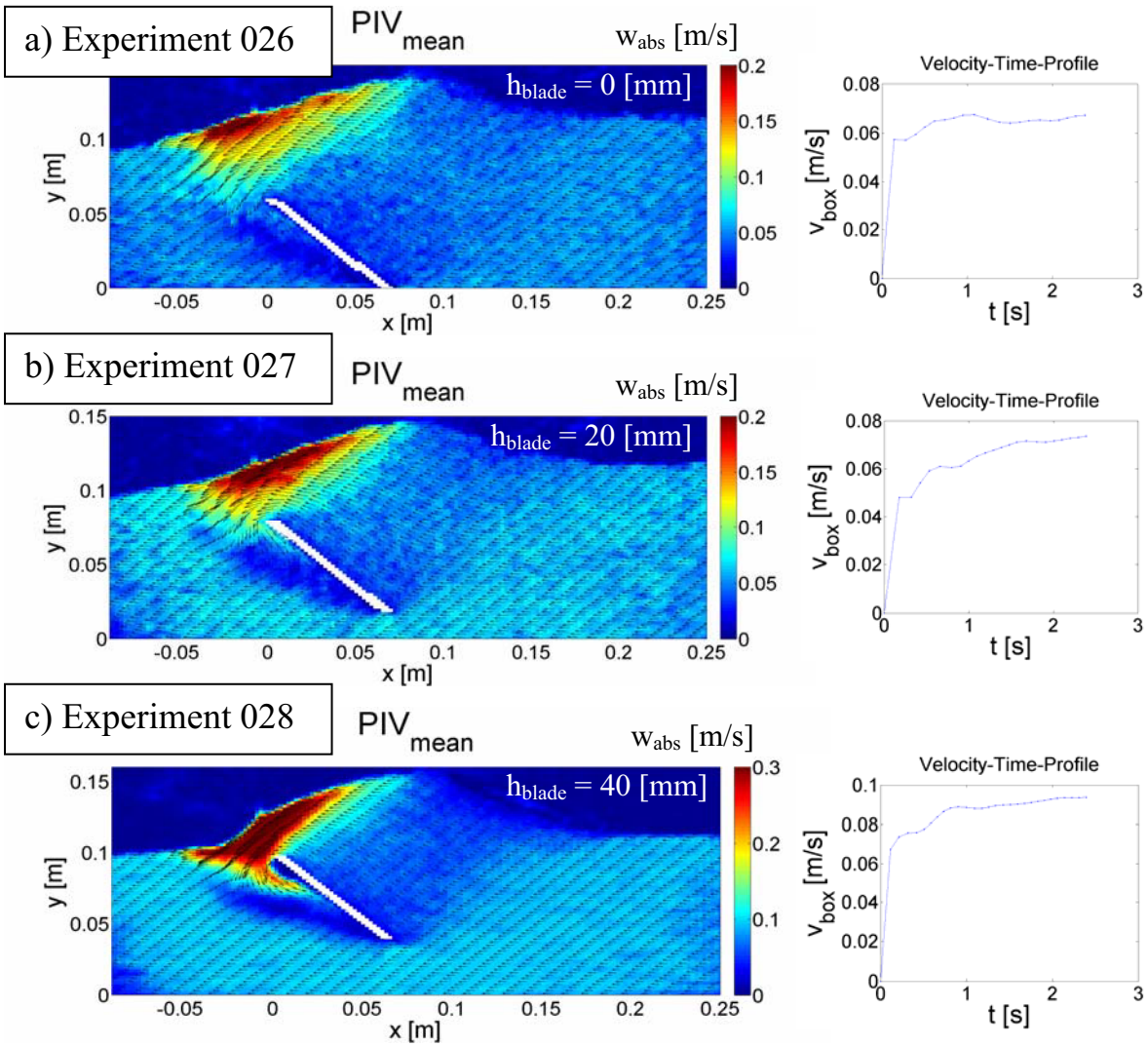

Figure 58: Comparison of velocity fields at three different blade positions (h_{blade}): (a) 0, (b) 20, (c) 40 [mm] (see Chapter 9.11 for details).

The Effect of the Blade Angle

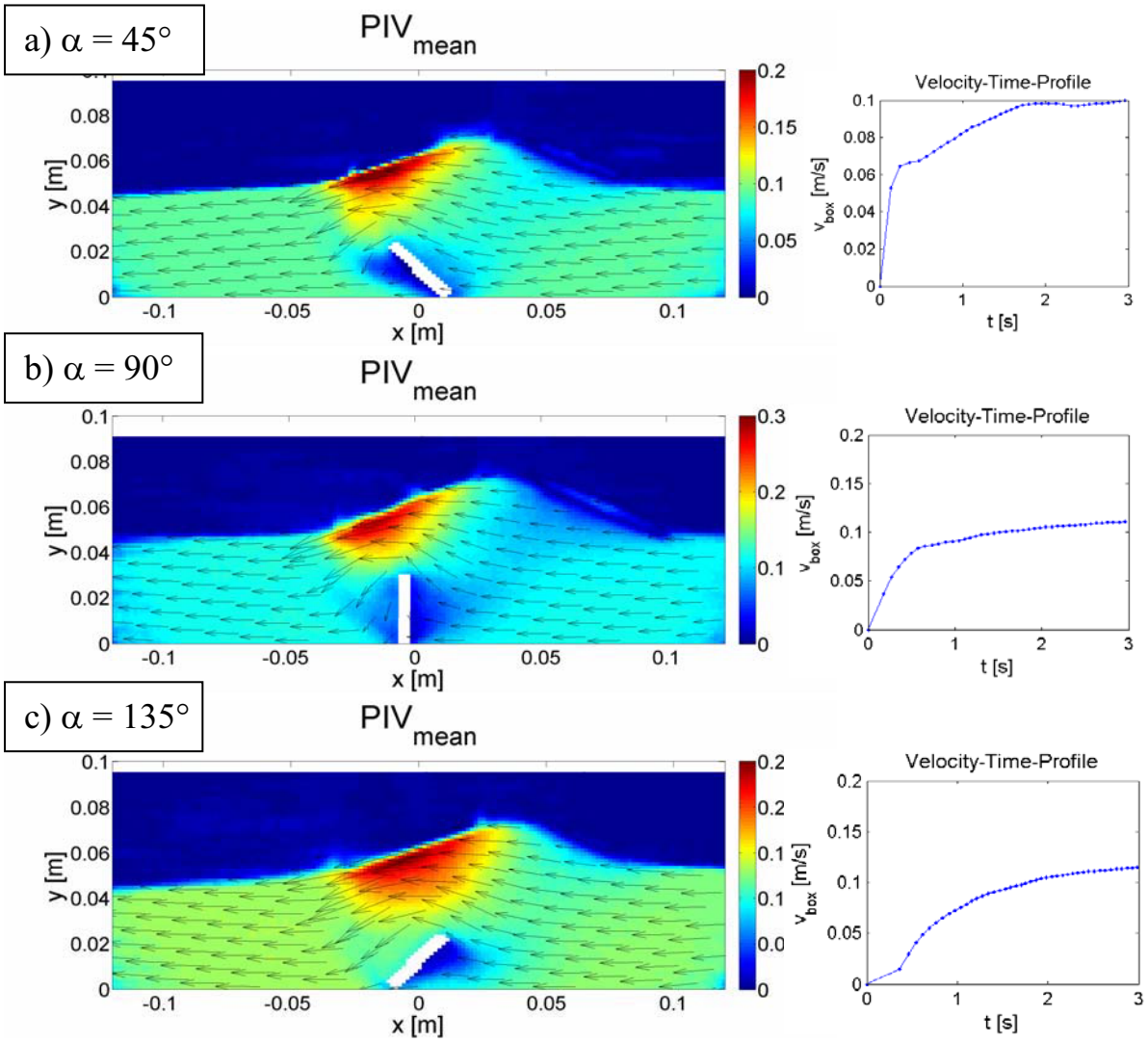

Figure 59: Figure shows the comparison of velocity fields by using three different blade angles (α): (a) 45 [°], (b) 90 [°], (c) 135 [°] (see Chapter 9.11 for details).

The Effect of the Particle Size

The resulting velocity fields (Figure 60), show that there is no significant difference in the flow behavior for particles with a diameter of 4 and 1.675 mm. However, the calculation of the velocity field when using 0.5 [mm] particles resulted in no useful data because particles were sticking to the front wall during the experiment.

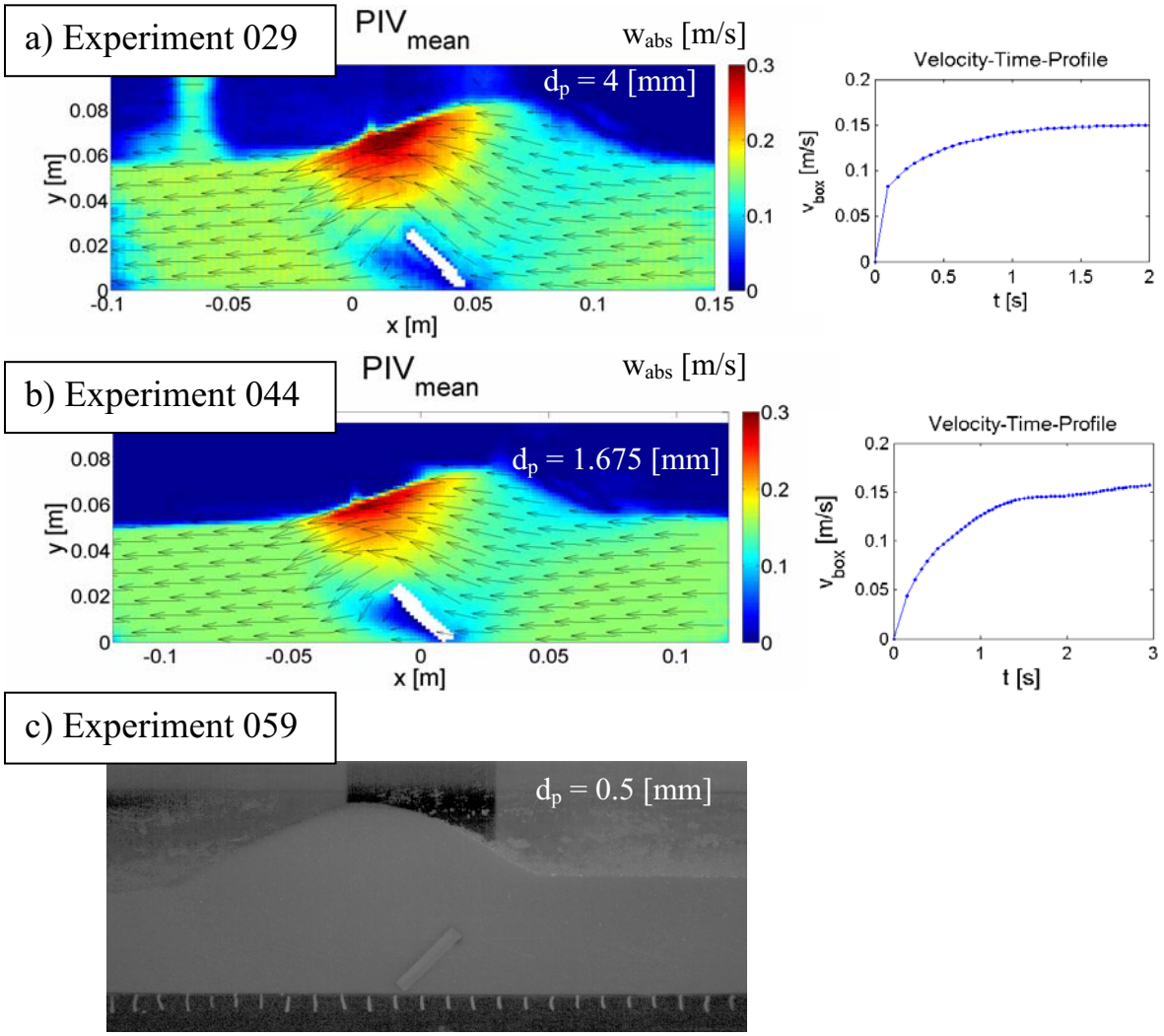

Figure 60: Velocity fields for different particle sizes (d_p): (a) 4, (b) 1.675 [mm]. (c) shows a raw image of the experiment using 0.5 [mm] particles (see Chapter 9.11 for details).

5. Conclusions and Outlook

5.1. Conclusions

In this diploma thesis we developed a novel two-dimensional experimental setup for the investigation of granular flows. This setup provides insight into granular flows in agitated devices. Additionally, we made observations of dry and wet granular flows in a four-bladed mixer. A comparison with literature data showed qualitative agreement with our experimental results.

The measured velocity fields in the four-bladed mixer clearly indicated regions of high velocity. This is caused by the stirrer blades, which are pushing forward a heap of particles. The velocity fields from the experiment in the two-dimensional setup also showed this high velocity region in front of the blade. Thus, we conclude that our two-dimensional experiments are able to mimic the flow situation in a four-bladed mixer reasonably well. Furthermore, we observed a recirculating region in front of the blade (stationary with respect to the blade) in our two-dimensional setup.

For the fine particles in the four-bladed mixer, we observed a smooth transition between the high velocity region and the region between the blades where the velocity was low. An irregular distribution of the velocity field (i.e., erratic velocity fluctuations) was observed for the larger particles. It is speculated that the gaps between the large particles were resulting in a roll-and-lock effect causing this irregular velocity distribution.

The velocity distribution, besides the absolute velocity, significantly changed with increasing stirrer speed. The heap's shape changed significantly between 60 and 120 rpm. The faster moving blade led to a higher pile and a greater slope angle.

When the particle size was small enough, i.e., below 1 [mm], the liquid bridge forces had an effect on the particle flow (particles with a size of 4 and 6 [mm] had no clear effect on the flow behavior). The gap between regions with a low velocity was getting smaller, when moisture was added to the particle bed. Thus, it is possible to distinguish between a dry and wet particle bed by analyzing the velocity field.

When the filling height increased, the effect of the stirrer speed on the bed's surface velocity became smaller. Bed height also had an effect on the flow behind the blade. The maximum velocity was decreasing when the bed height increased. Also, heaps were getting smaller until they disappeared.

Fixing the blade at a higher position had the inverse effect than increasing the bed height at constant blade position. The granular bed below the blade was essential unaffected by the blade motion. Thus, it is impossible to induce particle motion below the stirrer in a bladed mixer, a fact that has been recently found also by computer simulations (see Remy et al. [36]).

In the paper of Bagster D. F. and Bridgewater J. [28], the blade angle had an effect on the force on the blade. The different values of voltage (required energy) from the powersupply in our experiments confirmed with this thesis. Also the recirculating region was getting smaller for larger blade angles.

5.2. Outlook

For the improvement of the two-dimensional several points should be considered in future work:

- The installation of a cohesionless, and electrically conductive, transparent material as the front window for the box. Also, the humidity of the air inside the box should be controlled, in order to avoid electric charging of the particles. This should enable investigations of granular flow involving smaller particles.
- A measurement system for the force, which is acting on the blade.
- A changeable box width for investigating the effect of the particle beds thickness on the granular flow.

Furthermore, it would be interesting to compare the experimental results of the two-dimensional setup with computer simulations (e.g., using the discrete element method, DEM) in detail.

The investigation of segregation was not performed within this work, and maybe this topic is one of the most interesting in the field of granular mixing. With the two-dimensional setup, segregation experiments could be easily performed, as long as the smallest particle size is not below the critical diameter where electrostatic forces become relevant (i.e., currently approximately 0.5 mm). Also, the effect of other particle properties (e.g., particle shape, surface morphology, or the friction coefficient) should be investigated to obtain industry-relevant data on particle flow and mixing.

The investigations of wet granular flow in this study may help to develop new parameters and equations, which consider moisture in DEM simulations of granular flows. Also, the

information recorded in this study could be potentially useful to develop flow models for various types of granular matter, as well as to develop or optimize mixing equipment.

6. Nomenclature

a	length	[m]
Bo	Bond number	[-]
Co	collision number	[-]
D	flux of particles	[m^3/s]
d	diameter	[m]
F	force	[N]
f	length	[m]
g	gravitational acceleration	[m/s^2]
h	thickness	[m]
I	dimensionless shear rate	[-]
K	spring stiffness	[N/m]
l	length	[m]
M	moment	[Nm]
m	mass	[kg]
n	stirrer speed	[rev/s]
p	pressure	[P]
R, r	radius	[m]
t	time	[s]
u, v, w	velocity	[m/s]
V	volume	[m^3]
x, y	length, ordinate	[m]

Greek Letters

β	bridge angle	[°]
δ	contact angle	[°]

ϕ	volume fraction	[-]
Φ	moisture content	[vol%]
φ	angle	[°]
γ	surface tension	[N/m²]
κ	packing density parameter	[-]
η	ordinate length	[m]
μ	friction coefficient	[-]
θ	inclination angle	[°]
ρ	density	[kg/m³]
ω	rotational speed	[rad/s]
ξ	ordinate length	[m]
ζ	spring deformation	[m]

Indices

1, 2, i, j	number
abs	absolute
b	basal
Bg	Bagnold
C	collision
d	dynamic
dim	dimensionless
G	gravitational
g	granular
l	liquid
N	normal
p	particle
r	friction

R	radial
roll	rolling
tan	tangential
u	ordinate direction
w	weight
y	ordinate direction

7. List of Figures

8. References

[1] **Duran, J.**; Sands Powders and Grains, An Introduction to the Physics of Granular Materials, Springer-Verlag, New York Berlin Heidelberg, (2000),Chapter 4

[2] **Bagnold, R. A.** 1966. Shearing and Dilatation of Dry Sand and Singing Mechanism. Proceedings of the Royal Society of London Series A-Mathematical and Physical Sciences **295**:219-&.

[3] **Bak, P., C. Tang, and K. Wiesenfeld**. 1988. Self-Organized Criticality. Physical Review A **38**:364-374.

[4] **Bouchaud, J. P., M. E. Cates, and P. Claudin**. 1995. Stress-Distribution in Granular Media and Nonlinear-Wave Equation. Journal de Physique I **5**:639-656.

[5] **Bouchaud, J. P., M. E. Cates, J. R. Prakash, and S. F. Edwards**. 1995. Hysteresis and Metastability in A Continuum Sandpile Model. Physical Review Letters **74**:1982-1985.

[6] **Brochard-Wyart, F. and P. G. De Gennes**. 1996. Adhesion between rubbers and grafted solids. Journal of Adhesion **57**:21-30.

[7] **Forterre, Y. and O. Pouliquen**. 2008. Flows of dense granular media. Annual Review of Fluid Mechanics **40**:1-24.

[8] **Jaeger, H. M., S. R. Nagel, and R. P. Behringer**. 1996. Granular solids, liquids, and gases. Reviews of Modern Physics **68**:1259-1273.

[9] **Roux, J. N. and G. Combe**. 2002. Quasistatic rheology and the origins of strain. Computes Rendus Physique **3**:131-140.

[10] **Goldhirsch, I.** 2003. Rapid granular flows. Annual Review of Fluid Mechanics **35**:267-293.

[11] **Bagnold, R. A.** 1954. Experiments on a Gravity-Free Dispersion of Large Solid Spheres in A Newtonian Fluid Under Shear. Proceedings of the Royal Society of London Series A-Mathematical and Physical Sciences **225**:49-63.

[12] **Rajchenbach, J.** 2003. Dense, rapid flows of inelastic grains under gravity. Physical Review Letters **90**.

[13] **Deboeuf, S., E. Lajeunesse, O. Dauchot, and B. Andreotti**. 2006. Flow rule, self-channelization, and levees in unconfined granular flows. Physical Review Letters **97**.

[14] **Komatsu, T. S., S. Inagaki, N. Nakagawa, and S. Nasuno**. 2001. Creep motion in a granular pile exhibiting steady surface flow. Physical Review Letters **86**:1757-1760.

[15] **Savage, S. B. and K. Hutter**. 1989. The Motion of a Finite Mass of Granular Material Down A Rough Incline. Journal of Fluid Mechanics **199**:177-215.

[16] **Böge, A.** 1995. Technische Mechanik, Statik-Dynamik-Fluidmechanik-Festigkeitslehre, 23. Aufl.

[17] **Sveen, J.K.**: An Introduction to MatPIV v.1.6.1, Dept. of Math., University of Oslo (2004)

[18] **Gleirscher, M.:** Modellbasierte, computergestützte Analyse von Daten aus dem DPIV-Verfahren, Fakultät für Informatik, Technische Universität München (2004)

[19] **Brandl, D.**.: Granulare Partikel Image Velocimetry für einen Vakuumtrockner, Institut für Prozess- und Partikeltechnik, Technische Universität Graz, (2009)

[20] **Zhou, Y.C., Yu, A.B., Bridgewater, J**. 2003. Segregation of binary mixture of particles in a bladed mixer. Journal of Chemical Technology and Biotechnology 78:187-193.

[21] **Schubert, H**. Kapillarität in porösen Feststoffsystemen, Springer-Verlag, Berlin Heidelberg New York, (1982)

[22] **Schubert, H**. Untersuchungen zur Ermittlung von Kapillardruck und Zugfestigkeit von feuchten Haufwerken aus körnigen Stoffen, Diss. Universität Karlsruhe, (1972)

[23] **Sartor, K**. –H. Berechnung von Haftkraft, Kapillardruck und Flüssigkeitsvolumen am System einer Flüssigkeitsbrücke zwischen zwei gleich großen Kugeln. Diplomarbeit Nr. 190 des Instituts für Mechanische Verfahrenstechnik der Universität Karlsruhe (TH), (1971)

[24] **Schaber, K**. Berechnung rotationssymmetrischer Flüssigkeitsbrücken sowie experimentelle und theoretische Ermittlung der Stabilitätsgrenzen dieser Brücken. Diplomarbeit Nr. 231 des Instituts für Mechanische Verfahrenstechnik der Universität Karlsruhe (TH), (1973)

[25] **Li, H. and McCarthy, J.J.** Phase diagrams for cohesive particle mixing an segregation, Phys. Rev. E71 (2005)

[26] **Li, H. and McCarthy, J.J.** Cohesive particle mixing and segregation under shear, Powder Technology, 164 (2006), 58-64

[27] **Bagnold, R. A.** Experiments of a gravity free dispersion of large solid spheres in a Newtonian fluid under shear. Proc. R. Soc. 225 (1954), 4-63

[28] **Bagster, D. F. and Bridgewater J.** The Flow of a Granular Material over a Moving Blade, Powder Technology, 3(1969/70), 323-338

[29] **Bagster, D. F. and Bridgewater J.** The measurement of the force needed to move blades through a bed of cohesionless granules, Powder Technol., 1 (1967/66), 189

[30] **Bagster, D.** F. The prediction of the force needed to move blades through a bed of cohesionless granules, Powder technol. 3 (1969/70), 153

[31] **Lekhal A., Conway S. L., Glasser, J. and Khinast J. G.** Characterization of Granular Flow of Wet Solids in a Bladed Mixer, AIChE Journal, August (2006), Vol. 52, No. 8, 2757-2766

[32] **Parker D. J., Dijkstra A. E., Martin T. W. and Seville J. P. K.** Positron emission particle tracking studies of spherical particle motion in rotating drums , Chemical Engineering Science Volume 52, Issue 13, July 1997, Pages 2011-2022

[33] **Matlab:** Matlab 7.3.0 (R2008a). The Mathworks, Inc., 2008.

[34] **Remy B., Khinast J.G., Glasser B.J.** Discrete Element Simulation of Free Flowing Grains in a Four-Bladed Mixer. AIChE Journal. 2009; 55:2035-2048.

[35] **Remy B., Canty T.M., Khinast J.G., Glasser B.J.** Kinematics of Cohesionless Particulate Flows in a Bladed Mixer. Chem Eng Sci. 2009; (submitted)

[36] **Remy B., Glasser B.J., Khinast J.G.** The Effect of Mixer Properties and Fill Level on Granular Flow in a Bladed Mixer. AIChE Journal. 2010; 56:336-353.

[37] **Conway S.L., Lekhal A., Khinast J.G., Glasser B.J.** Granular flow and segregation in a four-bladed mixer. Chem Eng Sci. 2005; 60:7091-7107.

[38] **Radl S., Kalvoda E., Glasser B.J., Khinast J.G.** Mixing Characteristics of Wet Granular Matter in a Bladed Mixer. Powder Technology. 2010; 171-189.

[39] **Remy B., Canty T. M., Khinast J. G., Glasser B. J.** Experiments and simulations of cohesionless particles with varying roughness in a bladed mixer. Chemical Engineering Science. 2010.

[40] **LabVIEW:** National Instruments LabVIEW 8.6.

[41] **Cundall P.A., Strack O. D. L.** Discrete Numerical-Model for Granular Assemblies. Geotechnique. 47-65. 1979.

[42] **Seville J., Tüzün U., Clift R**. Processing of Particulate Solids. Blackie Academic and Professionel. London. 1997.

9. Appendix

9.1. Electrical Drive Calculation

Calculation for electrical drive

Force on blade (from D.F. BAGSTER: The flow of granular matter over a moving blade)

angle between floor and blade	α	[°]	45,00	
angle between free surface and horizontal surface	β	[°]	25,00	
angle between force on blade and normal face of blade	δ	[°]	15,00	
bed material	ϕ	[°]	26,00	
passive earth pressure coefficient (Figure. 10)	K_p	[]	10,70	11,6
dimensionless force on bade	F/(L*B^2*γ)	[]	8,49	
dimensionless horizontal force on bade	H/(L*B^2*γ)	[]	7,35	
bulk density of the glass beads	ρ	[kg/m³]	1200,00	
gravity force	g	[m/s²]	9,81	
porosity	ε	[]	0,43	
specific weight of material	γ	[kg/m²s²],[N/m]	6710,04	
blade length	L_{blade}	[m]	0,10	
blade width	B_{blade}	[m]	0,05	
horizontal dimension of the blade	B	[m]	0,07	
force on blade per length	F/L	[N]	255,78	
horizontal force on blade per lenght	H_{blade}/L	[N]	221,52	
force on blade	F_{blade}	[N]	12,79	
horizontal force on blade	**H_{blade}**	**[N]**	**11,08**	
horizontal force on blade	**M_{blade}**	**[kg]**	**1,13**	

$$K_P = \frac{\sin^2(\alpha-\phi)\cos\delta}{\sin\alpha\sin(\alpha+\delta)\left[1-\left(\frac{\sin(\phi+\delta)\sin(\phi+\beta)}{\sin(\alpha+\delta)\sin(\alpha+\beta)}\right)^{\frac{1}{2}}\right]^2} \quad (2)$$

The total force per unit length is

$$F/L = \tfrac{1}{2}\gamma P^2 K_P/(\sin\alpha\cos\delta) \quad (3)$$

and the horizontal force per unit length is

$$H_0/L = \tfrac{1}{2} K_P \gamma P^2 \sin(\alpha+\delta)/\sin\alpha\cos\delta. \quad (4)$$

Key	*Blade*	*b (cm)*	*Particles*	*ϕ (degrees)*	*δ (degrees)*	*K_P*
⊖	steel	2.00	glass beads—sheared	26	14½	3.85
●	steel	4.00	glass beads—sheared	26	14½	3.85
□	steel	6.00	glass beads—sheared	26	14½	3.85
×	steel	4.00	glass beads—loose poured	28	14½	4.26
◇	rough	4.00	glass beads—sheared	26	23	5.02
+	steel	4.00	coarse sand—sheared	37	25	11.6
⊕	steel	2.00	coarse sand—sheared	37	25	11.6
○	steel	4.00	polythene chips—sheared	37	7	5.15

Fig. 10. Correlation of frictional properties with dimensionless force and immersion, $\alpha = \pi/2$.

Bagster, D. F. and Bridgewater J. The Flow of a Granular Material over a Moving Blade, Powder Technology, 3(1969/70), 323-338

Technical data from construction

linear bearing made of aluminium	V_{bear_Al}	[m³]	0,0003
box volume fraction made of steel	V_{box_Al}	[m³]	0,0017
box volume fraction made of aluminium	V_{box_Fe}	[m³]	0,0003
density of steel	ρ_{Fe}	[kg/m³]	7850,00
density of aluminium	ρ_{Al}	[kg/m³]	2700,00
box mass fraction made of steel	m_{Box_Fe}	[kg]	2,19
box mass fraction made of aluminium	m_{Box_Al}	[kg]	5,51
weight of (empty) box	m_{Box}	[kg]	7,70
box filling z-length	l_{Box}	[m]	1,20
box filling y-length	b_{Box}	[m]	0,05
box filling (z-)heigth	h_{Box}	[m]	0,30
max filling volume of glass beads	$V_{füll}$	[m³]	0,02
weight of glass beads bed at max. filling heigth	m_{Sch}	[kg]	12,80
weight of box with glass beads bed	m_{ges}	[kg]	20,51
box velocity	v_{Box}	[m/s]	0,46
box moving distance	L_{move}	[m]	1,10

Roll resistance for the moving box (A. BÖGE: Technische Mechanik p.132)

force of box with glass beads bed	F_{Sch}	[N]	201,16
	f_1	[cm]	0,001
	f_2	[cm]	0,05
bearing ball diameter	d_{ball}	[mm]	4,00
roll resistance force	**F_{roll}**	**[N]**	**25,65**

Acceleration force for the moving box (A. BÖGE: Technische Mechanik)

max. velocity for moving box	v_{max}	[m/s]	0,50
acceleration track	s_{ac}	[m]	0,10
acceleration time	t_{ac}	[s]	0,40
acceleration	a_{ac}	[m/s²]	1,25
acceleration force	**F_{ac}**	**[N]**	**25,63**

Resulting force for moving box (A. BÖGE: Technische Mechanik)

resulting force for moving box	**F_{ac_res}**	**[N]**	**62,36**

Electrical motor 168.4111.30.04 (appendix file nr. 01_02_DC_motor_DOGA)

number of revolutions of electrical motor	n_{SM}	[rev/min]	500,00
torque of electrical motor (for n_{SM} = 500 [U/min])	M_{SM}	[Nm]	1,40
shaftdiameter of electrical motor	d_{SM}	[mm]	8,00

Spur wheel for electrical drive M1 25 Z (steel St 50)

gear module	m_{gear}	[mm]	1,00
wheel reference diameter	d_{0_wheel}	[mm]	25,00
bore diameter	d_{bore}	[mm]	6,00
hub diameter	d_{hub}	[mm]	14,00
hub lenght	l_{hub}	[mm]	6,00
gear lenght	l_{wheel}	[mm]	5,00
number of teeth	z_{gear}	[-]	25,00
wheel diameter	d_{wheel}	[mm]	27,00

Gear rack (hostaform C, α = 20°, polyacetal POM)

gear module	m_{gear}	[mm]	1,00
rack lenght	l_{rack}	[mm]	1100,00
rack wide	b_{rack}	[mm]	9,00
rack high	h_{rack}	[mm]	9,00
mesh high	h_{0_rack}	[mm]	8,00
feet high	h_{F_rack}	[mm]	6,80

Carrying capacity for the spur wheel (Roloff/Matek: Maschinenelemente p.542)

gear module	m	[mm]	1,00
tooth headlenght	h_a	[mm]	1,00
tooth feetlenght	h_f	[mm]	1,00
toothlenght	h	[mm]	2,00
number of teeth	z	[-]	25,00
wheel reference diameter	d_w	[mm]	25,00
outside diameter	d_a	[mm]	27,00
reference angle (profile angle, DIN 867)	α_P	[°]	20,00
limited tooth number	z_g	[-]	17,10
tangential force on tooth (equation 15.70, p. 545)	F_t	[N]	62,36
rated torque (equation 15.69, p. 544)	T_1	[Nm]	0,78
effective force on tooth (equation 15.71, p. 545)	F_{bn}	[N]	66,36
radial force on tooth (equation 15.72, p. 545)	F_r	[N]	22,70
gear lenght	b	[mm]	5,00
linear transition of force	F_t/b	[N/mm]	12,47
effective linear transition of force	$F_t/b*c_B$	[N/mm]	13,72
operating factor (Tab.3.6.: Roloff/Matek, Tabellen)	c_B	[-]	1,10
factor (Tab.15-18.: Roloff/Matek, Tabellen)	K_1	[-]	8,50
factor (Tab.15-18.: Roloff/Matek, Tabellen)	K_2	[-]	1,12
factor (Tab.15-18.: Roloff/Matek, Tabellen)	K_3	[-]	0,02
factor (Tab.15-18.: Roloff/Matek, Tabellen)	K_4	[-]	6,25
dynamic factor (Roloff/Matek: p.547 equation 15.76)	**K_V**	[-]	**5,47**
(dynamic factor (diagramm Tab.15-18.: Roloff/Matek,Tab))	(K_{vgraph})	[-]	1,74
correcture factor (Tab. 15-18.: Roloff/Matek, Tabellen)	f_F	[-]	2,45
factor (Tab.15-18.: Roloff/Matek, Tabellen)	$K_{350}*N$	[-]	0,30

gear wheel lenght factor (equation 15.78, p. 547)	**f_{SH}**	**[µm]**	**8,94**	
mean linear transition of force (Roloff/Matek: p.547)	$F_{m/b}$	[N/mm]	75,03	
factor (Tab 15-19: Roloff/Matek)	K'	[-]	1,33	
gear shaft	d_{SH}	[mm]	6,00	bearing dimension
bearing distance	l	[mm]	20,00	
gear distance	s	[mm]	10,00	
tooth line differences (equation 15.79, p. 548)	**f_{ma}**	**[µm]**	**3,44**	
assembly parameter	c	[-]	0,50	
gear line differences	$f_{H\beta}$	[µm]	6,88	
tooth quality(Tab 15-18 .:Roloff/Matek)	q_H	[-]	1,32	
effective centerline deviation before running-in (equation 15.80, p. 548)	**$F_{\beta x}$**	**[µm]**	**15,34**	
	$F_{\beta x\_min}$	[µm]	0,38	
effective centerline deviation after running-in (equation 15.81, p. 548)	**$F_{\beta y}$**	**[µm]**	**3,34**	
running-in parameter (Tab15-20.: Roloff/Matek)	y_β	[µm]	12,00	
lenght factor (equation 15.82, p. 548)	**$K_{H\beta}$**	**[-]**	**1,44**	
lenght factor (equation 15.83, p. 548)	**$K_{F\beta}$**	**[-]**	**1,27**	
relation tooth lenght/tooth height	N_F	[-]	0,64	
spur gear factor (Tab 15-22 a.:Roloff/Matek)	**$K_{F\alpha}$**	**[-]**	**1,20**	
spur gear factor (Tab 15-22 a.:Roloff/Matek)	**$K_{H\alpha}$**	**[-]**	**1,20**	
tooth base carrying capacity (equation 15.85, p. 549)	**K_{Fges}**	**[-]**	**9,14**	
tooth pit carrying capacity (equation 15.85, p. 549)	**K_{Hges}**	**[-]**	**3,23**	

Calculation of carrying capacity

occuring tooth base tension (equation 15.86, p. 550)	**σ_{F0}**	**[N/mm²]**	**32,25**	
tension correction factor (Tab 15-23 b.:Roloff/Matek)	Y_{Sa}	[-]	2,70	
shape factor (Tab 15-23 a.:Roloff/Matek)	Y_{Fa}	[-]	1,65	
overlap factor (equation 15.86, p. 550)	Y_ε	[-]	0,58	
chamfer factor (Tab 15-23 c.:Roloff/Matek)	Y_β	[-]	1,00	
overlap (equation 15.86, p. 550)	ε_α	[-]	2,27	
tooth base tension (equation 15.87, p. 550)	**σ_F**	**[N/mm²]**	**294,74**	
permitted tooth base tension (equation 15.88, p. 551)	**σ_{FP}**	**[N/mm²]**	**410,67**	**$\sigma_F < \sigma_{FP}$**
tension correction factor (equation 15.88, p. 551)	Y_{ST}	[-]	2,00	
durability factor (Tab 15-24 a.:Roloff/Matek)	Y_{NT}	[-]	2,00	
relative bearing number (Tab 15-24 b.:Roloff/Matek)	$Y_{\delta\_rel\_T}$	[-]	1,10	
relative surface factor (Tab 15-24 c.:Roloff/Matek)	$Y_{R\_rel\_T}$	[-]	1,00	
size factor (Tab 15-24 d.:Roloff/Matek)	Y_X	[-]	1,00	
tooth base endurance strenght (Tab 15-16.:Roloff/Matek)	σ_{F_lim}	[N/mm²]	140,00	
minimum safety factor (equation 15.88, p. 551)	s_{min}	[-]	1,50	

Calculation of tooth pit carrying capacity

occuring center pressure (equation 15.90, p. 551)	**σ_{H_max}**	**[N/mm²]**	**52,73**	
maximum pressure strength (equation 15.90, p. 551)	F_{FP}	[N]	201,16	
Poisson number (equation 15.90, p. 551)	ν	[-]	0,30	
E-modul steel (equation 15.90, p. 551)	E_{st}	[N/mm²]	206000,00	
E-modul POM	E_{POM}	[N/mm²]	2500,00	
reduced E-modul (equation 15.90, p. 551)	E	[N/mm²]	4940,05	
radius of curvature (equation 15.90, p. 551)	ρ	[mm]	12,50	
center pressure at pitch point (equation 15.93, p. 553)	**σ_{H0}**	**[N/mm²]**	**16,49**	
spread factor (Tab 15-25 a.:Roloff/Matek)	Z_H	[-]	2,50	
elasticity factor (equation 15.93, p. 552)	Z_E	[$N^{0,5}$/mm]	12,30	
overlap factor (equation 15.93, p. 553)	Z_ε	[-]	0,76	
chamfer factor (equation 15.93, p. 553)	Z_β	[-]	1,00	
center pressure at pitch circle (equation 15.94, p. 553)	**σ_H**	**[N/mm²]**	**53,27**	
permitted surface pressure (equation 15.95, p. 554)	**σ_{HP}**	**[N/mm²]**	**209,86**	**$\sigma_H < \sigma_{HP}$**
endurance value for stress (Tab 15-16.:Roloff/Matek)	σ_{H_lim}	[N/mm²]	360,00	
durability factor (Tab 15-26 d.:Roloff/Matek)	Z_{NT}		1,60	
minimum safety factor (equation 15.95, p. 554)	S_{Hmin}		1,30	
lubricant factor (Tab 15-26 a.:Roloff/Matek)	Z_L		1,04	
speed factor (Tab 15-26 b.:Roloff/Matek)	Z_v		0,81	
roughness factor (Tab 15-26 c.:Roloff/Matek)	Z_R		0,47	
material matching factor (Tab 15-26 e.:Roloff/Matek)	Z_w		1,20	
size factor (Tab 15-2 d.:Roloff/Matek)	Z_X		1,00	
viscosity at 40[°C] (equation 15.95, p. 553)	ν_{40}	[mm²/s]	200,00	
	C_{ZL}		0,72	
	C_{ZV}		0,74	
circumferential speed (equation 15.95, p. 553)	v		0,60	
	C_{ZR}		0,25	
relative roughness height (equation 15.95, p. 553)	R_{Z100}		6,40	

motor
moteur
Gleichstrommotor

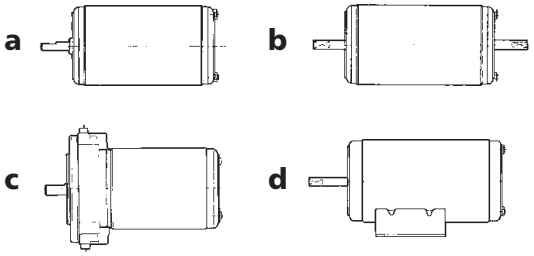

Referencia Référence number Référence Referenznummern	Tensión nominal Nominal voltage Tension nominale Nennspannung	Par nominal Nominal torque Couple nominal Drehmoment nominal	Velocidad nominal Nominal speed Vitesse nominale Geschwindigkeit nominal	Corriente nominal Nominal current Courant nominal Nominalstrom	Par de arranque Starting torque Couple de démarrage Anzugsdrehmoment	Corriente de Arranque Starting current Courant de démarrage Anlaufstrom	Eje Shaft Arbre Welle	Conexiones Connections Connexions Anschlußart	Esq. eléct. Wiring diag. Sch. élect. Schaltbild	Peso aproximado Approximate weight Poids approximatif Gewicht (ca.)	Grado de estanqueidad Watertightness Etanchéité Feuchtigkeitsschutzklasse	Diseño: a,b, c, d Design: a,b, c, d Dessin: a,b, c, d Abbildung: a,b, c, d	Curva Curve Courbe Kurve
	Un (V)	**Mn (N.m.)**	**Nn (r.p.m.)**	**In (A)**	**Ma (N.m.)**	**Ia (A)**				**P (kg)**	**IP**		
168.4105.20.04	12	0.50	1900	14	3.0	64	E8	C8	EE1	2.6	IP53	a	37
168.4105.30.04	24	0.50	1900	7	3.0	32	E8	C8	EE1	2.6	IP53	a	37
168.4107.20.04	12	0.50	2000	13	3.2	76	E46	-	EE1	2.6	IP53	c	38
168.4107.30.04	24	0.50	2000	6.5	3.2	38	E46	-	EE1	2.6	IP53	c	38
168.4108.20.04	12	0.45	2800	19	3.0	100	E9	C9	EE4	2.6	IP53	a	39
168.4108.30.04	24	0.45	2800	10	3.0	52	E9	C9	EE4	2.6	IP53	a	39
168.4111.20.04	12	0.75	1000	11	2.8	36	E11	C9	EE2	2.6	IP53	a	40
168.4111.30.04	24	0.75	1000	5.5	2.8	18	E11	C9	EE2	2.6	IP53	a	40
168.4112.20.04	12	0.70	1500	14	3.0	56	E12	C11	EE2	2.6	IP53	a	42
168.4112.30.04	24	0.70	1500	7	3.0	28	E12	C11	EE2	2.6	IP53	a	42
168.4115.30.04	24	0.50	3000	11	3.0	70	E13/E41	C13	EE2	2.6	IP53	a	41
168.4116.20.04	12	0.50	1900	14	3.0	64	E8	C8	EE1	2.6	IP53	d	37
168.4116.30.04	24	0.50	1900	7	3.0	32	E8	C8	EE1	2.6	IP53	d	37
168.4121.30.04E	24	0.50	3000	11	3.0	70	E11/E11	C13	F2	2.6	IP53	b	41
168.4122.30.04	24	0.75	1000	5.5	2.8	18	E13/E41	C13	EE2	2.6	IP53	a	40
168.4123.20.04	12	0.50	2100	16	3.0	76	E13/E41	C13	EE2	2.6	IP53	a	43
168.4123.30.04	24	0.50	2100	8	3.0	38	E13/E41	C13	EE2	2.6	IP53	a	43
168.4134.30.04	24	0.30	750	1.5	1.5	7	E59	C9	EE2	2.6	IP53	a	44

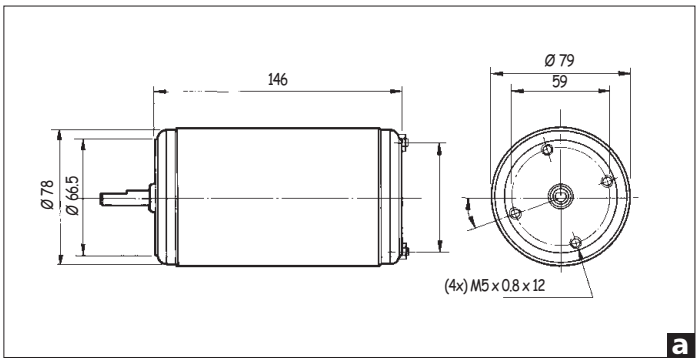

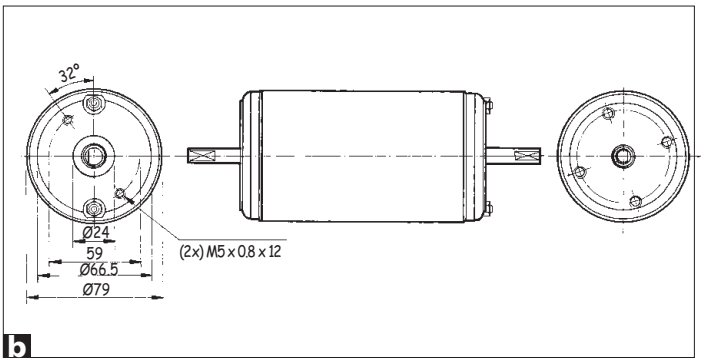

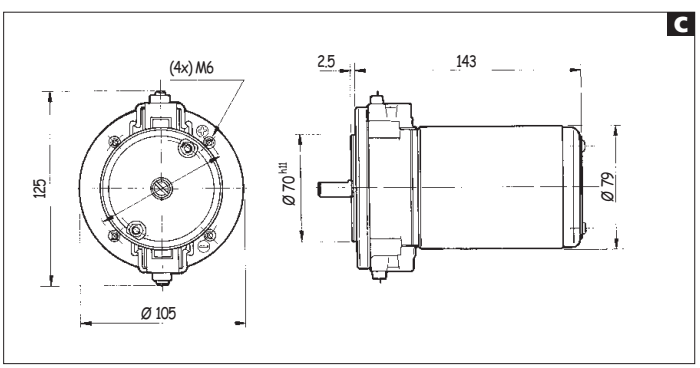

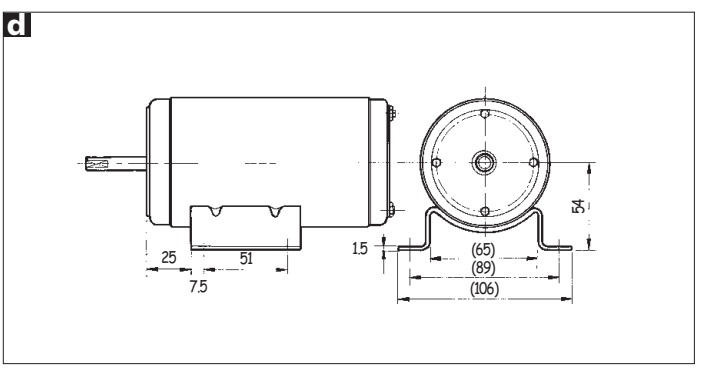

EJE - SHAFT - ARBRE - WELLE

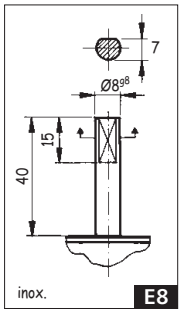

E8

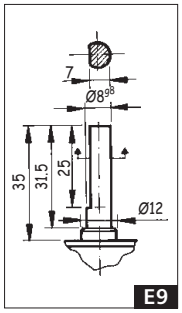

E9

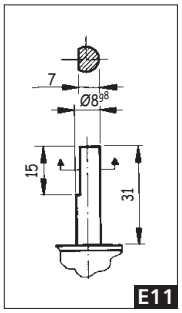

E11

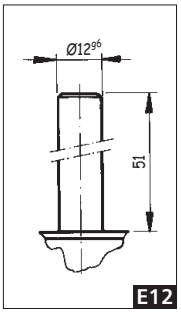

E12

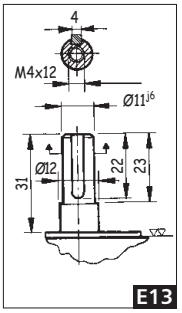

E13

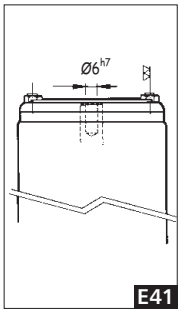

E41

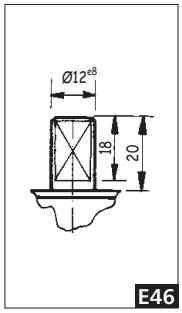

E46

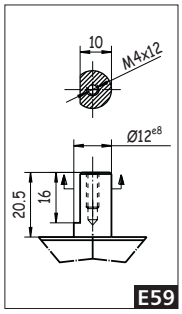

E59

CONEXIÓN - CONNECTION - CONNEXION - ANSCHLUSSART

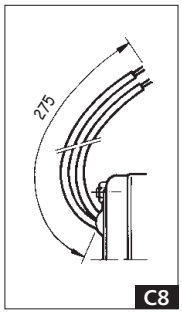

C8

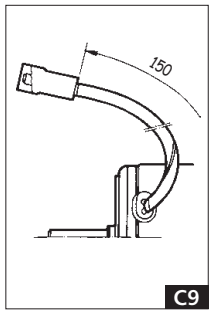

C9

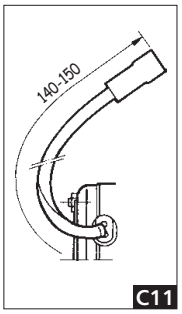

C11

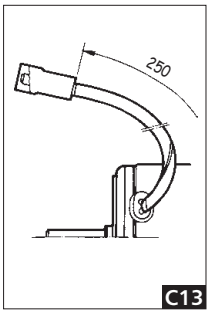

C13

ESQUEMA ELÉCTRICO - WIRING DIAGRAM - SCHÉME ÉLECTRIQUE - SCHALTBILD

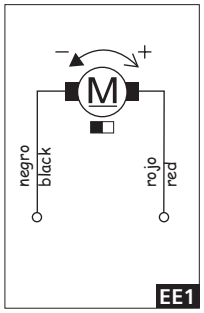

EE1

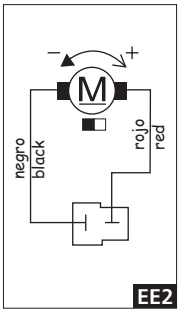

EE2

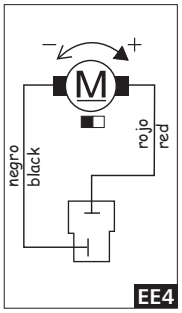

EE4

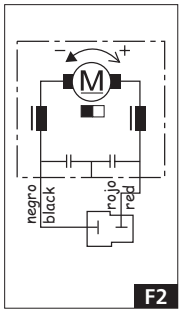

F2

CURVAS - CURVES - COURBES - KURVEN

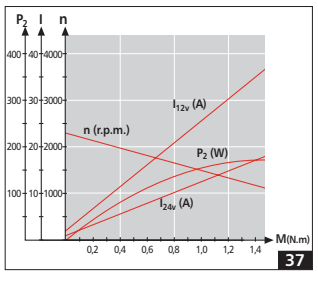

37

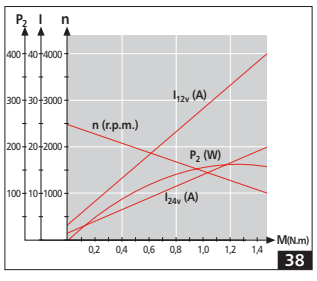

38

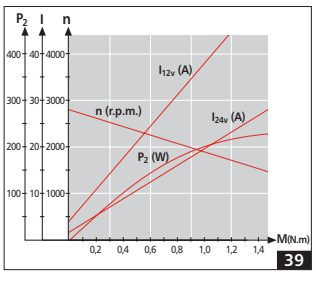

39

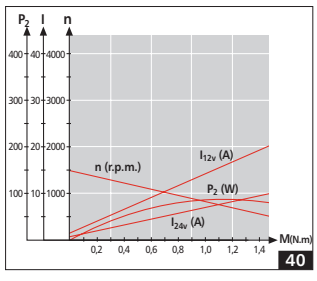

40

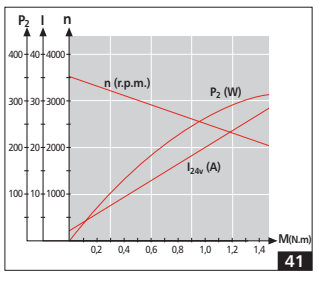

41

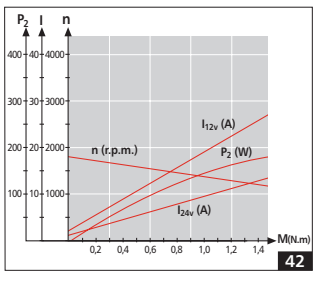

42

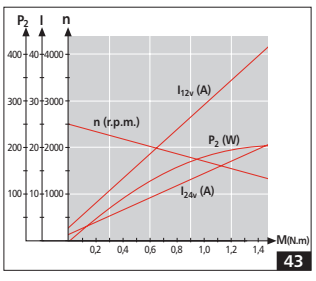

43

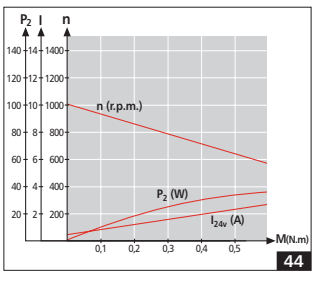

44

9.2. Drawings for the 2D Experimental Setup

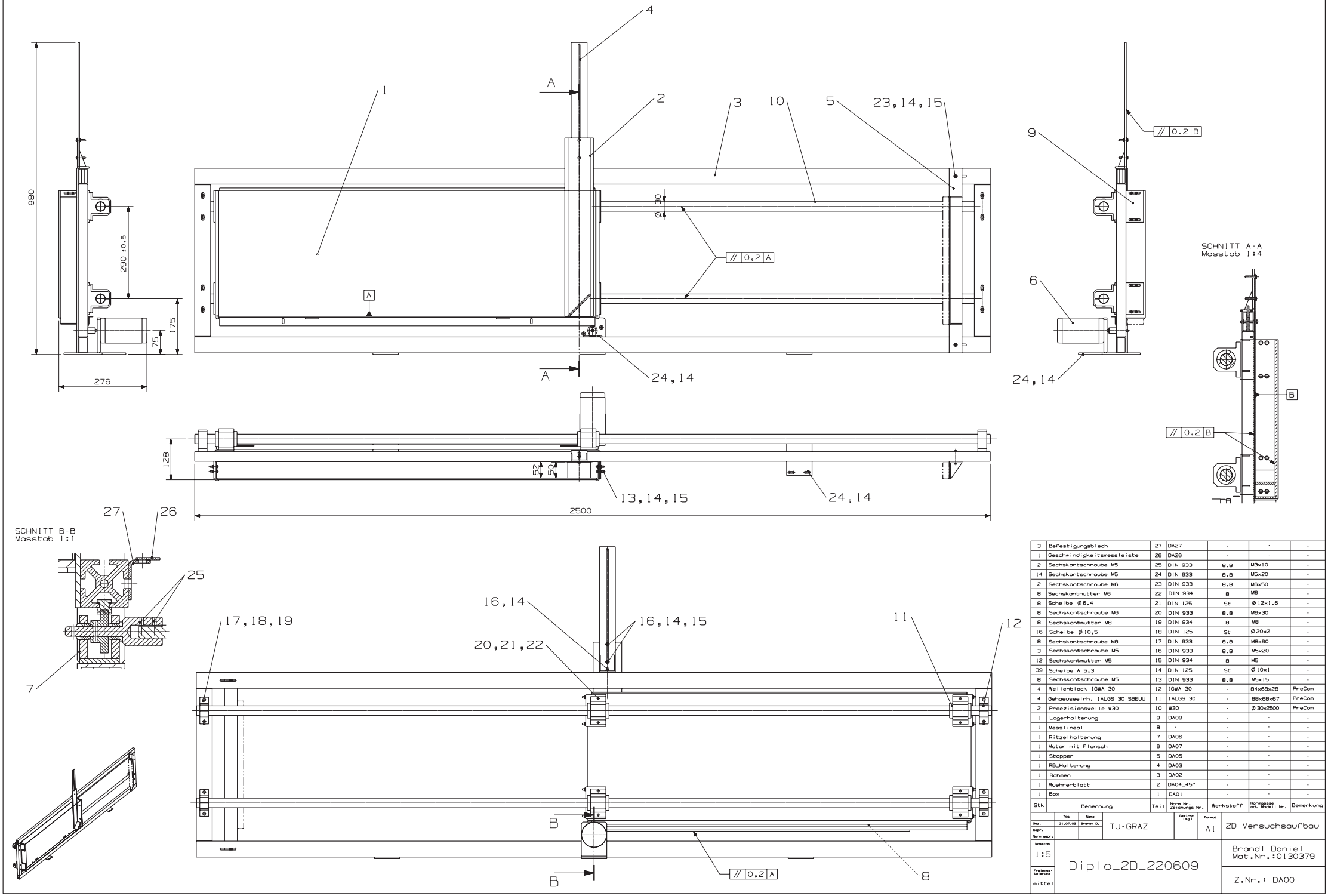

Stk	Benennung	Teil	Norm Nr., Zeichnungs Nr.	Werkstoff	Rohmasse od. Modell Nr.	Bemerkung
3	Befestigungsblech	27	DA27	-	-	-
1	Geschwindigkeitsmessleiste	26	DA26	-	-	-
2	Sechskantschraube M5	25	DIN 933	8.8	M3x10	-
14	Sechskantschraube M5	24	DIN 933	8.8	M5x20	-
2	Sechskantschraube M6	23	DIN 933	8.8	M6x50	-
8	Sechskantmutter M6	22	DIN 934	8	M6	-
8	Scheibe Ø6,4	21	DIN 125	St	Ø 12x1,6	-
8	Sechskantschraube M6	20	DIN 933	8.8	M6x30	-
8	Sechskantmutter M8	19	DIN 934	8	M8	-
16	Scheibe Ø10,5	18	DIN 125	St	Ø 20x2	-
8	Sechskantschraube M8	17	DIN 933	8.8	M8x60	-
3	Sechskantschraube M5	16	DIN 933	8.8	M5x20	-
12	Sechskantmutter M5	15	DIN 934	8	M5	-
39	Scheibe A 5,3	14	DIN 125	St	Ø 10x1	-
8	Sechskantschraube M5	13	DIN 933	8.8	M5x15	-
4	Wellenblock IGWA 30	12	IGWA 30	-	84x68x28	PreCom
4	Gehaeuseeinh. IALGS 30 SBEUU	11	IALGS 30	-	88x68x67	PreCom
2	Praezisionswelle W30	10	W30	-	Ø 30x2500	PreCom
1	Lagerhalterung	9	DA09	-	-	-
1	Messlineal	8	-	-	-	-
1	Ritzelhalterung	7	DA06	-	-	-
1	Motor mit Flansch	6	DA07	-	-	-
1	Stopper	5	DA05	-	-	-
1	RB_Halterung	4	DA03	-	-	-
1	Rahmen	3	DA02	-	-	-
1	Ruehrerblatt	2	DA04_45°	-	-	-
1	Box	1	DA01	-	-	-

	Tag	Name			
Gez.	21.07.09	Brandl D.	TU-GRAZ	Gewicht [kg] -	Format A1
Gepr.					2D Versuchsaufbau
Norm gepr.					
Massstab 1:5			Diplo_2D_220609		Brandl Daniel Mat.Nr.:0130379
Freimass-toleranz mittel					Z.Nr.: DA00

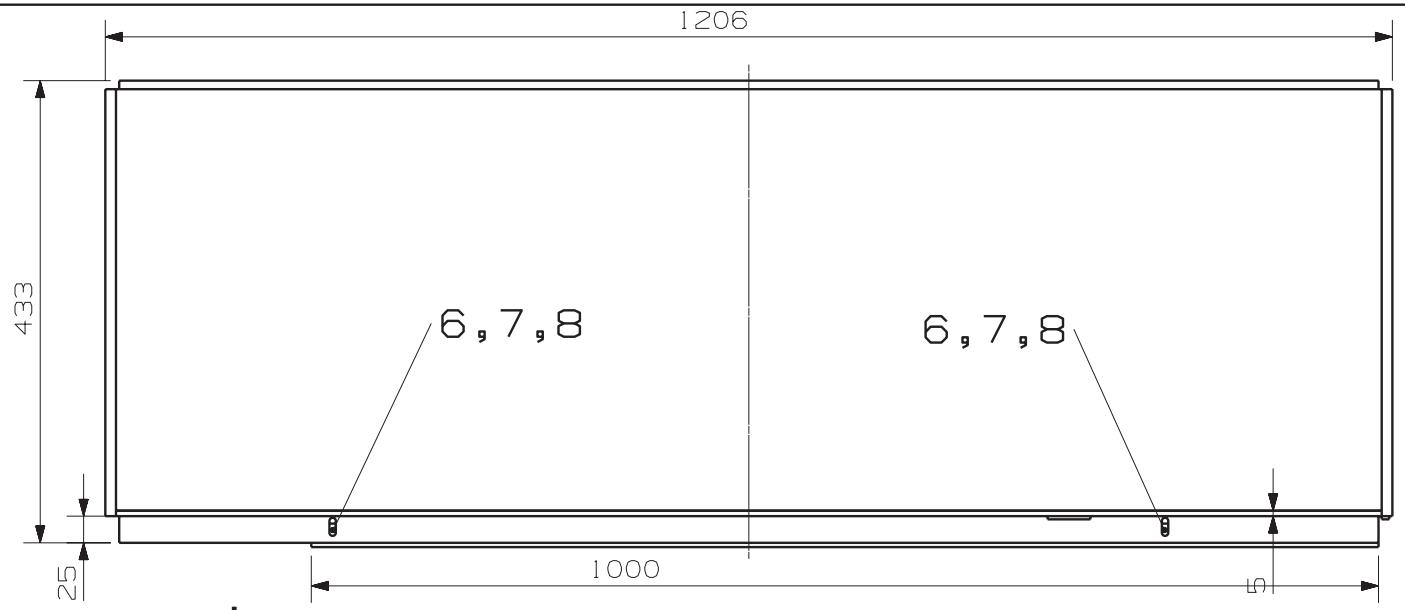

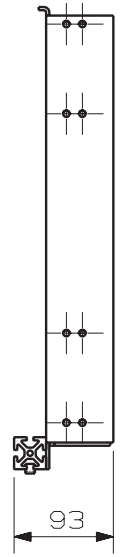

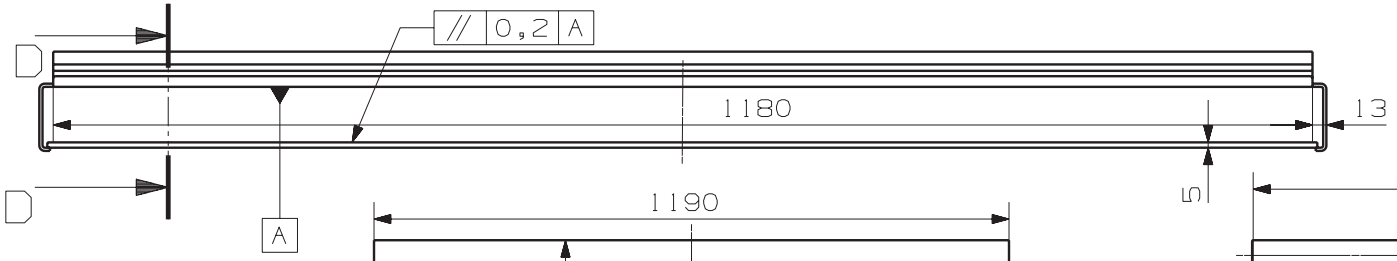

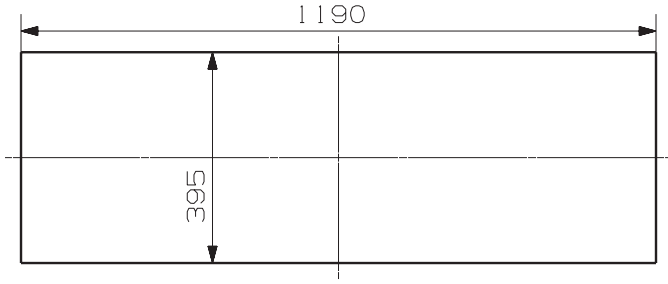

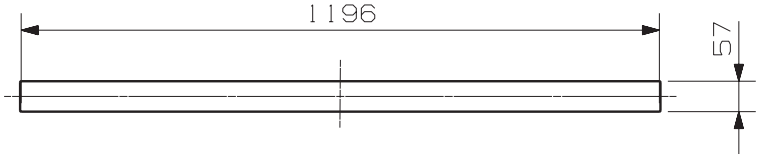

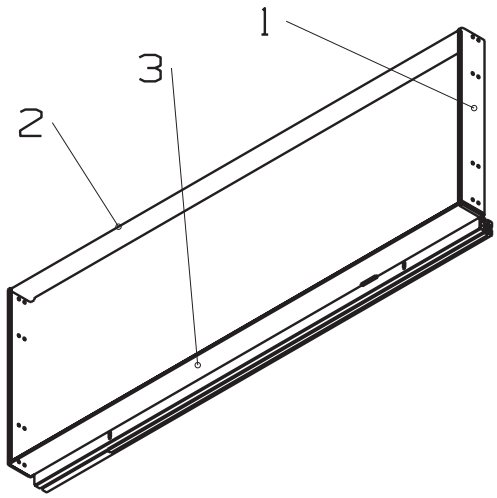

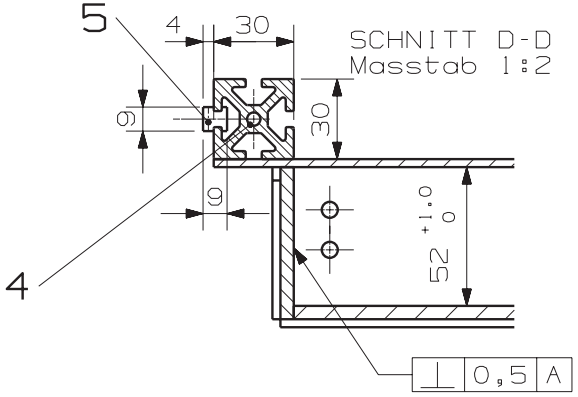

Stk	Benennung	Teil	Norm Nr. Zeichnungs Nr.	Werkstoff	Rohmasse od. Modell Nr.	Bemerkung
2	Abschlusselement	8	-	-	-	-
2	Scheibe A5,3	7	DIN 125	St	Ø 10x1	-
2	Sechskantschraube M5	6	DIN 933	8.8	M5x10	-
1	Zahnstange M1	5	-	POM	1000x9x9	-
1	Fuehrungsleiste	4	-	-	1180x30x30	-
1	Glasscheibe	3	-	Polystyrol	1196x57x5	-
1	Glasscheibe	2	-	Polystyrol	1190x395x5	-
1	Grundblech	1	DA01-01	-	-	-

	Tag	Name		Gewicht [kg]	Format	
Gez.	15.06.09	Brandl D.	TU-GRAZ	18	A3	2D Versuchsaufbau
Gepr.						
Norm gepr.						
Masstab 1:5			Box komplett			Brandl Daniel Mat.Nr.:0130379
Freimass-toleranz mittel						Z.Nr.: DA01

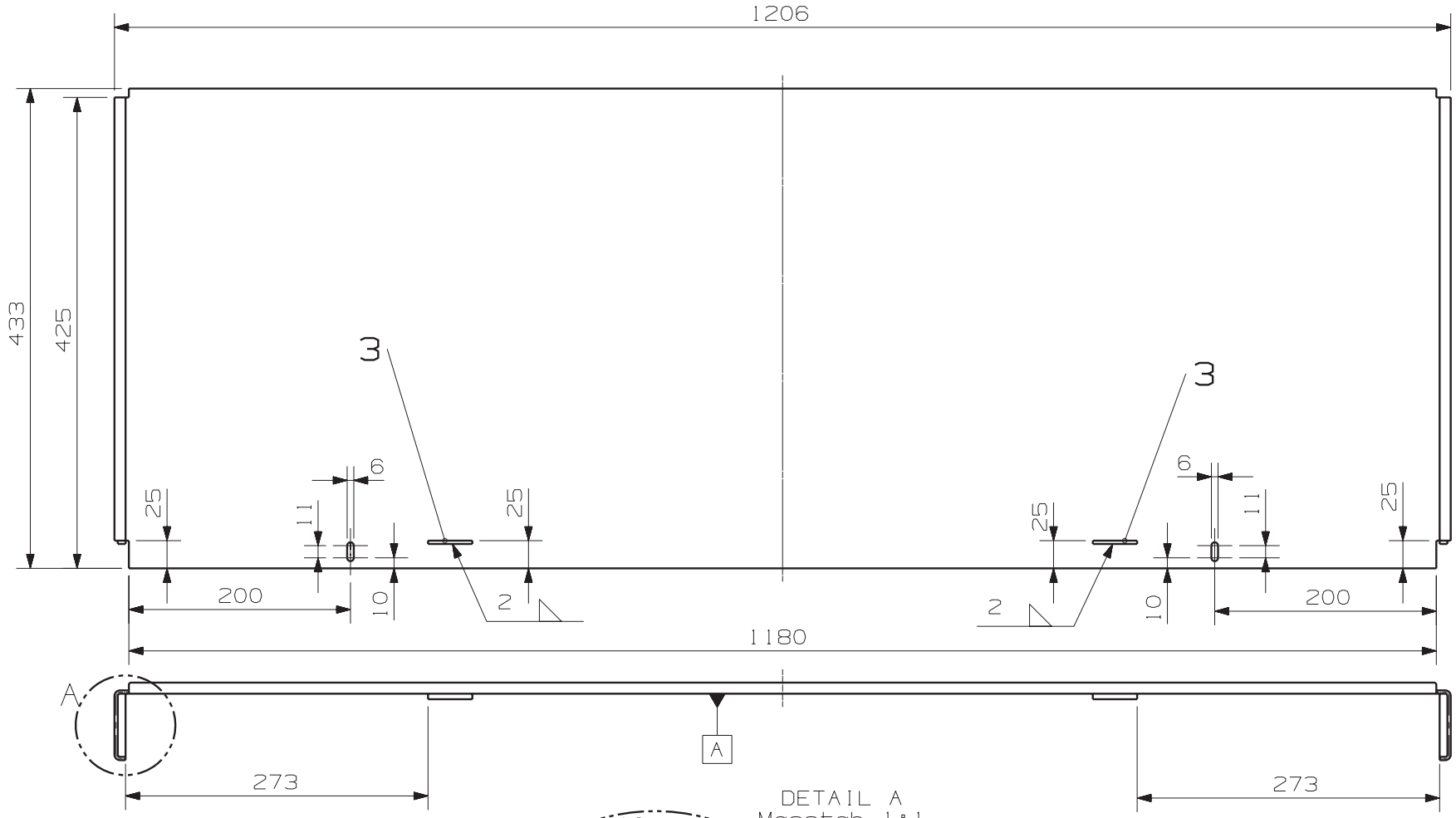

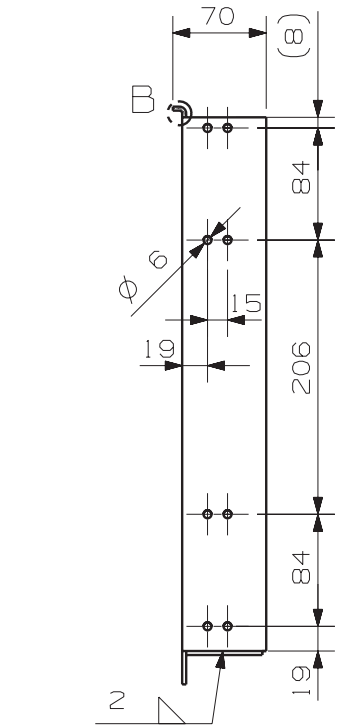

DETAIL B
Masstab 1:1

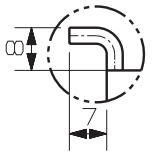

Teile 1,2 und 3
aus Blechzuschnitte
Z.Nr.: DA

DETAIL A
Masstab 1:1

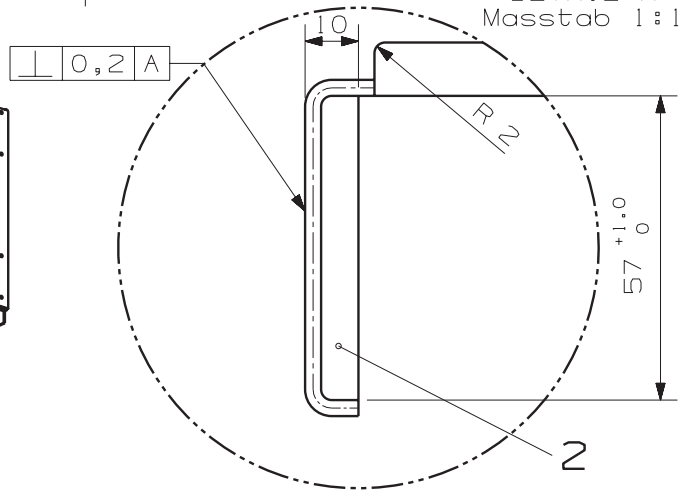

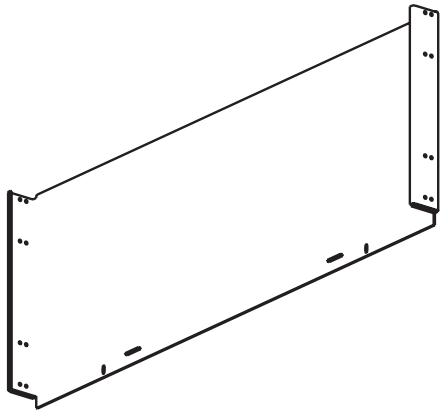

2	Blech	3	DA01-02	-	-	-
2	Blech	2	DA01-02	-	-	-
1	Blech	1	DA01-02	-	-	-
Stk	Benennung	Teil	Norm Nr. Zeichnungs Nr.	Werkstoff	Rohmassse od. Modell Nr.	Bemerkung

	Tag	Name		Gewicht [kg]	Format	
Gez.	15.06.09	Brandl D.	TU-GRAZ	18	A3	2D Versuchsaufbau
Gepr.						
Norm gepr.						
Masstab 1:4	Box Grundblech gebogen u. gebohrt					Brandl Daniel Mat.Nr.:0130379
Freimass-toleranz mittel						Z.Nr.: DA01-01

Teil 1

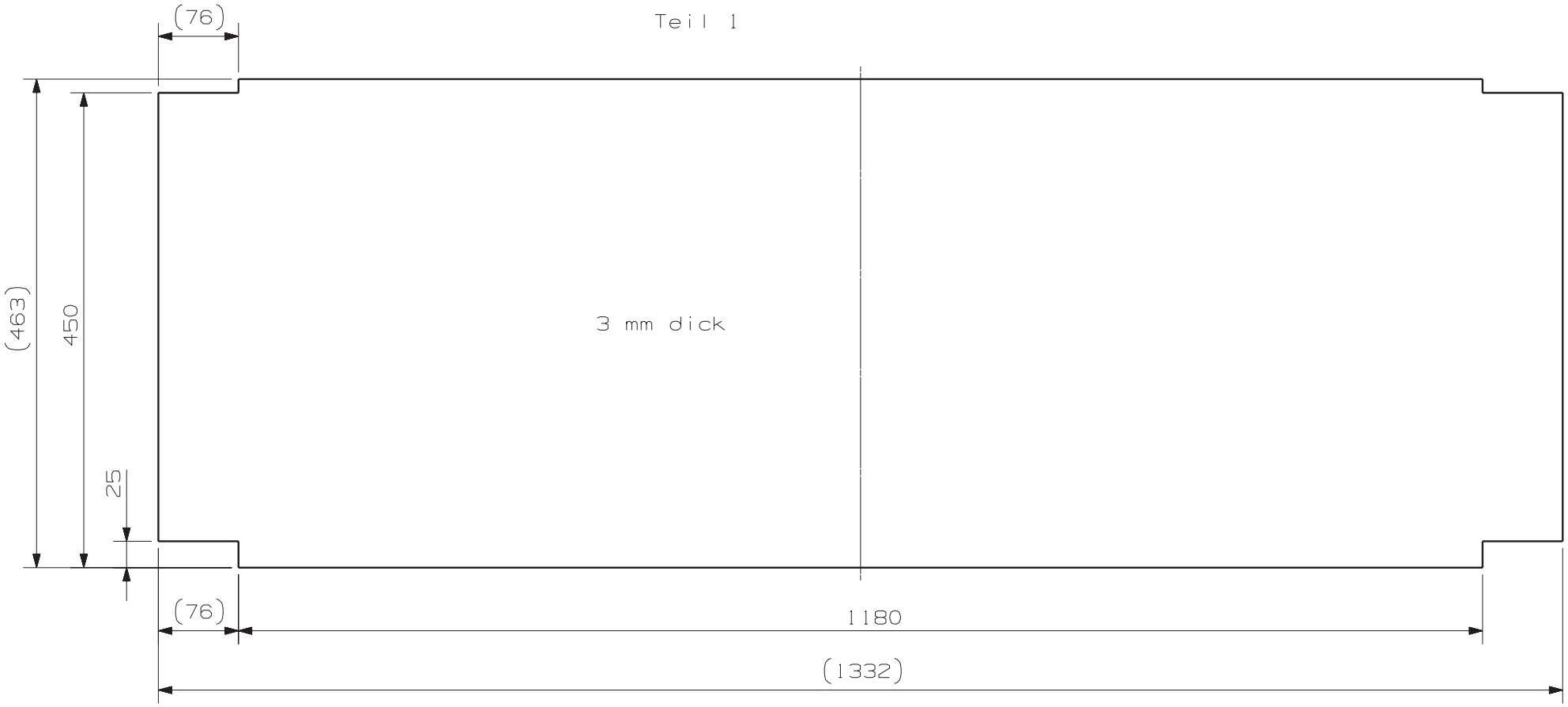

Teil 2
Masstab 1:1

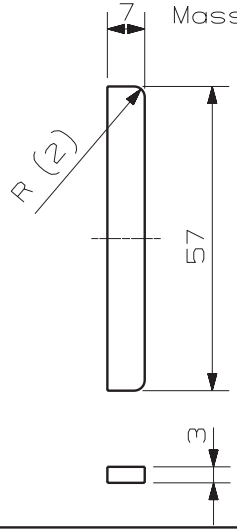

Teil 3
Masstab 1:1

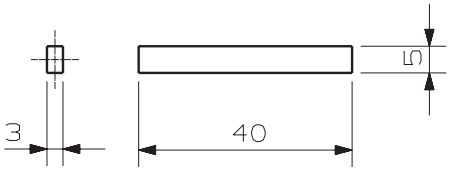

Die Klammermasse haengen
vom Biegeradius ab!
(siehe ZNr.: DA01-01)

Stk	Benennung	Teil	Norm Nr. Zeichnungs Nr.	Werkstoff	Rohmasse od. Modell Nr.	Bemerkung
2	Blech	3	-	Al	40x5x3	-
2	Blech	2	-	Al	57x7x3	-
1	Blech	1	-	Al	1332x463x3	-

	Tag	Name		Gewicht [kg]	Format	
Gez.	15.06.09	Brandl D.	TU-GRAZ	18	A3	2D Versuchsaufbau
Gepr.						
Norm gepr.						
Masstab 1:4	Blech-zuschnitte					Brandl Daniel Mat.Nr.:0130379
Freimass-toleranz mittel						Z.Nr.: DA01-02

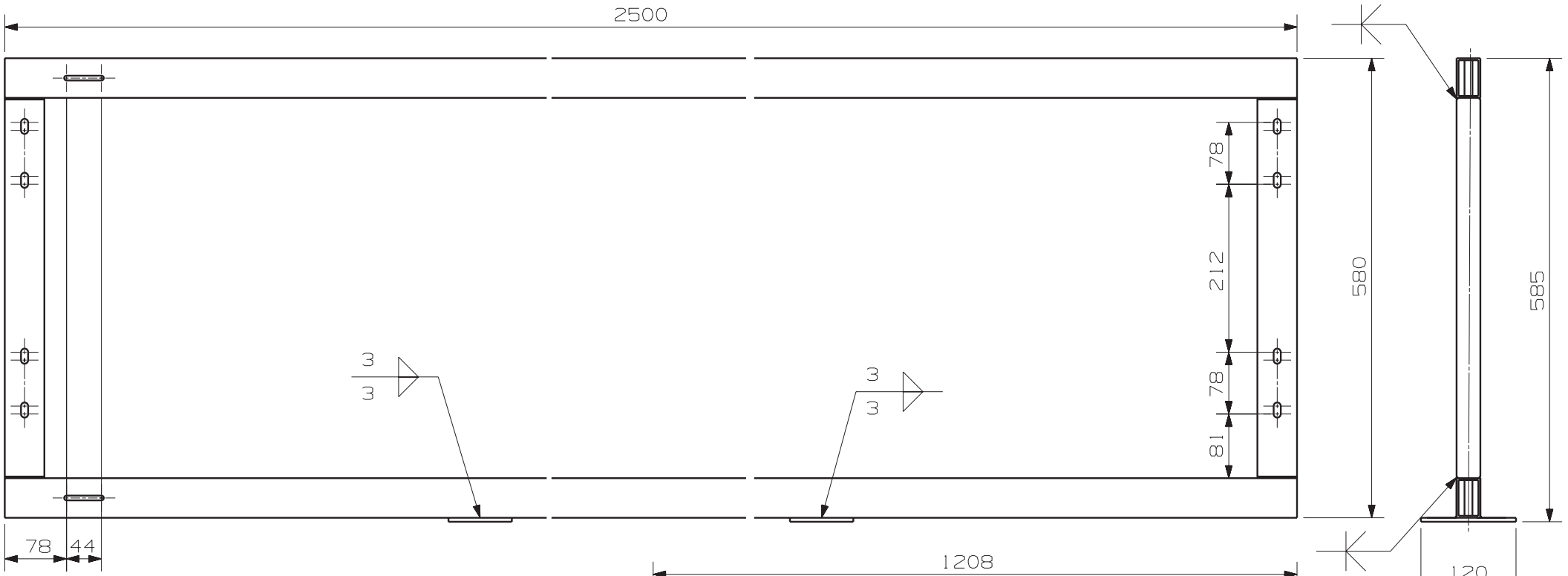

SCHNITT H-H
Masstab 1:2

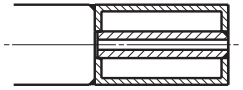

Teil 4
Masstab 1:2

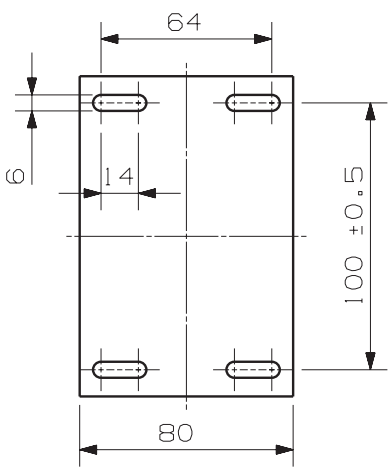

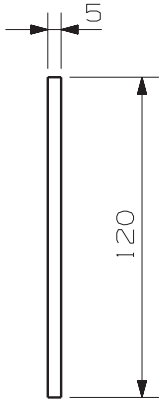

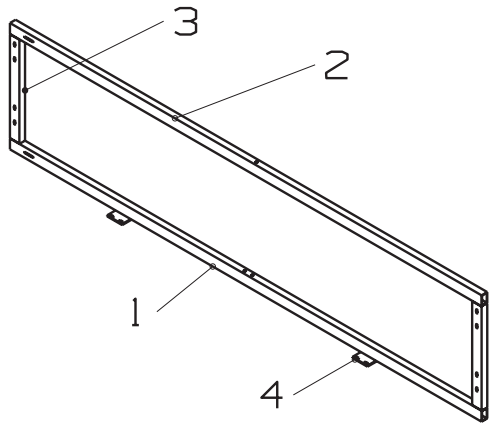

Stk	Benennung	Teil	Norm Nr. Zeichnungs Nr.	Werkstoff	Rohmasse od. Modell Nr.	Bemerkung
2	Blech	4	-	-	120x80x5	-
2	Vierkant Formrohr	3	DA02-03	-	-	-
1	Vierkant Formrohr	2	DA02-02	-	-	-
1	Vierkant Formrohr	1	DA02-01	-	-	-

	Tag	Name		Gewicht [kg]	Format	
Gez.	15.06.09	Brandl D.	TU-GRAZ	18	A3	2D Versuchsaufbau
Gepr.						
Norm gepr.						
Masstab 1:5			Rahmen komplett			Brandl Daniel Mat.Nr.:0130379
Freimass-toleranz mittel						Z.Nr.: DA02

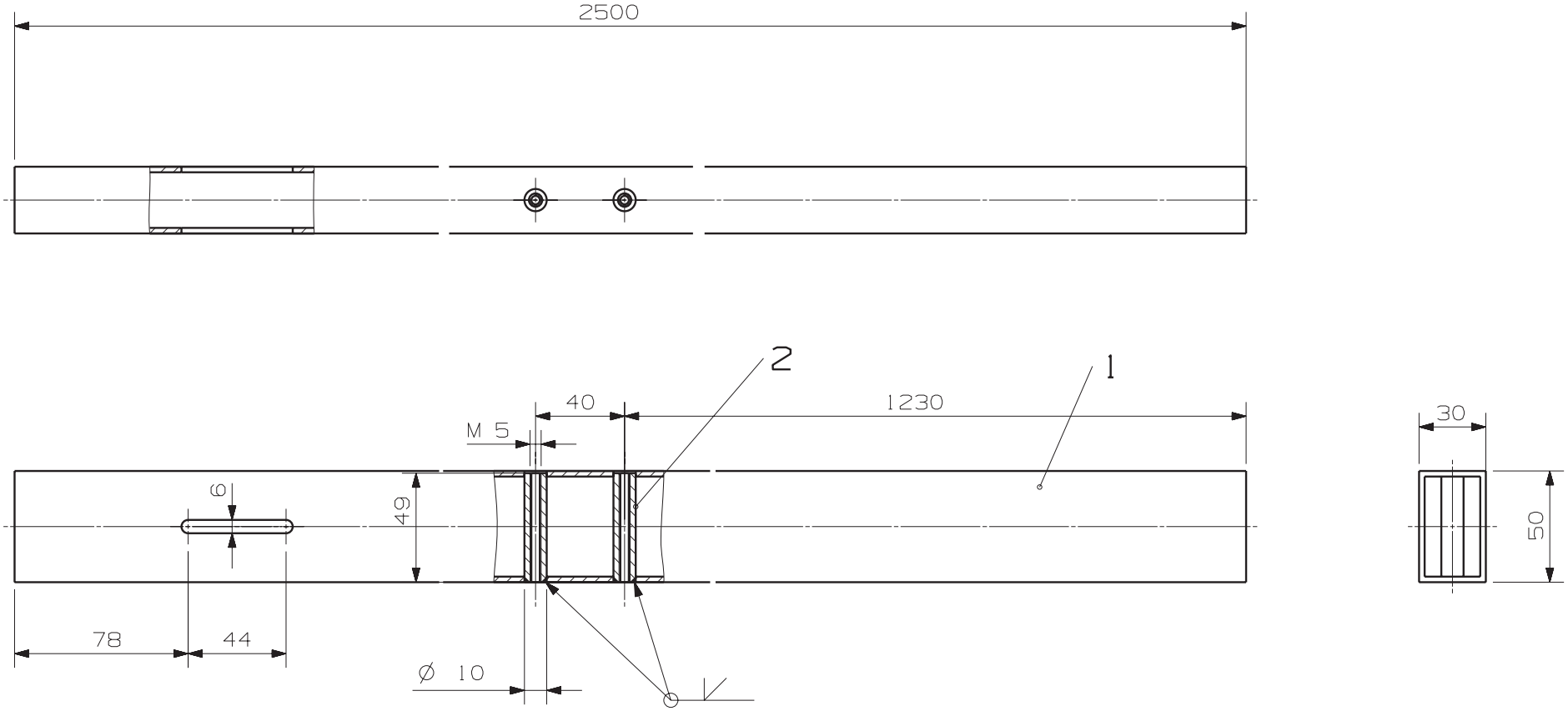

Stk	Benennung	Teil	Norm Nr. Zeichnungs Nr.	Werkstoff	Rohmasse od. Modell Nr.	Bemerkung
2	Rund	2	-	-	Ø 10x49	-
1	Vierkant Formrohr	1	-	-	2600x50x30	-

	Tag	Name		Gewicht [kg]	Format	
Gez.	15.06.09	Brandl D.	TU-GRAZ	12	A3	2D Versuchsaufbau
Gepr.						
Norm gepr.						

Masstab		
1:2	Formrohr01	Brandl Daniel Mat.Nr.:0130379
Freimass-toleranz: mittel		Z.Nr.: DA02-01

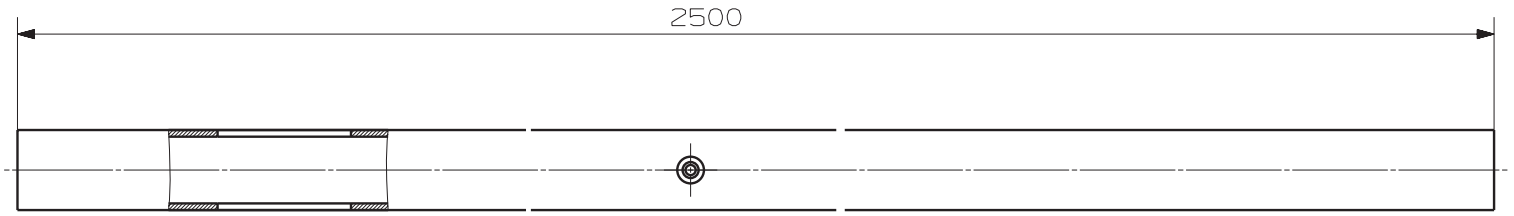

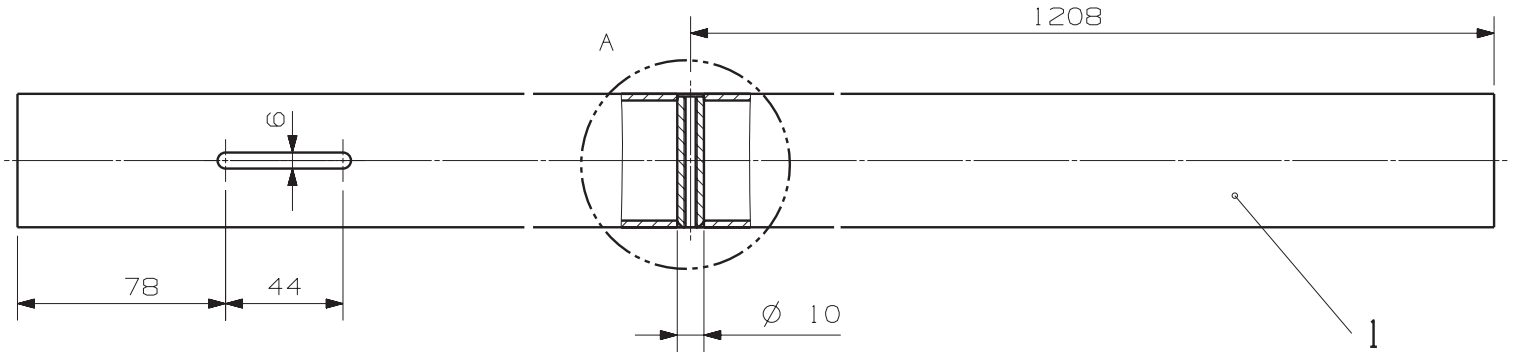

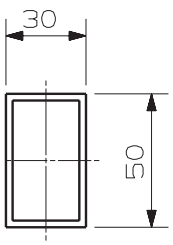

DETAIL A
Masstab 1:1

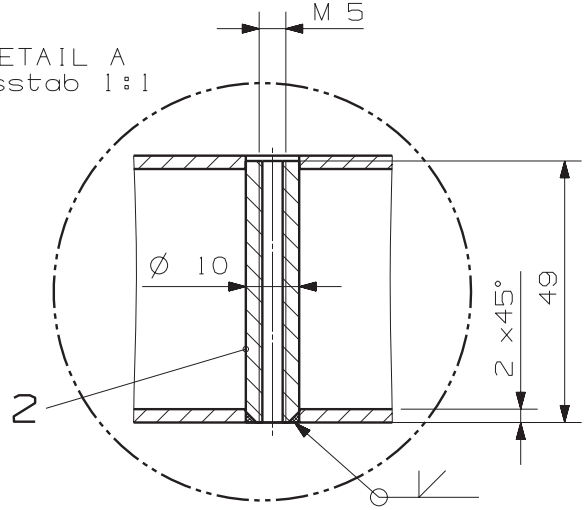

1	Rund	2	-	-	Ø 10x50	-
1	Vierkant Formrohr	1	-	-	2600x50x30	-
Stk	Benennung	Teil	Norm Nr. Zeichnungs Nr.	Werkstoff	Rohmasse od. Modell Nr.	Bemerkung

	Tag	Name		Gewicht [kg]	Format	
Gez.	15.06.09	Brandl D.	TU-GRAZ	12	A3	2D Versuchsaufbau
Gepr.						
Norm gepr.						

Masstab 1:2	Formrohr02	Brandl Daniel Mat.Nr.:0130379
Freimass-toleranz mittel		Z.Nr.: DA02-02

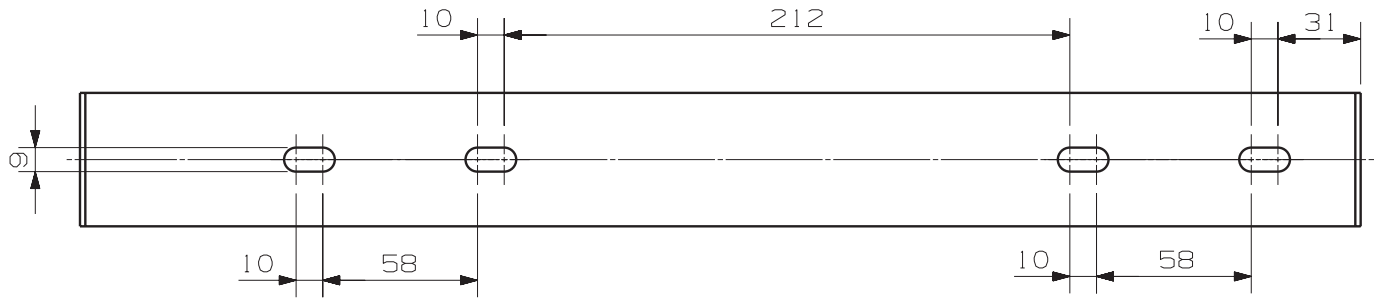

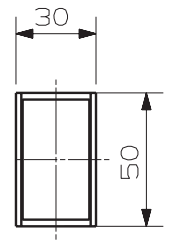

1	Vierkant Formrohr	1	-	-	500x50x30	-
Stk	Benennung	Teil	Norm Nr. Zeichnungs Nr.	Werkstoff	Rohmasse od. Modell Nr.	Bemerkung

	Tag	Name		Gewicht [kg]	Format	
Gez.	15.06.09	Brandl D.	TU-GRAZ	2,3	A3	2D Versuchsaufbau
Gepr.						
Norm gepr.						

Masstab 1:2	Formrohr03	Brandl Daniel Mat.Nr.:0130379
Freimass-toleranz mittel		Z.Nr.: DA02-03

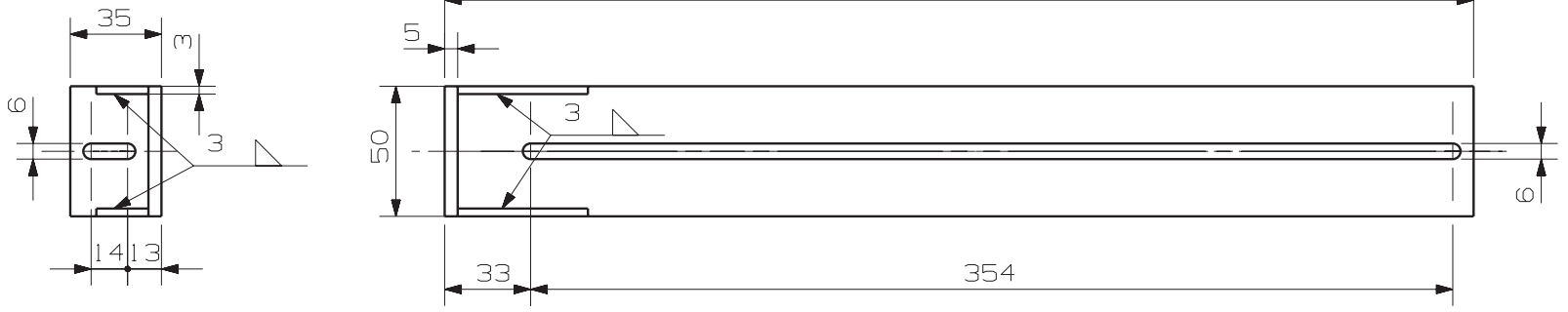

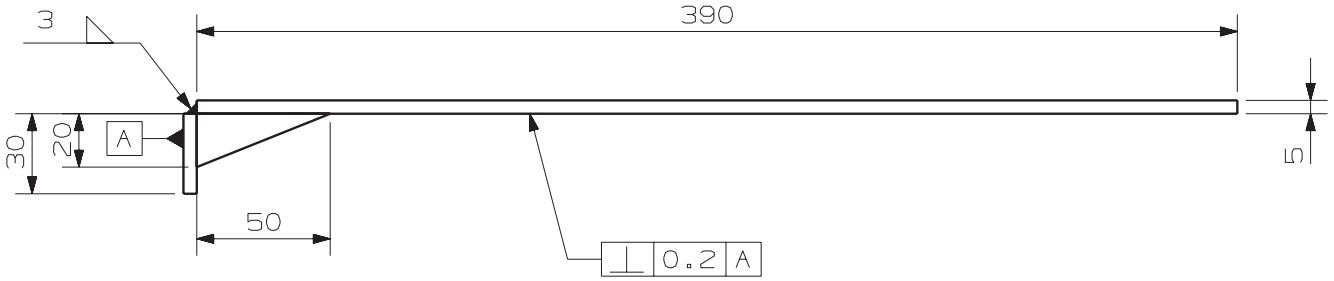

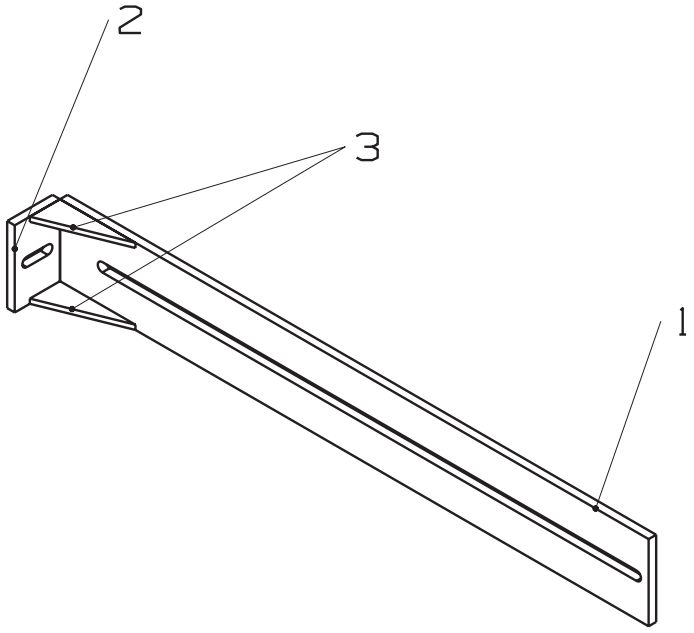

Stk	Benennung	Teil	Norm Nr. Zeichnungs Nr.	Werkstoff	Rohmasse od. Modell Nr.	Bemerkung
2	Blech	3	-	-	50x20x3	-
1	Blech	2	-	-	50x30x5	-
1	Blech	1	-	-	390x50x5	-

	Tag	Name		Gewicht [kg]	Format	
Gez.	22.06.09	Brandl D.	TU-GRAZ	0,77	A3	2D Versuchsaufbau
Gepr.						
Norm gepr.						

Masstab		
1:2	Halterung	Brandl Daniel Mat.Nr.:0130379
Freimass-toleranz: mittel		Z.Nr.: DA03

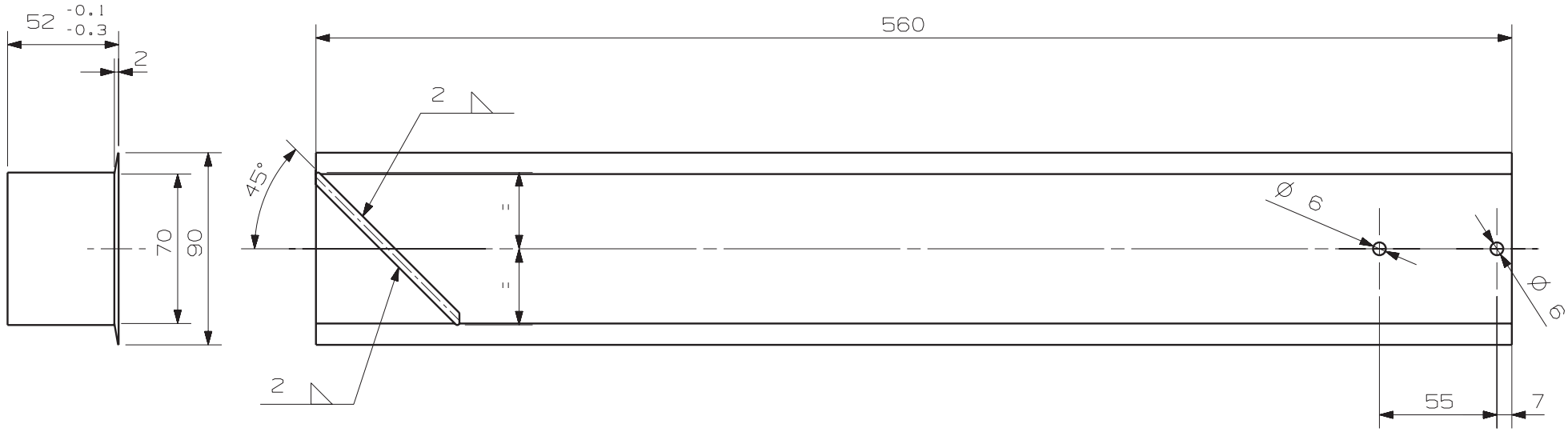

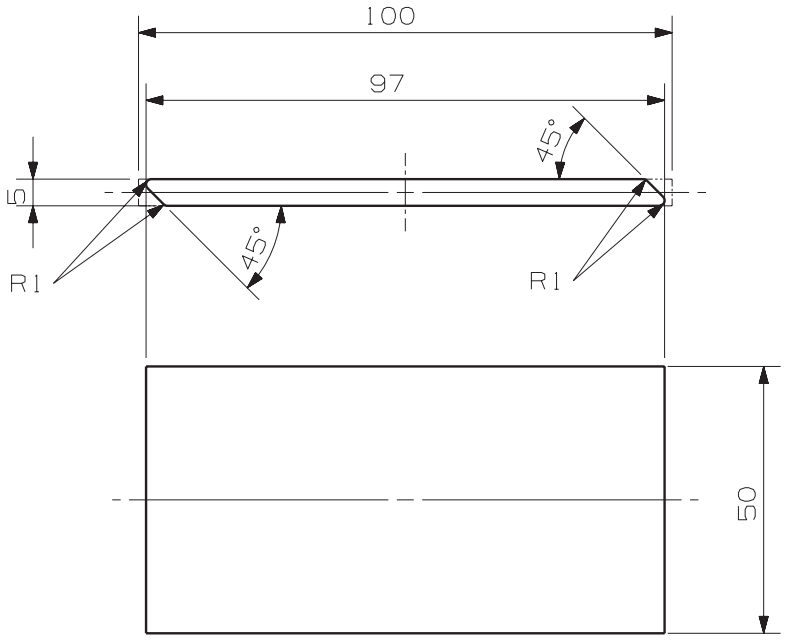

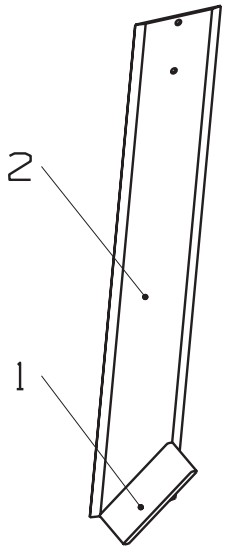

-Schweissnaehte versetzt schweissen

1	Blech	2	-	-	100x50x5	-
1	Blech	1	-	-	550x100x2	-
Stk	Benennung	Teil	Norm Nr. Zeichnungs Nr.	Werkstoff	Rohmasse od. Modell Nr.	Bemerkung

	Tag	Name		Gewicht [kg]	Format	
Gez.	16.06.09	Brandl D.	TU-GRAZ	18	A3	2D Versuchsaufbau
Gepr.						
Norm gepr.						

Masstab 1:2	Ruehrerblatt	Brandl Daniel Mat.Nr.:0130379
Freimass-toleranz mittel		Z.Nr.: DA04_45°

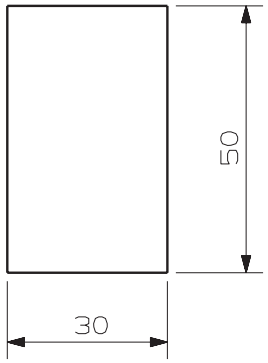

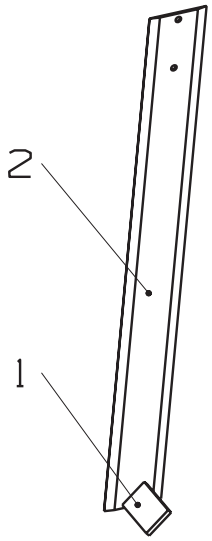

-Schweissnaehte versetzt schweissen

1	Blech	2	-	-	50x30x5	-
1	Blech	1	-	-	550x100x2	-
Stk	Benennung	Teil	Norm Nr. Zeichnungs Nr.	Werkstoff	Rohmasse od. Modell Nr.	Bemerkung

	Tag	Name		Gewicht [kg]	Format	
Gez.	16.06.09	Brandl D.	TU-GRAZ	18	A3	2D-Experimental Device
Gepr.						
Norm gepr.						
Masstab 1:2	Ruehrerblatt					Brandl Daniel Mat.Nr.:0130379
Freimass-toleranz mittel						Z.Nr.: DA04S_45°

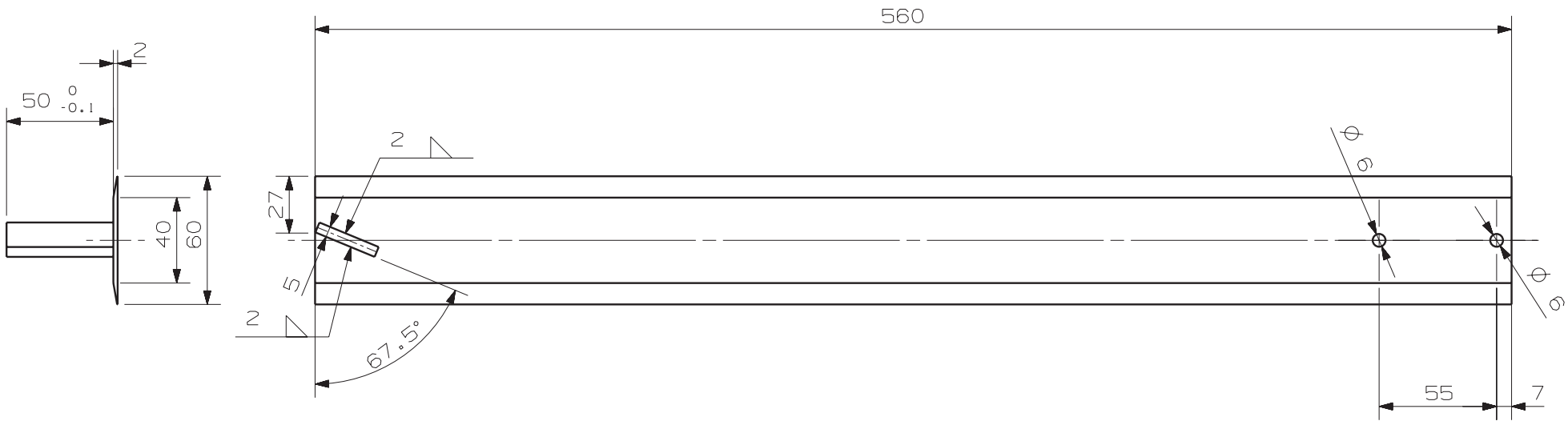

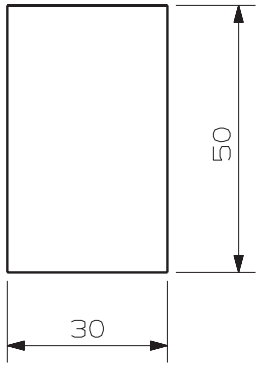

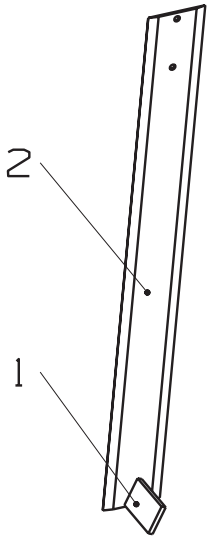

-Schweissnaehte versetzt schweissen

1	Blech	2	-	-	50x30x5	-
1	Blech	1	-	-	550x100x2	-
Stk	Benennung	Teil	Norm Nr. Zeicnungs Nr.	Werkstoff	Rohmassse od. Modell Nr.	Bemerkung

	Tag	Name		Gewicht [kg]	Format	
Gez.	16.06.09	Brandl D.	TU-GRAZ	18	A3	2D-Experimental Device
Gepr.						
Norm gepr.						

Masstab 1:2	Ruehrerblatt	Brandl Daniel Mat.Nr.:0130379
Freimass-toleranz mittel		Z.Nr.: DA04_67.5°

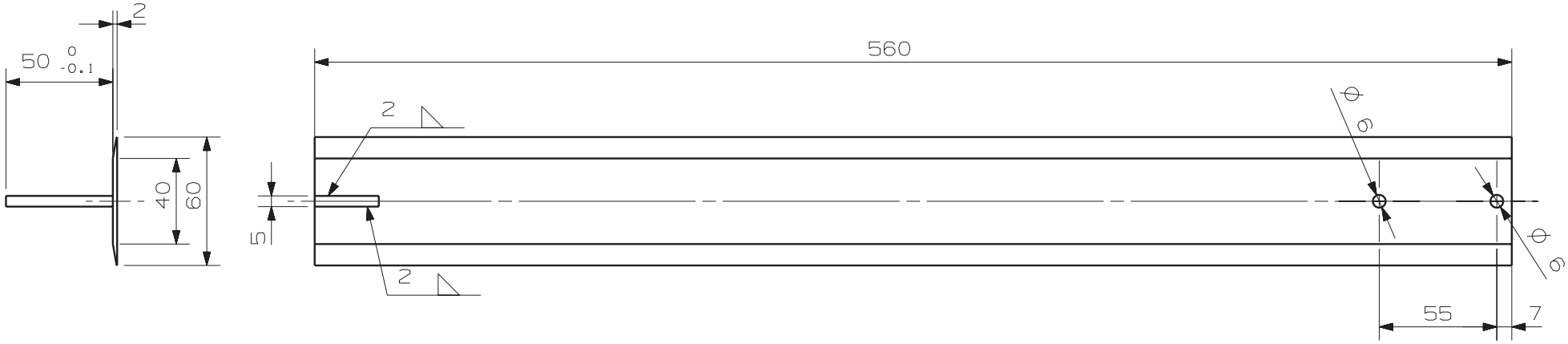

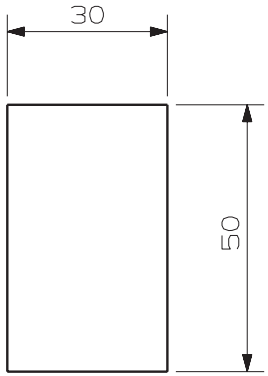

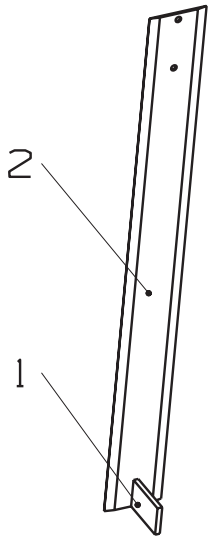

-Schweissnaehte versetzt schweissen

1	Blech	2	-	-	50x30x5	-
1	Blech	1	-	-	550x100x2	-
Stk	Benennung	Teil	Norm Nr. Zeichnungs Nr.	Werkstoff	Rohmasse od. Modell Nr.	Bemerkung

	Tag	Name		Gewicht [kg]	Format	
Gez.	16.06.09	Brandl D.	TU-GRAZ	18	A3	2D-Experimental Device
Gepr.						
Norm gepr.						

Masstab 1:2	Ruehrerblatt	Brandl Daniel Mat.Nr.:0130379
Freimass-toleranz mittel		Z.Nr.: DA04S_90°

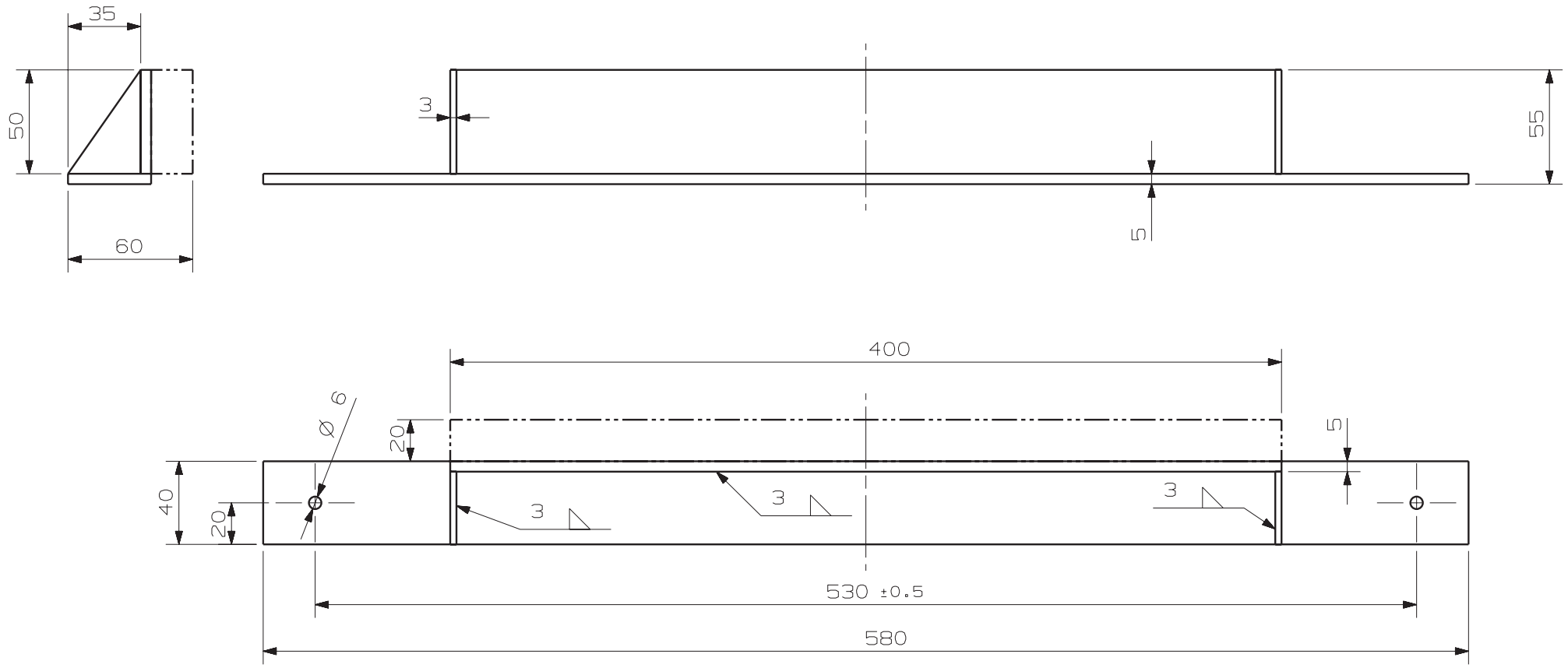

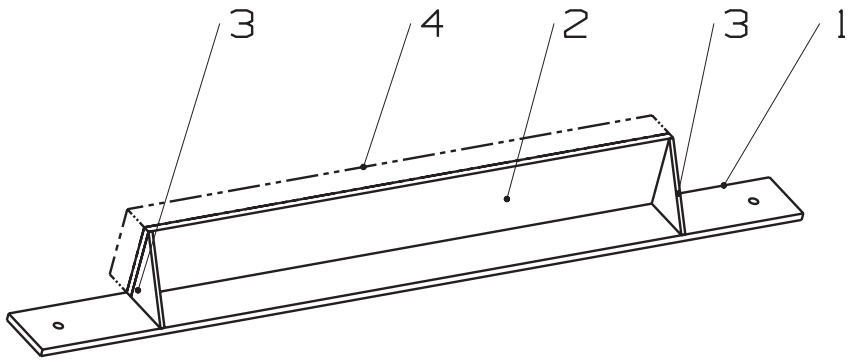

1	Schaumstoff	4	-	-	400x50x20	-
2	Blech	3	-	-	50x35x3	-
1	Blech	2	-	-	400x50x5	-
1	Blech	1	-	-	550x40x5	-
Stk	Benennung	Teil	Norm Nr. Zeichnungs Nr.	Werkstoff	Rohmasse od. Modell Nr.	Bemerkung

	Tag	Name		Gewicht [kg]	Format	
Gez.	22.06.09	Brandl D.	TU-GRAZ	1,7	A3	2D Versuchsaufbau
Gepr.						
Norm gepr.						

Masstab 1:2	Stopper	Brandl Daniel Mat.Nr.:0130379
Freimass-toleranz mittel		Z.Nr.: DA05

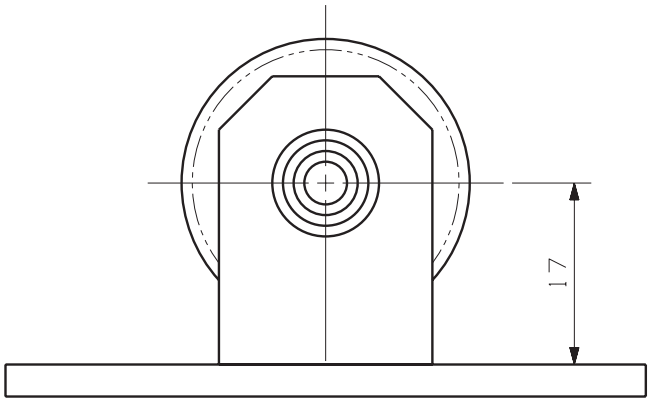

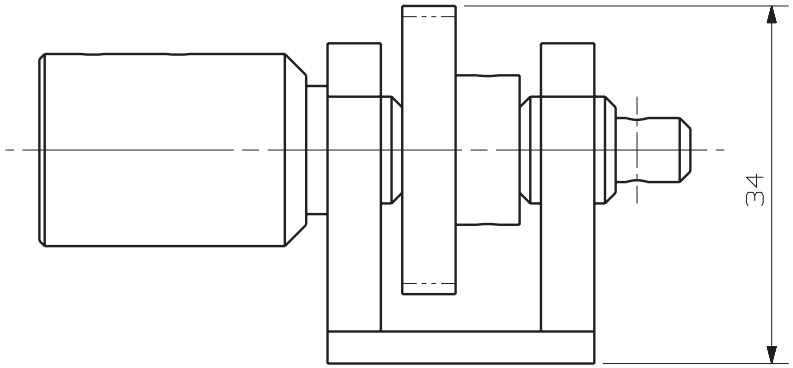

Teil 5
Masstab 2:1

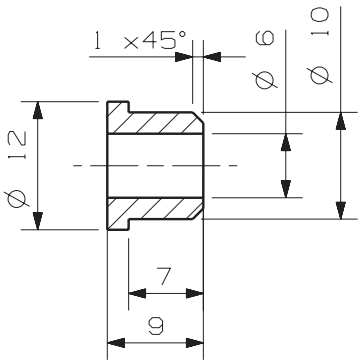

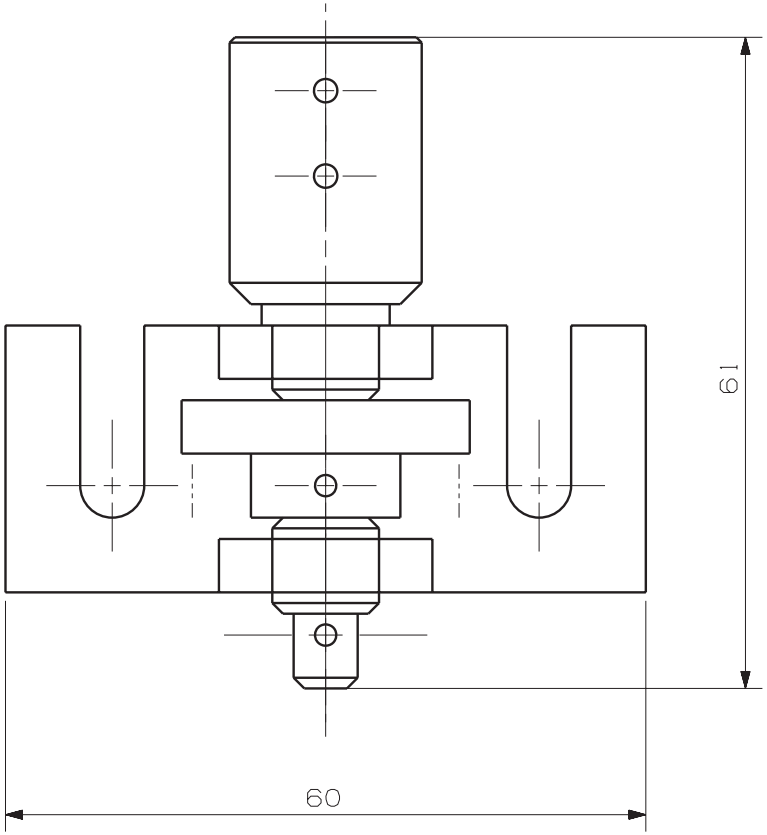

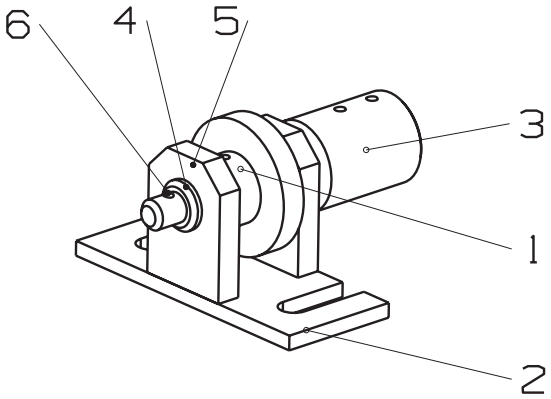

Teil 4
Masstab 2:1

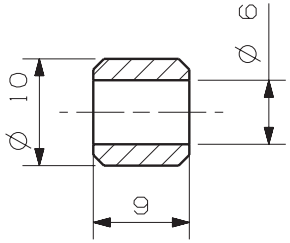

Stk	Benennung	Teil	Norm Nr. Zeichnungs Nr.	Werkstoff	Rohmasse od. Modell Nr.	Bemerkung
1	Splint Ø1,6	5	DIN 94	St	Ø1,6x12	-
1	Gleitlager	5	-	PET	Ø10x9	-
1	Gleitlager	4	-	PET	Ø12x9	-
1	Kuppplung	3	DA06-02	-	100x80x5	-
1	Halterung	2	DA06-01	-	100x80x5	-
1	Zahnrad	1	M1-25Z	St	Ø27x11	-

	Tag	Name		Gewicht [kg]	Format	
Gez.	15.06.09	Brandl D.	TU-GRAZ	-	A3	2D Versuchsaufbau
Gepr.						
Norm gepr.						

Masstab		
1:1	Ritzelhalterung komplett	Brandl Daniel Mat.Nr.:0130379
Freimass-toleranz: mittel		Z.Nr.: DA06

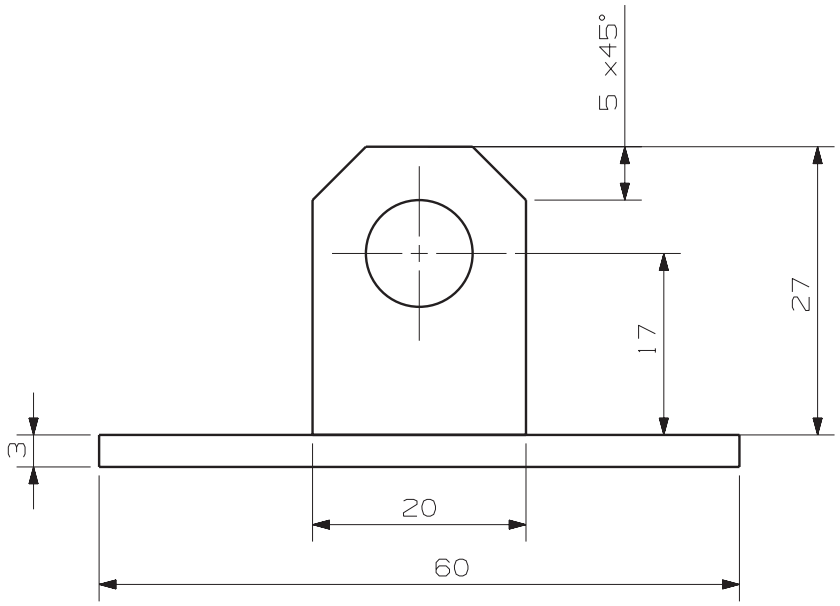

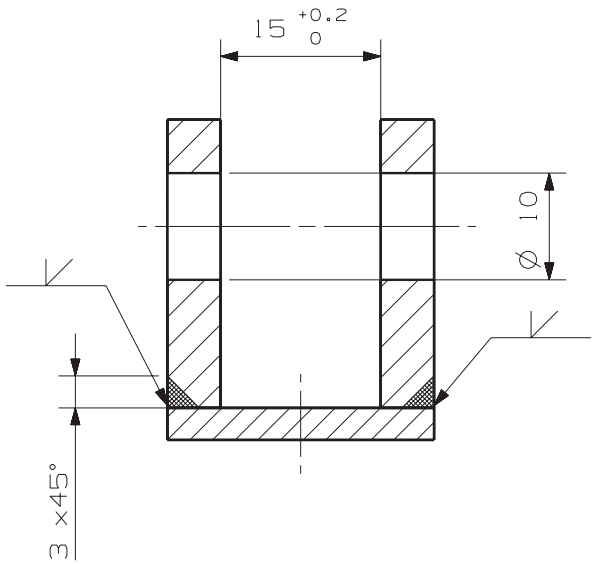

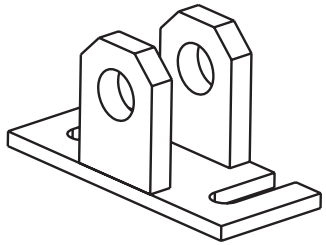

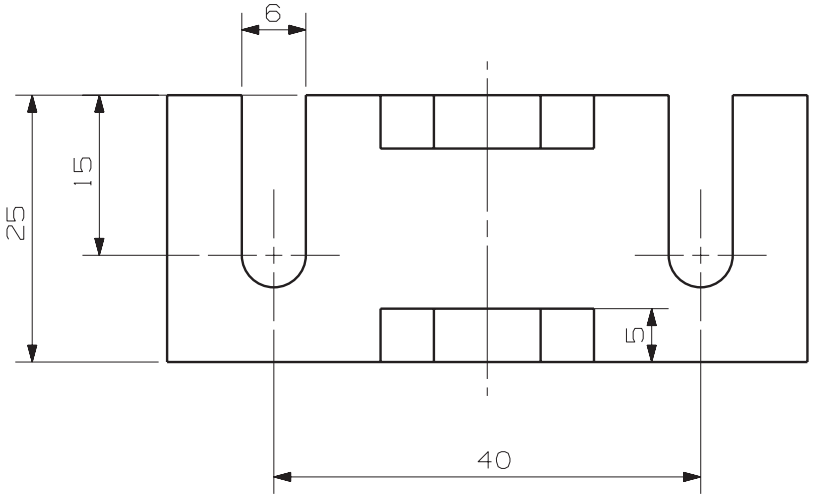

2	Blech	2	-	-	27x20x5	-
1	Blech	1	-	-	60x25x3	-
Stk	Benennung	Teil	Norm Nr. Zeichnungs Nr.	Werkstoff	Rohmasse od. Modell Nr.	Bemerkung

	Tag	Name		Gewicht [kg]	Format	
Gez.	15.06.09	Brandl D.	TU-GRAZ	0,07	A3	2D Versuchsaufbau
Gepr.						
Norm gepr.						

Masstab 1:1	Halterung	Brandl Daniel Mat.Nr.:0130379
Freimass-toleranz mittel		Z.Nr.: DA06-01

SCHNITT B-B

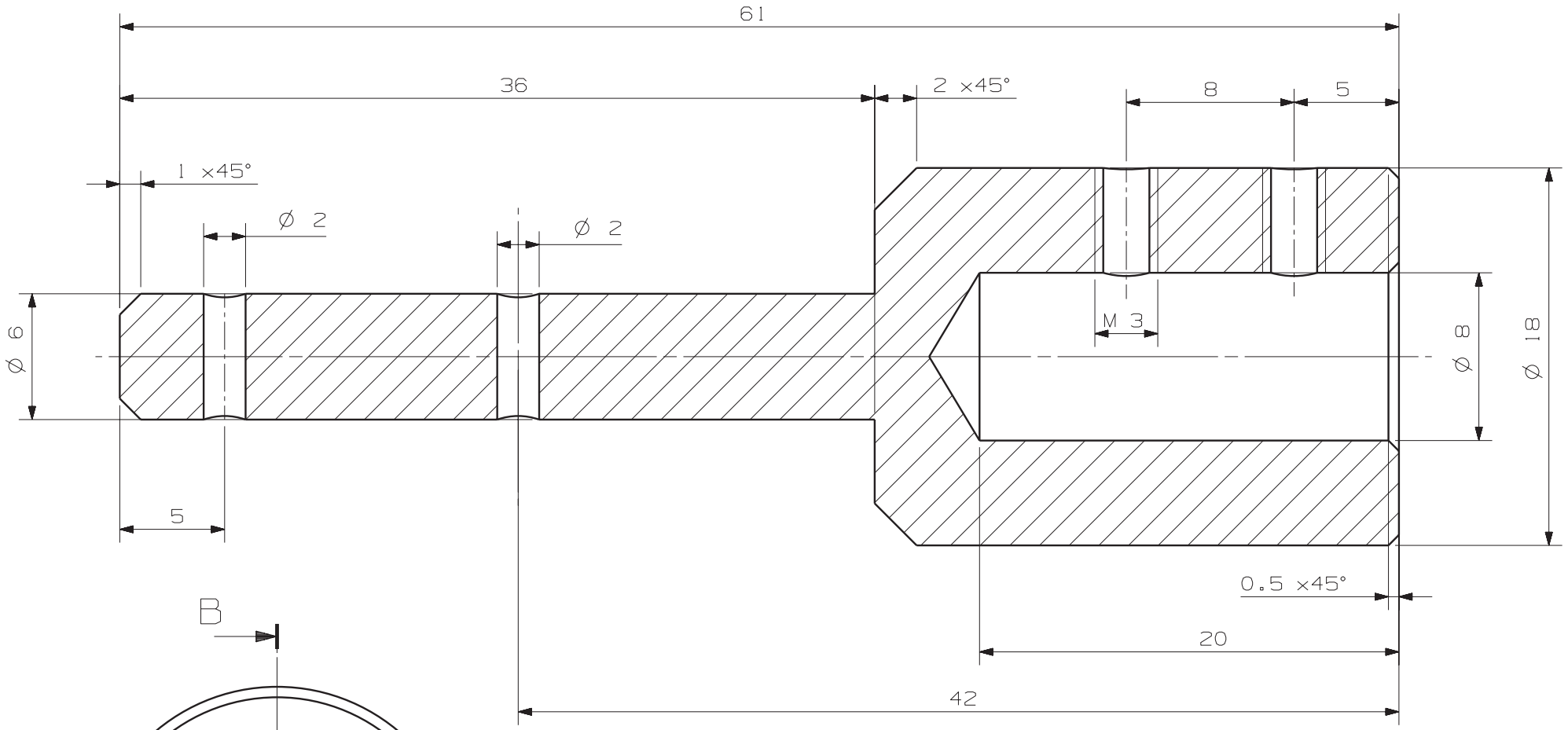

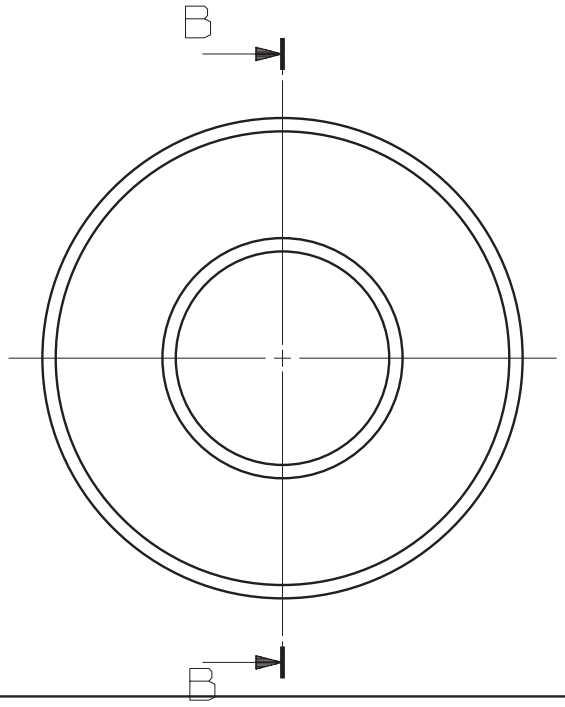

1	Rund		1	-	-	Ø 20×65	-
Stk	Benennung		Teil	Norm Nr. Zeichnungs Nr.	Werkstoff	Rohmasse od. Modell Nr.	Bemerkung

	Tag	Name		Gewicht [kg]	Format	
Gez.	15.06.09	Brandl D.	TU-GRAZ	0,03	A3	2D Versuchsaufbau
Gepr.						
Norm gepr.						

Masstab 1:1	Kupplung	Brandl Daniel Mat.Nr.:0130379
Freimass-toleranz mittel		Z.Nr.: DA06-02

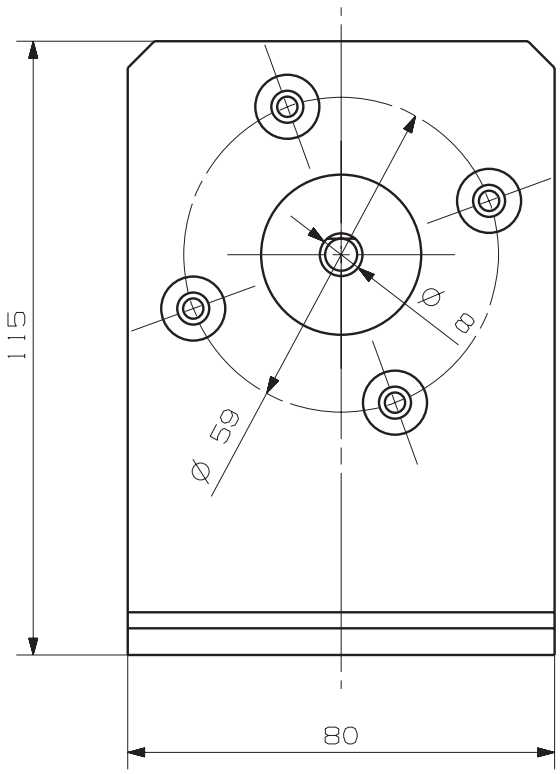

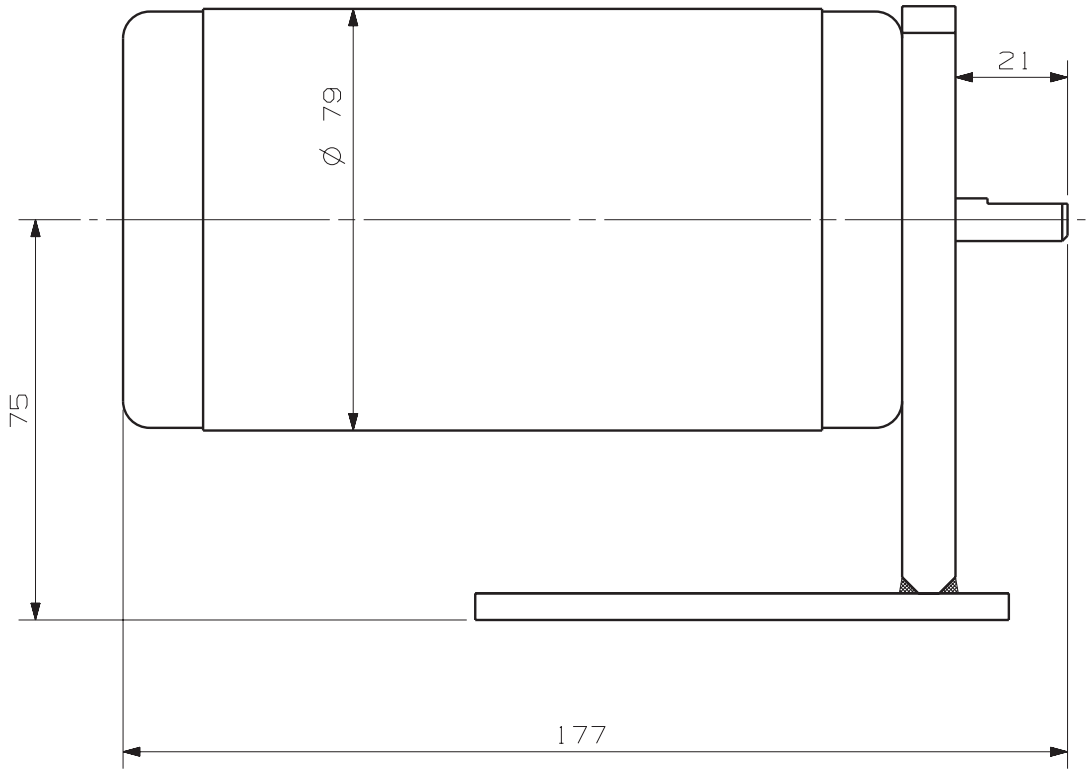

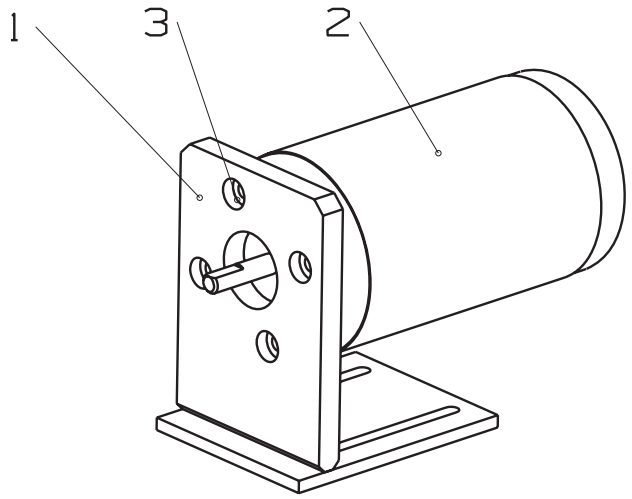

Stk	Benennung	Teil	Norm Nr. Zeichnungs Nr.	Werkstoff	Rohmasse od. Modell Nr.	Bemerkung
4	Innensechskantschraube M5	3	DIN 912	8.8	M5x40	-
1	Gleichstrommotor	2	129.4111.30	-	Ø 79x177	-
1	Wellenflansch	1	DA07-01	-	-	-

	Tag	Name		Gewicht [kg]	Format	
Gez.	15.06.09	Brandl D.	TU-GRAZ	-	A3	2D Versuchsaufbau
Gepr.						
Norm gepr.						

Masstab 1:1	Motor mit Flansch	Brandl Daniel Mat.Nr.:0130379
Freimass-toleranz mittel		Z.Nr.: DA07

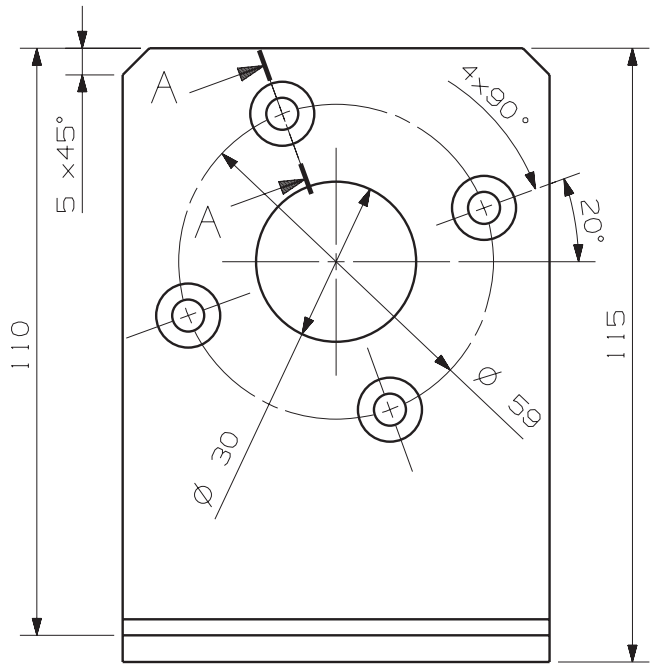

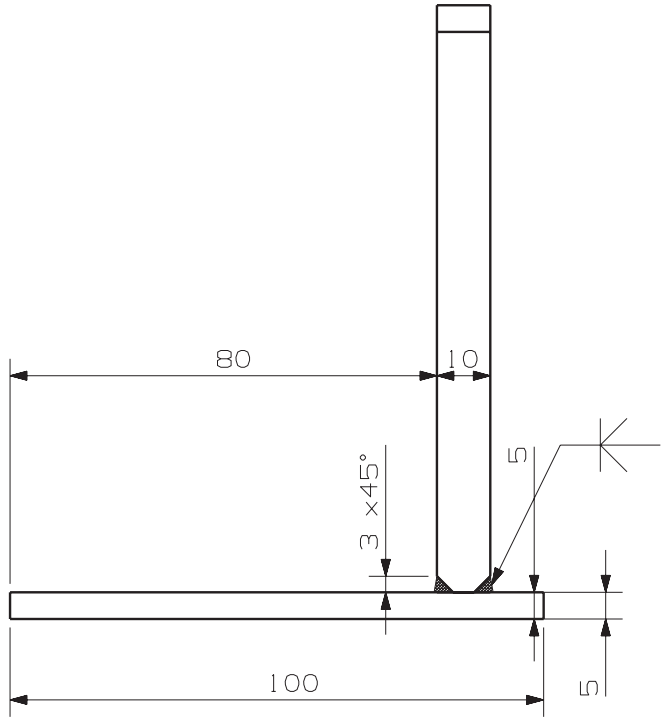

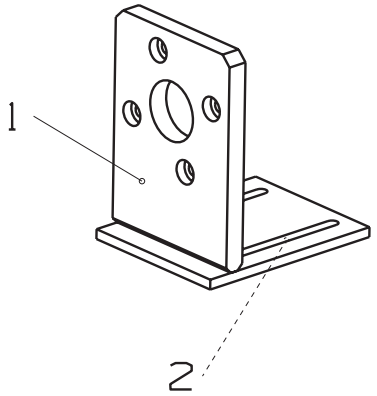

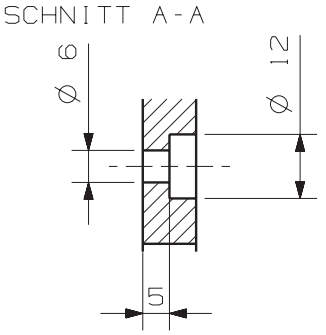

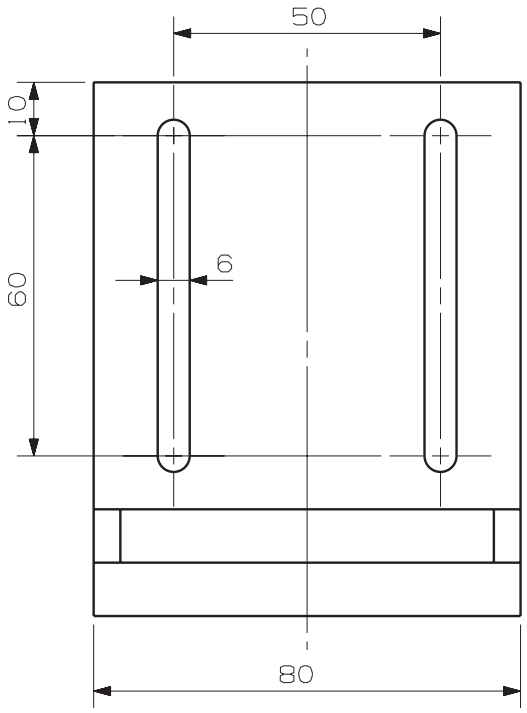

1	Blech	2	-	-	100x80x5	-
1	Blech	1	-	-	110x80x10	-
Stk	Benennung	Teil	Norm Nr. Zeichnungs Nr.	Werkstoff	Rohmasse od. Modell Nr.	Bemerkung

	Tag	Name		Gewicht [kg]	Format	
Gez.	15.06.09	Brandl D.	TU-GRAZ	0,9	A3	2D Versuchsaufbau
Gepr.						
Norm gepr.						

Masstab 1:1	Motorflansch	Brandl Daniel Mat.Nr.:0130379
Freimass-toleranz mittel		Z.Nr.: DA07-01

SCHNITT G-G

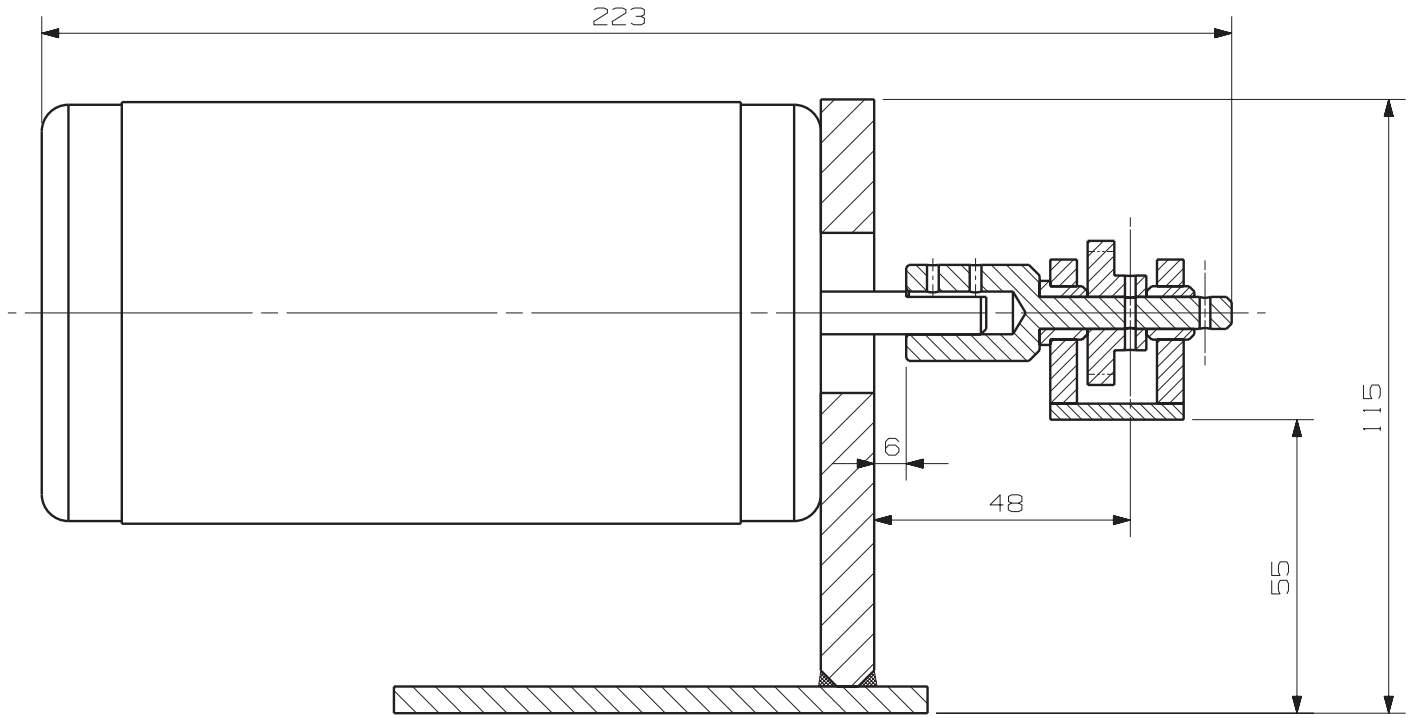

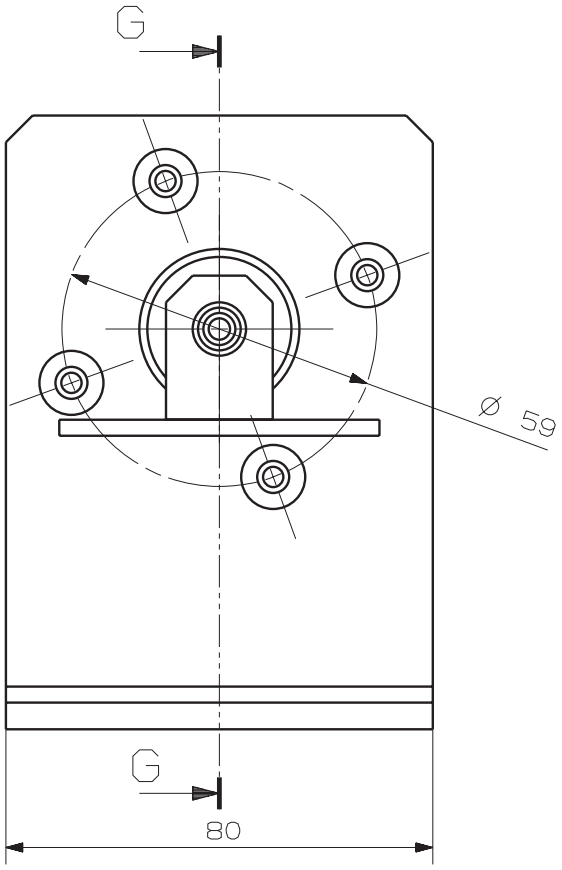

1	Ritzelhalterung komplett	2	DA06	-	-	-
1	Motor mit Wellenflansch	1	DA07	-	-	-
Stk	Benennung	Teil	Norm Nr. Zeichnungs Nr.	Werkstoff	Rohmasse od. Modell Nr.	Bemerkung

	Tag	Name		Gewicht [kg]	Format	
Gez.	15.06.09	Brandl D.	TU-GRAZ	-	A3	2D Versuchsaufbau
Gepr.						
Norm gepr.						

Masstab 1:1	Antrieb komplett	Brandl Daniel Mat.Nr.:0130379
Freimass-toleranz mittel		Z.Nr.: DA08

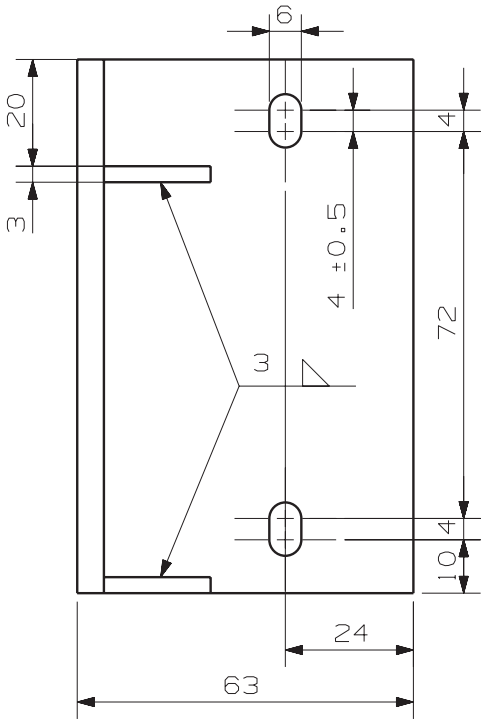

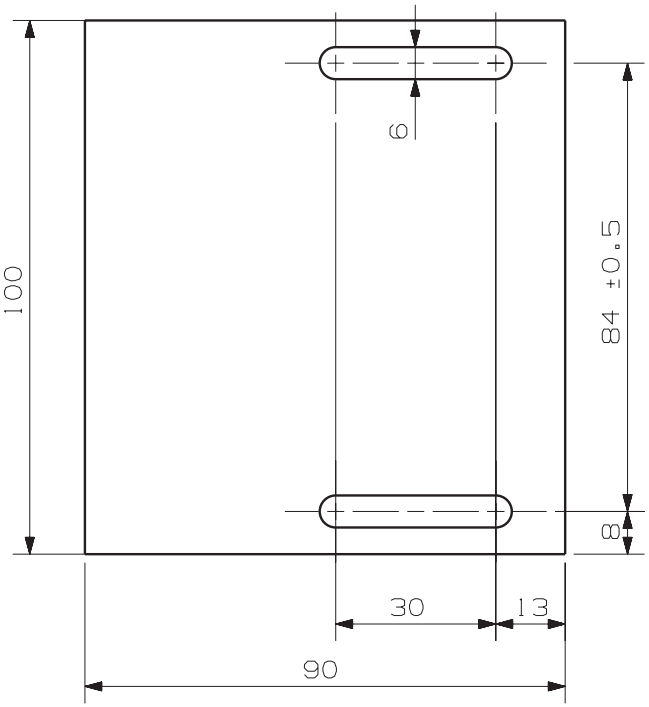

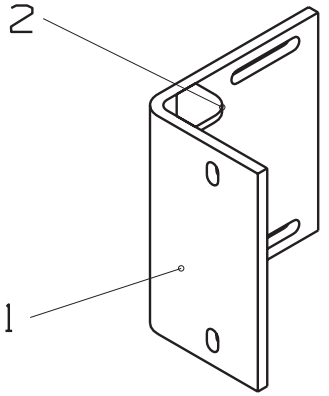

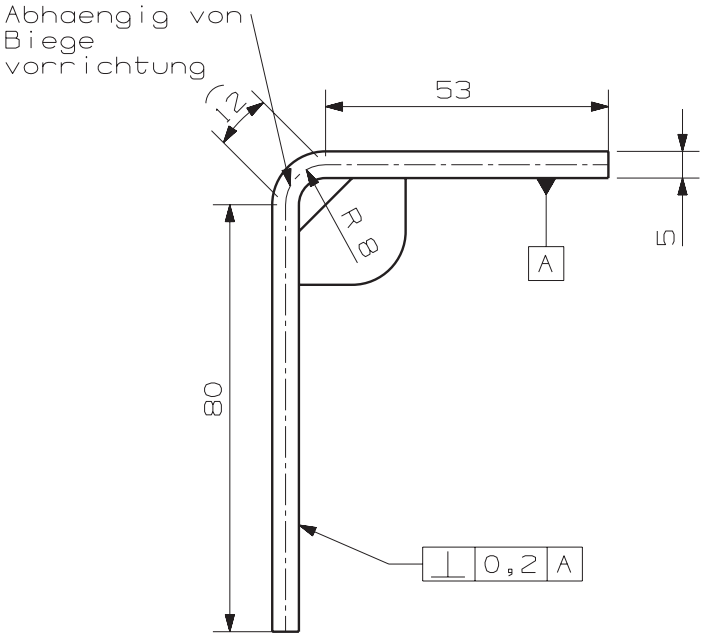

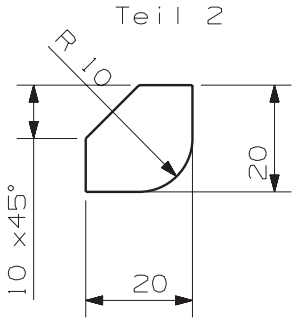

Laenge Teil 1 vor Biegen = 145 mm

6,4

2	Blech	2	-	-	20x20x3	-
1	Blech	1	-	-	130x100x5	-
Stk	Benennung	Teil	Norm Nr. Zeichnungs Nr.	Werkstoff	Rohmasse od. Modell Nr.	Bemerkung

	Tag	Name		Gewicht [kg]	Format	
Gez.	10.07.09	Brandl D.	TU-GRAZ	0,5	A3	2D Versuchsaufbau
Gepr.						
Norm gepr.						

Masstab 1:1	Lagerbefestigung	Brandl Daniel Mat.Nr.:0130379
Freimass-toleranz mittel		Z.Nr.: DA09

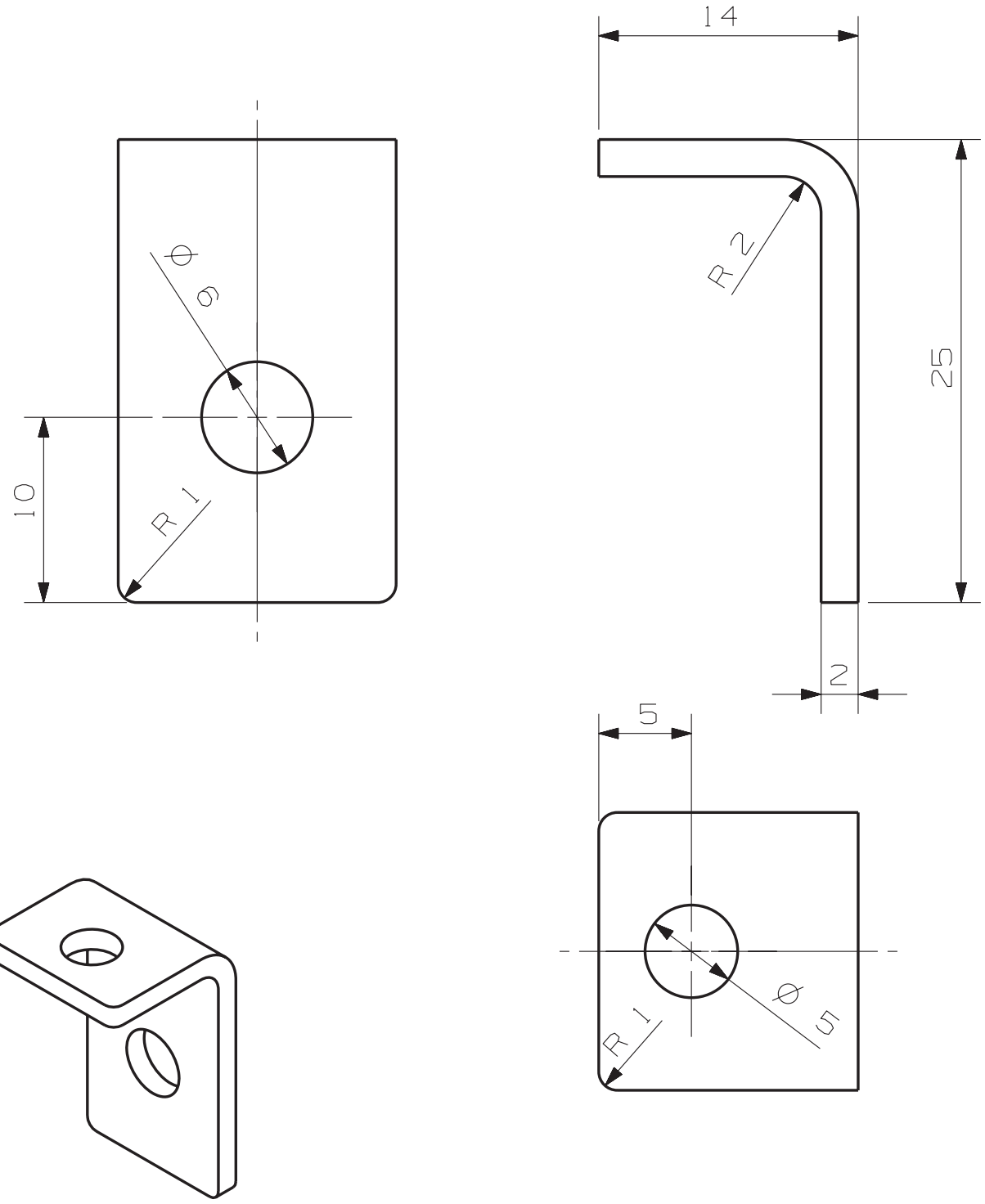

1	Blech	1	-	-	60x15x2	-
Stk	Benennung	Teil	Norm Nr. Zeichnungs Nr.	Werkstoff	Rohmasse od. Modell Nr.	Bemerkung

	Tag	Name		Gewicht [kg]	Format	
Gez.	10.07.08	Brandl D.	TU-GRAZ	-	A4	2D-Versuchsaufbau
Gepr.						
Norm gepr.						

Masstab 1:1	Befestigungsblech	Brandl Daniel Mat.Nr.:0130379
Freimass-toleranz mittel		Z.Nr.: DA27

9.3. Drawings for the 3D Experimental Setup

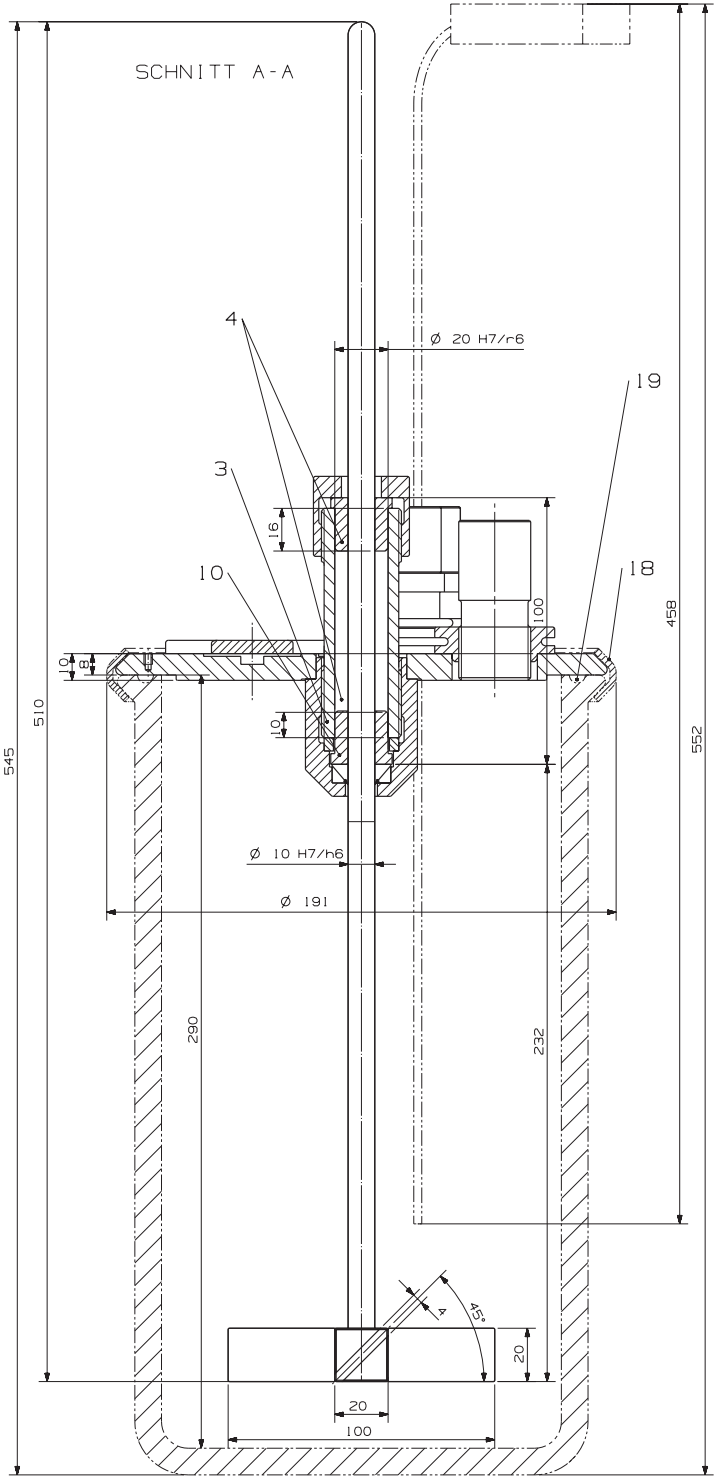

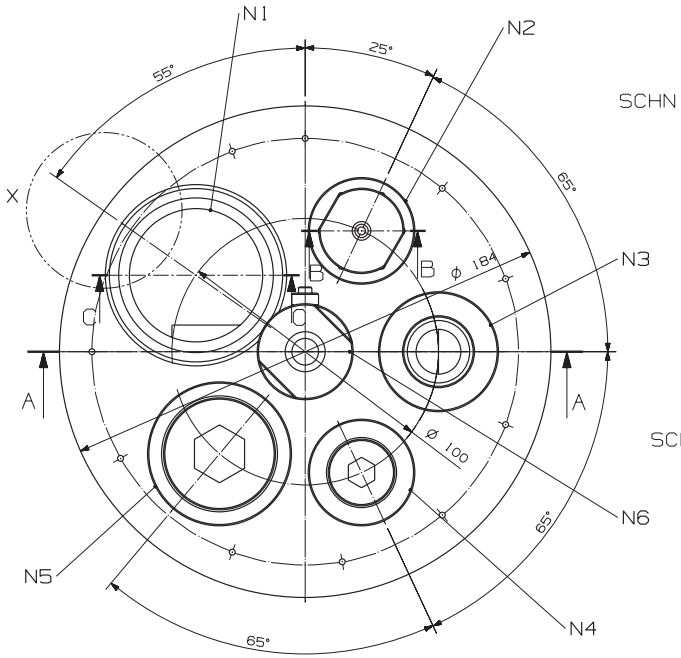

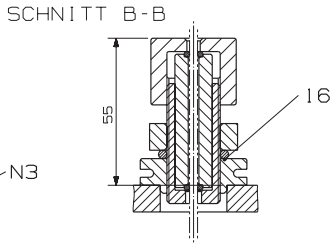

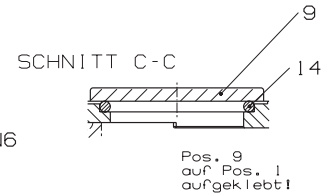

Pos. 9
auf Pos. 1
aufgeklebt!

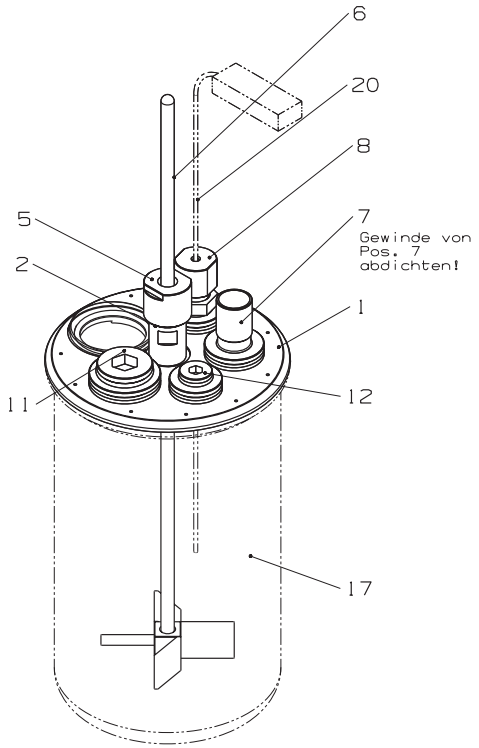

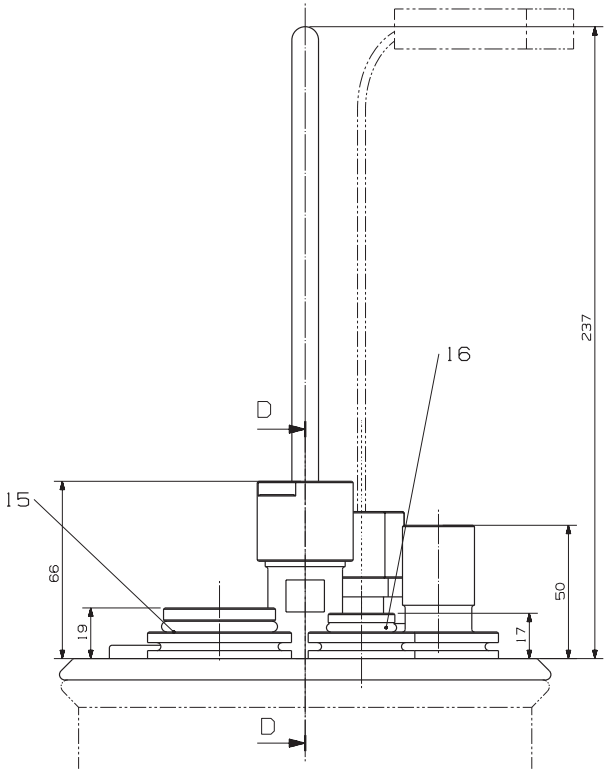

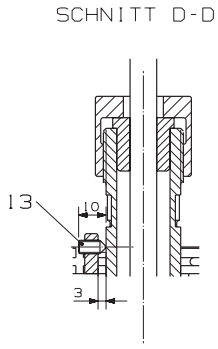

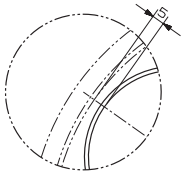

N6	Ruehrerlagerung		ø 42	-	-
N5	Einfuelloeffnung		ø 54	-	-
N4	Zusatzanschluss		ø 40	-	-
N3	Vakkumanschluss		ø 45	-	-
N2	Temperaturfuehler		ø 40	-	-
N1	Schauloch		ø 50	-	-
Stutzen Nr.	Bezeichnung		Groesse	Nenndruck	Norm

1	Temperaturfuehler	20	-	-	-	Bestand
1	Rundichtringe	19	-	-	-	Bestand
1	Verschlusskranz	18	-	-	-	Bestand
1	Glasbehaelter	17	-	-	-	Bestand
2	Runddichtring ø20	16	DIN 3770	NBR	ø20 x 3,15	-
1	Runddichtring ø35,5	15	DIN 3770	NBR	ø35,5 x 4	-
1	Rundichtring ø50	14	DIN 3770	NBR	ø50 x 4	-
1	Gewindstift M5	13	DIN 913	A2	M5 x 10	-
1	Verschlusschraube M20x1,5	12	DIN 908	A2	M20 x 18	-
1	Verschlusschraube M36x1,5	11	DIN 908	A2	M36 x 21	-
1	Wellendichtring ø10	10	DIN 3760	NB	ø22 x 6	Form A
1	Glasscheibe	9	TD15	-	-	-
1	Temperaturfuehler Anschluss	8	TD11	-	-	-
1	Vakkumanschluss	7	TD18	-	-	-
1	Ruehrer	6	TD10	-	-	-
1	Verschlusshuelse	5	TD19	-	-	-
2	Gleitlager	4	TD16	-	-	-
1	Zwischenring	3	TD20	-	-	-
1	Lagerhuelse	2	TD17	-	-	-
1	Dechel nachbearbeitet	1	TD02	-	-	-
Stk	Benennung	Teil	Norm Nr. Zeichnungs Nr.	Werkstoff	Rohmasse od. Modell Nr.	Bemerkung

	Tag	Name			
Ges.	10.07.08	Brandl D.	TU-GRAZ	Gewicht [kg] 3,5	Format A3	Trocknerdeckel
Gepr.						
Norm gepr.						
Massstab 1:1	Zusammenstellung Trocknerdeckel					Brandl Daniel Mat.Nr.:0130379
Freimass-toleranz mittel						Z.Nr.: TD01

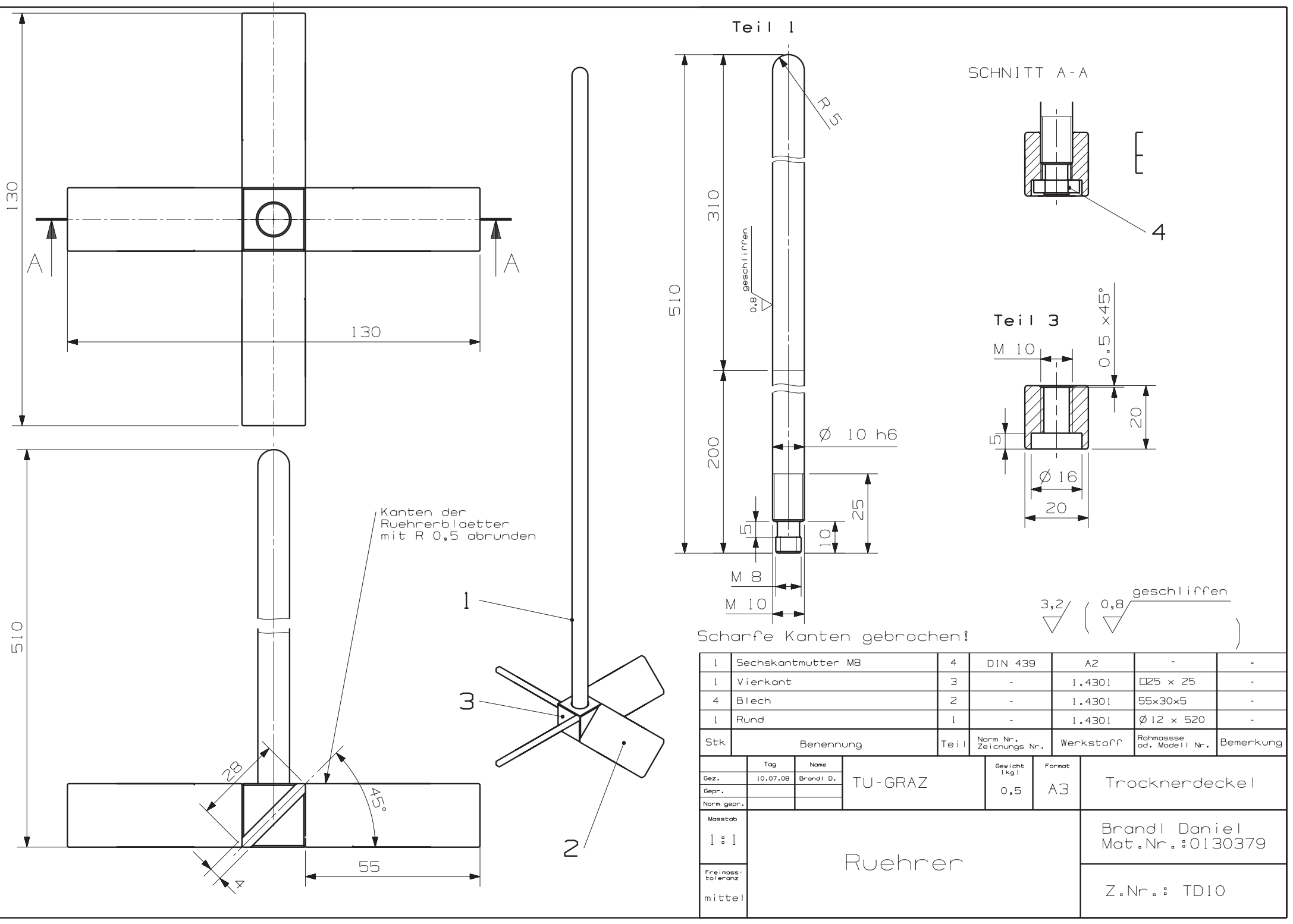

Stk	Benennung	Teil	Norm Nr. Zeichnungs Nr.	Werkstoff	Rohmasse od. Modell Nr.	Bemerkung
1	Sechskantmutter M8	4	DIN 439	A2	-	-
1	Vierkant	3	-	1.4301	□25 x 25	-
4	Blech	2	-	1.4301	55x30x5	-
1	Rund	1	-	1.4301	Ø12 x 520	-

	Tag	Name		Gewicht [kg]	Format	
Gez.	10.07.08	Brandl D.	TU-GRAZ	0,5	A3	Trocknerdeckel
Gepr.						
Norm gepr.						
Masstab 1:1			Ruehrer			Brandl Daniel Mat.Nr.:0130379
Freimass-toleranz mittel						Z.Nr.: TD10

9.4. PIV Camera Specifications

Minimized. For Maximum Effect.

M-SERIES

REDLAKE DIGITAL IMAGING SYSTEMS

M-Series

1.3 megapixels at 520 fps

Key features:

Compact and rugged solution for use in harsh environments

Direct streaming of 1.3 megapixel images at over 500 frames per second

Circular buffering with pre and post triggering for event capture

External triggering and synchronization

Fully integrated with MotionPro X imaging suite

The MotionScope M-series comprises two configurations of area scan cameras that are designed for use in industrial and research environments. The M-3 features a 1.3 megapixel sensor delivering over 500 fps via a standard Camera Link® interface, whereas the M-5 provides a very high resolution image with 4 million pixels and sustained rates over 150 fps. The camera electronics are packaged in a very compact and rugged housing capable of withstanding high g-forces and vibration.

Image capture to a computer system is done via a full camera link frame grabber. To ensure the best possible performance and ease of use, the M-series have been seamlessly integrated to operate with the MotionPro X software suite and the CORECO X64 Camera Link PCI-E board solution. The MotionPro X suite and SDK integrates the M-series in a single software platform with IDT X-series, and Redlake MotionXtra camera systems.

The camera benefits from such features such as pre and post triggering for event capture, circular buffering, external synchronization, and flexible choice of ROI. When very long record times are required this compact camera system is configured with a dedicated disk array system.

This flexible and compact camera system is well suited for a variety of vision inspection applications as well as for R&D laboratory usage.

**supported frame grabbers:*
Coreco
National Instruments
Epix

Technical Data

	M-3	M-5
Maximum fps @ Full Resolution	520 fps @ 1280 x 1024	170 fps @ 2352 x 1728
Array Size	1.3 megapixels	4 megapixels
Max fps @ Reduced Resolution	33,000 fps @ 1280 x 16	18,000 fps @ 2352 x 16
Sensitivity	3000 ASA Mono 1000 ASA Color	3000 ASA Mono 1000 ASA Color
Pixel Size	12x12 µm	7x7 µm
Color Mono	Available Available	Available Available
Memory Options	PC RAM 4 GB (Win 32) 16 GB (Win 64 Direct to Disk	PC RAM 4 GB (Win 32) 16 GB (Win 64)) Direct to Disk
Trigger	TTL & Switch	TTL & Switch
Sync (Input)	Phase-lock TTL	Phase-lock TTL
IRIG	N/A	N/A
GPS Time Code	N/A	N/A
Sync (Output)	Frame sync / Strobe	Frame sync / Strobe
HDMI	N/A	N/A
Comp Video	N/A	N/A
Camera Link	Full	Full
Ethernet	N/A	N/A
USB 2.0	N/A	N/A
Shock/Vibration rating	N/A	N/A
Battery Back-up	N/A	N/A
MotionPro X	Mac or Windows	Mac or Windows
Motion Central	N/A	N/A
Plug-ins/MotionPro X	LabVIEW or MatLab	LabVIEW or MatLab
File Formats - MotionPro X	TIF BMP AVI MRF MCF	TIF BMP AVI MRF MCF
File Formats - Motion Central	N/A	N/A
H x W x L	55x55x75 mm	55x55x75 mm
Weight	0.32 kg	0.32 kg

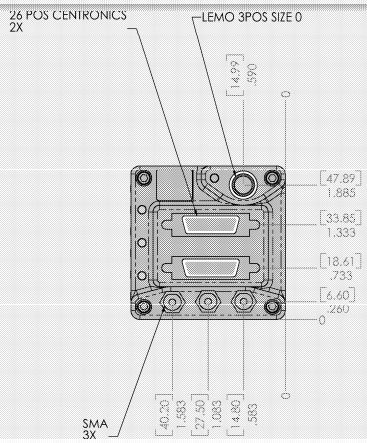

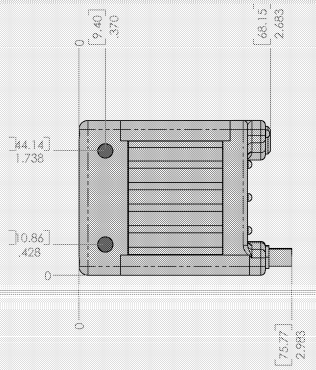

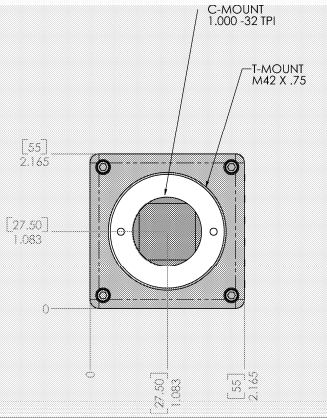

all dimensions shown in mm

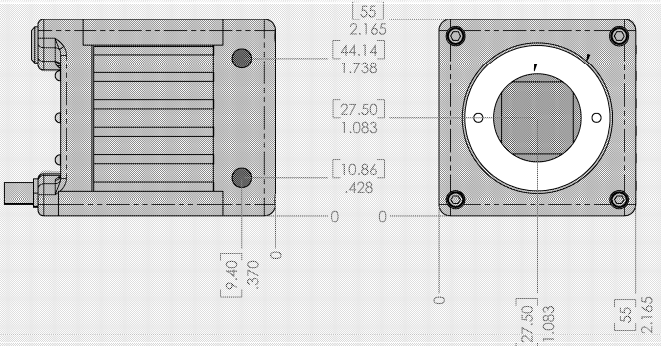

NORTH AMERICA
1202 E Park Ave
Tallahassee, FL 32301
United States
P: (+001) 850-222-5939
F: (+001) 850-222-4591

1 West Mountain Street,
Suite 3
Pasadena, CA 91103-3070
United States
P: (+001) 626-794-4649
F: (+001) 626-794-4651

www.idtvision.com

EUROPE
Via Pennella, 94
I-38057
Pergine Valsugana (TN)
Italy
P: (+39) 0461-532112
F: (+39) 0461-532104

Eekhoornstraat, 22
B-3920 - Lommel
Belgium
P: (+32) 11 551065
F: (+32) 11 554766

ASIA
Unit 6, 9F, 77, Hun Hua S. Road
Section 2, Taipei, Taiwan
P: (+02) 2706-2110
F: (+02) 2706-3837

No.388, Caonong Road,
Songjiang Industry Zone,
Shanghai, China
Zip Code: 201612
P: (+86) 21-57687667
F: (+86) 21-57686418

6F Sakurai Bidg.
2-8-19 Fukagawa,Koto-ku,Tokyo
135-0033, Japan
P: (+81) 3-5639-2773
F: (+81) 3-5639-2808
www.idt-japan.co.jp

POWERED BY IDT

9.5. Summary of Experiments

Summary of 3D Experiments

Classification of experiments from 09.03.2009														
Exp. Nr.:	bed height	stirrer position	stirrer speed	stirrer diameter	stator diameter	blade height	blade thickness	blade angle	number of blades	particle size		moisture	fluid	camera position
	h_{bed}	$h_{stirrer}$	$n_{stirrer}$	$d_{stirrer}$	d_{stator}	h_{blade}	s_{blade}	α	i_{blade}	d_{pmin}	d_{pmax}	w		
	[mm]	[mm]	[U/min]	[mm]	[mm]	[mm]	[mm]	[°]	[]	[mm]		[%]	[]	[]
001	40,00	20,00	60	135,00	145,00	20,00	5,00	45,00	4	6,00	6,00	dry	-	top
002	40,00	20,00	120	135,00	145,00	20,00	5,00	45,00	4	6,00	6,00	dry	-	top
003	40,00	10,00	60	135,00	145,00	20,00	5,00	45,00	4	4,00	4,00	dry	-	top
004	40,00	10,00	120	135,00	145,00	20,00	5,00	45,00	4	4,00	4,00	dry	-	top
005	40,00	10,00	60	135,00	145,00	20,00	5,00	45,00	4	0,40	0,60	dry	-	top
006	40,00	10,00	120	135,00	145,00	20,00	5,00	45,00	4	0,40	0,60	dry	-	top
007	40,00	20,00	60	135,00	145,00	20,00	5,00	45,00	4	0,40	0,60	dry	-	top
008	40,00	20,00	120	135,00	145,00	20,00	5,00	45,00	4	0,40	0,60	dry	-	top
009	40,00	10,00	60	135,00	145,00	20,00	5,00	45,00	4	0,40	0,60	2,0%	d. water	top
010	40,00	10,00	120	135,00	145,00	20,00	5,00	45,00	4	0,40	0,60	2,0%	d. water	top
011	40,00	20,00	60	135,00	145,00	20,00	5,00	45,00	4	0,40	0,60	2,0%	d. water	top
012	40,00	20,00	120	135,00	145,00	20,00	5,00	45,00	4	0,40	0,60	2,0%	d. water	top
013	40,00	10,00	60	135,00	145,00	20,00	5,00	45,00	4	4,00	4,00	2,0%	d. water	top
014	40,00	10,00	120	135,00	145,00	20,00	5,00	45,00	4	4,00	4,00	2,0%	d. water	top

Classification of experiments from 28.07.2009														
Experiment Nr.:	bed height	stirrer position	stirrer speed	stirrer diameter	stator diameter	blade height	blade thickness	blade angle	number of blades	particle size		moisture	fluid	camera position
	h_{bed}	$h_{stirrer}$	$n_{stirrer}$	$d_{stirrer}$	d_{stator}	h_{blade}	s_{blade}	α	i_{blade}	d_{pmin}	d_{pmax}	w		
	[mm]	[mm]	[U/min]	[mm]	[mm]	[mm]	[mm]	[°]	[]	[mm]		[%]	[]	[]
203	40,00	10,00	10	135,00	145,00	20,00	5,00	45,00	4	0,40	0,60	dry	-	top
204	40,00	10,00	5	135,00	145,00	20,00	5,00	45,00	4	0,40	0,60	dry	-	top
205	40,00	10,00	1	135,00	145,00	20,00	5,00	45,00	4	0,40	0,60	dry	-	top
206	40,00	10,00	10	135,00	145,00	20,00	5,00	45,00	4	0,40	0,60	0,1%	d. water	top
207	40,00	10,00	5	135,00	145,00	20,00	5,00	45,00	4	0,40	0,60	0,1%	d. water	top
208	40,00	10,00	1	135,00	145,00	20,00	5,00	45,00	4	0,40	0,60	0,1%	d. water	top
209	40,00	10,00	10	135,00	145,00	20,00	5,00	45,00	4	0,40	0,60	0,1%	d. water	top
210	40,00	10,00	10	135,00	145,00	20,00	5,00	45,00	4	0,40	0,60	0,2%	d. water	top
211	40,00	10,00	5	135,00	145,00	20,00	5,00	45,00	4	0,40	0,60	0,2%	d. water	top
212	40,00	10,00	1	135,00	145,00	20,00	5,00	45,00	4	0,40	0,60	0,2%	d. water	top
213	40,00	10,00	10	135,00	145,00	20,00	5,00	45,00	4	0,40	0,60	0,2%	d. water	top
214	40,00	10,00	10	135,00	145,00	20,00	5,00	45,00	4	0,40	0,60	0,3%	d. water	top
215	40,00	10,00	5	135,00	145,00	20,00	5,00	45,00	4	0,40	0,60	0,3%	d. water	top
216	40,00	10,00	1	135,00	145,00	20,00	5,00	45,00	4	0,40	0,60	0,3%	d. water	top
217	40,00	10,00	10	135,00	145,00	20,00	5,00	45,00	4	0,40	0,60	0,3%	d. water	top
218	40,00	10,00	10	135,00	145,00	20,00	5,00	45,00	4	0,40	0,60	0,4%	d. water	top
219	40,00	10,00	5	135,00	145,00	20,00	5,00	45,00	4	0,40	0,60	0,4%	d. water	top
220	40,00	10,00	1	135,00	145,00	20,00	5,00	45,00	4	0,40	0,60	0,4%	d. water	top
222	40,00	10,00	10	135,00	145,00	20,00	5,00	45,00	4	0,40	0,60	0,5%	d. water	top
223	40,00	10,00	5	135,00	145,00	20,00	5,00	45,00	4	0,40	0,60	0,5%	d. water	top
224	40,00	10,00	1	135,00	145,00	20,00	5,00	45,00	4	0,40	0,60	0,5%	d. water	top
225	40,00	10,00	10	135,00	145,00	20,00	5,00	45,00	4	0,40	0,60	0,5%	d. water	top

Classification of experiments 19.08.2009														
Experiment Nr.:	bed height	stirrer position	stirrer speed	stirrer diameter	stator diameter	blade height	blade thickness	blade angle	number of blades	particle size		moisture	fluid	camera position
	h_{bed}	$h_{stirrer}$	$n_{stirrer}$	$d_{stirrer}$	d_{stator}	h_{blade}	s_{blade}	α	i_{blade}	d_{pmin}	d_{pmax}	w		
	[mm]	[mm]	[U/min]	[mm]	[mm]	[mm]	[mm]	[°]	[]	[mm]		[%]	[]	[]
300	40,00	10,00	10	135,00	145,00	20,00	5,00	45,00	4	0,40	0,60	dry	-	top
301	40,00	10,00	5	135,00	145,00	20,00	5,00	45,00	4	0,40	0,60	dry	-	top
302	50,00	10,00	10	135,00	145,00	20,00	5,00	45,00	4	0,40	0,60	dry	-	top
303	50,00	10,00	5	135,00	145,00	20,00	5,00	45,00	4	0,40	0,60	dry	-	top
304	60,00	10,00	10	135,00	145,00	20,00	5,00	45,00	4	0,40	0,60	dry	-	top
305	60,00	10,00	5	135,00	145,00	20,00	5,00	45,00	4	0,40	0,60	dry	-	top
306	70,00	10,00	10	135,00	145,00	20,00	5,00	45,00	4	0,40	0,60	dry	-	top
307	70,00	10,00	5	135,00	145,00	20,00	5,00	45,00	4	0,40	0,60	dry	-	top
308	80,00	10,00	10	135,00	145,00	20,00	5,00	45,00	4	0,40	0,60	dry	-	top
309	80,00	10,00	5	135,00	145,00	20,00	5,00	45,00	4	0,40	0,60	dry	-	top
310	90,00	10,00	10	135,00	145,00	20,00	5,00	45,00	4	0,40	0,60	dry	-	top
311	90,00	10,00	5	135,00	145,00	20,00	5,00	45,00	4	0,40	0,60	dry	-	top
312	100,00	10,00	10	135,00	145,00	20,00	5,00	45,00	4	0,40	0,60	dry	-	top
313	100,00	10,00	5	135,00	145,00	20,00	5,00	45,00	4	0,40	0,60	dry	-	top
314	110,00	10,00	10	135,00	145,00	20,00	5,00	45,00	4	0,40	0,60	dry	-	top
315	110,00	10,00	5	135,00	145,00	20,00	5,00	45,00	4	0,40	0,60	dry	-	top
316	120,00	10,00	10	135,00	145,00	20,00	5,00	45,00	4	0,40	0,60	dry	-	top
317	120,00	10,00	5	135,00	145,00	20,00	5,00	45,00	4	0,40	0,60	dry	-	top

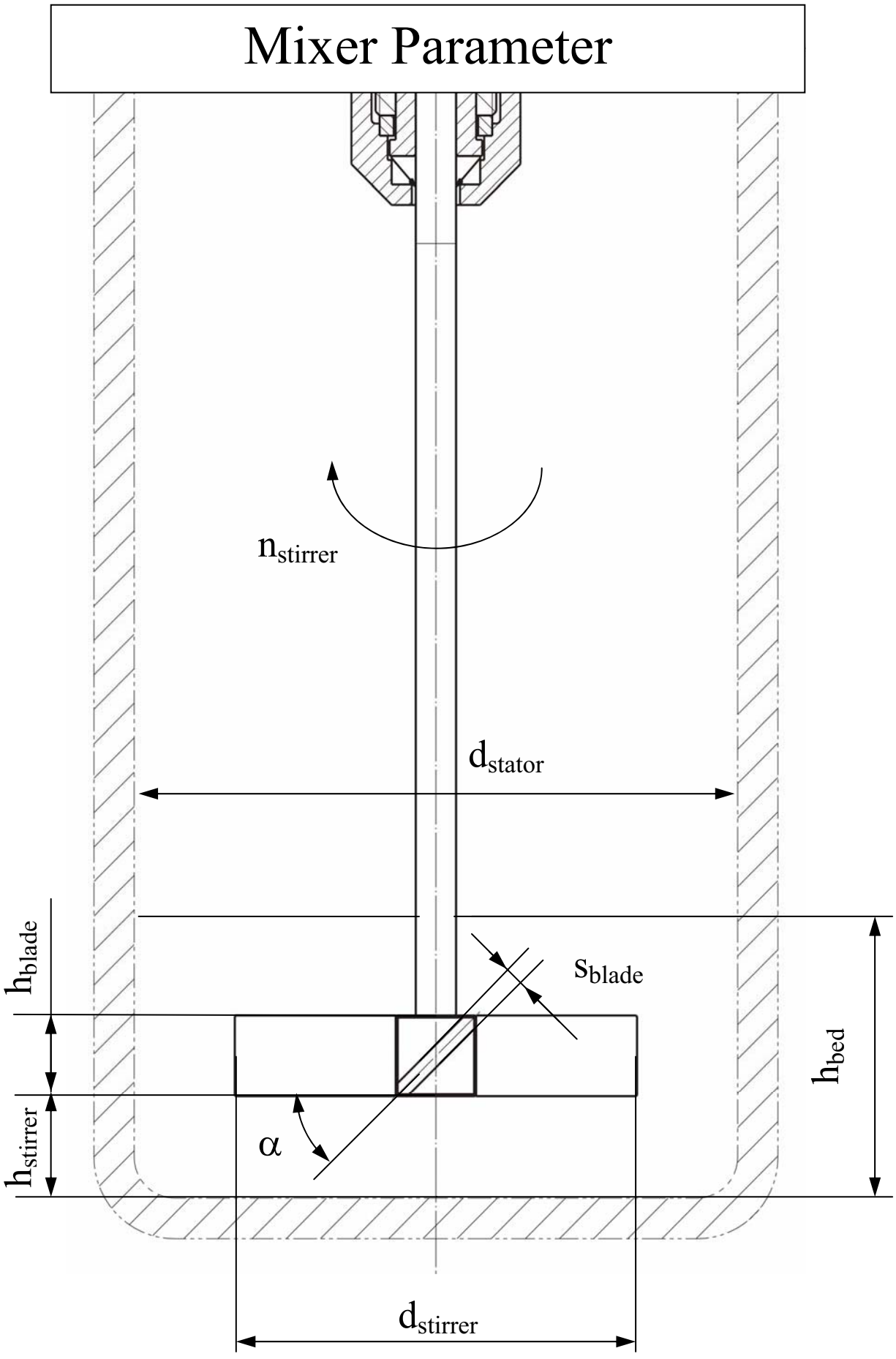
Mixer Parameter
$n_{stirrer}$
d_{stator}
h_{blade}
s_{blade}
h_{bed}
$h_{stirrer}$
α
$d_{stirrer}$

Summary of 2D Experiments

Experiments from 26.10.2009											
Experiment Nr.:	bed height	blade position	voltage of powersupply	particle size		blade dimensions	blade angle	upper edge of blade	number of images	box velocity	time range of image series
	h_{bed}	h_{blade}	U	d_{pmin}	d_{pmax}	l_{blade} x b_{blade} x s_{blade}	α	h_{bup}		v_{box}	t
	[mm]	[mm]	[V]	[mm]	[mm]	[mm]	[°]	[mm]	[]	[m/s]	[s]
015	40,00	0,00	10,00	4,00	4,00	97x50x5	45,0	70,71	199	0,14	2,0 - 2,4
016	40,00	0,00	15,00	4,00	4,00	97x50x5	45,0	70,71	199	0,23	2,0 - 2,4
017	40,00	0,00	20,00	4,00	4,00	97x50x5	45,0	70,71	199	0,24	2,0 - 2,4
018	60,00	0,00	10,00	4,00	4,00	97x50x5	45,0	70,71	99	0,14	1,8 - 2,0
019	60,00	0,00	15,00	4,00	4,00	97x50x5	45,0	70,71	49	0,21	0,8 - 0,9
020	60,00	0,00	20,00	4,00	4,00	97x50x5	45,0	70,71	49	0,22	0,82 - 0,92
021	80,00	0,00	10,00	4,00	4,00	97x50x5	45,0	70,71	49	0,13	0,8 - 0,9
022	80,00	0,00	15,00	4,00	4,00	97x50x5	45,0	70,71	49	0,135	0,8 - 0,9
023	80,00	0,00	20,00	4,00	4,00	97x50x5	45,0	70,71	49	0,14	0,8 - 0,9
024	100,00	0,00	-	4,00	4,00	97x50x5	45,0	70,71	99	0,13	1,4 - 1,6
025	100,00	0,00	-	4,00	4,00	97x50x5	45,0	70,71	99	0,13	1,4 - 1,6
026	120,00	0,00	-	4,00	4,00	97x50x5	45,0	70,71	49	0,065	1,9 - 2,0
027	120,00	20,00	-	4,00	4,00	97x50x5	45,0	90,71	49	0,07	1,8 - 1,9
028	120,00	40,00	-	4,00	4,00	97x50x5	45,0	110,71	99	0,09	2,2 - 2,4

Summary of 2D Experiments

Experiments from 20.11.2009												
Experiment Nr.:	bed height	blade position	voltage of powersupply	particle size		blade dimensions	blade angle	upper edge of blade	number of images	box velocity	time range of image series
	h_{bed}	h_{blade}	U	d_{pmin}	d_{pmax}	l_{blade} x b_{blade} x s_{blade}	α	h_{bup}		v_{box}	t
	[mm]	[mm]	[V]	[mm]	[mm]	[mm]	[°]	[mm]	[]	[m/s]	[s]
029	50,00	0,00	8,20	4,00	4,00	50x30x5	45,0	21,21	200	0,15	1,6 - 2.0
030	50,00	0,00	9,50	4,00	4,00	50x30x5	45,0	21,21	200	0,21	1,1 - 1,5
031	100,00	0,00	20,00	4,00	4,00	50x30x5	45,0	21,21	100	0,1	1,6 - 1,8
032	100,00	50,00	9,00	4,00	4,00	50x30x5	45,0	71,21	200	0,21	1,0 - 1,4
034	50,00	0,00	9,00	4,00	4,00	50x30x5	135,0	21,21	200	0,155	1,6 - 2,0
035	50,00	0,00	10,00	4,00	4,00	50x30x5	135,0	21,21	200	0,205	1,3 - 1,7
036	100,00	0,00	35,00	4,00	4,00	50x30x5	135,0	21,21	100	0,11	0,8 - 1,0
037	100,00	50,00	10,00	4,00	4,00	50x30x5	135,0	71,21	200	0,21	1,3 - 1,7
039	50,00	0,00	9,20	4,00	4,00	50x30x5	90,0	30,00	200	0,15	1,6 - 2,0
040	50,00	0,00	10,00	4,00	4,00	50x30x5	90,0	30,00	200	0,205	1,6 - 2,0
041	100,00	0,00	36,00	4,00	4,00	50x30x5	90,0	30,00	100	0,085	1,8 - 2,0
042	100,00	50,00	10,00	4,00	4,00	50x30x5	90,0	80,00	200	0,22	1,6 - 2,0

Summary of 2D Experiments

Experiments from 20.11.2009											
Experiment Nr.:	bed height	blade position	voltage of powersupply	particle size		blade dimensions	blade angle	upper edge of blade	number of images	box velocity	time range of image series
	h_{bed}	h_{blade}	U	d_{pmin}	d_{pmax}	l_{blade} x b_{blade} x s_{blade}	α	h_{bup}		v_{box}	t
	[mm]	[mm]	[V]	[mm]	[mm]	[mm]	[°]	[mm]	[]	[m/s]	[s]
044	50,00	0,00	9,00	1,50	1,85	50x30x5	45,0	21,21	200	0,145	1,7 - 2,1
045	50,00	0,00	9,80	1,50	1,85	50x30x5	45,0	21,21	200	0,22	2,3 - 2,7
046	50,00	0,00	8,00	1,50	1,85	50x30x5	45,0	21,21	200	0,1	1,8 - 2,2
049	50,00	0,00	9,00	1,50	1,85	50x30x5	135,0	21,21	200	0,14	2,0 - 2,4
050	50,00	0,00	10,40	1,50	1,85	50x30x5	135,0	21,21	200	0,2	2,0 - 2,4
051	50,00	0,00	8,50	1,50	1,85	50x30x5	135,0	21,21	200	0,1	1,8 - 2,2
054	50,00	0,00	9,90	1,50	1,85	50x30x5	90,0	30,00	200	0,15	2,5 - 2,9
055	50,00	0,00	11,10	1,50	1,85	50x30x5	90,0	30,00	200	0,2	2,4 - 2,8
056	50,00	0,00	9,00	1,50	1,85	50x30x5	90,0	30,00	200	0,1	1,8 - 2,2

Summary of 2D Experiments

Experiments from 20.11.2009											
Experiment Nr.:	bed height	blade position	voltage of powersupply	particle size		blade dimensions	blade angle	upper edge of blade	number of images	box velocity	time range of image series
	h_{bed}	h_{blade}	U	d_{pmin}	d_{pmax}	l_{blade} x b_{blade} x s_{blade}	α	h_{bup}		v_{box}	t
	[mm]	[mm]	[V]	[mm]	[mm]	[mm]	[°]	[mm]	[]	[m/s]	[s]
059	50,00	0,00	11,00	0,40	0,60	50x30x5	45,0	21,21	200	0,21	2,0 - 2,4
060	50,00	0,00	9,00	0,40	0,60	50x30x5	45,0	21,21	200	0,11	1,6 - 2,0
061	50,00	0,00	9,20	0,40	0,60	50x30x5	45,0	21,21	150	0,16	1,4 - 1,7
064	50,00	0,00	11,00	0,40	0,60	50x30x5	135,0	21,21	150	0,21	1,3 - 1,6
065	50,00	0,00	9,00	0,40	0,60	50x30x5	135,0	21,21	200	0,11	1,4 - 1,8
066	50,00	0,00	9,20	0,40	0,60	50x30x5	135,0	21,21	200	0,145	2,6 - 3,0
069	50,00	0,00	10,00	0,40	0,60	50x30x5	90,0	30,00	200	0,21	1,2 - 1,6
070	50,00	0,00	9,40	0,40	0,60	50x30x5	90,0	30,00	200	0,15	2,4 - 2,8
071	50,00	0,00	8,80	0,40	0,60	50x30x5	90,0	30,00	200	0,11	1,1 - 1,5

2D Setup Parameter

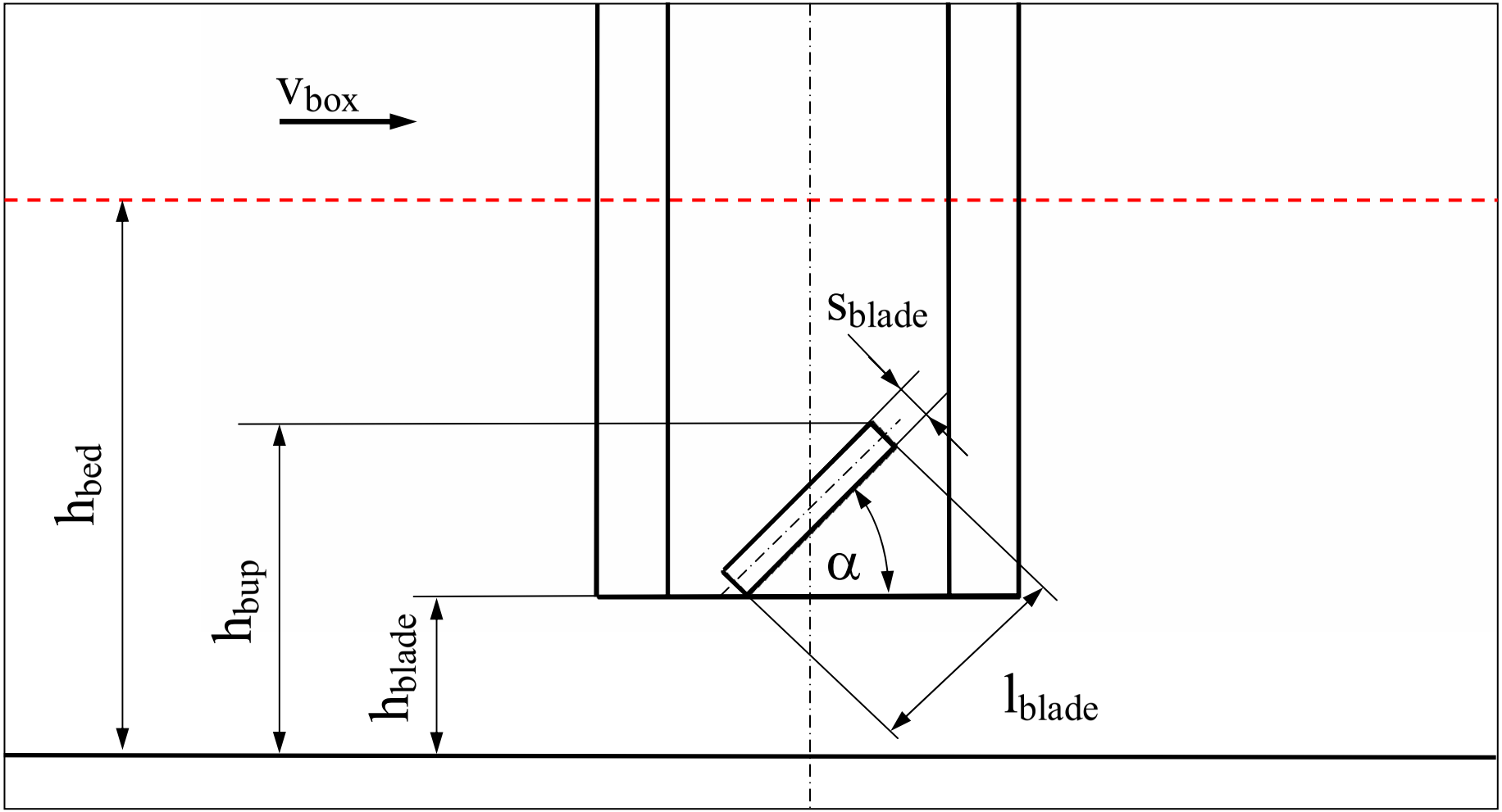

9.6. Comparison of 3D Velocity Fields

Particle Size

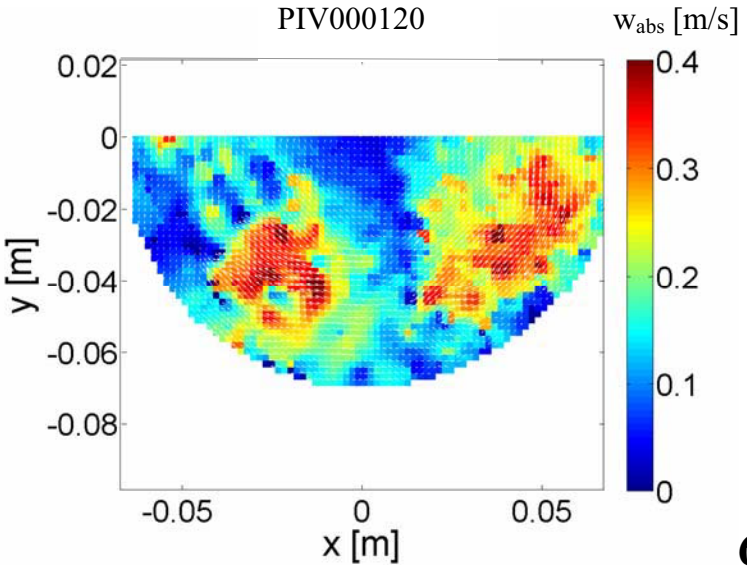

6 [mm] (case 001)

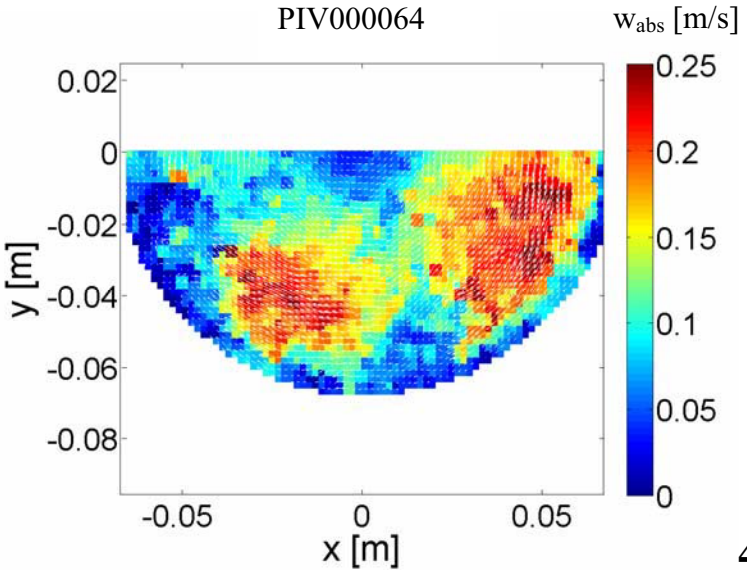

4 [mm] (case 003)

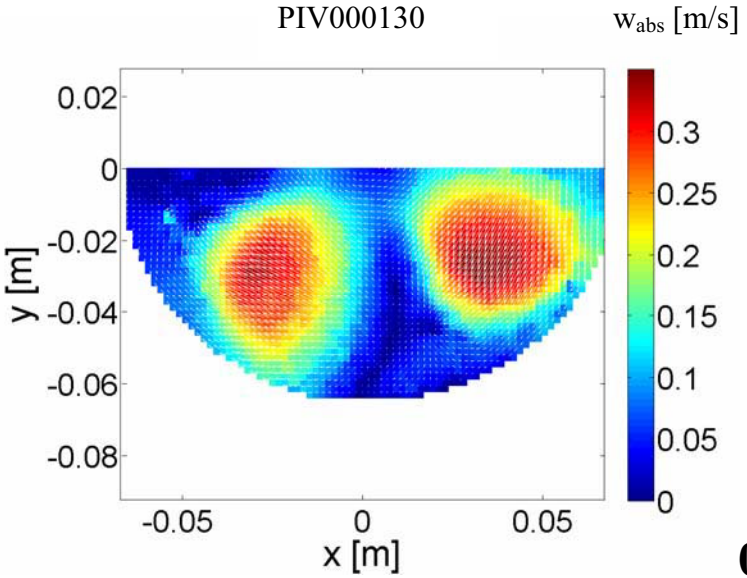

0.5 [mm] (case 005)

Stirrer Speed

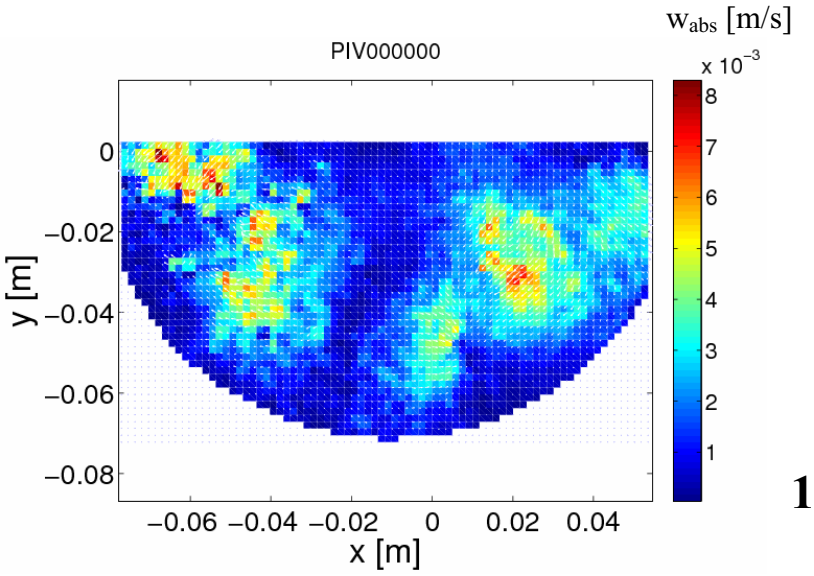

1 [rev/min] (case 205)

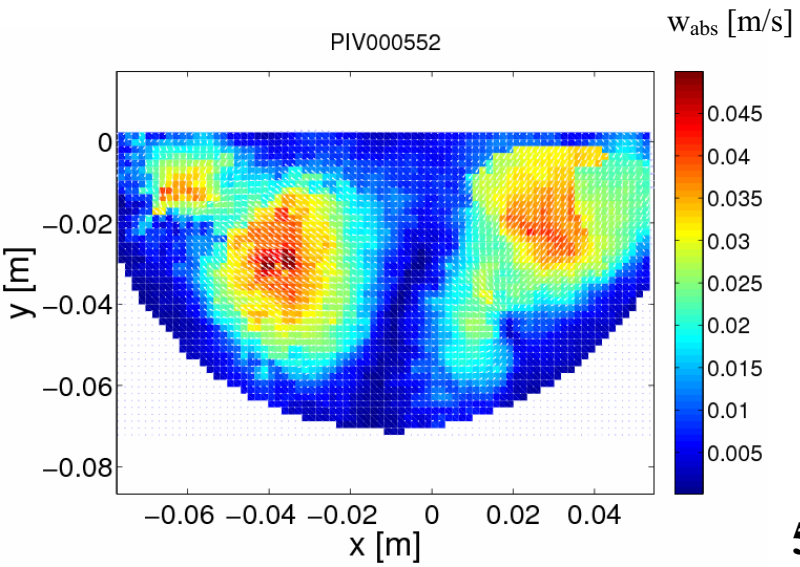

5 [rev/min] (case 204)

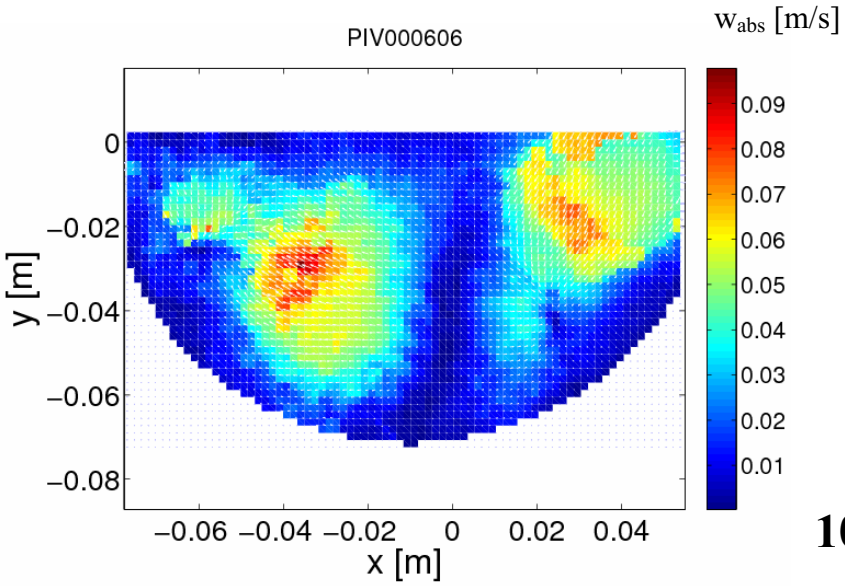

10 [rev/min] (case 203)

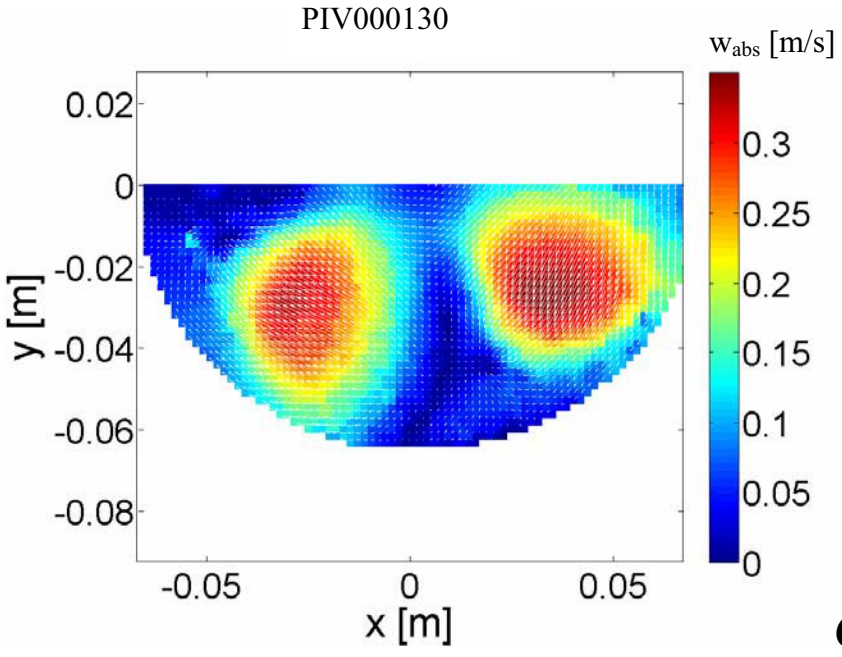

60 [rev/min] (case 005)

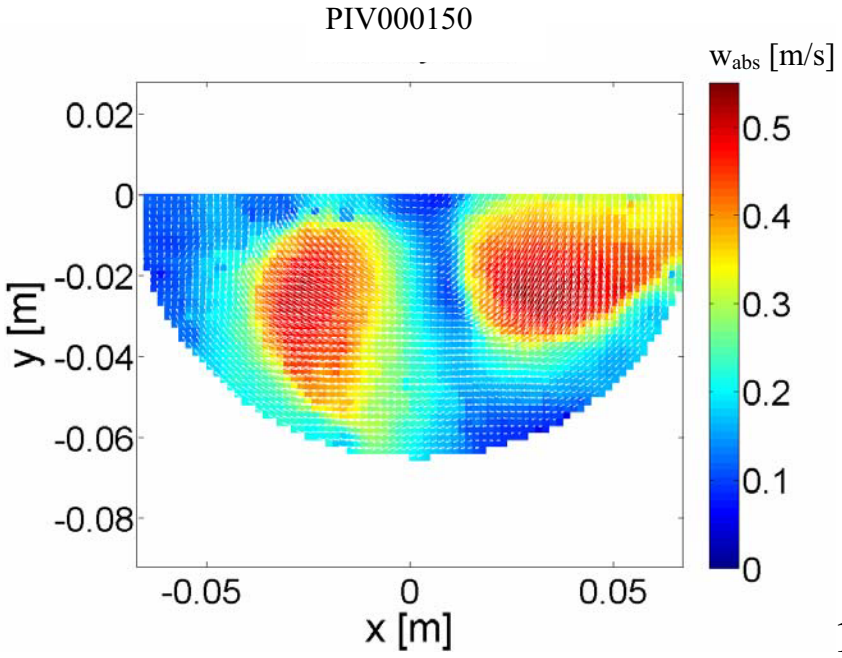

120 [rev/min] (case 006)

Stirrer Position

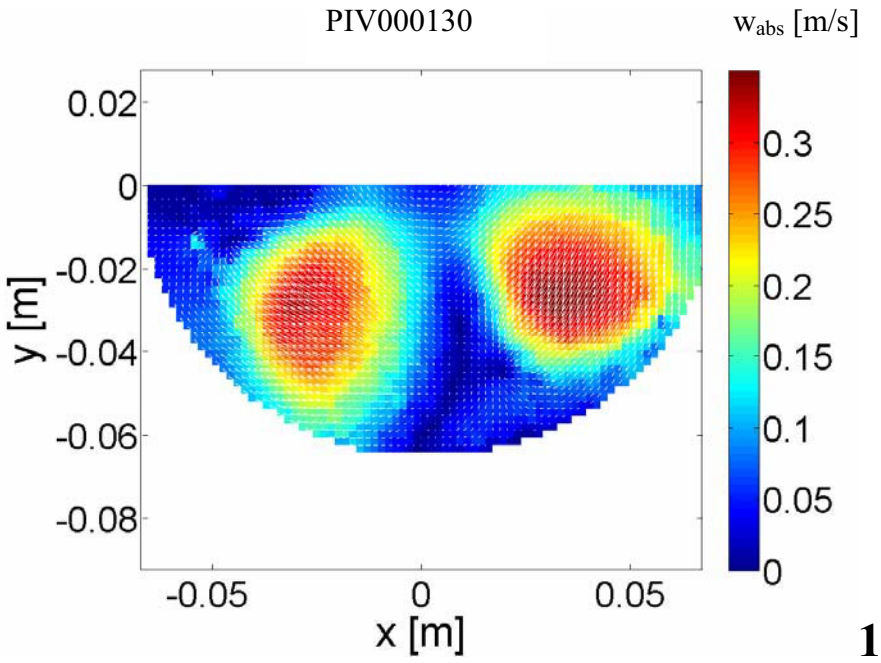

10 [mm] (case 005)

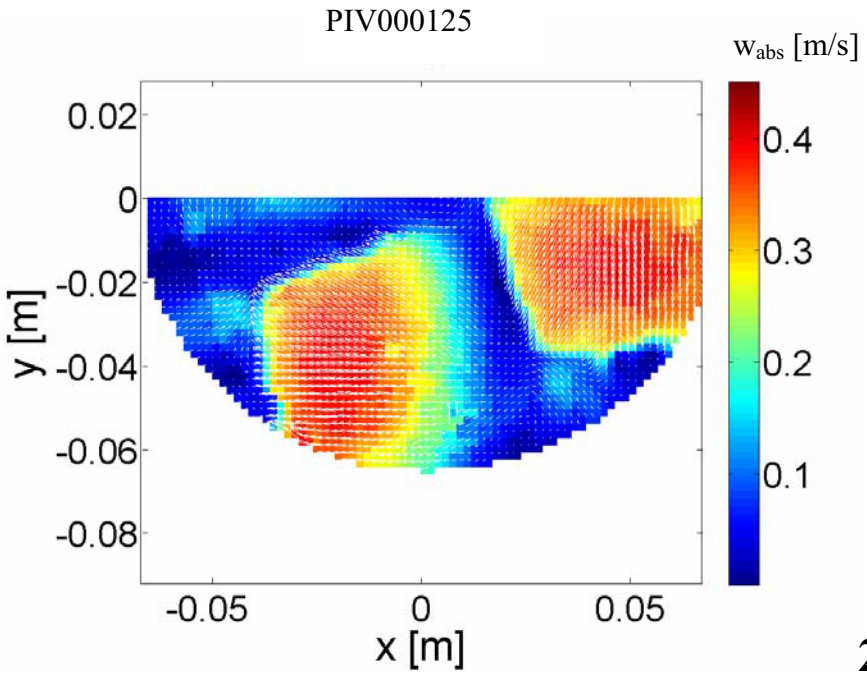

20 [mm] (case 007)

Moisture Content

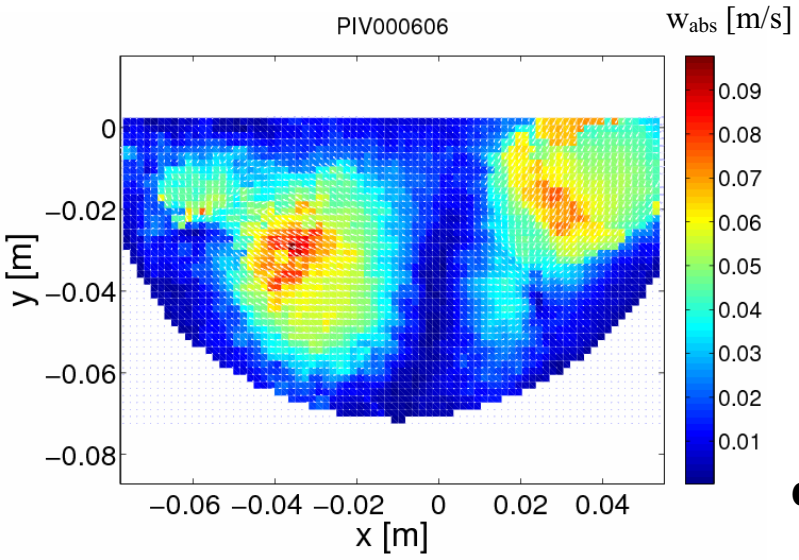

dry (case 203)

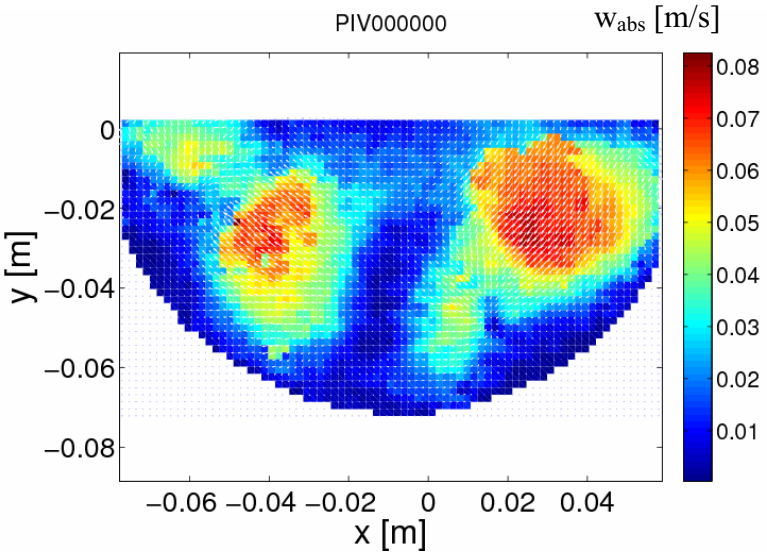

0.1 [vol%] (case 209)

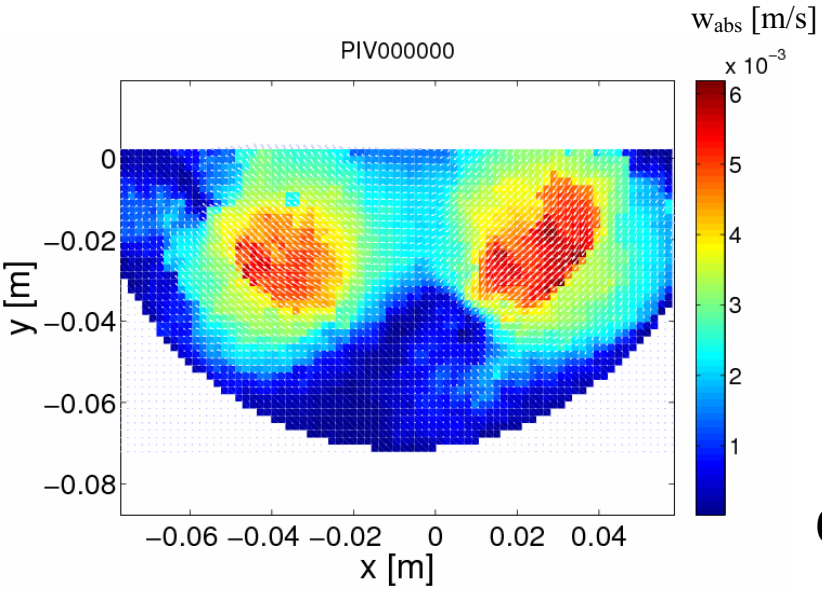

0.2 [vol%] (case 212)

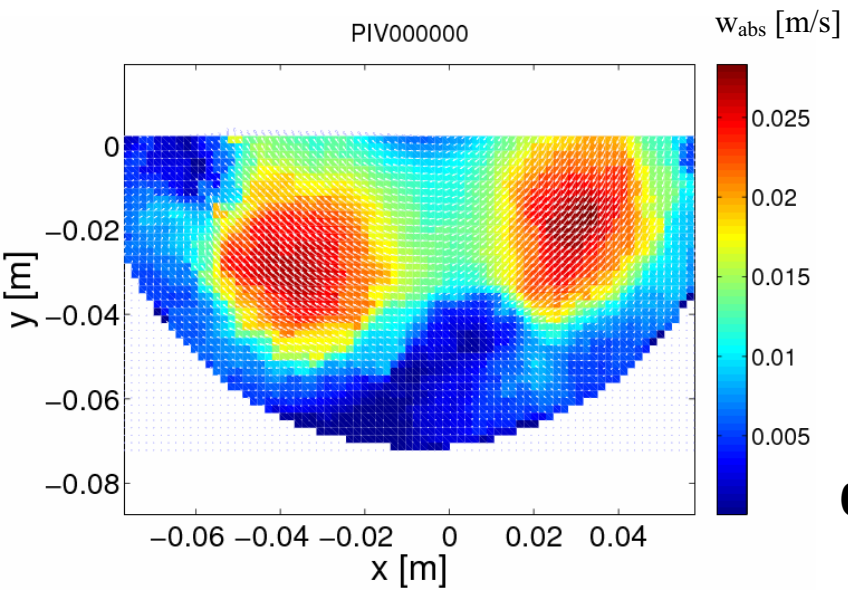

0.3 [vol%] (case 215)

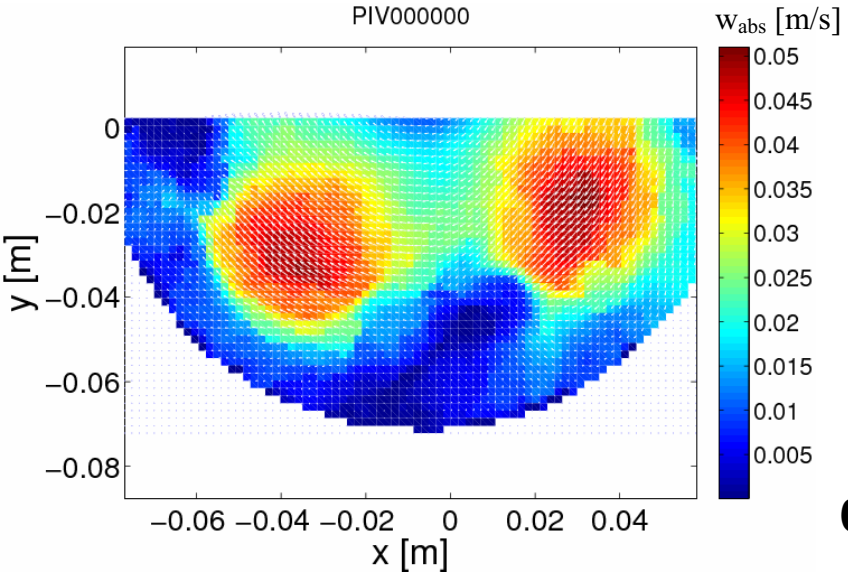

0.4 [vol%] (case 218)

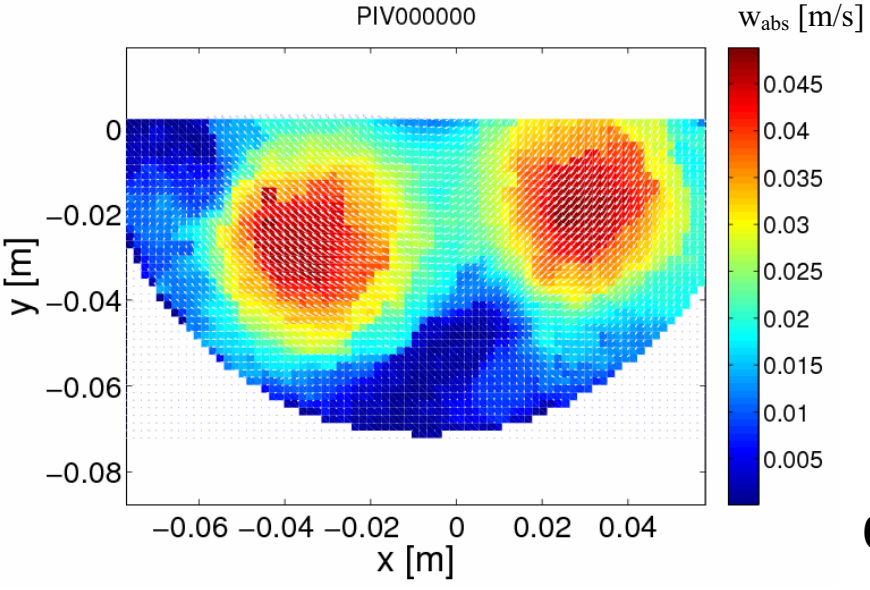

0.5 [vol%] (case 221)

Filling Height

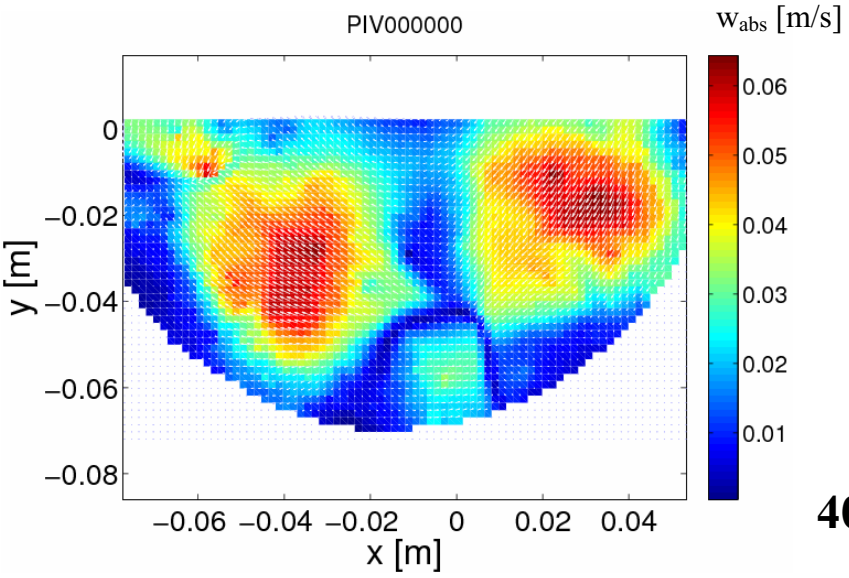

40 [mm] (case 300)

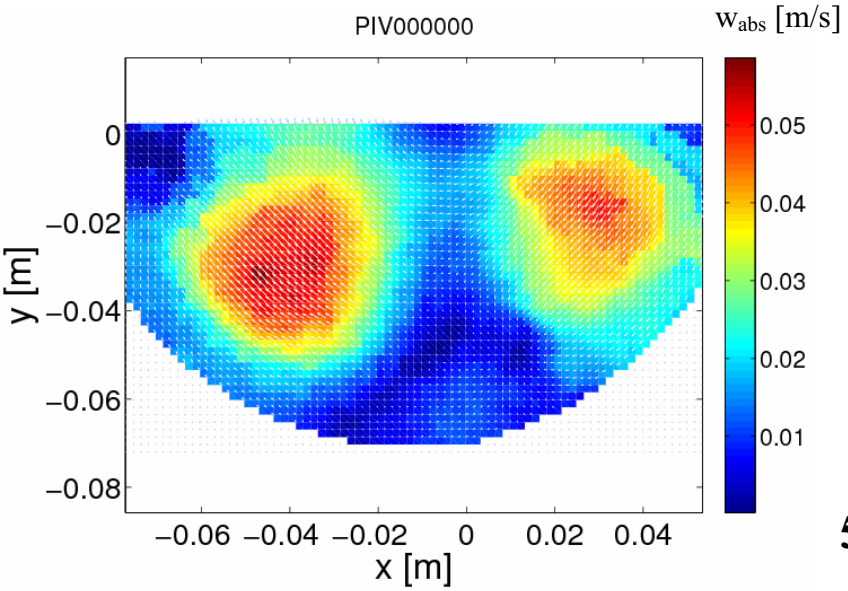

50 [mm] (case 302)

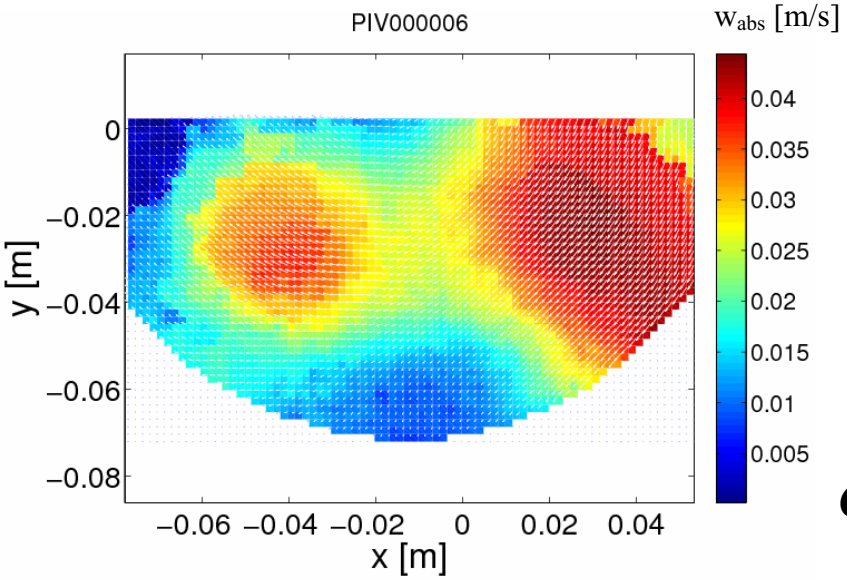

60 [mm] (case 304)

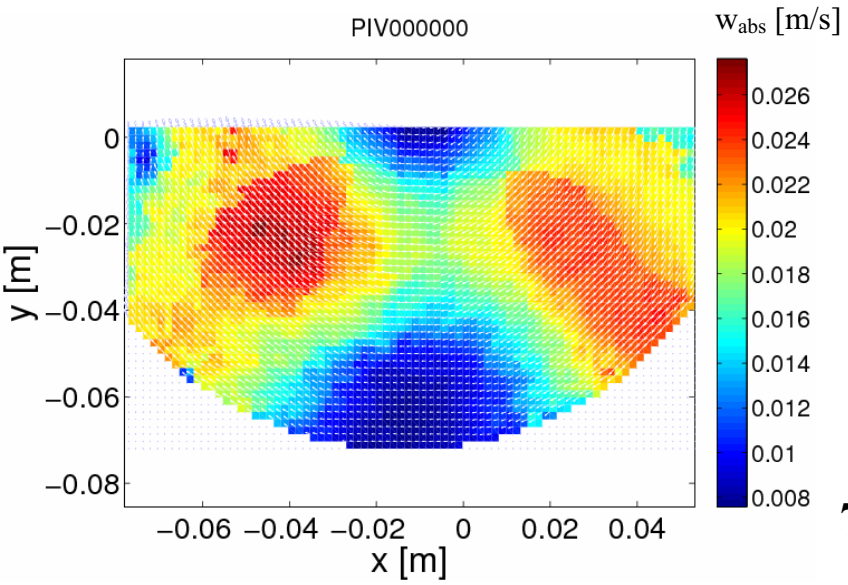

70 [mm] (case 306)

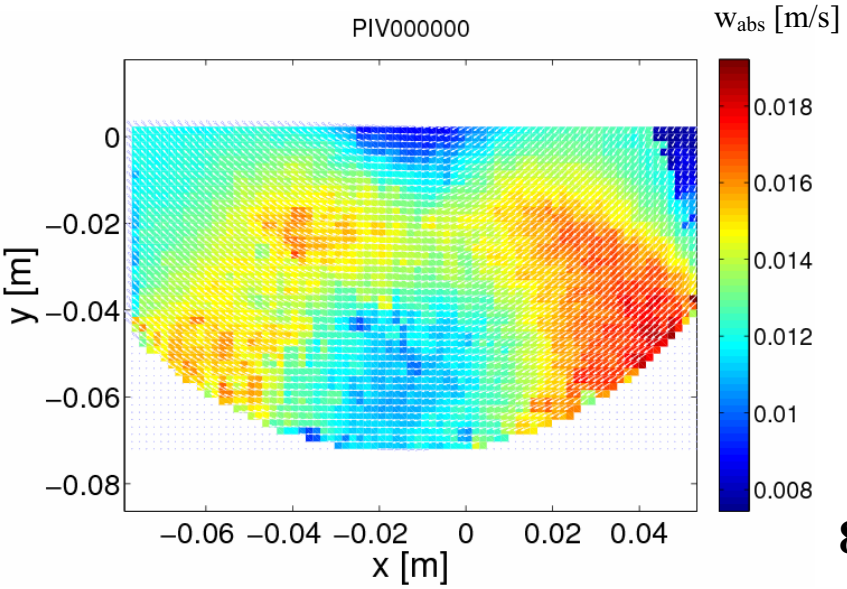

80 [mm] (case 308)

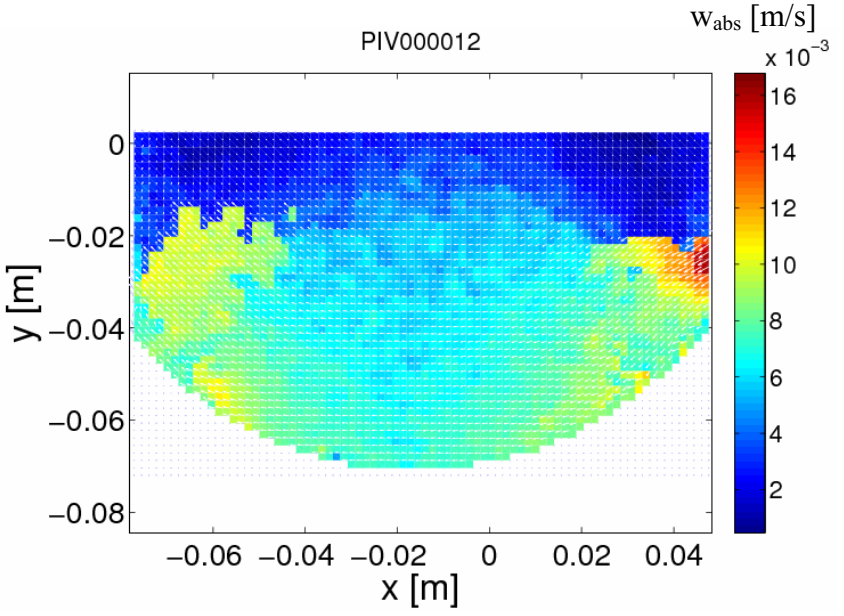

90 [mm] (case 310)

9.7. Comparison of 2D Mean Velocity Fields

Box Velocity

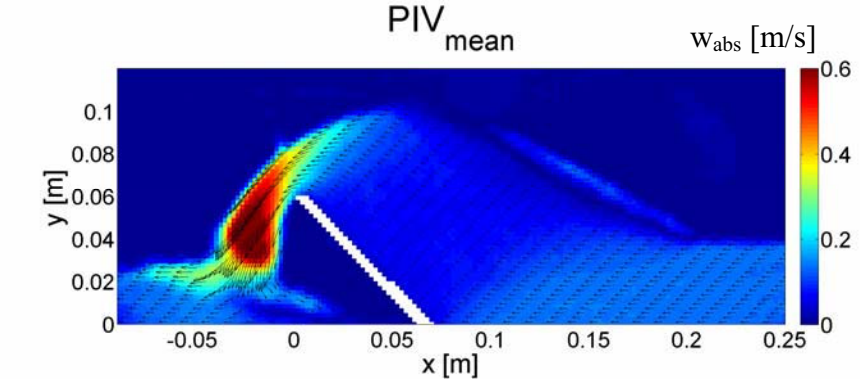

0.14 [m/s] (case 015)

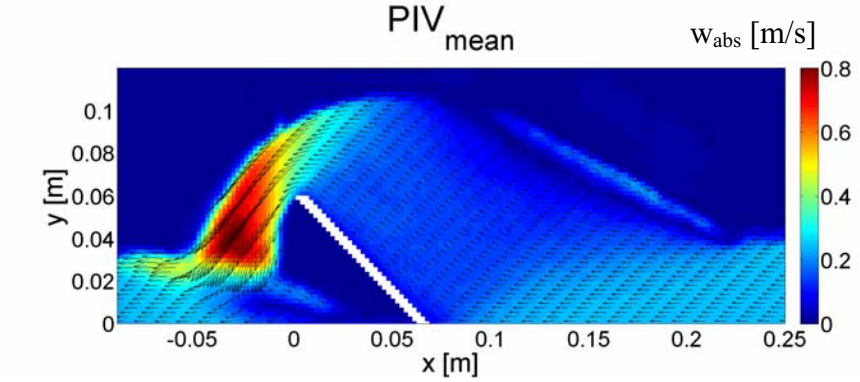

0.23 [m/s] (case 016)

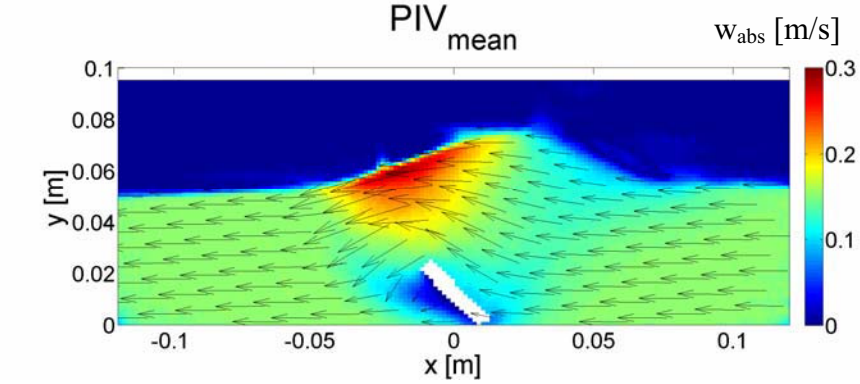

0.145 [m/s] (case 044)

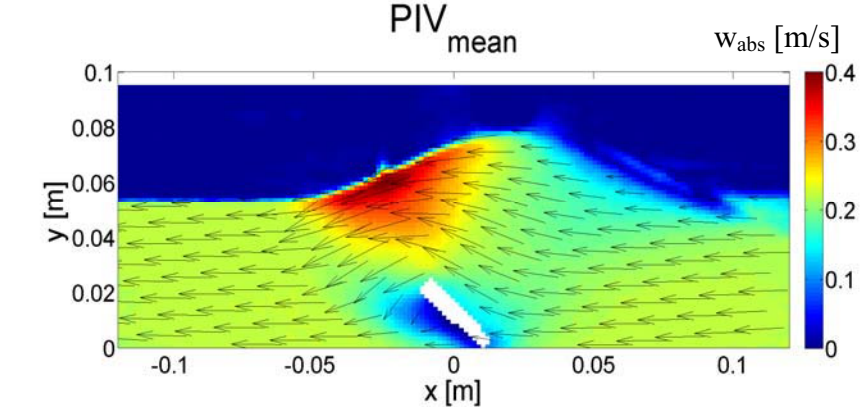

0.22 [m/s] (case 045)

Bed Height

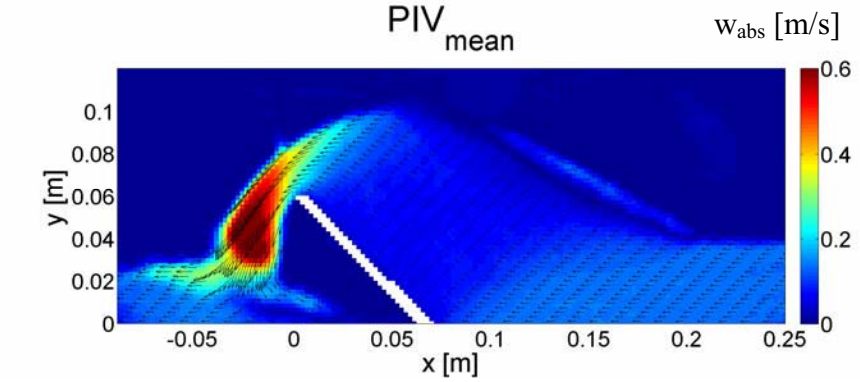

40 [mm] (case 015)

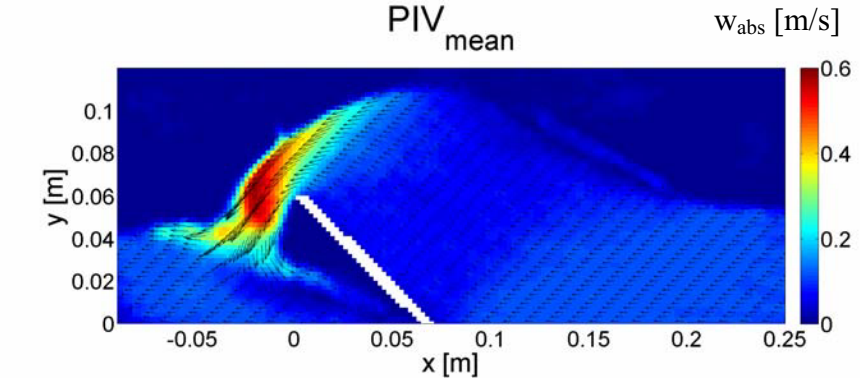

60 [mm] (case 018)

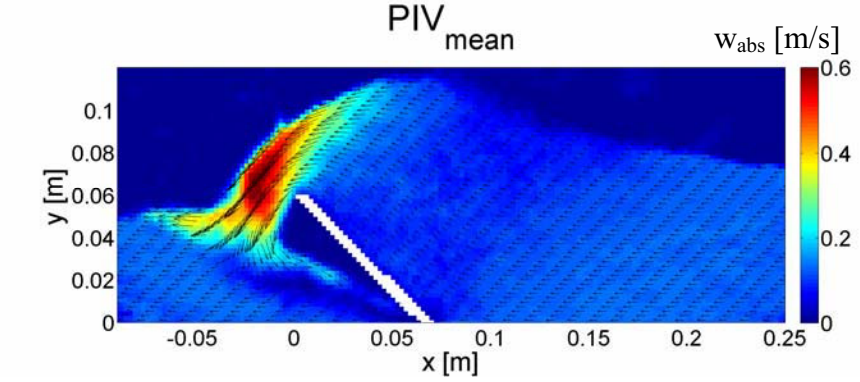

80 [mm] (case 023)

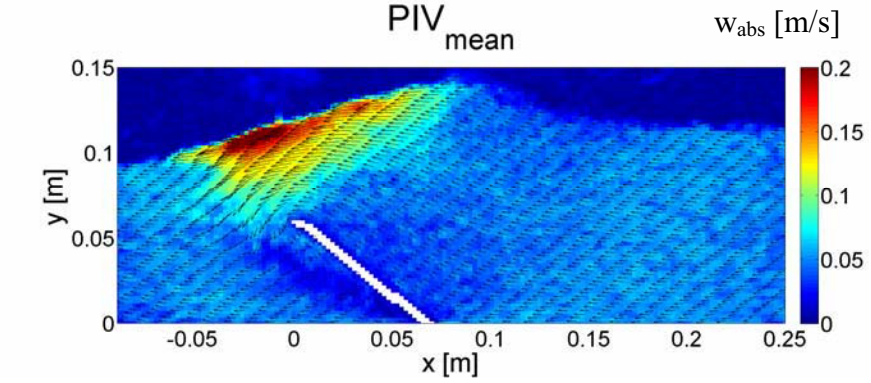

120 [mm] (case 026)

Blade Position

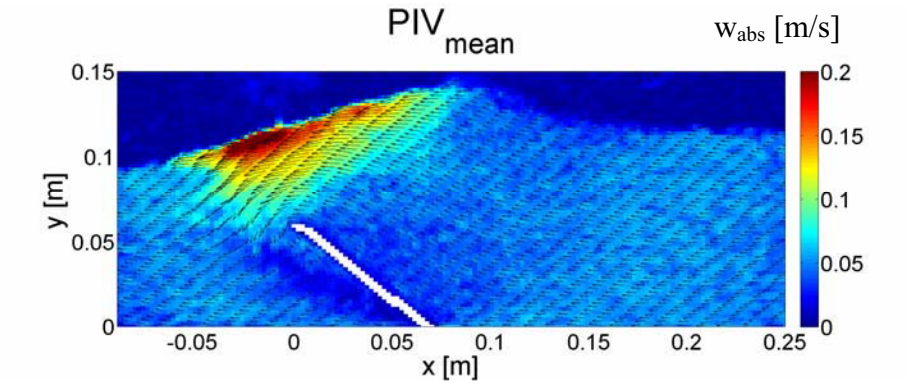

0 [mm] (case 026)

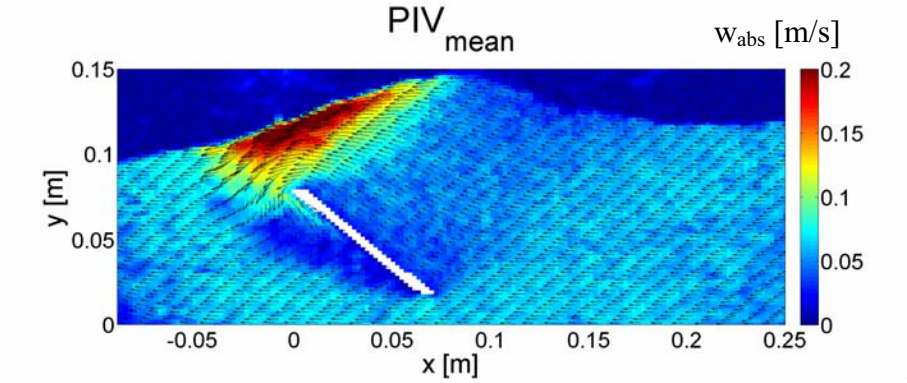

20 [mm] (case 027)

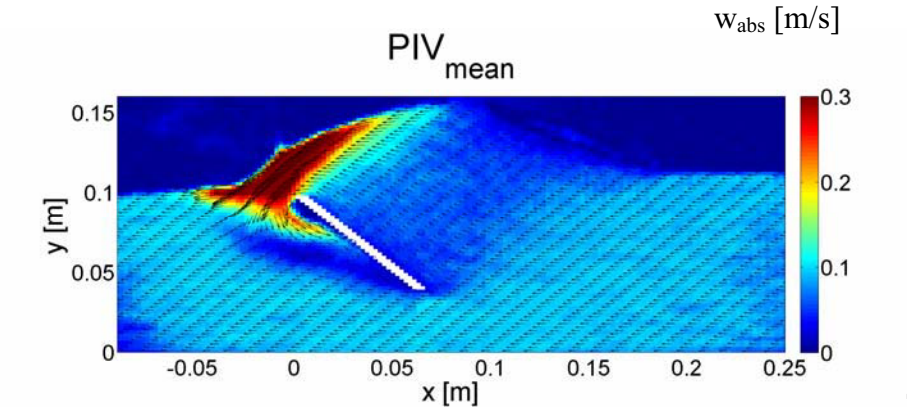

40 [mm] (case 028)

Blade Angle

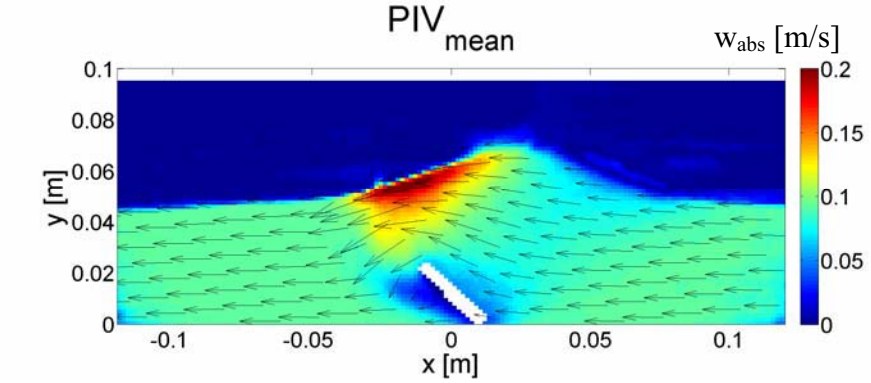

45 [°] (case 046)

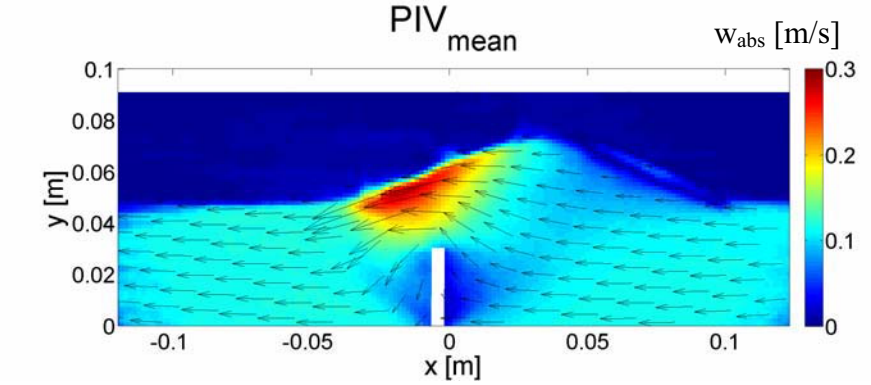

90 [°] (case 056)

135 [°] (case 051)

Particle Size

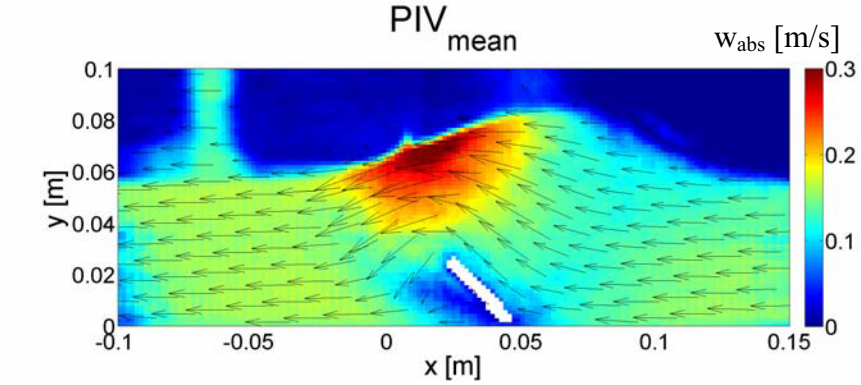

4 [mm] (case 029)

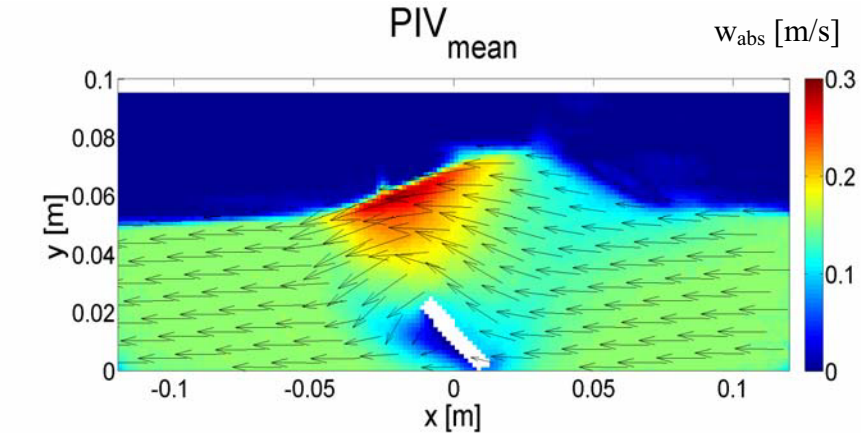

1.675 [mm] (case 044)